The evolution of low-metallicity massive stars

Dissertation
zur
Erlangung des Doktorgrades (Dr. rer. nat.)
der
Mathematisch-Naturwissenschaftlichen Fakultät
der
Rheinischen Friedrich-Wilhelms-Universität Bonn

von
Dorottya Szécsi
aus
Budapest, Ungarn

Bonn, 2016

Dieser Forschungsbericht wurde als Dissertation von der
Mathematisch-Naturwissenschaftlichen Fakultät der Universität Bonn angenommen und ist
auf dem Hochschulschriftenserver der ULB Bonn
http://hss.ulb.uni-bonn.de/diss_online elektronisch publiziert.

1. Gutachter:	Prof. Dr. Norbert Langer
2. Gutachter:	Prof. Dr. Peter Schneider
Tag der Promotion:	4. Juli 2016
Erscheinungsjahr:	2016

Contents

Abstract

Massive star evolution taking place in astrophysical environments consisting almost entirely of hydrogen and helium – in other words, low-metallicity environments – is responsible for some of the most intriguing and energetic cosmic phenomena, including supernovae, gamma-ray bursts and gravitational waves. This thesis aims to investigate the life and death of metal-poor massive stars, using theoretical simulations of the stellar structure and evolution.

Evolutionary models of rotating, massive stars (9-600 $M_{\odot}$) with an initial metal composition appropriate for the low-metallicity dwarf galaxy I Zwicky 18 are presented and analyzed. We find that the fast rotating models ($\gtrsim$ 300 km/s) become a particular type of objects predicted only at low-metallicity: the so-called Transparent Wind Ultraviolet INtense (TWUIN) stars. TWUIN stars are fast rotating massive stars that are extremely hot (90 kK), very bright and as compact as Wolf–Rayet stars. However, as opposed to Wolf–Rayet stars, their stellar winds are optically thin. As these hot objects emit intense UV radiation, we show that they can explain the unusually high number of ionizing photons of the dwarf galaxy I Zwicky 18, an observational quantity that cannot be understood solely based on the normal stellar population of this galaxy.

On the other hand, we find that the most massive, slowly rotating models become another special type of object predicted only at low-metallicity: core-hydrogen-burning cool supergiant stars. Having a slow but strong stellar wind, these supergiants may be important contributors in the chemical evolution of young galactic globular clusters. In particular, we suggest that the low mass stars observed today could form in a dense, massive and cool shell around these, now dead, supergiants. This scenario is shown to explain the anomalous surface abundances observed in these low mass stars, since the shell itself, having been made of the mass ejected by the supergiant's wind, contains nuclear burning products in the same ratio as observed today in globular clusters stars.

Further elaborating the fast rotating TWUIN star models, we predict that some of them will become Wolf–Rayet stars near the end of their lives. From this we show that our models can self-consistently explain both the high ionizing flux and the number of Wolf–Rayet stars in I Zwicky 18. Moreover, some of our models are predicted to explode as long-duration gamma-ray bursts. Thus, we speculate that the high ionizing flux observed can be a signpost for upcoming gamma-ray bursts in dwarf galaxies.

Although our models have been applied to interpret observations of globular clusters and dwarf galaxies, we point out that they could also be used in the context of other low-metallicity environments as well. Understanding the early Universe, for example, requires to have a solid knowledge of how massive stars at low-metallicity live and interact with their environments. Thus, we expect that the models and results presented in this thesis will be beneficial for not only the massive star community, but for the broader astronomy and cosmology community as well.

CHAPTER 1

Introduction

I have walked a stair of swords,
I have worn a coat of scars.
I have vowed with hollow words,
I have lied my way to the stars

– Catherine Fisher: Songs of Sapphique

1.1 The night-sky and beyond

Looking up to the night-sky, one is impressed by the most wondrous of all miracles of the world.

Stars.

Shining bright, they lie there persistently and gloriously, inspiring our fragile human soul since the beginning of time to reach out and explore their mysteries. They have shown the way for us to navigate and discover land and sea, they have made us unravel the secrets of the atom and the nucleus.

They have taught us about our humble place in the Universe.

Stars are isolated gas-spheres in outer space, bound together by gravity, radiating away light released by nuclear fusion. But their story is not that simple, as anyone who looks through a telescope would soon figure out. Because there are stars in the dark spots of the sky, too faint for the naked eye, but well-resolved by the telescope. There are stars in real isolation, there are stars with a companion, there are stars that mostly emit red light, or yellow light, or blue light. There are even stars that emit light in the invisible ultraviolet band and so on, and there are stars surrounded by shining nebulae.

Then, there are giant congregations of stars called clusters, and there are even larger congregations of stars called galaxies.

And then there are the stellar explosions.

This work aims to expand our knowledge about stars: in particular, about massive stars at low metallicity. These special objects, as we will see, have an important role in the Universe in several aspects. Their lives are short but intense: having strong stellar winds and therefore losing a remarkable amount of mass, and then ending their lives with an explosion as supernova or gamma-ray burst, they influence their environment by changing the chemical composition and triggering or stopping the nearby star formation.

The initial chemical composition of a star influences its whole evolution, internal structure, circumstellar surroundings and its death as well. The Sun, as well as all the stars that are visible on the night-sky, are composed of 73.81% hydrogen ($X_\odot$), 24.85% helium ($Y_\odot$) and 1.34% heavier elements ('metals', $Z_\odot$ Asplund et al., 2009). However, stars in the two neighbor galaxies, the Large and Small Magellanic Clouds (LMC, SMC) have different compositions, with subsolar metallicities of Z_{LMC} =0.47% and Z_{SMC} =0.21%, respectively (Brott et al., 2011).

But we can observe environments at even lower metallicity.

1.2 Low-metallicity environments

1.2.1 The high-redshift Universe

Since the speed of light is a physical constant, the light that we see today when looking at far-away stars or galaxies must have been emitted in the past. This also means that the the more distant objects we observe, the older the version of the Universe we see (as illustrated by Fig. 1.1). This is fortunate because that way we can obtain observational constraints on how stars evolved in the past.

One aspect of observing the early Universe is that the wavelength, λ_{emi} of the light that arrives from these sources is shifted towards the red part of the observed spectrum: $\lambda_{obs} > \lambda_{emi}$ (Dodelson, 2003). This is due to the expansion of the Universe: since these galaxies are moving away from us, the light that we collect from them is necessarily redshifted (cf. Doppler effect). Because the emitted light rays travel through a developing and expanding Universe, distances

Figure 1.1. Excerpt of the Hubble Deep Field: an image taken by the Hubble Space Telescope from a small part of the sky with almost no galactic foreground stars in the field. The long exposure revealed about 3000 galaxies, some of which are among the youngest and most distant known. Credit: *hubblesite.org*.

on these cosmological scales cannot be easily related to the traditional length units such as kilometers or parsecs. Instead, we usually use the redshift, z, defined as $z = \lambda_{obs}/\lambda_{emi} - 1$, as a measure of the distance of a given object from us. The larger the redshift, the more distant (and the older) the object. Hence the term high-redshift Universe refers to the early Universe.

Another aspect of observing the early Universe is that one needs very efficient, highly-resolving telescopes, collecting light with a long exposure time. Fortunately, we have such telescopes today. Some orbiting around the Earth in outer space (like the Hubble Space Telescope), some built on the top of special mountains (like the W. M. Keck Observatory on Mauna Kea, Hawaii), these instruments are able to picture galaxies up to a redshift of $z \sim 7$ (see e.g. Abraham et al., 1996; Sobral et al., 2015). Additionally, we catch bright and short transient events associated with stellar explosion such as supernovae and gamma-ray bursts on a daily basis. Some of them came from sources as far away as $z = 9.4$ (Cucchiara et al., 2011).

After the primordial nucleosynthesis and before the first stars were born, the Universe consisted of mostly hydrogen and helium with a ^{7}Li mass fraction of 10^{-9} (Mathews et al., 2005). The first generation of stars (massive stars in particular, initially consisting of the primordial hydrogen and helium) synthesized heavy elements via nuclear fusion, either in hydrostatic equilibrium or during an explosion. Stars that have formed from material processed by the first stars therefore have non-zero metallicity. The feedback of this second generation of stars with non-zero, but still very low metallicity may be important for solving cosmological problems concerning the re-ionization history and chemical evolution of the early Universe (Yoshida et al., 2007; Greif et al., 2010; Hosokawa et al., 2012). Therefore, a clear theoretical understanding of the physics of massive stars at low-metallicity is not only of astrophysical interest, but a cosmological one as well.

1.2.2 Compact dwarf galaxies

Although a great progress has been done recently in gaining information about the high-redshift Universe, direct observational diagnostics of massive stars at these distances is not (yet) feasible. To understand their behaviors and the ways they interact with their environments, however, we would optimally need data of a large number of them with the same age at known distance, preferably in the local Universe, so constraints on their evolution could be obtained.

It is imperative to know the distance of a given star in order to say anything about its evolutionary stage: the brightness of a star, as seen from Earth, depends not only on the total

Figure 1.2. The blue compact dwarf galaxy I Zwicky 18 as fotographed by the Hubble Space Telescope. Credit: *hubblesite.org*.

amount of light emitted, but also on how far it is from us. Knowing the distance, we can obtain the star's absolute brightness, i.e. the total amount of light emitted. As our main goal is to understand what happens inside the star in terms of nuclear physics and thermodinamics, the absolute brightness is one of the most important indicators, as it corresponds to the total amount of energy that is produced by nuclear reactions over time (radiant power, or *luminosity*).

An ideal place to look for populations of low-metallicity massive stars is nearby blue compact dwarf galaxies (BCDG) (Searle and Sargent, 1972; Zhao et al., 2013). BCDGs are typically small, high surface-brightness galaxies of low metallicity, that form massive stars at a high rate (D. Hunter and Thronson, 1995; Vaduvescu et al., 2007; Annibali et al., 2013). Additionally, all stars in a given galaxy are, practically, at the same distance from us (the error of measuring the distance of a galaxy is usually larger than the diameter of the galaxy). Given that their metallicity is observed to be low, BCDGs are proposed to be used as laboratories to study the evolution of metal-poor massive stars (Y. Izotov and Thuan, 2002; Y. Izotov and Thuan, 2004; Kehrig et al., 2013). Studying low-metallicity massive stars in the nearby BCDGs can lead us closer to understand the evolution of metal-poor stars in the early Universe.

One of the near BCDGs that is mentioned later in this thesis is called I Zw 18 (Zwicky, 1964, see Fig. 1.2). According to first studies by Searle and Sargent (1972), I Zw 18 is at a distance of 18 Mpc (Aloisi et al., 2007), has a metallicity of Z_{IZw18}=0.02% and is of constant scientific interest (D. Hunter and Thronson, 1995; Y. I. Izotov et al., 1997; Aloisi et al., 1999; Y. Izotov and Thuan, 2004; Papaderos and Östlin, 2012; Annibali et al., 2013; Lebouteiller et al., 2013; Heap et al., 2015; Kehrig et al., 2015b; Szécsi et al., 2015b). It has a high star-formation rate (0.1 $M_\odot$/yr, Lebouteiller et al., 2013) and contains an unusually high amount of ionized gas (Kehrig et al., 2015b). But despite the measurements becoming more and more precise during the decades since its discovery, our understanding of the evolutionary status of I Zw 18 is still far from satisfying. Photometric studies give different results for the upper age limit: 0.01, 0.1, 0.5, 1, or even 5 Gyr (Kunth and Östlin, 2000; Papaderos et al., 2002; Papaderos and Östlin, 2012). The Hubble Space Telescope data (Aloisi et al., 1999; Y. Izotov and Thuan, 2004) implied that either there were two star formation episodes and I Zw 18 has an underlying older

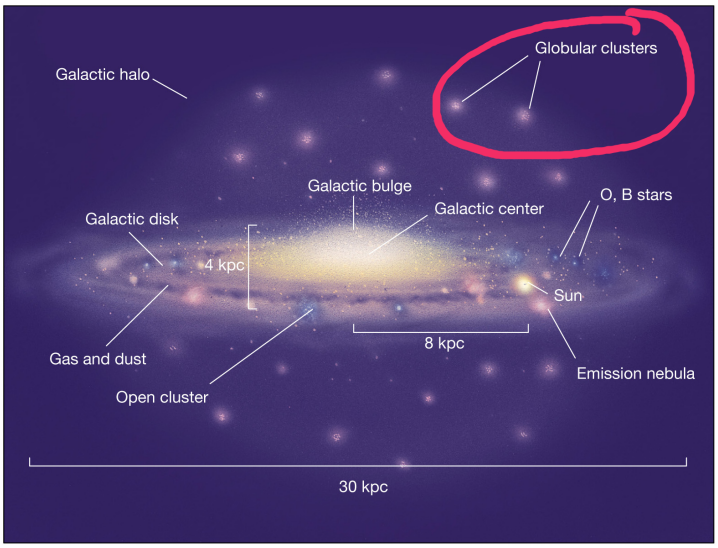

Figure 1.3. Schematic look of our galaxy, the Milky Way. Highlighted are globular clusters, i.e. spherical, gravitationally bound congregations of old, low-mass stars. These clusters are oribiting around the galactic center. Credit: Chaisson and McMillan (2004).

generation of stars, or I Zw 18 is a young galaxy undergoing its first star formation episode. (The number of underlying stellar generations plays a role in the age determination, which partly explains the diversity of the age limits.) However, photometric studies rely on stellar evolutionary models, a comprehensive set of which (using the composition of I Zw 18 and including stellar rotation) has been computed in this thesis.

With our new set of stellar models, the evolutionary status and age of I Zw 18 may be specified more accurately in the future. In turn, understanding this galaxy more accurately may provide us tighter constrains on massive stellar evolution at low-metallicity.

1.2.3 Globular clusters

A globular cluster (GC) is a congregation of stars that are closely bound together by gravity. More than 150 GCs are known currently in our own galaxy (cf. Fig. 1.3), but other galaxies such as Andromeda also have them in a large number. GCs consist of low-mass old stars with the same age, with the same initial composition and, importantly, at the same distance from us. Thus, they also may be used as natural laboratories of stellar evolution.

However, there is no star-formation going on in GCs. Since the total lifetime of a star scales inversely with its mass ($\tau \sim M^{-3}$), an old cluster can only contain low-mass stars. What nonetheless makes GCs an essential part of our study of low-metallicity *massive* stars is that they probably wear the chemical imprint of a first generation of massive stars. Certain anomalies in the light element abundances of GC stellar spectra are observed (such as, for instance, unusually high sodium and unusually low oxygen content, see e.g. Yong et al., 2003; Da Costa et al., 2013). These anomalies are attributed to the pollution coming from massive stars (Gratton et al., 2004; Bastian et al., 2013; Tailo et al., 2015). Since the metallicity of the old stars currently residing in GCs are observed to be, in general, quite low (Z_{GC} = 0.01...0.05%, Gratton et al., 2004), and since the now-dead massive stars should have had the same composition, our low-metallicity massive stellar models are used to investigate the role that this now-dead

generation could have played in the early GCs.

1.2.4 Other low-Z environments

The Universe is large and of course there are other environments where low-metallicity massive stars can or could form. Only those listed above are investigated further in this thesis. However, we note that our evolutionary models may be used in the context of, for example, the extremely metal-poor stars in the halo of our galaxy (Beers and Christlieb, 2005; Keller et al., 2014), or the intermediate-redshift galaxies, called Green Peas, which are also observed to have subsolar metallicity (Amorín et al., 2010; Jaskot and Oey, 2014).

1.3 The tools of theoretical stellar evolution

1.3.1 What is a star?

We understand a star as a hot, dense, ionized plasma which is, most of the time at least, in hydrostatic and thermal equilibrium maintained by (1) its own self-gravity pushing inwards and (2) the radiation-pressure released by the nuclear fusion that is going on inside, in the hottest and densest regions, pushing outwards.

The composition of the plasma may vary. Young stars, right after their formation, are composed of the same material as their birth environment, the star-forming molecular cloud, with about 74% hydrogen, ∼25% helium and ∼1% metal content. When a star becomes older, some of its material has undergone nuclear fusion, converting lighter elements into heavier ones. In most cases, this conversion takes place inside the inner core of the star, while the surface keeps the initial composition.

But how can we define the surface of an object made of plasma? Indeed, this is a tricky question, and the answer is usually the following. Even outside the burning regions (meaning mostly, but not always, the inner core), the plasma is so dense that the photons scatter on the ions. Where the temperature and the density is low enough so that photons can finally escape without any more interaction, this place is called the surface or the photosphere of the star. Since the star is in thermal equilibrium, the photosphere has a black body spectrum.

The photosphere is how deep our telescopes can actually see into the star. Everything below the photosphere is hidden from us; at least from our traditional, optical telescopes. There are two techniques which can be used to study these hidden layers. One is the exciting and rapidly developing new field of asteroseismology, which deals with oscillation modes of pulsating stars to provide information about the density structure of the inner regions (Cunha et al., 2007).

The other technique is the theoretical simulation of the stellar structure and evolution, the subject of this thesis.

1.3.2 The evolutionary simulations

The set of physical parameters describing the structure of a hot, isolated gas sphere as computed from the assumptions of mass-, momentum- and energy-conservation, including a proper treatment of energy transport, is called a *stellar model*. The structure of the stellar model is determined by its composition. Therefore, with the composition of the model changing due to nuclear reactions in the hot plasma, the structure of the stellar model is changing as well: this

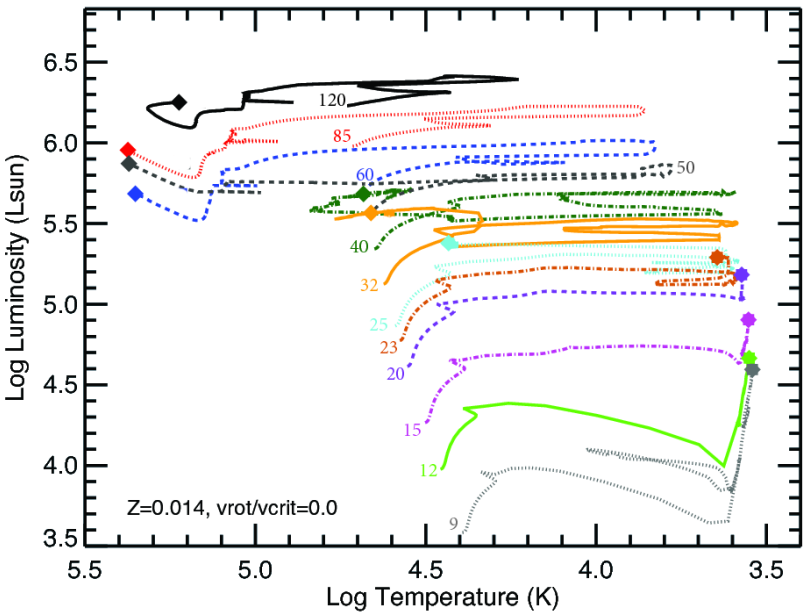

Figure 1.4. HR diagram showing massive stellar evolutionary model sequences with solar composition and without rotation. The zero-age main sequence is marked with labels of the initial stellar mass (in units of solarmass). The end of the evolution is marked with diamond/octagram symbols. Credit: *Groh et al. (2013)*.

process is called stellar evolution. Hence, consecutive stellar models are called *evolutionary sequences*. [1]

With today's computer power, one single stellar evolutionary sequence can be computed in a few hours, covering the whole evolution from the moment of birth (but excluding the star-formation process) to the last stages of life.

The most common tool in stellar evolution is the surface-temperature vs. surface-luminosity diagram or Hertzsprung–Russell (HR) diagram (e.g. in Fig. 1.4). The x-axis of the HR diagram is decreasing for historical reasons. We refer to its left hand side as 'blue' (i.e. high temperature) and its right hand side as 'red' (i.e. low temperature).

1.4 Massive stellar evolution at solar metallicity

Evolution of massive stars at solar metallicity has been investigated in the past decades. Here we shortly summarize their typical behavior following Schwarzschild (1958) and Kippenhahn and Weigert (1990). This summary is essential for putting the subject of the thesis, massive stars that have subsolar composition, in context.

1.4.1 High-mass stars are different from low-mass stars

Almost all the stars that one can see on the sky with a naked eye are low-mass stars, including our Sun. Low-mass stars are much more common than high-mass (i.e. massive) stars because

[1] Somtimes the literature, including this thesis, uses the term evolutionary model to describe a sequence of models. However, it is important to always keep the difference in mind.

(1) the lifetime of a star is longer when its mass is lower, so at any given timepoint, one has a higher chance to find a star at lower mass; (2) low-mass stars are more likely to form than high-mass stars. (Consequently, if one wants to observe massive stars in large numbers, they need to look for special places where the stars are young, some of them even currently forming.)

The main distinction between low-mass and high-mass stars is which type of hydrogen-burning chain-reaction dominates in them. Low-mass stars process hydrogen into helium via the pp-chain (pp stands for proton-proton), in which two protons fuse to form a deuterium, which then fuses with another proton to form a helium-3 isotope and so on: the majority of the end-products consist of stable helium-4 isotopes, and there is some lithium and beryllium created as well. (Note that the stellar material is ionized: therefore, all elements that we talk about here and below are, in fact, ions. Consequently, 'hydrogen' means 'the ion of the hydrogen-1 isotope', i.e. a proton.)

High-mass stars, on the other hand, process hydrogen into helium in another way: via the CNO-cycle. The C, N and O stands for carbon, nitrogen and oxygen, as these elements serve as catalysts when fusing four protons into one helium-4. The reason why high-mass stars process the hydrogen-fusion differently from low-mass stars is that the efficiency of both chains of reactions depends strongly on the temperature. The pp-chain is efficient at around $4\text{-}16\times10^6$ K, where the CNO-cycle has no important contribution: therefore, the pp-chain dominates in low-mass stars, whose core is around that temperature. In turn, the CNO-cycle becomes efficient above 17×10^6 K: these temperatures are reached in massive stars during core-hydrogen-burning. Provided that there are C, N and O in the plasma initially (which is indeed true for almost all cases, except for perfectly metal-free stars), massive stars are dominated by the CNO-cycle.

Based on which reaction is dominant, the defining line between low- and high-mass stars is at $\sim$2 $M_\odot$: stars less massive than twice the Sun are considered low-mass, while those more massive are considered high-mass stars. However, stars in the mass range of 2–9 $M_\odot$ are usually considered intermediate-mass stars for the following reason.

After the hydrogen is exhausted from the core, low-mass stars develop a degenerate helium core, while intermediate-mass stars develop a non-degenerate helium core. When the core is degenerate, the helium burning occurs as a runaway event called core-helium-flash. When the core is non-degenerate, the helium-burning is thermally stable. Both low- and intermediate-mass stars lose their envelopes due to stellar winds at the end of helium burning, and become carbon-oxygen white dwarfs after that, surrounded by planetary nebulae formed from their lost envelopes.

Massive stars (>9 $M_\odot$), on the other hand, do not develop degenerate helium (nor carbon-oxygen) cores, but start to burn carbon, and then oxygen, and then neon, and then silicon in thermal equilibrium. They fall out of equilibrium only when the core is composed of iron, the element which cannot be burned into anything anymore via nuclear fusion because iron is such a stable element that fusing it would *require* energy instead of releasing energy.

From now on, our focus is on massive stars, i.e. stars with 9 $M_\odot$ and above.

1.4.2 Evolutionary paths

Massive stars at *solar metallicity* evolve from the zero-age main sequence (ZAMS) towards lower effective-temperatures ('redward') and towards higher luminosities, as shown in Fig. 1.4. During the main-sequence (i.e. core-hydrogen-burning) lifetime, a distinct core–envelope structure develops with the core changing its composition due to the nuclear reactions and the

Figure 1.5. Wolf–Rayet star WR124. Part of the constellation Sagitta, surrounded by a ring nebula of ejected material. Wolf–Rayet stars are pure helium stars. They are the final evolutionary stage of solar metallicity massive stars above a certain mass ($\gtrsim$20 $M_\odot$). Credit: *hubblesite.org*.

envelope keeping its original composition. At the end of the main sequence phase (corresponding to the first, rather small hook of the tracks in Fig. 1.4), the core needs to contract to reach helium burning temperatures. Therefore, the star goes through a restructuring phase during which the core contracts, the envelope expands, while hydrogen is burned in a shell and the radius grows to $\gtrsim$1000 $R_\odot$: the star becomes a red supergiant.

In case the stars are less massive than 25 $M_\odot$ (in the case of non-rotating stars with solar composition, cf. Fig. 1.4), core-helium-burning is happening on the red supergiant branch. Above a certain mass ($\sim$25 $M_\odot$ initial mass in Fig. 1.4, but this limit decreases to $\sim$20 $M_\odot$ when rotation is included into the models, see Groh et al., 2013), stars lose their envelopes due to strong mass loss and become hot Wolf–Rayet (WR) stars (i.e. pure helium stars with dense, optically thick nebulae around them, see Fig. 1.5) during core-helium-burning.

The core-hydrogen-burning phase of a massive star lasts about ten times longer than the core-helium-burning phase. The further burning phases are even shorter, making up less than one percent of the total stellar lifetime.

1.4.3 The post-main-sequence structure

As mentioned above, as the hydrogen fraction in the core becomes very small, the central temperature increases substantially due to an overall contraction, and the star falls out of thermal equilibrium. When the layers above the core that still contain hydrogen reach the temperature needed for hydrogen-ignition, the so-called shell-hydrogen-burning takes place in these layers. The contraction of the core nonetheless continues until helium is ignited. Core-helium-burning is then followed by shell-helium-burning, core-carbon-burning, shell-carbon-burning, and core-neon-burning. These subsequently starting phases give rise to an onion-like structure, in which the shells consist of different burning products.

In massive stellar models with solar-metalliciy, these burning phases continue with shell-neon-burning, core-oxygen-burning, shell-oxygen-burning and core-silicon-burning. At this point, the core of the solar-metallicity massive star consists mainly of iron. Since iron burning

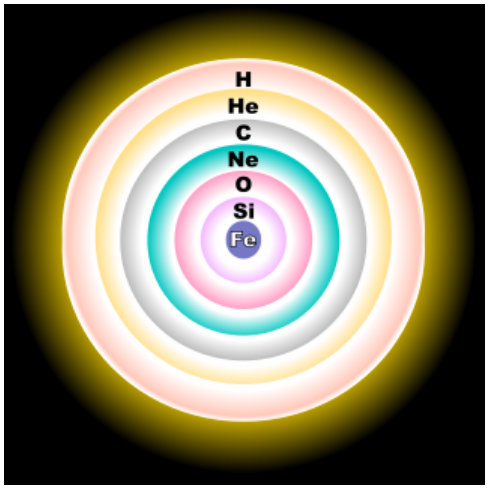

Figure 1.6. The structure of massive stars with solar metallicity right before the core collapse (onion-like structure; the size of the layers in this figure is arbitrary). Credit: *wikipedia.org*.

would require energy instead of producing it, the iron core falls out of equilibrium and collapses into a compact object (a neutron star or a black hole), in most cases producing a supernova explostion as well.

1.4.4 Final explosion and remnants

As discussed above, massive stars at solar metallicity burn higher elements until the core consists mainly of iron. At this point the structure of the massive star becomes unstable because there is no nuclear energy release that could maintain the equilibrium: the core collapses. This represents the end of the stellar evolution and the start of the (core-collapse-type) supernova explosion.

The supernova event starts with the very rapid collapse of the core until most of its neutrons become degenerate (C. Fryer, 2004). The in-falling material (the outermost layers of the core) rebound from the degenerate inner core and bounce outwards giving rise to a shock-wave. This energetic shock-wave then reaches the stellar surface and produces a ~30 minutes long X-ray emission that is observable with space-instruments (for example the Swift or the Chandra satellites). Depending on the size and the composition of the envelope, the supernova lightcurves (the intensity of the emission as a function of time) can be categorized into several types such as type II-P type II-L or type Ib (Langer, 2012). Further follow-up observations with ground-based optical telescopes can shed light on important details like the composition of the ejecta. During the explosion, elements heavier than iron can form.

What remains is the degenerate core that, depending on its mass, either becomes a neutron-star (when the initial stellar mass at ZAMS was below ~20 $M_\odot$, but this limit depends strongly on the details of stellar evolution such as the mass-loss rate) or a black hole (when the initial mass was between 20-50 $M_\odot$ C. Fryer, 2004). Neutron stars are very compact (~20 km diameter) objects with such a high density (10^{17} kg/m^3) that protons and electrons of the former stellar plasma combine to form neutrons. The stability of these objects against their self-gravity is maintained by the degeneracy pressure of the neutron gas (neutrons are fermions, so their gas properties are determined by the Pauli exclusion principle). Black holes are the results of collapsing cores that are even more massive: in this case, self-gravity overcomes the neutron

star's internal pressure, creating a compact object with such a strong gravitational field around that nothing, not even particles and electromagnetic radiation such as light, can escape from it. Stars initially more massive than 50 $M_\odot$ (at solar metallicity) are believed not to undergo a supernova explosion but fall into black holes directly after the core collapse.

1.4.5 Rotation

Massive stars are generally rapid rotators. Rotation influences the evolution and changes the general outcome described above for solar metallicity massive stars. For example, rotating stars have larger cores, so they live longer. Furthermore, rotation induces strong mixing between the core and the envelope, so the surface can be enriched by nuclearly processed material (Brott et al., 2011). Also, the mass-limit above which the stars evolve to be WR stars decreases when rotation is included in the models (Groh et al., 2013). However, all the roles that rotation plays at solar metallicity are only minor contributions compared to what rotation can produce at low or zero metallicity (Yoon et al., 2006; Brott et al., 2011; Ekström et al., 2011; Yoon et al., 2012, as well as later on in this thesis).

1.5 Massive stellar evolution at zero metallicity

As mentioned in Sect. 1.2.1, the first stars in the Universe are thought to be very massive and metal-free. Since these objects have serious cosmological implications, several theoretical studies have been performed to understand their behaviour. We discuss them here because these metal-free massive stars (also called Population III or Pop III stars), while being very different from their solar-metallicity counterparts, show many similarities to those at low-metallicity.

1.5.1 Evolutionary paths

Non-rotating Pop III stellar models above $M_{ZAMS} > 30\ M_\odot$ evolve to the cool, red part of the HR diagram, as seen in Fig. 1.7 – as opposed to solar metallicity stars with the same mass, which eventually become hot, blue WR stars, as seen in Fig. 1.4. As for the rotating stellar models, the so-called (quasi) chemically homogeneous evolution takes place in a certain mass and velocity range (for masses of $13 \lesssim M_{ZAMS}/M_\odot \lesssim 190$ and for rotational velocities of ~0.3–0.8 times the break-up velocity, see Figs. 1, 2 and 12 of Yoon et al., 2012, for the precise mass and velocity limits). Chemically homogeneous evolution has many important consequences for the life, as well as for the possible death, of the stellar models. Amongst its most important consequences are the high ionizing-photon emission, the high surface-enrichment of nuclear burning products (most importantly: helium, carbon, nitrogen, oxygen), and the fact that the model is rotating very fast at the moment of the core collapse. For this last reason, chemically homogeneous evolution is proposed to be a possible stellar evolutionary channel through which long-duration gamma-ray bursts can be produced.

1.5.2 Gamma-ray bursts

Gamma-ray bursts (GRBs) have been discovered in the late 1960s by US military satellites. Initially, these satellites were to detect nuclear experiments carried out here on Earth, but instead they found energetic explosions of cosmic origin (Balázs et al., 1999; Bagoly et al., 2003; Szécsi et al., 2013). Indeed, the optical follow-up of the explosion GRB 970228 by Lipunov

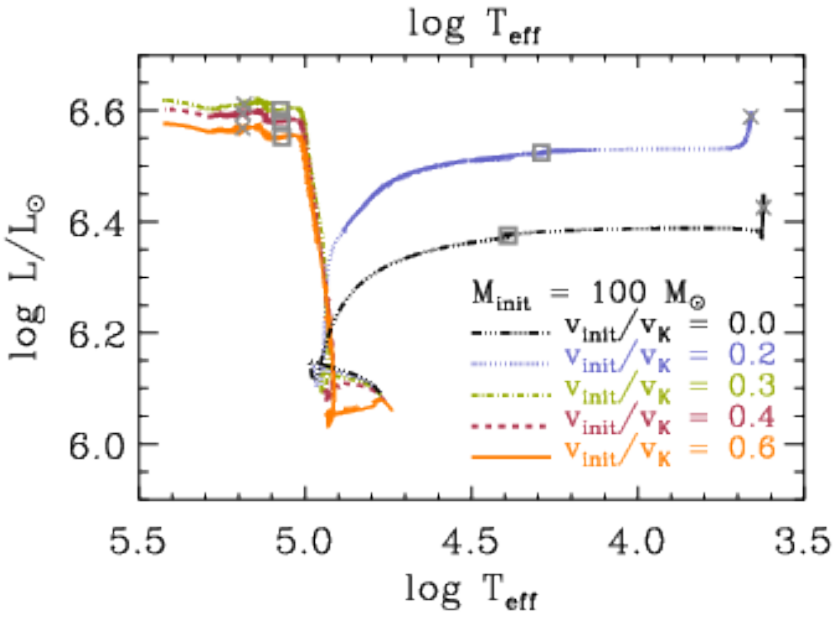

Figure 1.7. Evolution in the HR diagram: zero-metallicity stellar models with initial mass of 100 $M_\odot$ and initial rotational rates indicated by the labels (in units of the break-up velocity, v_K). Above a certain initial rotational rate ($\gtrsim 0.3$), the models evolve chemically homogeneously and bluewards, i.e. towards high surface temperatures. Squares and crosses mark the end of the core-hydrogen-burning and the core-helium-burning phase of the models, respectively. *Credit: Yoon et al. (2012).*

et al. (1997) confirmed for the first time that the event happened at a redshift of $z = 0.7 \pm 0.1$. Today, the total number of GRBs observed is in the order of a few thousand (and growing, due to modern gamma-ray detecting satellites such as Swift, Fermi and INTEGRAL, Foley et al., 2008; Vianello et al., 2009; Butler et al., 2010; Gruber et al., 2014; Horváth et al., 2014; Lien et al., 2014; Balázs et al., 2015; Bagoly et al., 2015). About 400 of them have reliable redshift measurements and information about the host-galaxy, so their cosmic origin is an established fact (Le Floc'h et al., 2003; Thöne et al., 2014; Friis et al., 2015; Krühler et al., 2015; Perley et al., 2015; Schaerer et al., 2015).

The duration of the gamma-ray emission is typically something between a dozen milliseconds and a few minutes (but there are a few ultra-long bursts lasting for hours). Since the statistical distribution of the durations show two distinct peaks (at least, cf. Mészáros et al., 2000; Horváth et al., 2006; Vavrek et al., 2008; Horváth et al., 2010), GRBs are usually classified into one of two categories: short-duration GRBs or long-duration GRBs (the separating duration value being at around 2 sec, Zhang, 2007). These two statistical categories are interpreted to originate from two different astrophysical processes. Long-duration GRBs are produced by collapsing massive single stars surrounded by large accretion discs (Woosley and Heger, 2006). Short-duration GRBs are produced by the merger of compact binary systems (Berger, 2014). In most cases, GRBs are followed by an optical afterglow (Kawai et al., 2006; Hartoog et al., 2015) that may last for days or weeks.

Gamma-ray bursts are *not* supernovae (although some of them have been associated with a supernova event, see e.g. Woosley et al., 1999; D'Elia et al., 2015). While both groups of explosions, GRBs and supernovae, contain events of various duration and spectral features, the difference in general is that supernovae are not observed at gamma wavelengths. Additionally,

GRB afterglows show a special break in the lightcurve (Sari et al., 1999) which is attributed to the fact that GRBs are produced in relativistic jets (as opposed to most supernovae, which are thought to be symmetric).

A connection between long-duration GRBs and metal-poor environments have been observationally established, as the majority of the host-galaxies are measured to have low metallicity (Levesque et al., 2010; Modjaz et al., 2011; Graham and Fruchter, 2013). As mentioned above, fast-rotating, metal-free, massive single stars have been proposed to be progenitors of long-duration GRBs (Yoon et al., 2012) via the stellar evolutionary channel called chemically homogeneous evolution.

1.5.3 Pair-instability

Chemically homogeneous evolution is not the only special feature found only in metal-free or (as we shall see in this thesis) low-metallicity massive stellar models. Another important process that metal-free and metal-poor models may undergo is the so-called pair-instability.

As seen in Sect. 1.4.3, massive stars at solar metallicity burn helium, carbon, neon, oxygen and silicon in their cores. Metal-free massive stars, on the other hand, may encounter an instability during neon or oxygen burning, the consequence of which is that the subsequent evolution may never occur and that the star collapses (with or without a supernova explosion, Burbidge et al., 1957; Langer, 1991; Heger et al., 2003; Langer et al., 2007; Yoon et al., 2012; Kozyreva et al., 2014). This instability happens due to pair-creation. At a certain temperature and density ($T \gtrsim 10^9$ K and $\rho \gtrsim 10^5$ g cm^{-3}), the photons released by the nuclear fusion create pairs of an electron and a positron. The number of photons therefore drops and the stability of the stellar model, maintained by the balance between its self-gravity and the radiation pressure of the photons released, is compromised.

If the stellar model undergoes pair-instability, one of the following three things happens (Langer, 1991; C. L. Fryer et al., 2001; Heger and Woosley, 2002; Heger et al., 2003; Yoon et al., 2012). (1) In case of very massive cores ($\gtrsim$130 M$_\odot$), the star collapses directly into a black hole without an explosion. (2) In case of less massive cores, however, the collapse would be stopped and reversed by the nuclear energy release of *explosive* oxygen burning. In this case, a pair-instability supernova (PISN) event happens, which disrupts the whole star leaving no remnant. (3) For even less massive cores ($\lesssim$64 M$_\odot$) the instability results in violent pulsations, but no complete disruption. As a consequence of the pulsations, the star expels some of its outer layers, and thus regaining its stability continues its hydrostatic evolution until an iron-core forms. The expelled layers may produce a so called pulsational pair-instability supernova (pPISN).

PISNe and pPISNe have been proposed to be responsible for some of the superluminous supernovae observed (Quimby et al., 2013; Kozyreva et al., 2014; Gal-Yam, 2012).

1.6 Massive stellar evolution at low metallicity – this thesis

The main goal of this thesis is to present detailed evolutionary simulations of massive, rotating single stars at low-metallicity, and compare them to observations of environments with corresponding metallicity. The stellar evolutionary model sequences presented and analyzed here have been computed with an initial composition that reflects the observed composition of the blue compact dwarf galaxy I Zw 18 (cf. Sect. 1.2.2). Before summarizing the main results

of this thesis, we need to discuss some important aspects of how we can match our theory to observations.

1.6.1 Matching theory to observations

There is of course no guaranty that our theory correctly describes reality until we can explain observations with it. The following three aspects are important to keep in mind when one tries to follow what we do and why we do it, because most of the time we aim to overcome one or more of these basic obstacles. The stellar properties we choose to analyze, the methods we decide to apply, and probably even the questions we raise and try to answer are necessarily determined by these three aspects of how theory can match observations. This short overview should, hopefully, help the general reader to follow the arguments and reasonings that are put forth in this thesis.

Observing only the surface

The fact that only the surface of the star can be observed means that every time a stellar evolutionary model sequence is computed, only its surface properties can be verified (or rejected). Even if the surface properties of the model match that of the observed star, it does not necessarily mean that the internal properties would match as well. It is important to point out here that, according to theory, the stellar material of the inner regions (the core) undergoes nuclear burning, while the outer regions (the envelope) usually retain the original composition. Therefore, it is not at all straightforward to verify out theoretical understanding of the nuclear processes of the core based on observations of the surface. However, this approach is the best we got (apart from the new and rapidly developing results of asteroseismology), so we usually try to predict and match as many surface properties as possible to strengthen our theory's cause.

Observing only a snapshot of the star's life

The total life of a star, even the shortest-living one, is of the order of millions of years. Obviously, it would be not possible to wait that long just to check if our theoretical computations are correct. To put it somehow differently, we observe only a snapshot of a star's million-years-long life. In order to test if our evolutionary computations are reliable, we observe a large number of stars; and then we expect that there would be stars currently undergoing all possible evolutionary stages in this sample. This issue is further complicated by the fact that the structure of a star is not only a function of its age, but also of its mass, rotation and composition (and its companion, as discussed below in Sect. 1.6.2). This is one of the reasons why we like to observe regions where all stars have the same age, such as clusters and star-forming regions.

Stellar wind and mass-loss

Moreover, stars are not *really* isolated in space: they are surrounded by and interacting with their own stellar winds. The stellar wind is an outflow of particles from the star, removed and accelerated by some force. In the case of most massive stars, this force is maintained by the photons released at the surface: they interact with the particles here and push them away from the star (Lamers and Cassinelli, 1999). The modeling of this region above the photosphere (the so-called stellar atmosphere) is a crucial task because (1) the light that we observe has traveled

through it: if we want to understand the observed spectrum, we need to take all the atmospheric interactions into account; (2) over the millions of years of the star's life, the wind removes a significant amount of mass. The structure and evolution of a star is fundamentally influenced by its mass: if the star loses mass due to its wind, the evolution proceeds differently than it would in the absence of mass-loss. For these two reasons, stellar evolutionary simulations should take the atmosphere of the star into account. However, modeling the atmosphere is a very difficult and computationally expensive thing to do because one needs to follow all the particle interactions in the wind one by one. As a consequence, stellar evolutionary simulations rely on a very simplistic and approximate approach to handle the wind. This approach brings additional uncertainties into the theory.

1.6.2 Binary stars

So far we only considered the evolution of isolated single stars. However, the majority of massive stars may form in binary systems (Chini et al., 2012; Sana et al., 2012). In these systems, the two stars are orbiting around a common center of mass. If their orbit is tight enough, the stars can interact with each other during their lives, exchanging mass between each other. This can drastically affect their evolution (Eldridge et al., 2008; Eldridge et al., 2011) and lead to different types of supernova events (such as type IIb, Langer, 2012). Compact object binary mergers (the remnants of massive star binaries) are though to lead to even more energetic explosions, namely the short-duration gamma-ray bursts (Berger, 2014).

Moreover, the gravitational wave (GW) event that happened on the 14th September 2015 was originated most certainly from the merger of a double black hole binary system with masses of 36^{+5}_{-4} $M_\odot$ and 29^{+4}_{-4} $M_\odot$ (B. P. Abbott et al., 2016a; B. P. Abbott et al., 2016b). There are two ways massive stellar evolution can lead to such a system. In the most commonly adopted scenario, two massive stars are orbiting around each other forming black holes after their supernova explosions (Dominik et al., 2012). The caveat in this case is that when the primary becomes a red supergiant in the last ten percent of its lifetime, the secondary finds itself orbiting *inside* the supergiant's envelope. This is called a common envelope evolution, an intensively investigated but not yet well understood phase (Ivanova et al., 2013). The most probable outcome is that the envelope is ejected, and the primary becomes a pure helium-star and, eventually, a black hole. Then another common envelope phase follows when the secondary becomes a red supergiant, incorporates the black hole, ejects the envelope and becomes a black hole itself. The two black holes then slowly spiral into each other, their merger producing a GW event.

Another promising scenario was proposed by de Mink et al. (2009) and elaborated in the context of gravitational waves recently by Marchant et al. (2016). In this model, the two low-metallicity massive stars are orbiting around each other in such a tight orbit that their rotational periods are initially synchronized with the orbital period (cf. Fig. 1.8). Due to the fast rotation, these stars evolve homogeneously and never expand (as described by Szécsi et al., 2015b, for single, homogeneously evolving stars; also see Chapter 2 of this thesis). Avoiding the supergiant phase and thus the common envelope, this scenario is able to explain the double black hole system without dealing with all the uncertainties of the common envelope phase.

Massive star binaries are therefore an important field of research. Since stars in binary systems are, in general, fast rotators due to the tidal force that synchronizes their periods to their orbit, binaries at low-metallicity, where the contribution of rotation in forming the evolutionary behavior is more pronounced, are even more intriguing. However, in order to understand them, we need to understand single massive stars at low-metallicity first.

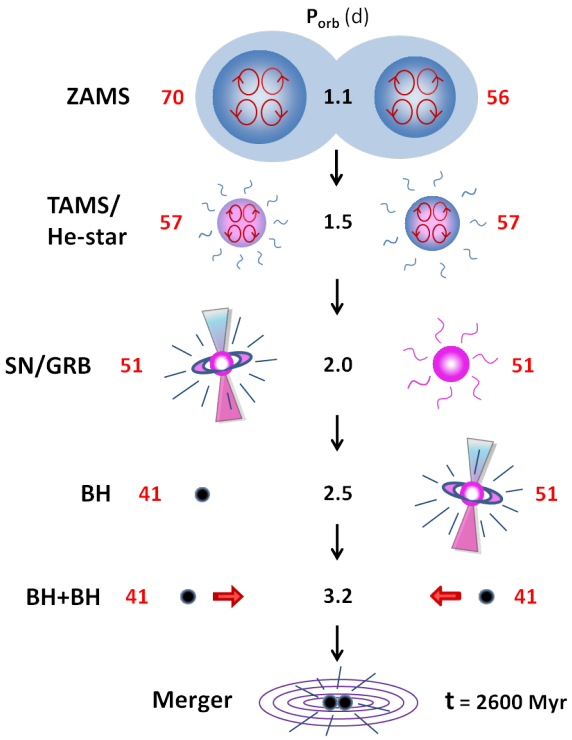

Figure 1.8. Illustration of the binary stellar evolution leading to a BH+BH merger. The initial metallicity is $Z_{\odot}/50$, the masses of the stars in solar masses are indicated with red numbers, and the orbital periods in days are given as black numbers. A phase of contact near the ZAMS causes mass exchange. Acronyms used in the figure. ZAMS: zero-age main sequence; TAMS: termination of hydrogen burning; He-star: helium star; SN: supernova; GRB: gamma-ray burst; BH: black hole. *Credit: Marchant et al. (2016).*

1.6.3 Main results of this thesis

The stellar evolutionary models of low-metallicity massive stars are presented in Chapter 2, where we describe their evolutionary behaviors and their structure in detail. According to our simulations, low-metallicity massive stellar evolution produces two new type of stars: TWUIN stars, and the core-hydrogen-burning cool supergiants.

TWUIN stars (Transparent Wind Ultraviolet INtense stars) are the evolutionary outcome of the fast rotators amongst our stellar models. These stars are predicted to be hot and compact and, as opposed to WR stars which have optically thick winds, having optically thin winds due to the low mass-loss rates at this composition. We show that TWUIN stars may be the explanation for the unusually high ionizing flux observed in I Zw 18 .

Core-hydrogen-burning cool supergiants are the outcome of slowly rotating stellar models with an initial mass above 80 $M_{\odot}$. They are special because they spend 10% of their main-sequence lifetime on the supergiant branch. They are extremely bright (~19 mag in I Zw 18), and may contribute to the composition of their environment significantly, due to strong and slow stellar winds. In Chapter 3, our low-metallicity models are applied to model the first generation of massive stars in globular clusters. If a large population of massive stars formed in a very tight place such as the early globular cluster, photoionization-confined shells could form around the core-hydrogen-burning cool supergiant stars due to the strong ionization emitted by the TWUIN stars. We show that in these dense and cool shells a second generation of low-mass

stars could possibly form, which could help to explain the anomalous stellar compositions observed in today's globular clusters.

Massive stars at low-metallicity are not only interesting for their longstanding main-sequence lifetimes, however. Their post-main-sequence evolution and their final fates have equally important astrophysical implications in store for us as well. In particular, our models predict several types of supernova explosions, including the superluminous supernovae. Therefore, we investigate the post-main-sequence evolution of our TWUIN star models in Chapter 4. We find that the winds of the most massive models are predicted to be optically thick during the post-main-sequence lifetime: these objects might be observed as Wolf–Rayet stars with a peculiar composition. The winds of the less massive models are, however, still transparent during these evolved phases. Our models emit as much He II ionizing photons during core-helium-burning as they do during core-hydrogen burning. They are predicted to explode as superluminous supernovae in either the pair-instability, the pulsational-pair-instability or the magnetar-powered scenario, and some of them are predicted to produce long-duration gamma-ray burst explosions. We also investigate the effect of using an alternative mass-loss rate and find that our models' predictions are significantly altered. From this, we conclude that although TWUIN stars can be responsible for observational phenomena such as the unusually high photoionization in dwarf galaxies or certain types of superluminous supernovae and gamma-ray bursts, reliable mass-loss rate prescriptions of hot and very hot massive stars of low-metallicity are needed in order to understand real stellar populations in low-metallicity environments – such as those in compact dwarf galaxies or those in the early Universe.

As a conclusion in Chapter 5, we draw a link between the life and the death of low-metallicity massive stars: if TWUIN stars are indeed responsible for the ionizing radiation in I Zw 18 , and possibly in other low-metallicity environments too, then we must expect long-duration gamma-ray bursts happening in low-metallicity environments, and in particular in dwarf galaxies, as a necessary outcome of massive stellar evolution.

CHAPTER 2

Evolutionary models applicable to I Zwicky 18

ABSTRACT

Low-metallicity environments such as the early Universe and compact star-forming dwarf galaxies contain many massive stars. These stars influence their surroundings through intense UV radiation, strong winds and explosive deaths. A good understanding of low-metallicity environments requires a detailed theoretical comprehension of the evolution of their massive stars. We aim to investigate the role of metallicity and rotation in shaping the evolutionary paths of massive stars and to provide theoretical predictions that can be tested by observations of metal-poor environments.

Massive rotating single stars with an initial metal composition appropriate for the dwarf galaxy I Zw 18 ([Fe/H]=−1.7) are modelled during hydrogen burning for initial masses of 9-300 $M_\odot$ and rotational velocities of 0-900 km s^{-1}. Internal mixing processes in these models were calibrated based on an observed sample of OB-type stars in the Magellanic Clouds.

Even moderately fast rotators, which may be abundant at this metallicity, are found to undergo efficient mixing induced by rotation resulting in quasi chemically-homogeneous evolution. These homogeneously-evolving models reach effective temperatures of up to 90 kK during core hydrogen burning. This, together with their moderate mass-loss rates, make them Transparent Wind Ultraviolet INtense stars (TWUIN star), and their expected numbers might explain the observed He II ionizing photon flux in I Zw 18 and other low-metallicity He II galaxies. Our slowly rotating stars above ∼80 $M_\odot$ evolve into late B- to M-type supergiants during core hydrogen burning, with visual magnitudes up to 19^m at the distance of I Zw 18. Both types of stars, TWUIN stars and luminous late-type supergiants, are only predicted at low metallicity.

Massive star evolution at low metallicity is shown to differ qualitatively from that in metal-rich environments. Our grid can be used to interpret observations of local star-forming dwarf galaxies and high-redshift galaxies, as well as the metal-poor components of our Milky Way and its globular clusters.

D. Szécsi, N. Langer, S.-C. Yoon, D. Sanyal, S.E. de Mink, C.J. Evans, T. Dermine
Published by: Astronomy and Astrophysics v.581, A15 (2015)

2.1 Introduction

Many of the first stars in the Universe are thought to have started out very massive and almost metal-free (Abel et al., 2002; Bromm and Larson, 2004; Frebel et al., 2005). Direct observations of these stars are not possible with current telescopes. However, low-metallicity massive stars can also be found in the local Universe: some of the nearby dwarf galaxies form massive stars at a high rate (Tolstoy et al., 2009; Weisz et al., 2014). As these galaxies can be directly observed and as their metallicity happens to be close to that of the first stars, they can be used as laboratories to study massive stellar evolution at low (i.e. substantially subsolar) metallicity. Such studies may lead us to a better understanding of the metallicity dependence of stellar evolution, including the first stars in the Universe.

Apart from the cosmological implications of stars at high redshift, there are another reasons to study stellar evolution at low metallicity. The initial chemical composition of a star influences the whole evolutionary path, internal structure, circumstellar surroundings and even the final fate of the star (Meynet and Maeder, 2002; Hirschi et al., 2005; Meynet and Maeder, 2005; Brott et al., 2011; Yoon et al., 2012; Yusof et al., 2013). There is observational evidence that long-duration gamma-ray bursts tend to prefer low-metallicity environments (Levesque et al., 2010; Modjaz et al., 2011; Graham and Fruchter, 2013) and high redshifts (Horváth et al., 2014; Balázs et al., 2015). Theoretical studies have shown that fast rotating stars at low metallicity may evolve quasi chemically-homogeneously (Yoon et al., 2006; Brott et al., 2011). These homogeneously-evolving stellar models are predicted to become fast rotating Wolf–Rayet (WR) type objects during the post main-sequence phase. They are, therefore, candidates of long-duration gamma-ray burst progenitors within the collapsar scenario (MacFadyen and Woosley, 1999; Yoon and Langer, 2005; Woosley and Heger, 2006). Moreover, broad line type Ic supernovae (Arcavi et al., 2010; Sanders et al., 2012) that are associated with gamma-ray bursts (Modjaz et al., 2011; Graham and Fruchter, 2013) as well as the recently identified superluminous supernovae (Quimby et al., 2011; Lunnan et al., 2013) occur preferentially in low-metallicity dwarf galaxies. This may corroborate the idea that reduced wind mass-loss at low metallicity (Vink et al., 2001; Mokiem et al., 2007) may allow for rapid rotation rates (Yoon et al., 2006; Georgy et al., 2009) and very massive (Langer et al., 2007; Yusof et al., 2013; Kozyreva et al., 2014) supernova progenitors. A good understanding of the evolution of metal-poor massive stars is, therefore, important to probe the origin of these extremely energetic explosions.

The first stars are thought to have consisted of mostly hydrogen and helium with a ^{7}Li mass fraction of about 10^{-9} (Mathews et al., 2005). This first generation synthesized heavy elements via nuclear fusion, either in hydrostatic equilibrium or during an explosion. Stars that have formed from material processed by the first stars therefore also have non-zero metallicity. This second generation of stars may also be important in the re-ionisation history and chemical evolution of the early Universe (Yoshida et al., 2007; Greif et al., 2010; Hosokawa et al., 2012). Additionally, the imprint of the first nucleosynthesis events is thought to be present in extremely metal-poor Galactic halo stars (Beers and Christlieb, 2005; Keller et al., 2014), for which our understanding is still incomplete (Heger and Woosley, 2010; Lee et al., 2014).

Galactic globular clusters are also observed to have a low metal content ([Fe/H]=−2.2...−0.2) (Gratton et al., 2001; Yong et al., 2003; Carretta et al., 2005; D'Antona and Ventura, 2010; Caretta, 2010). Although we observe only low-mass stars in globular clusters today, there was probably a generation of massive stars during their early epoch (Portegies Zwart et al., 2010; Denissenkov and Hartwick, 2014; Longmore et al., 2014). A theoretical understanding of

massive stars at this metallicity might help to explain some of the most intriguing phenomena concerning globular clusters, e.g. the abundance anomalies and multiple populations observed in these objects (Decressin et al., 2007; de Mink et al., 2009; Bastian et al., 2013).

We can observe environments at very low but finite metallicity, if we turn to nearby blue compact dwarf galaxies (BCDG) (Searle and Sargent, 1972; Zhao et al., 2013). BCDGs are typically small, high surface-brightness galaxies of low metallicity, with blue colours and intense emission lines (D. Hunter and Thronson, 1995; Vaduvescu et al., 2007). Additionally, some of them contain WR stars, e.g. I Zw 18 (Legrand et al., 1997; Aloisi et al., 1999; Schaerer et al., 1999a; Shirazi and Brinchmann, 2012; Kehrig et al., 2013). Moreover, nearby BCDGs form massive stars at a high rate of up to 1 $M_\odot$ yr^{-1} (Annibali et al., 2013). Given that their metallicity is observed to be low, they are laboratories to study the evolution of metal-poor massive stars (Y. Izotov and Thuan, 2002; Y. Izotov and Thuan, 2004; Annibali et al., 2013). As mentioned above, modelling stellar evolution with a composition suitable for these dwarf galaxies can be an important step towards a deeper understanding of low-metallicity environments.

Recent studies theorized about the presence of metal-free Population III (Pop III) stars in finite-metallicity environments to explain various observational phenomena such as unusually high He II and Lyman-α emission in local dwarf galaxies or high-redshift galaxies (Heap et al., 2015; Kehrig et al., 2015b; Sobral et al., 2015). However, the detailed evolutionary behaviour of low- but finite-metallicity massive stars has not been investigated comprehensively. With this study, we aim to shed new light on this issue.

We computed stellar evolutionary sequences of single stars in the mass range 9-300 $M_\odot$ with rotational velocities between 0-900 km s^{-1} and with an initial composition of Z=0.0002. Here we present the core-hydrogen-burning phase of these models. We emphasize therefore that the present study applies only to the main-sequence evolution of low-metallicity massive stars. The post-main-sequence evolution and final fates of our models will be discussed in a following study.

We include rotation into our models because massive stars are generally rapid rotators (Penny and Gies, 2009; Huang et al., 2010; Ramírez-Agudelo et al., 2013; Dufton et al., 2013). Rotation may influence the life of massive stars in many ways (Heger et al., 2000; Meynet and Maeder, 2000; Hirschi et al., 2005; Yoon et al., 2006; Ekström et al., 2008; Georgy et al., 2012). at low metallicity, rotation may be particularly important because the stellar wind induced spin-down is much weaker (cf. Brott et al., 2011), and the stars remain rapidly rotating such that rotational mixing is facilitated (Maeder and Meynet, 2000; Langer, 2012).

We consider the evolution of isolated single stars. The majority of massive stars may form in binary systems that lead to interaction during their lives (Chini et al., 2012; Sana et al., 2012), often already during their main-sequence evolution. This can drastically affect their evolution (Eldridge et al., 2008; Eldridge et al., 2011) and binary products may be abundantly present among the brightest stars in dwarf galaxies (de Mink et al., 2014; Schneider et al., 2014). However, in many cases stars are spun up early during their evolution (de Mink et al., 2013). This means that our models provide a fair approximation to the evolution of stars spun up in binary systems.

Our paper is organised as follows. First we summarise the physical assumptions made for calculating the stellar evolutionary models in Sect. 2.2. Then we give an overview of the grid of stellar model sequences and the classification system that describes the different types of evolution at low metallicity in Sect. 2.3. We explain the behaviour of individual stellar tracks in the Hertzsprung–Russell (HR) diagram in Sect. 2.4. In Sect. 2.5, we analyse the models that evolve into core-hydrogen-burning cool supergiants. In Sect. 2.6, we present the models

that evolve into transparent wind UV-intense stars. An analysis of the helium abundance at the surface and in the core is given in Sect. 2.7. A closer look into the mass-loss history is taken in Sect. 2.8. The evolution of the rotational velocity is presented in Sect. 2.9. In Sect. 2.10, we provide information on the ionizing fluxes predicted by our models. In Sect. 2.11, we discusse the results in context of previous publications of massive-star evolution at low metallicity. A summary of the results is given in Sect. 2.12. Appendix 2.12 provides isochrones, Appendices 2.12 and 2.12 (available only in the online version) provide a summary of the models and a table of the ionizing fluxes, respectively. All the evolutionary model sequences and isochrones are available via the CDS archive.

2.2 Physical assumptions

We use a one-dimensional hydrodynamic binary evolutionary code (BEC) to compute rotating and non-rotating single stellar evolutionary sequences (see Heger et al., 2000; Heger and Langer, 2000; Brott et al., 2011; Yoon et al., 2012, and references therein). BEC solves the five stellar structure equations using the implicit Henyey method. It contains detailed state-of-the-art treatment of rotation, magnetic fields, angular momentum transport and mass-loss.

Stellar model sequences are computed under the physical assumptions described in this section. The time between two consecutive models in the sequence is chosen adaptively, resolving the structural changes in detail. We typically resolve the core-hydrogen-burning evolution with ~2000 time steps, for which each stellar model is resolved into a similar number of mass shells. The whole set of evolutionary sequences with different initial masses and rotational velocities (but the same initial composition) is referred to as our grid of models.

The calculations were stopped when the central helium abundance reaches Y_C=0.98. We choose this as the terminal age main-sequence (TAMS). After this point, as the hydrogen fraction in the core becomes very small, the central temperature increases substantially due to an overall contraction, and the star falls out of thermal equilibrium. For this reason, we exclude this short contracting phase from the analysis of the main-sequence evolution of our stellar models.

2.2.1 Initial chemical composition

Stellar models with the same initial mass M_{ini} and same initial rotational velocity v_{ini} but different initial composition Z_{ini} may evolve differently for at least two reasons. First, the metallicity has a fundamental impact on the mass-loss rate of a star: the higher the total metal abundance at the surface, the stronger the stellar wind (Kudritzki et al., 1987; Vink et al., 2001; Mokiem et al., 2007; Puls et al., 2008). Second, due to the reduced radiative opacity and the low amount of CNO nuclei as initial catalysts, metal-poor stars are more compact than corresponding metal-rich ones (Ekström et al., 2011; Yoon et al., 2006).

We compare recent observations of the metal abundance pattern of the Sun and the dwarf galaxy I Zw 18 in Fig. 2.1. In particular carbon and nitrogen are under abundant compared to scaled solar abundances (see also Nicholls et al., 2014). We also plot the composition of the Small Magellanic Cloud (SMC) scaled down by ten. The metal abundance patterns of BCDGs in general are different from that of the Sun (Y. I. Izotov et al., 1999; Vink et al., 2001; Tramper et al., 2011; Lebouteiller et al., 2013; Nicholls et al., 2014), showing that the metal abundance pattern of the SMC, which is the nearest metal-poor irregular dwarf galaxy, is a

better approximation for the composition of e.g. I Zw 18 than the solar abundance pattern. Hence, to obtain theoretical predictions for the massive stars in I Zw 18 , we take the abundance pattern of the SMC as in Brott et al. (2011), scale it down by a factor of ten and calculate massive stellar evolutionary models with this composition. The metallicity of our models (i.e. the sum of all metals as mass fraction) is then Z=0.0002.

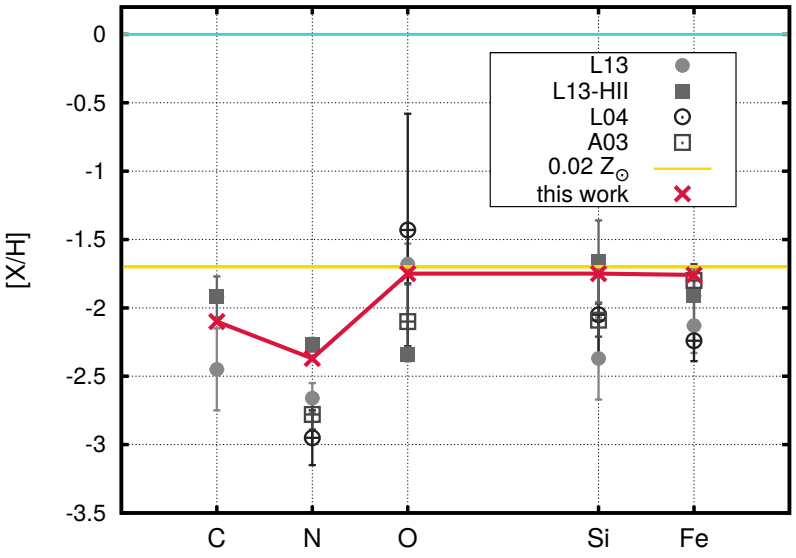

Figure 2.1. Recent measurements of abundances in I Zw 18 compared to our applied composition (i.e. SMC composition scaled down by ten; shown by a red line with crosses). Carbon, nitrogen, oxygen, silicon and iron abundances are given relative to solar (Asplund et al., 2009): [X/H]=log(X/H)−log(X/H)$_\odot$. *L13*: first column of Table 7 in Lebouteiller et al. (2013). *L13-HII*: last column of the same table, composition of the HII regions. *L04* and *A03*: data of previous measurements, taken from Lecavelier des Etangs et al. (2004) and Aloisi et al. (2003), respectively. *0.02 $Z_\odot$*: solar abundances of Asplund et al. (2009) scaled down by a factor of 50.

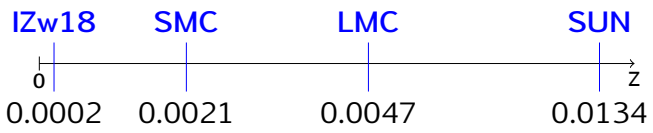

Figure 2.2. Metallicities on a linear scale. SUN: solar metallicity given by Asplund et al. (2009). LMC, SMC: Large and Small Magellanic Clouds (I. Hunter et al., 2007; Brott et al., 2011). IZw18: $Z_{IZw18} \simeq 0.1 \times Z_{SMC}$. The zero value corresponds to the metal-free Pop III stars.

Fig. 2.2 shows the metallicities of the local group galaxies SMC and LMC (as in Brott et al., 2011), and of the Sun (Asplund et al., 2009) as well as the metallicity of our I Zw 18 models. The zero value corresponds to the nearly metal-free first stars in the Universe called Population III stars. The metallicity of I Zw 18 is very close to that of Pop III stars on a linear scale; however,

there are differences between our models and models of Pop III stars (see Sect. 2.10 and Yoon et al., 2012).

For the initial value of helium, we assume that the mass fraction scales with the metallicity between the primordial helium mass fraction (Peimbert et al., 2007) and the solar value (Grevesse et al., 1996). Thus, the initial helium abundance in our Z_{ini}=0.0002 stellar models is Y_{ini}=0.2477.

Radiative opacities were interpolated from the OPAL tables (Iglesias and Rogers, 1996) with solar-scaled metal abundances, with their iron abundance used as the interpolation parameter for metals. Our models thus correspond to a metallicity of [Fe/H]=−1.7 and Z≈$Z_{\odot}$/50.

2.2.2 Physics of the stellar interior

All the mixing processes considered here are modelled as diffusive processes. Convection is treated according to the mixing-length theory (MLT) (Böhm-Vitense, 1958) with an MLT parameter of $\alpha_{\rm MLT}$ = 1.5 (Langer, 1991). Semi-convection is considered with an efficiency parameter of $\alpha_{\rm SEM}$ = 1 (Langer et al., 1983; Langer, 1991), although it has minor effects on the models during the main-sequence evolution. As no calibration of the convective core overshooting parameter exists for stars of the considered metallicity, we rely on the work of Brott et al. (2011) who calibrated the overshooting against the rotational properties of B-type stars from the VLT-FLAMES survey (I. Hunter et al., 2008; Vink et al., 2010) as $\alpha_{\rm over} = 0.335 H_p$, where H_p is the local pressure scale height. It has been suggested by Castro et al. (2014) and confirmed by McEvoy et al. (2015) that convective core overshooting of Galactic stars is probably mass-dependent and, at high mass ($\gtrsim 15\ M_{\odot}$), stronger than previously thought. However, the metallicity dependence of this effect still needs to be investigated.

Rotationally-induced mixing of chemical elements is treated with an efficiency parameter f_c = 0.0228 (Heger et al., 2000; Heger and Langer, 2000), calibrated by Brott et al. (2011). Furthermore, transport of angular momentum by magnetic fields due to the Spruit–Taylor dynamo (H. Spruit, 2002; Heger et al., 2005) is included, which is assumed here not to lead to additional transport of chemical elements (H. C. Spruit, 2006; Suijs et al., 2008).

2.2.3 Mass-loss

For the early evolutionary stages of our models, we use the mass-loss rate prescription of Vink et al. (2000), which includes a bi-stability jump at ∼25 kK. The dependence of mass-loss on the metallicity is additionally implemented according to Vink et al. (2001) as $\dot{M} \sim Z^{0.86}$. Approaching the empirical Humphreys–Davidson limit (thought to be connected to the Eddington limit), O and B stars may experience an increase in mass-loss, which is taken into account by using the empirical mass-loss rate prescription of Nieuwenhuijzen and Jager (1990) (with the same Z dependence as above) if its predicted mass-loss rate is higher than that of Vink et al. (2000) and Vink et al. (2001) at any effective temperature smaller than ∼22 kK.

Since we find some of our models to evolve into cool supergiants ($T_{\rm eff} \lesssim 12$ kK) even during their main-sequence lifetime, we need to take the mass-loss of cool supergiant stars into consideration. In general, mass-loss of such stars is observed to be higher than that of O and B stars due to the low surface gravity at their large radii (>1000 $R_{\odot}$) and possibly due to dust formation in cool atmospheres (Groenewegen et al., 2009). However, quantitative physical models of such winds still have deficiencies, hence we rely on the empirical parametrization of the mass-loss rate following the prescription of Nieuwenhuijzen and Jager (1990). This

prescription is a revised version of that of de Jager et al. (1988), which has been shown by Mauron and Josselin (2011) to be still applicable in the light of new observations of *bona-fide* red supergiants. The metallicity dependence of these winds is implemented as $\dot{M} \sim Z^{0.85}$ according to Vink et al. (2001). This formula is in accordance with the results of Mauron and Josselin (2011) who find that the metallicity exponent should be between 0.5 and 1.

Our calculations predict strong surface helium enrichment even during core hydrogen burning as a result of fast rotation (see Sects. 2.6 and 2.7). We use the prescription of Hamann et al. (1995) for the winds of our models when the surface helium abundance is $Y_S \geq 0.7$ with reduction by a factor of 10 as suggested by Yoon et al. (2006). This reduction gives a mass-loss rate comparable to the most commonly adopted one by Nugis and Lamers (2000) (see Fig. 1 of Yoon, 2015). The Hamann et al. (1995) prescription is applied together with a metallicity dependence of $\dot{M} \sim Z^{0.86}$ (Vink et al., 2001). For stars with surface helium abundances of $0.7 \geq Y_S \geq 0.55$, we interpolate linearly between the reduced Hamann et al. (1995) mass-loss rate and the rate of Vink et al. (2000) and Vink et al. (2001).

A mass-loss enhancement is implemented for stars rotating near their critical rotation which includes their Eddington factor (Langer, 1997; Yoon and Langer, 2005). It remains unclear whether rapid rotation *per se* leads to an increase in mass-loss (Müller and Vink, 2014). However, as discussed in Müller and Vink (2014), it still appears reasonable to consider that the mass-loss rate does increase close to the Eddington limit (Langer, 1997; Gräfener et al., 2011).

2.3 The grid of stellar models

Stellar model sequences were computed under the physical assumptions described in Sect. 2.2. Each sequence is represented by one dot in the diagram in Fig. 2.3.

The distribution of the sequences in the initial parameter space is chosen to support a study of synthetic populations. For such a study, an interpolation between the sequences would be needed, which is easier to do if the model grid is dense enough – especially in the regions where the models are most varied. Therefore, we increased the number of computed models in the yellow region, which represents the transition between normal and chemically-homogeneous evolution, because these models show more variations. Additionally, we increased the number of computed models in the corner of the very massive slow rotators (which become core-hydrogen-burning cool supergiants) in order to study their evolution in more detail.

The initial masses of the models in our grid are chosen roughly equidistant on a logarithmic scale. The most massive stars found so far in the local universe are suggested to have an initial mass around 300 $M_\odot$ (Crowther et al., 2010; Schneider et al., 2014). Therefore, while stars more massive than this might be important in the presence of a top-heavy initial mass function (e.g. Ciardi et al., 2003; Dabringhausen et al., 2009) or in large starbursts (Treu et al., 2010; Sonnenfeld et al., 2012; Chabrier et al., 2014), we use 294 $M_\odot$ here as an upper limit.

The colouring of the dots in Fig. 2.3 represents the surface helium mass fraction at the end of the main sequence (cf. Sect. 2.7). The red, yellow and blue regions indicate the type of evolution a given model undergoes, as described in Sects. 2.3.3 and 2.7.

2.3.1 Rotational velocities

The Y-axis in Fig. 2.3 refers to the initial equatorial rotational velocity at the surface of our models. We chose to cover a wide range in initial rotational velocity from zero up to 600 km s^{-1}.

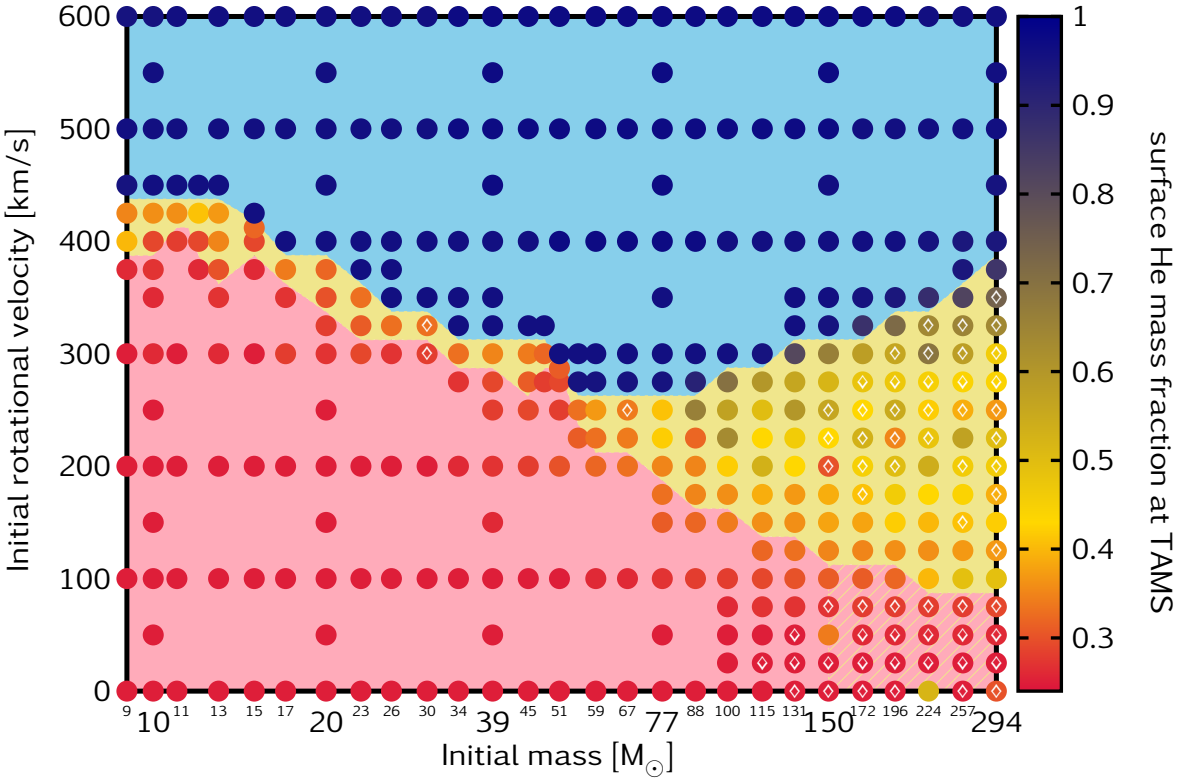

Figure 2.3. Grid of 375 evolutionary sequences of single stars. Each evolutionary sequence of our grid is represented by one dot in this diagram. Sequences inside the blue shaded region follow chemically-homogeneous evolutionary paths evolving bluewards in the HR diagram and having a surface helium abundance of $Y_S \simeq 0.98$ at the TAMS. Sequences inside the red region follow normal evolution, keeping Y_S close to the initial value of $\simeq 0.24$. Sequences inside the yellow region deviate from normal evolution: either they start their lives evolving chemically homogeneously and then switch to normal evolution, or they start normal evolution and mass-loss uncovers their helium-rich layers (cf. Sect. 2.7). Diamonds mark the sequences that have not reached the TAMS (i.e. the calculation was stopped between $0.82<Y_C<0.98$), and the yellow-dashed pattern indicates that the separation line between the red and yellow regions is uncertain at the highest masses.

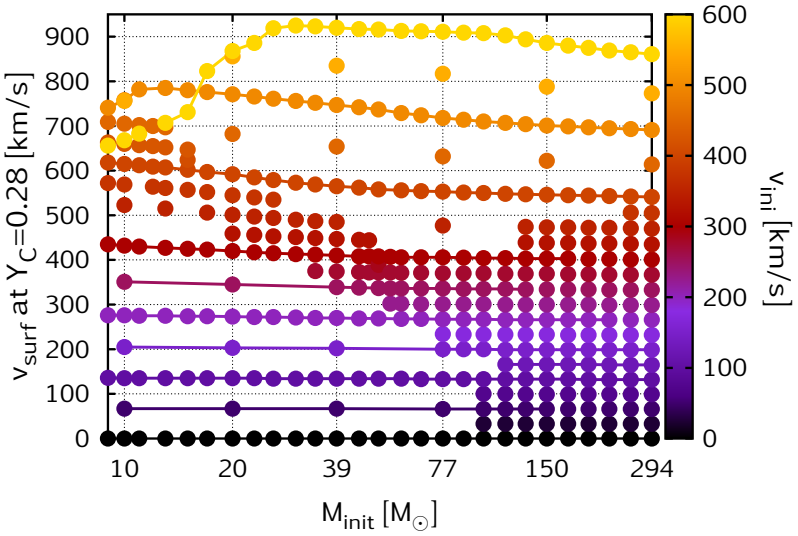

Figure 2.4. Surface rotational velocity at the ZAMS (cf. Sect. 2.3.1). Every dot represents one evolutionary sequence, cf. Fig. 2.3. The colours refer to the *initial* surface rotational velocity, v_{ini}. Sequences with v_{ini}=50, 100, 125, 150, 200, 250, 300, 400, 500 and 600 km s^{-1} are connected by lines.

The models start out chemically homogeneous and in hydrostatic and thermal equilibrium initially. We emphasise that the initial rotational velocities refer to the values with which the calculations were started, and are generally significantly lower than the rotational velocity after hydrogen burning has reached CNO equilibrium, i.e. at central helium abundance $Y_C \simeq 0.28$ (Fig. 2.4). We define this point in time as the zero-age main-sequence (ZAMS). The reason for the rotational velocity at the ZAMS being higher than initially is that at the beginning of the calculation, the star undergoes a short phase of structural changes while approaching CNO equilibrium. During this adjustment phase, the star contracts, spins up and thus continues its evolution with increased rotation. On average, our models rotate about 30% faster than the nominal (i.e. Y-axis in Fig. 2.3) initial rotational velocity indicates.

Stellar models in the left top corner of Fig. 2.4 with M$\lesssim$17 $M_\odot$ and v_{ini}=600 km s^{-1} rotate slower at the ZAMS than models with v_{ini}=500 km s^{-1}. This is because although the models with v_{ini}=600 km s^{-1} also spin up initially, they nearly reach their Keplerian velocity during the early contraction phase. Stellar models close to the breakup rotation undergo enhanced mass-loss, so they lose mass and spin down at the beginning of the evolution. In this phase, the one-dimensional models only provide crude approximations of fast rotating stars (see e.g. Decressin et al., 2007; Chiappini et al., 2011; Krtička et al., 2011; Espinosa Lara and Rieutord, 2013, for a discussion of stars close to the breakup rotation). In particular, when the surface rotational velocity approaches the break-up velocity, angular momentum may be removed by losing mass into an equatorial, viscous decretion disc, as discussed by Krtička et al. (2011). The effects of the decretion disc on the evolution of our fast rotating massive stars still remains to be studied.

2.3.2 Normal, homogeneous and transitionary evolution

The grid in Fig. 2.3 consists of 375 sequences, from which 142 are classified as normal evolution (NE), 123 as (quasi) chemically-homogeneous evolution (CHE), and 110 as transitionary evolution (TE). The calculation of some sequences with NE and TE were stopped before reaching the TAMS due to numerical difficulties. However, all the sequences in the grid reached a core helium mass fraction of $Y_C \gtrsim 0.82$. In Fig. 2.4, the sequences that were not followed until the TAMS are marked.

Models with NE develop a core-envelope structure: the core is chemically mixed through convection and fuses hydrogen into helium, while the envelope largely retains its initial composition. Their radii increase during the main-sequence lifetime because a chemical gradient develops and because the envelope inflates in the case of the highest-mass models (see the discussion in Sect. 2.5). We also refer to Sect. 2.4 for the discussion of the HR diagram, in which the models evolve towards lower effective temperatures (redwards).

Chemically-homogeneous evolution was first described by Maeder (1987) in the context of rotation. Several authors have since investigated this evolutionary behaviour (see e.g Yoon and Langer, 2005; Yoon et al., 2006; Cantiello et al., 2007; Meynet and Maeder, 2007) and have reported observational support for it (Walborn et al., 2004; Eldridge and Stanway, 2012; Martins et al., 2013). Models with CHE develop only shallow chemical gradients between the core and the envelope and all the nuclear products are mixed throughout the star and reach the surface. We investigate their surface helium abundance and the optical depth of their winds in Sect. 2.6.

Transitionary evolution was introduced by Yoon et al. (2012) for Pop III sequences where the surface helium mass fraction Y_S becomes larger than 0.7 at the TAMS, but the post-main-sequence evolution proceeds redwards. However, in their grid of 51 stellar sequences, only three sequences were identified as TE. We decided to use this expression in a broader sense: to describe a behaviour when the model starts evolving homogeneously and, at some point of the main-sequence lifetime, turns to normal evolution due to angular momentum loss in the stellar wind (see also Sect. 2.7). Note that this revised definition of TE considers only the main-sequence phase.

2.3.3 The structure of the grid

In this section, we analyse the grid of stellar sequences shown in Fig. 2.3. A prominent feature for our grid is the shape of the transition region shown in yellow in Fig. 2.3. This region is narrow in the lower-mass regime (9-55 $M_\odot$). For higher masses (55-294 $M_\odot$), however, it covers a larger range of initial rotational velocities. The higher the mass, the more sequences follow TE.

At masses lower than ~55 $M_\odot$ in Fig. 2.3, the bifurcation between NE and CHE is sharp, and there is a very small transitionary region between them. For these masses, the initial rotational velocity at which a star evolves homogeneously decreases with the initial mass. This is consistent with the finding of Yoon et al. (2012), who showed for stars in the mass range of 13-60 $M_\odot$ that the ratio of the timescale of the Eddington–Sweet circulation τ_{ES}, which governs the mixing in our models, and the main-sequence lifetime τ_{MS} is systematically smaller for a higher-mass star. The ratio τ_{ES}/τ_{MS} becoming lower with mass is related to higher radiation pressure and lower density in higher-mass stars. Therefore, for a given initial rotational rate, CHE is favoured in higher-mass stars. Although Yoon et al. (2012) applied this reasoning

to metal-free massive stars, our low-metallicity stellar models nevertheless follow the same principles.

In the regime above 55 $M_\odot$ in Fig. 2.3, mass-loss effects are contributing significantly. Mass-loss influences the evolution at least in two ways. First, mass-loss removes angular momentum (Langer, 1998). This can make an initially fast rotating star spin down and turn to normal, redwards evolution. Second, if enough mass is lost, deeper, helium-rich layers can be uncovered. This way the star appears more blue. Which effect of these two is more dominant, depends on the actual angular momentum and the size of the convective core, as explained below.

Slow rotators follow normal redward evolution, and angular momentum loss has no significant effect on them. At masses $\gtrsim$80 $M_\odot$, slowly rotating ($v_{ini} \lesssim$100 km s^{-1}) models evolve into cool supergiants before core-hydrogen exhaustion due to envelope inflation (Sect. 2.5). As we show in Sect. 2.7, these supergiant models may expose helium-rich layers near the TAMS due to the strong mass-loss and the deep convective envelope. Therefore, some of them are marked by orange coloured dots in Fig. 2.3.

The normally-evolving models that are close to the yellow transition region also have orange colours. This implies that there is no clear separation between normally-evolving and transitionary-evolving models in the mass range 100-294 $M_\odot$. The transition here happens smoothly, and the separation line between the red and yellow regions that we draw in Fig. 2.3 in this mass range is somewhat arbitrary.

Additionally, as Fig. 2.4 shows, for most of the sequences in the bottom right corner of the grid the calculation of the last model did not converge, so the simulations were stopped before reaching the TAMS. If these sequences were continued until Y_C=0.98, they would probably expose deeper layers and would also appear more orange in Fig. 2.3, and that would move the separation line between the red and yellow regions towards slower rotations, so we marked this uncertain part of the diagram with a dashed pattern. However, the fact that some of the models are unevolved does not explain all the diversity in the surface helium and the colours in the bottom right corner of the grid in Fig. 2.3. The two consequences of mass-loss (the induced spin down due to angular-momentum loss and the uncovering of the deep-lying helium-rich layers) shape the surface properties of the models at the TAMS. Additionally, these models increase their radii, making the stars appear more red and, due to the effective core-envelope coupling (Sect. 2.9.1), spin up. The consequence of these two competing mechanisms is that the models in the bottom right corner of the grid show diversity in the surface helium value at the TAMS (and also in the surface rotational velocity at the TAMS, as we discuss in Sect. 2.9.2).

At moderate initial rotation (~200-350 km s^{-1}) angular momentum loss is important for very massive stellar models ($\gtrsim$88 $M_\odot$) and can turn the evolution from homogeneous to transitionary. The loss of angular momentum causes mixing to become inefficient. A star with inefficient mixing starts to possess a steep chemical gradient between the mixed core and a non-mixed envelope. This prevents CHE for the very massive stellar models in the upper part of the transitionary region. Their spindown behaviour shapes the boundary between the blue and yellow regions: models with TE in the yellow region would be models with CHE if there were no mass and angular momentum loss. The borderline velocity between the blue and the yellow region is increasing with mass above 55 $M_\odot$.

If the rotation is fast enough, mass-loss cannot spin the star down enough to prevent the overall mixing. The fastest rotators therefore undergo CHE over their whole lifetime. They are enclosed in the blue region in Fig. 2.3.

Summarising, the slowest initial rotation (250 km s^{-1}) showing chemically-homogeneous evolution occurs for stars of 55-88 $M_\odot$. Stars less and more massive than this need to rotate

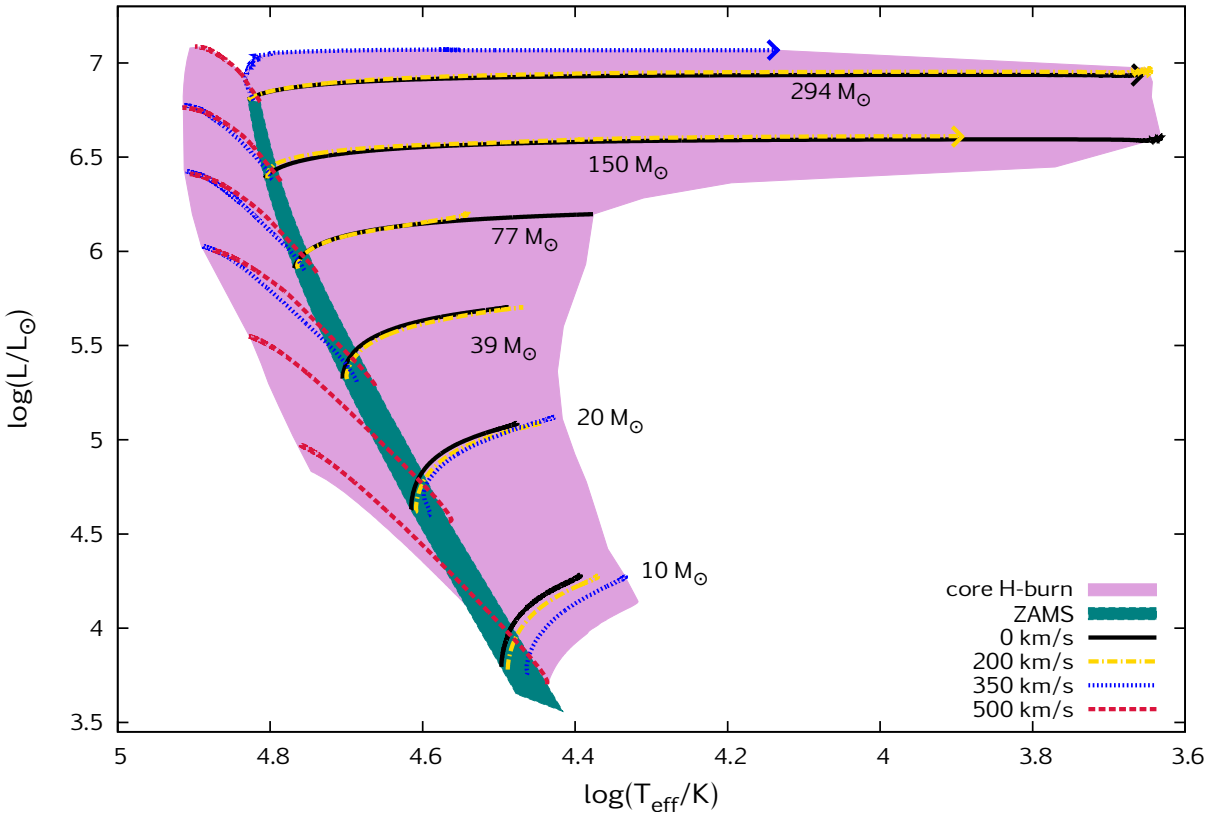

Figure 2.5. Evolutionary tracks in the HR diagram during core hydrogen burning for models with initial masses between 9-300 $M_\odot$ (see labels) and initial rotational velocities of 0, 200, 350 and 500 km s^{-1}, with a composition of 1/10 Z_{SMC}. The lighter (purple) shading identifies the region in which all models of our grid undergo core hydrogen burning. The darker (green) shading identifies the zero-age main-sequence. An arrow marks the end of the tracks for models that were stopped before the terminal age main-sequence was reached. Core-hydrogen-burning objects are expected to be found on both sides of the ZAMS, inside the purple coloured region.

faster than 250 km s^{-1} initially to follow a homogeneous evolutionary path, because either the Eddington–Sweet timescale is too large (in the case of the lower-mass regime) or too much angular momentum is lost in the wind (in the case of the higher-mass regime).

2.4 Evolutionary tracks in the HR diagram

In this section, we discuss the evolution of our low-metallicity massive stars in the HR diagram (see Fig. 2.5). The tracks that are plotted constitute a representative subset of our grid. Here we summarise their typical behaviour.

Slow rotators (v_{ini}=0-200 km s^{-1} in Fig. 2.5, more precisely those in the red region of Fig. 2.3) evolve from the ZAMS towards lower effective temperatures (i.e. *redwards*) and towards higher luminosities, which represents normal evolution. In contrast, fast rotating stars ($\gtrsim$500 km s^{-1} in Fig. 2.5, those in the blue region of Fig. 2.3) turn towards higher temperatures (bluewards) from the beginning, following CHE (Maeder, 1987). The bifurcation between redward NE and blueward CHE has been studied by e.g. Brott et al. (2011) who showed that the lower the

metallicity, the more predominant the CHE becomes.

Models shown in Fig. 2.5 with intermediate initial rotational velocities (~200-350 km s^{-1}) might evolve either normally or chemically-homogeneously, depending on their mass. In some cases, however, we can classify them neither NE nor CHE because the model shows properties of both evolutionary classes. For example, the 294 $M_\odot$ model with 350 km s^{-1} evolves first chemically-homogeneously then turns to normal evolution, which is defined as transitionary evolution (represented by the yellow region in Fig. 2.3).

The type of evolution is not only a function of the rotational velocity but also of the initial mass. In Fig. 2.5 one can observe the behaviour of the 350 km s^{-1} models: the lowest mass models (9-23 $M_\odot$) undergo NE, i.e. they evolve normally and redwards in the HR diagram, while higher mass models (26-257 $M_\odot$) undergo CHE, i.e. they evolve chemically-homogeneously and bluewards. The 294 $M_\odot$ model with 350 km s^{-1} is a transitionary case. We investigate the dependence of the evolutionary types on initial mass and rotation in Sect. 2.3.3.

The ZAMS positions of our models is shown by the green shaded region in Fig. 2.5. It is a broad region instead of a line due to the different rotation rates of the ZAMS models. Centrifugal acceleration reduces the effective gravity so while the radius of the rotating stellar model is higher, its temperature and luminosity are lower compared to a non-rotating stellar model of the same mass (cf. Fig.3 in Köhler et al., 2015).

Purple shading in Fig. 2.5 represents the region which encloses all our models that burn hydrogen in their core. Due to the presence of the stars with CHE at this low metallicity, the purple main-sequence region encompasses the green ZAMS region. Our evolutionary calculations thus predict *hydrogen-burning massive stars to be found on both sides of the ZAMS*.

Some of the tracks stopped at the upper red side of the purple region due to numerical instabilities (see also the white diamonds in Fig. 2.4). Therefore, the upper borderline of the main-sequence region is approximate and might change (however not significantly) if all models were continued until $Y_C = 0.98$.

There is a significant difference between the redwards evolving lower- and higher-mass stellar sequences. Lower-mass ($\lesssim 80\ M_\odot$) models stay more or less close to the ZAMS, never reaching $\log(T_{\rm eff}/K)$ values lower than ~4.3. Higher-mass models, on the other hand, evolve all the way to the cool supergiant region ($T_{\rm eff} < 12$ kK) before core-hydrogen exhaustion. These high-mass objects are, therefore, *core-hydrogen-burning cool supergiants* during the last 5-15% of their main-sequence lifetimes.

2.5 Core-hydrogen-burning cool supergiants

The models of $\gtrsim 80\ M_\odot$ in our grid with slow or intermediate rotation rates spend the last 5-15% of their main-sequence evolution on the cool supergiant branch with $T_{\rm eff} < 12$ kK. We call this evolutionary phase the core-hydrogen-burning cool supergiant phase.

Fig. 2.6 shows the radius of our stellar models at the TAMS. The fast rotating, chemically-homogeneously-evolving models all remain compact and blue, while the massive ($M_{\rm ini} \gtrsim 80\ M_\odot$) models with normal and transitionary evolution expand during the main-sequence lifetime. They may reach $T_{\rm eff}$ values below 12 kK and radii larger than 1000 $R_\odot$, and become core-hydrogen-burning cool supergiants near the TAMS.

The reason for the expansion of our massive unmixed models is their proximity to the Eddington limit. Köhler et al. (2015) and Sanyal et al. (2015) find that this occurs for stars

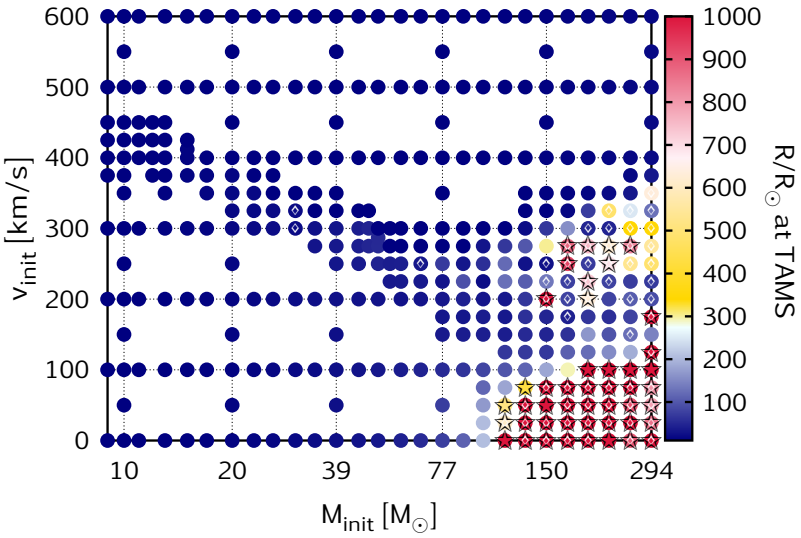

Figure 2.6. Radius at the end of the main-sequence evolution as a function of initial mass and rotational velocity. The core-hydrogen-burning cool supergiants (defined as $T_{\rm eff}^{\rm TAMS} < 12$ kK) are found at high mass and slow or intermediate rotation. We mark them with a star symbol. White diamonds mark the sequences that have not reached the TAMS (i.e. the calculation was stopped between $0.82<Y_C<0.98$).

above ~50 $M_\odot$ in LMC models, whose mass-loss, however, removes the hydrogen-rich envelope such that stars above ~100 $M_\odot$ do not become that cool. We note that even very massive zero-metallicity models have been shown to become red supergiants during core hydrogen burning (Marigo et al., 2003; Yoon et al., 2012).

Fig. 2.7 shows the evolution of our slowly rotating stellar sequence with 294 $M_\odot$ in the HR diagram. After the first 1.5 Myr, the radius inflates from 150 $R_\odot$ to 5100 $R_\odot$ within 0.2 Myr. Thus, the model spends ~0.3 Myr (15% of the total main-sequence lifetime) as a core-hydrogen-burning cool supergiant before hydrogen exhausts in the core. During this time, the mass-loss rate is very high (up to $4{\cdot}10^{-4}$ $M_\odot$/yr). The star loses mass rapidly and ends up with 244 $M_\odot$ at the TAMS. However, it still retains a hydrogen-rich envelope of ~60 $M_\odot$ at this time.

As seen in Fig. 2.6, several sequences evolve similarly to the 294 $M_\odot$ sequence discussed above, reaching surface temperatures below 12 kK. There are two distinct regions containing core-hydrogen-burning supergiants, one at high mass and slow rotation, and the other at high mass and around 275 km s^{-1} initial rotation. The slow rotators evolve normally during the first part of their main-sequence lifetimes, while those at intermediate rotation rates evolve homogeneously initially, and turn to normal evolution due to angular momentum loss (transitionary evolution).

The stability of the extended envelopes of the core-hydrogen-burning cool supergiants is uncertain. Moriya and Langer (2015) suggest that their likely pulsational instability may lead to enhanced mass-loss. This may significantly shorten this evolutionary stage.

Nevertheless, should they exist, they may be extremely bright stars. As their bolometric correction is essentially zero, the cool supergiants predicted by our model grid with $\log(L/L_\odot)$=6.3...7 would have visual magnitudes in I Zw 18 , adopting a distance of 18 Mpc (Aloisi et al., 2007), in the range of 20.3 mag...18.6 mag. Brightness variations with periods of

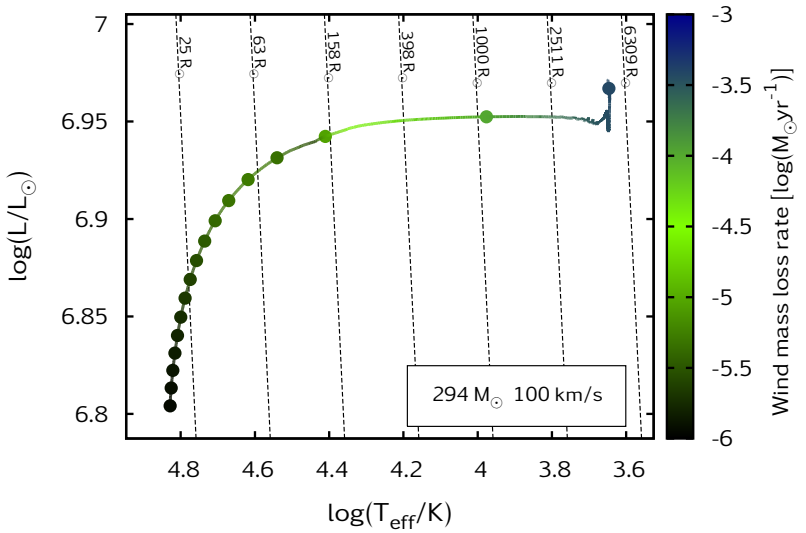

Figure 2.7. Evolutionary track of our model with M_{ini}=294 $M_\odot$ and v_{ini}=100 km s^{-1} during core hydrogen burning in the HR diagram. Dots mark every 10^5 years of evolution. The stellar wind mass-loss rate is colour coded; black dashed lines of constant radii are labelled according to their radius value. The star becomes a core-hydrogen-burning cool supergiant during the last 15% of its main-sequence evolution.

the order of months to years due to pulsations may reveal them as stars rather than star clusters in photometric multi-epoch observations.

There may also be other ways to look for core-hydrogen-burning cool supergiants in nature. According to our simulations, core-hydrogen-burning supergiants lose a significant amount of mass during the red supergiant phase. In the case of the 294 $M_\odot$ star analysed above, for example, as much as ~40 $M_\odot$ of material is lost in the red supergiant wind. As the material lost in the wind has undergone CNO processing, the material that returns to the circumstellar gas pollutes the environment with hydrogen-burning products. The low wind velocity may allow this gas to be retained in the vicinity of the star-forming region which produced the cool supergiants, and thus pollute the gas from which further stars in the same region may form. E.g., our cool supergiants may have an impact on the understanding of abundance anomalies in globular clusters (Caretta, 2010; Bastian et al., 2013, and Szécsi et al. in prep.).

2.6 Transparent Wind Ultraviolet Intense stars

Stars of all masses that evolve homogeneously mixed during their main-sequence lifetime occupy the left purple region in Fig. 2.5, i.e. blueward from the ZAMS.

These models have OB-type mass-loss initially. WR-type mass-loss is adopted for Y_S>0.7, see the top panel in Fig 2.8. Therefore, from the evolutionary point of view, these models might be considered as core-hydrogen-burning WR stars. However, from the observational point of view, WR stars are characterized by the presence of strong emission lines, which indicate optically-thick winds. We estimate the optical depth of their winds following Eq. (14) of Langer

(1989) as:

$$\tau(R) = \frac{\kappa \dot{M}}{4\pi R(v_\infty - v_0)} \ln \frac{v_\infty}{v_0}, \tag{2.1}$$

where R designates the radius of the stellar model without taking the wind into account. This equation is derived from a β-velocity law with β=1. In that, we use the electron scattering opacity $\kappa = \sigma(1+X)$, σ being the Thomson scattering cross-section, an expansion velocity of v_0=20 km s^{-1} at the surface of the stellar model, and a terminal wind velocity of $v_\infty = \sqrt{\frac{GM}{R}}$.

Fig 2.8 (bottom panel) shows the optical depth of the stellar winds as calculated from Eq. (2.1) for our homogeneously-evolving stellar models. The behaviour of the wind optical depth seen in this figure is mostly related to the mass-loss rate (cf. Sect. 2.8), which is increasing with mass. While these numbers are only approximate, they show that the winds of the lower-mass ($M_{ini} \lesssim 80$ M$_\odot$) models with CHE, even when applying WR-type mass-loss, remain optically thin ($\tau < 1$) throughout their main-sequence lifetime. Even the higher-mass models ($M_{ini} \gtrsim 80$ M$_\odot$) keep optically-thin winds for most of core hydrogen burning, and the wind optical depth does not exceed $\tau \simeq 3$ even up to core hydrogen exhaustion for the most luminous stars.

Our fully mixed stars are extremely hot (up to $T_{eff} \simeq 80$ kK) and bright (up to 10^7 L$_\odot$) objects which have an optically-thin wind. Additionally, they emit intense mid- and far-UV radiation (see also Sect. 2.10), so we call them Transparent Wind Ultraviolet INtense stars or TWUIN stars.

We emphasize that TWUIN stars are only expected at very low-metallicity. Their mass-loss, which depends on the metallicity, is not strong enough to spin them down to prevent homogeneous evolution (Szécsi et al. in prep.). They remain compact, i.e. the radii remain small, typically around 10-20 R$_\odot$. Additionally, they develop no core-envelope structure, so most of the hydrogen in the envelope is mixed into the burning regions and converted into helium. TWUIN stars therefore finish their main-sequence evolution as massive fast-rotating helium stars which make them strong candidates for long-duration gamma-ray bursts (Yoon and Langer, 2005; Woosley and Heger, 2006). Their rotational rate at the TAMS is discussed in Sect. 2.9.2.

2.7 The helium abundance at the surface and in the core

In the surface helium vs. central helium mass fraction (Y_S-Y_C) diagram, every stellar evolutionary sequence can be represented by one line, and the core helium mass fraction merely serves as a clock. During the core-hydrogen-burning stage, the slope of the line tells us about the efficiency of mixing helium from the core through the radiative envelope to the surface by rotation-induced turbulence. Thus, the steeper the slope, the more helium reaches the surface. Tracks of normally-evolving stellar models form a horizontal line while tracks of homogeneously-evolving models lie close to the diagonal in the Y_S-Y_C diagram. Furthermore, tracks of models with transitionary evolution lie between the horizontal and the diagonal lines. Consequently, it is easy to distinguish these three evolutionary behaviours in the Y_S-Y_C diagram.

Fig. 2.9 presents some of our stellar sequences in the Y_S-Y_C diagram. The non-rotating sequence of 77 M$_\odot$ evolves close to the X-axis of the Y_S-Y_C diagram, which indicates that there is no mixing between the core and the surface.

Sequences of intermediate rotational velocities (such as the models of 100 M$_\odot$-225 km s^{-1}, 150 M$_\odot$-300 km s^{-1} and 172 M$_\odot$-275 km s^{-1}) start their life homogeneously and with a slight

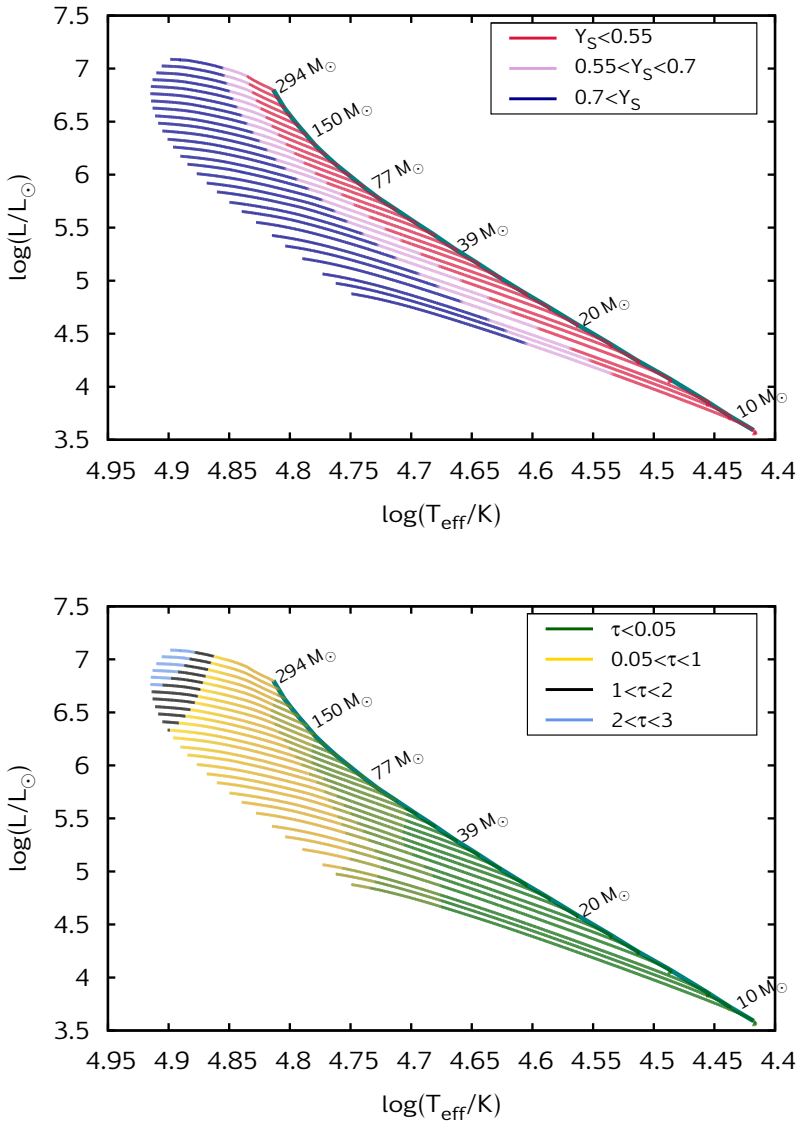

Figure 2.8. *Top:* HR diagram of models with v_{ini}=500 km s^{-1} (chemically-homogeneous evolution) and masses between 9-294 $M_\odot$. The thick green line marks the ZAMS. The colouring marks the surface helium mass fraction as indicated by the legend. For Y_S<0.55, OB-type mass-loss is applied; for Y_S between 0.55 and 0.7, an interpolation between OB- and WR-type mass-loss is applied; and for Y_S>0.7, WR-type mass-loss is applied (cf. Sect. 2.2.3). *Bottom:* HR diagram of the same collection of models as above. The colouring marks the wind optical depth τ according to Eq. (2.1).

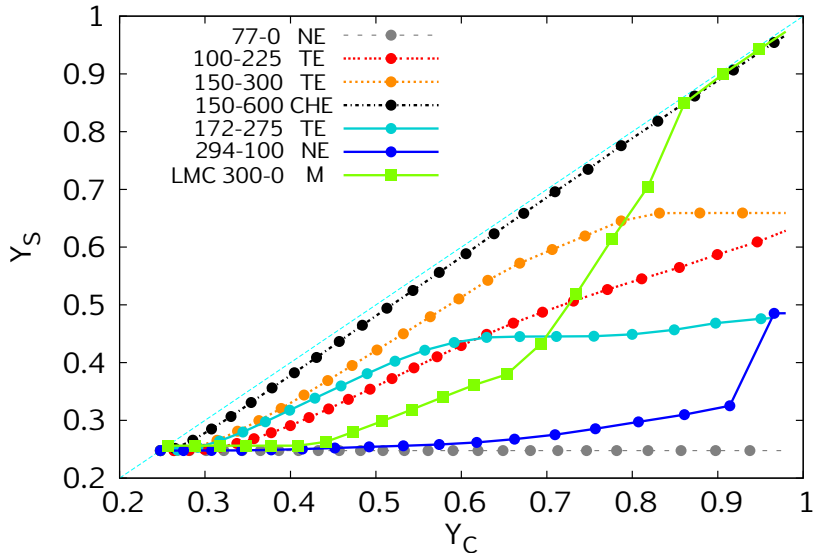

Figure 2.9. Mass fraction of helium at the stellar surface (Y_S) as a function of that in the core (Y_C) for sequences of different initial masses and rotational velocities as indicated by the legend, in units of $M_\odot$-km s^{-1}. Dots mark every 10^5 years of the evolution. The diagonal line (Y_C=Y_S) is marked by a lightblue (dashed) line. Stars that evolve chemically-homogeneously (CHE) lie close to the diagonal, while those that undergo normal evolution (NE) trace a horizontal line; stars with transitionary evolution (TE) lie between (see also Fig. 2.3). One non-rotating sequence (of type M) with M_{ini}=300 $M_\odot$ from the LMC grid of Köhler et al. (2015) is shown for comparison.

rise in the Y_S-Y_C diagram, but after a while they lose enough angular momentum so they turn to normal evolution and show a horizontal slope in the diagram. Therefore, we consider these sequences having transitionary evolution.

Fast rotating sequences of 600 km s^{-1} undergo CHE, turning bluewards in the HR diagram and following the diagonal line in the Y_S-Y_C diagram. In these models, the ashes of nuclear burning are mixed between the core and the surface, enhancing the surface with burning products (e.g. helium) and supplying unprocessed material to the hydrogen-burning region.

Köhler et al. (2015), who analysed stellar models with LMC composition, introduced Type M evolution, which stands for an evolutionary behaviour during which mass-loss is so efficient that the homogeneous layers of the stellar interior are uncovered. Fig. 2.9 shows one LMC sequence which is of Type M.

None of our sequences undergo evolution classified as Type M. This is simply because the mass-loss at our low-metallicity is less effective than at LMC metallicity. Although some sequences (e.g. the one with 294 $M_\odot$ and 100 km s^{-1} in Fig. 2.9) show effects of mass-loss near the TAMS, this effect is not strong enough to make the model homogeneous (i.e. $Y_C \simeq Y_S$).

The evolution leading to a core-hydrogen-burning cool supergiant star (Sect. 2.5) is represented by the track of 294 $M_\odot$ with 100 km s^{-1} initial rotation in Fig. 2.9. During the last $\sim 10^5$ years of the simulated evolution, the surface helium abundance increases rapidly for two reasons. The first reason is that the supergiant mass-loss takes over, leading to a significant increase in the surface helium abundance. The second reason is that a deep convective envelope develops in the outer layers of the star, which dredges out helium from the core. This model spends the last phase of its main-sequence evolution (between $Y_C \gtrsim 0.92$ and the TAMS) as a

core-hydrogen-burning red supergiant with $T_{\rm eff} \approx 4500$ K.

Another example of a core-hydrogen-burning supergiant is given by the track of 172 $M_\odot$ with 275 km s^{-1} initial rotational velocity. This model is categorised as transitionary evolution, since Y_S increases with Y_C initially (as in the case of the homogeneously-evolving models). Between $0.6 \lesssim Y_C \lesssim 0.8$, however, Y_S stays constant (typical for normal evolution). At $Y_C \sim 0.8$, a slight increase in the surface helium abundance happens again as the sequence proceeds towards lower effective temperatures and the mass-loss becomes more effective. Amongst our core-hydrogen-burning cool supergiant models, the highest surface helium mass fraction we find is 0.52.

2.8 Mass-loss history

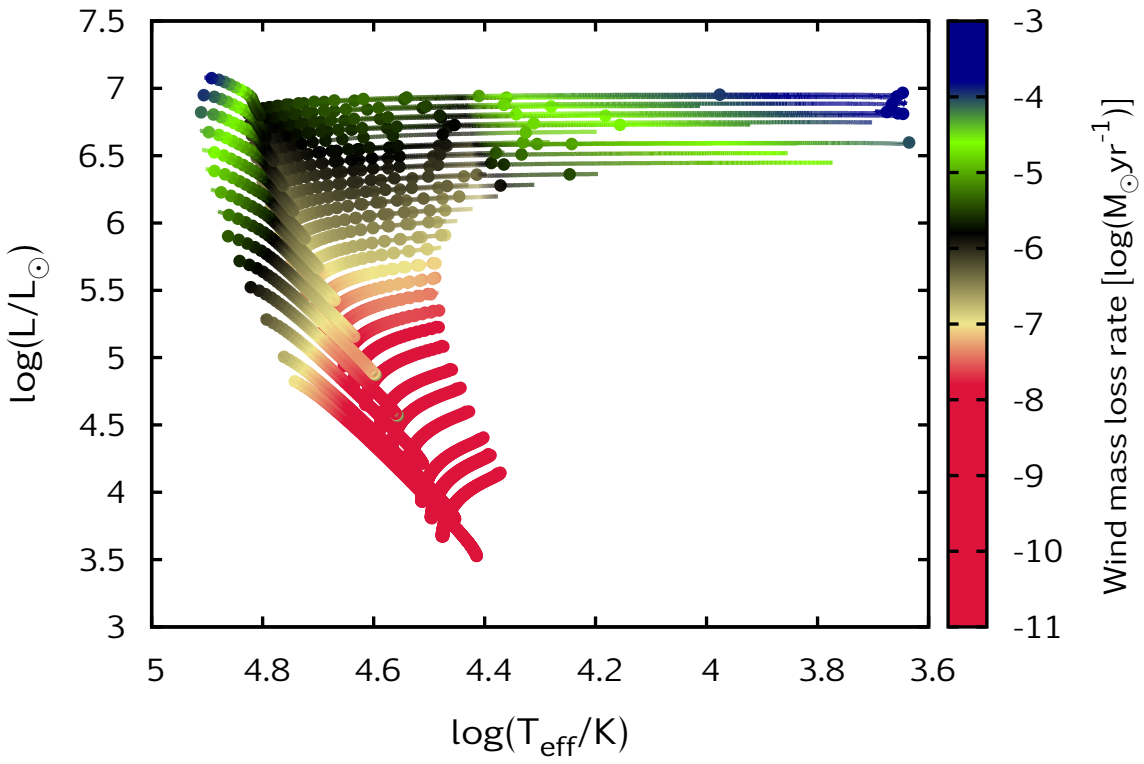

Figure 2.10. HR diagram showing sequences with $v_{\rm ini}$=0 and 500 km s^{-1} for all masses of our grid. Mass-loss rates are colour coded. Dots mark every 10^5 years of evolution.

While the mass-loss rates adopted for our models (Sect. 2.2.3) depend strongly on the initial metallicity (Vink et al., 2001, and Szécsi et al., in prep.), and our models lose less mass than their counterparts at, for example, LMC composition (Köhler et al., 2015), in the most extreme cases of the most massive TWUIN stars and the core-hydrogen-burning supergiants, our stellar models reach mass-loss rates as high as $4{\times}10^{-4}$ $M_\odot$ yr^{-1}. This is demonstrated by Fig. 2.10,

which shows the mass-loss rate of some of our models in the HR diagram.

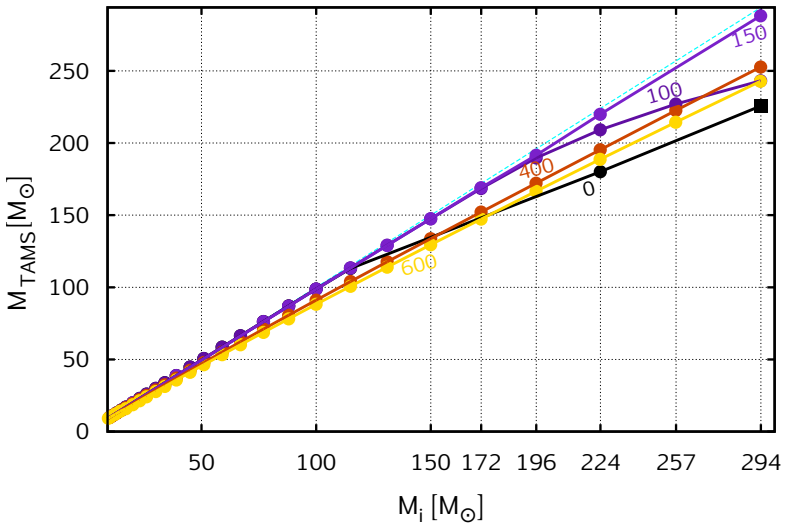

Figure 2.11. Initial mass vs. final mass (at the TAMS). Every dot marks one evolutionary sequence. Sequences with the same initial rotational velocity v_{ini} are connected, labels indicate the value of the corresponding v_{ini} in km s^{-1}. Only models that evolved until the TAMS are shown, except for the non-rotating one with M_{ini}=294 $M_\odot$ (marked by a rectangle), for which the final mass is extrapolated.

Fig. 2.11 shows the M_{ini} vs. M_{TAMS} relation for our stellar sequences. Overall, none of the tracks deviate much from the diagonal line, meaning that the mass-loss is quite weak for our models. However, there are some differences in how much mass the models with different evolutionary paths retain during their main-sequence lifetimes.

In the lower-mass regime ($\lesssim$100 $M_\odot$), the fast rotating, chemically-homogeneously-evolving sequences of 400 and 600 km s^{-1} end up having less mass than the slow rotating, normally-evolving sequences. This is due to the WR-type mass-loss rate that applies for the sequences with CHE during the second part of their main-sequence evolution.

For the high-mass ($\gtrsim$100 $M_\odot$) sequences, however, another behaviour is present: the very massive slow rotators (represented by the models of 0-100 km s^{-1} in Fig. 2.11) become core-hydrogen-burning cool supergiants. The efficiency of mass-loss increases when a star approaches the cool supergiant phase because the mass-loss prescription applied here has a radius dependence of $\dot{M} \sim R^{0.81}$. Thus, the mass-loss in this phase may be even stronger than the WR-type mass-loss, which means that stellar models that evolve to the cool supergiant phase during the main sequence may end up less massive than models with CHE of the same mass. Note that the model marked with a rectangle in Fig. 2.11 is stopped at Y_C = 0.87. For this model, we predicted the final mass based on the mass-loss rate in the last computed model and on the remaining hydrogen-burning lifetime.

Intermediate rotation rates (150-350 km s^{-1}) are represented by the models at 150 km s^{-1} in Fig. 2.11. These models eventually evolve normally but stay bluer due to enhanced surface helium abundance by rotational mixing (cf. models with TE in Fig. 2.9). They therefore undergo neither WR-type mass-loss nor cool supergiant mass-loss and only lose small amounts of mass due to the OB-type mass-loss that applies to them during their whole main-sequence lifetime.

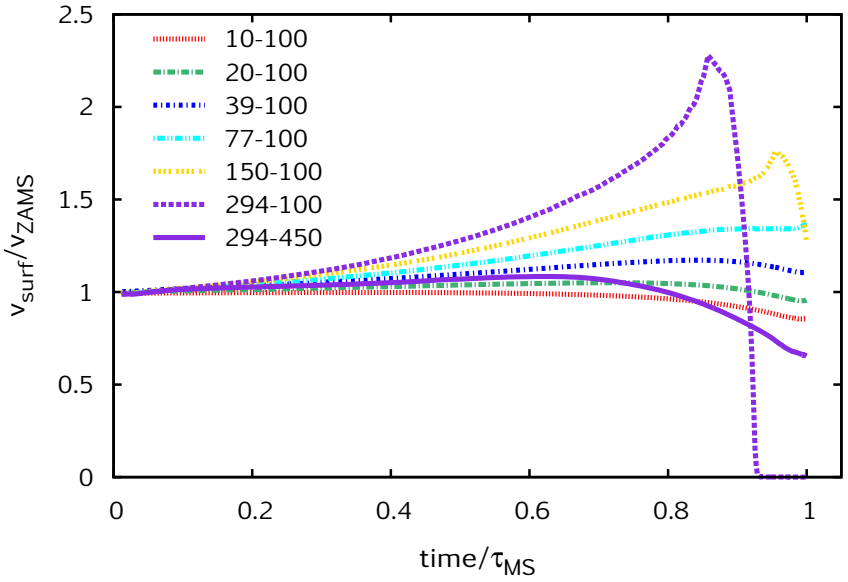

Figure 2.12. Surface rotational velocity as function of time for models with different initial masses and rotational velocities as indicated by the legend (units are [$M_\odot$]-[km s^{-1}]). The time is normalised to the main-sequence lifetime of the stars and the rotational velocity is normalised to the ZAMS value (see Sect. 2.3.1). The track of the 294 $M_\odot$–450 km s^{-1} model which evolves chemically homogeneously is plotted with a dotted line for comparison.

2.9 Rotation

At higher metallicity (e.g. Solar or LMC), rotating massive stars would be spun down during the main-sequence evolution because of mass and angular momentum loss via winds (Langer, 1998; Köhler et al., 2015). At the metallicity of I Zw 18 , in contrast, mass-loss is less efficient and the stars can retain a more or less constant amount of angular momentum. If there are efficient mechanisms transporting angular momentum in the interior between the core and the envelope, the surface rotational velocity might increase during the main-sequence evolution even when the star evolves towards lower surface temperature and larger radius (Ekström et al., 2008; de Mink et al., 2013). In this section we show how this core-envelope coupling plays a role in shaping the rotational history of our stars.

2.9.1 Evolution of the surface rotational velocity

The evolution of the surface rotational velocity for some of our models is presented in Fig. 2.12. The surface rotation of the 10 $M_\odot$-100 km s^{-1} model gradually decreases. Higher-mass models at 100 km s^{-1} from our grid, however, all increase their surface rotational velocity during the first ~80% of their main-sequence lifetime. The most massive models then reach a maximum and start a rapid decrease and spin down – in case of the 294 $M_\odot$-100 km s^{-1} model all the way to zero. This sequence evolves into a core-hydrogen-burning cool supergiant.

To understand this behaviour we need to consider the following mechanisms. In our stellar models, angular momentum can be transported from the core to the envelope due to meridional circulations and shear turbulence, as well as by magnetic torques (Sect. 2.2.2). The angular momentum transport aims to make the whole star rotate with constant angular velocity. During the main-sequence phase of a normally-evolving model, the stellar core contracts, the envelope

expands and the star evolves redwards in the HR diagram. Although the radius increases, angular momentum can be effectively transported from the contracting core outwards, at least during the first ∼80% of the main-sequence lifetime. As a result, the surface rotational velocity of the star must increase during this evolutionary phase.

The star therefore spins up. According to Fig. 2.12, the maximum velocity depends on the initial mass, being greater for higher-mass objects. The reason of this mass dependence is that the higher the mass the more massive the stellar core. The angular momentum which is transported from this more massive core to the envelope is therefore higher. The rotation rate can increase to more than twice the initial value in the case of the 294 $M_\odot$ model. In contrast, the 10 $M_\odot$ model does not show any increase of surface rotation because its core is relatively small.

For the highest mass models of 150 $M_\odot$–100 km s^{-1} and 294 $M_\odot$–100 km s^{-1}, a sudden drop happens at ∼85% and ∼95% of the main-sequence lifetime, respectively. This is further illustrated by Fig. 2.13 which shows the evolution of the radius and the mass-loss rate, as well as the angular velocity distribution inside the 150 $M_\odot$ model. The angular velocity is approximately constant until t≈0.80 τ_{MS}. Then the radial expansion becomes so pronounced that the angular momentum transport through the core-envelope coupling cannot keep the star rigidly rotating and the surface layers slow down. Additionally, the mass-loss increases at $\sim 0.94\ \tau_{MS}$ when the star encounters the bi-stability jump at $T_{eff} \sim 25$ kK (Vink et al., 2000). As a result, a significant amount of mass and angular momentum is lost contributing to the fast decrease of the surface rotational velocity.

At the TAMS, stars that have not become cool supergiants during the main-sequence still rotate rapidly (see also Sect. 2.9.2). The core-hydrogen-burning supergiants, represented by the 294 $M_\odot$–100 km s^{-1} model in Fig. 2.12, have negligible surface rotation at the TAMS in our calculations.

Our results support the finding of Meynet and Maeder (2002) and Ekström et al. (2008) that normally-evolving stars may increase their surface rotation during the main-sequence evolution if the mass-loss is low. This implies that the rotational velocity distribution of hydrogen-burning massive stars to be observed in low-metallicity environments is expected to be significantly different than that in higher-metallicity environments.

For fast rotators, the angular velocity distribution inside the star is always close to constant during the main-sequence lifetime. They are represented by the 294 $M_\odot$–450 km s^{-1} model in Fig. 2.12. This model evolves with only a slight radius increase during the first half of the main-sequence. When the WR-type mass-loss turns on at $\sim 0.65\ \tau_{MS}$, the mass-loss increases and spins the star down. However, WR-type mass-loss at this metallicity is not strong enough to remove all the angular momentum. Therefore these stars still rotate rapidly at the TAMS (see Sect. 2.9.2) and, if there is little angular momentum loss afterwards, also during their post-main-sequence phases (see Sect. 2.10.5).

2.9.2 Surface rotational velocity at the TAMS

Here we discuss the rotational rates of our models at the end of the main sequence. The rotational velocity of a model at the TAMS depends on its rotational behaviour during the main-sequence evolution, which in turn depends on the actual evolutionary path (normal, transitionary or homogeneous evolution, as seen in Sect. 2.9.1). Also, we refer to Sect. 2.3.1 where we discuss the rotational velocities of our models at the ZAMS.

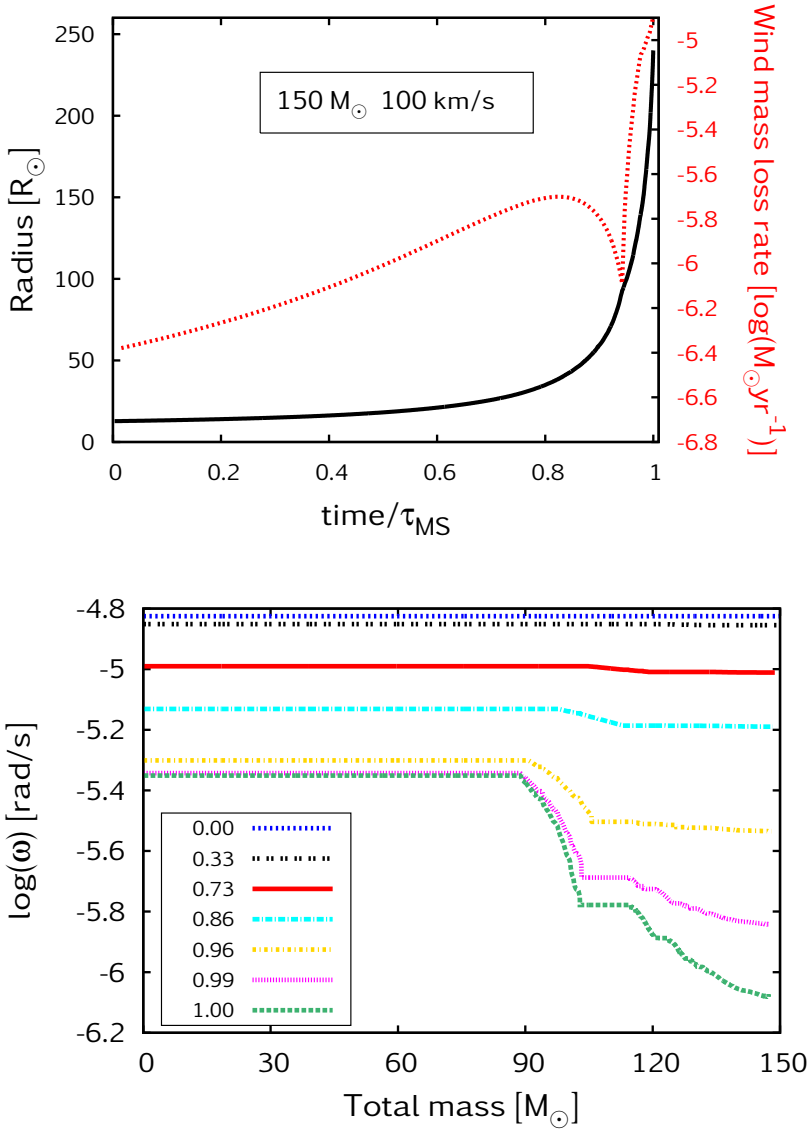

Figure 2.13. *Top:* Radius and mass-loss rate as a function of the main-sequence lifetime for the stellar sequence with M_{ini}=150 $M_\odot$ and v_{ini}=100 km s^{-1} (yellow track in Fig. 2.12). *Bottom:* Angular velocity (ω) distribution inside the same sequence at the fractions of main-sequence lifetime, t/τ_{MS}, indicated by the legend, where $\tau_{MS} = t^{Y_C=0.98} - t^{Y_C=0.28}$.

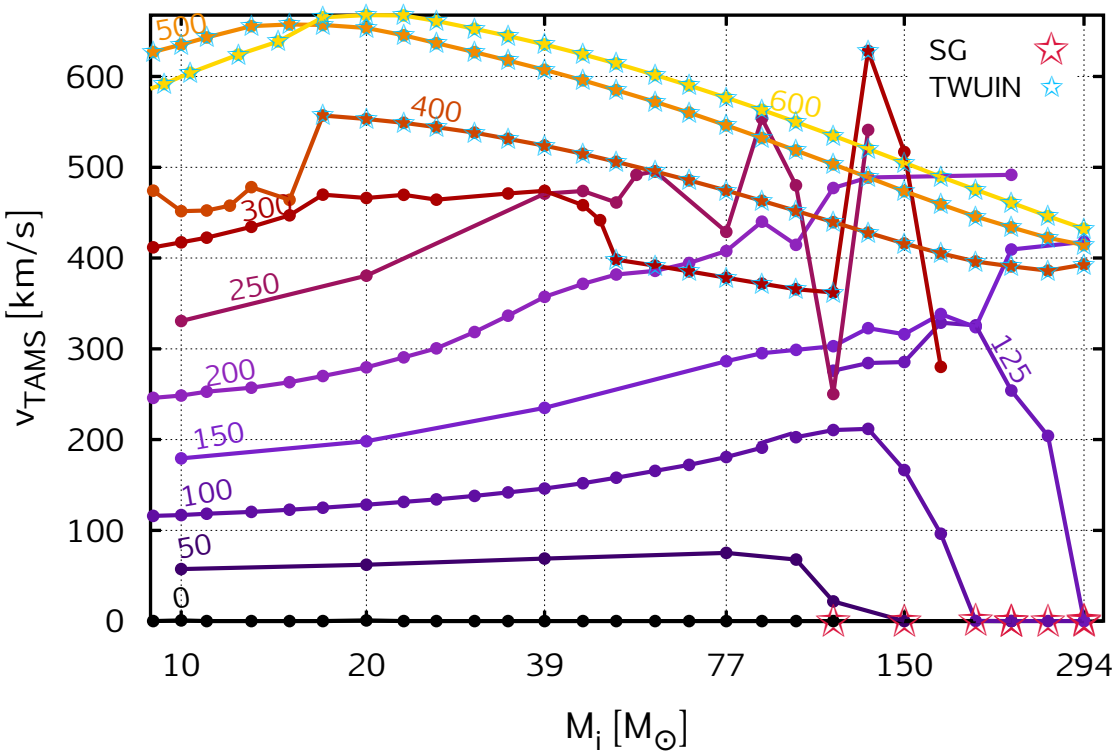

Figure 2.14. Rotational velocity at the terminal age main-sequence (TAMS) as a function of initial mass. Every dot represents one evolutionary sequence. The colours refer to the initial rotational velocity; dots of model sequences with the same initial rotational velocity are connected and labelled (units in km s^{-1}). Only those sequences that have reached Y_C=0.98 have been plotted. (See also Fig. 2.4 which shows the rotational velocity at the ZAMS: here the same models are connected as in Fig. 2.4.) Core-hydrogen-burning cool supergiants (SG) are marked with large red stars, chemically-homogeneous TWUIN stars (Y_S^{TAMS}>0.7) are marked with small blue stars.

Redward evolving stars

Fig. 2.14 presents the surface rotational velocity of our models at the TAMS. Sequences that are marked by red star symbol or not marked with any symbol undergo normal or transitionary evolution. In both cases, the models evolve redwards in the HR diagram.

Sequences in the left bottom corner of the figure with initial masses $\lesssim$ 26 $M_\odot$ and initial rotational velocities $\lesssim$ 150 km s^{-1} reduce their rotational velocity gradually, the same way as the sequence 10 $M_\odot$–100 km s^{-1} in Fig. 2.12. The reason that their rotational velocities are still above 100 km s^{-1} at the TAMS is the spin up during the adjustment phase at the beginning of their evolution, as discussed in Sect. 2.3.1.

The rotational velocity at the TAMS of the higher-mass models (between 26-131 $M_\odot$ in the case of the 100 km s^{-1} line) with slow initial rotation ($\lesssim$ 150 km s^{-1}) is an increasing function of the initial mass. As we have explained in the discussion of Fig. 2.12, this is because the higher the mass, the more angular momentum can be released by the contracting core and transported to the envelope. Stars more massive than 80 $M_\odot$ have, in the last ~20% of the main-sequence

lifetime, undergone envelope inflation. They have encountered the bi-stability jump and spun down in the same way as the models of 150 $M_\odot$–100 km s^{-1} and 294 $M_\odot$–100 km s^{-1} shown in Fig. 2.12. Those which rotate very slowly at the TAMS have evolved into core-hydrogen-burning cool supergiants. Accordingly, sequences with $T_{\rm eff}^{\rm TAMS} < 12$ kK are marked with large red star symbols.

Lower-mass ($\lesssim 50$ $M_\odot$) sequences with initial velocities of 200-300 km s^{-1} evolve normally. Their behaviour is similar to those of lower mass at 100 km s^{-1}: the surface rotational velocity at the TAMS is an increasing function of the initial mass. Higher-mass ($\gtrsim 50$ $M_\odot$) sequences with initial velocities of 200-300 km s^{-1}, on the other hand, have variable values of surface rotational velocity at the TAMS. They undergo transitionary evolution. The following effects contribute significantly in shaping their evolution. (1) mass-loss uncovers helium-rich layers, and the star appears bluer due to the lower opacities at the surface. Furthermore, the mass-loss, which depends on the surface composition and the effective temperature, removes angular momentum. (2) The radius increases during the main-sequence evolution, and the star appears redder. At the same time, the core contracts, and the star increases the surface rotational velocity due to the core-envelope coupling. The net effect of these competing mechanisms can be that the model at the TAMS is either fast rotating and blue, or slow rotating and red, or somewhere in between.

Homogeneously-evolving stars

The fastest rotators (400-600 km s^{-1}) are chemically-homogeneously-evolving TWUIN stars (marked in Fig. 2.14 with small blue stars). They undergo WR-type mass-loss at the TAMS (i.e. $Y_S^{\rm TAMS} \geq 0.7$), mostly have optically thin winds (as seen in Sect. 2.6) and emit intense UV radiation (as seen in Sect. 2.10).

Low-mass ($\lesssim 20$ $M_\odot$) stars with CHE reach breakup rotational rates early during the main-sequence evolution because the breakup velocity is less for lower masses. When the models spin up to close to breakup, they manage to spin down again by losing mass through rotationally-enhanced stellar winds. As a consequence, they rotate slower at the TAMS than they would if they had not reached breakup rotation or if there was no rotationally-enhanced mass-loss included in the calculations. This is why the surface rotational velocity at the TAMS of the fast rotators increases at low mass and does not follow the decreasing trend of the more massive stars which undergo CHE. Although rotating massive stars at breakup have gained some interest in the past (Decressin et al., 2007), theoretical suggestions by Müller and Vink (2014) disfavour the concept of rotationally-enhanced stellar winds. Since the physical assumptions in these stellar models are currently under debate, we do not analyse this issue further at this point.

High mass (>20 $M_\odot$) sequences which undergo CHE, on the other hand, are hardly influenced by the rotational mass-loss enhancement. Their surface rotational velocity at the TAMS is decreasing as a function of the initial mass. This decreasing trend is a consequence of the stellar wind being more efficient at higher mass (but not efficient enough to turn them back to TE). Their typical behaviour is presented in Fig. 2.12 by the sequence 294 $M_\odot$–450 km s^{-1}: their rotational velocity does not change much during the first two-thirds of their main-sequence lifetime, and then they slightly spin down due to the WR-type mass-loss. However, they still rotate at least as fast as 350 km s^{-1} at the TAMS. This fast rotation, if not reduced during the post-main-sequence evolutionary phases, might lead to the formation of a long-duration gamma-ray burst in the collapsar scenario (Sect. 2.10.5).

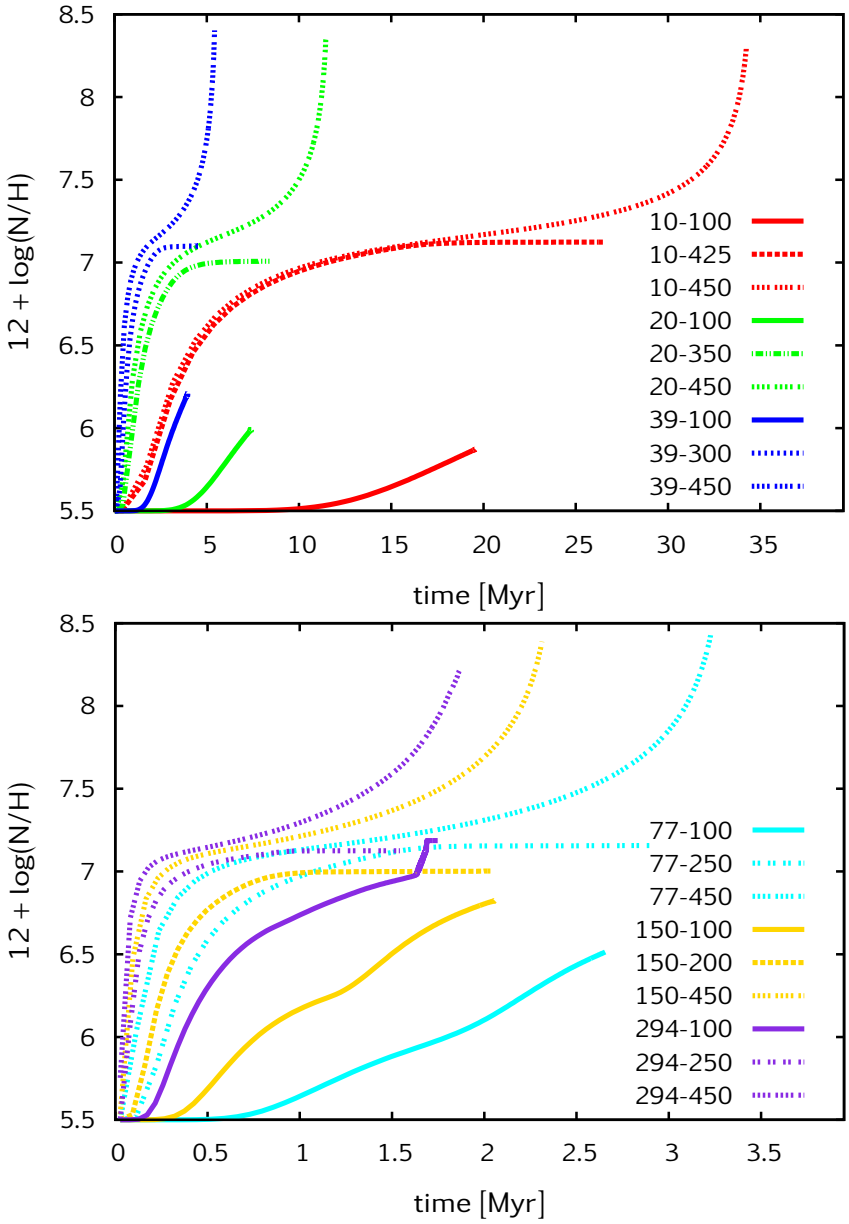

Figure 2.15. Surface nitrogen abundance as a function of time for models with different initial masses and rotational velocity as indicated by the legend (units are $[M_\odot]$-[km s^{-1}]). Models are chosen to represent all mass ranges and the three classes of evolution.

2.9.3 Surface nitrogen abundance and internal mixing

The surface nitrogen abundance of a star traces the internal mixing efficiency (e.g. Köhler et al., 2015). Fig. 2.15 shows the evolution of the surface nitrogen mass fraction for some of our stellar models relative to their surface hydrogen mass fraction. Three tracks are plotted for every mass representing the three classes of evolution (NE, TE, CHE). Due to hydrogen-burning, the N/H ratio cannot decrease during the main-sequence lifetime plotted here. The CNO equilibrium abundance of nitrogen for normal hydrogen and helium abundances corresponds roughly to

12+log(N/H)=7. Higher values in Fig. 2.15 imply a reduced hydrogen abundance.

Stars which undergo NE (represented by the tracks of 100 km s^{-1} in Fig. 2.15) are slow rotators. They mix some amount of nitrogen but the surface nitrogen abundance remains far from the CNO equilibrium abundance, indicating that rotational mixing is not very efficient. However, the higher the mass the larger the convective core and the more nitrogen appears at the surface.

The 294 $M_{\odot}$–100 km s^{-1} sequence becomes a core-hydrogen-burning red supergiant near the end of the main-sequence evolution. When the model approaches the red supergiant branch, the mass-loss becomes higher and deeper layers are uncovered. This causes a rapid increase of the N/H ratio at the stellar surface near the TAMS.

The intermediate rotators (represented by the tracks of 200-425 km s^{-1} in Fig. 2.15) undergo TE (cf. Sect. 2.7). These models are mixed during the first part of their evolution, but then a chemical gradient develops between the core and the envelope which prevents further mixing. The fastest rotators (represented by the tracks of 450 km s^{-1} in Fig. 2.15) are chemically-homogeneously-evolving stars. They are, per definition, mixed throughout: every chemical change in the core is apparent at the surface as well.

Brott et al. (2011) computed the N/H ratio for stellar models with Galactic, LMC and SMC composition. The initial abundance of nitrogen in our models is much lower than that in the Brott models. However, our rotating models with NE and TE reach surface N/H ratios at the TAMS which can be higher than that in the adopted (initial) LMC and SMC compositions. Moreover, our models with CHE, even the less massive ones, have surface N/H abundance ratios as high as 8.4. This value is higher than any value predicted by the Galactic, LMC and SMC models without CHE. The reason of this high N/H value in our models is the homogeneous mixing which transports all the hydrogen supply into the burning regions where it is destroyed. Consequently, observing surface N/H abundance ratios as high as 8.4 for a massive single star in a low-metallicity environment might imply that the star evolved chemically-homogeneously.

2.10 Photoionizing fluxes

Massive stars ionise their surroundings through their intense UV radiation (Schaerer et al., 1999b; Peters et al., 2010). To estimate the amount of ionizing radiation released by low-metallicity main-sequence stars, we discuss the ionizing fluxes of our stellar models based on the black body approximation (see also Table 2.3).

In this section, we first present the ionizing fluxes and photon numbers calculated in the Lyman continuum (i.e. $\lambda < 912$), in the HeI continuum (i.e. $\lambda < 504$) and in the He II continuum (i.e. $\lambda < 228$). We then analyse the time evolution of the emission and the validity of the black body approximation. Finally, we discuss two aspects of our stellar models in terms of observational constraints: the total He II flux measured in I Zw 18 and the connection of our models to gamma-ray bursts and superluminous supernovae.

2.10.1 Time-integrated ionizing fluxes

The top panel in Fig. 2.16 shows the time-integrated energy, i.e. the total energy that is emitted by our models in the Lyman continuum during their core-hydrogen-burning lifetimes. The total emitted flux is an increasing function of the initial mass for the following reason. Although the main-sequence lifetime becomes shorter for a higher-mass model, both the luminosity and

the surface temperature increase with the mass so much that the most massive model is able to radiate $\sim 10^3$ times more ionizing energy during its main-sequence lifetime than the lowest mass one.

According to Fig. 2.16, the emitted flux also depends on the initial rotation rate. On one hand, rotation increases the lifetime of a model (more fuel is mixed into the core due to rotational mixing), therefore increasing the time-integrated energy. Amongst the less massive, normally-evolving models, on the other hand, the lowest amount of ionizing energy is produced in the sequence with 9 $M_\odot$-375 km s^{-1} (see Table 2.1), while the non-rotating model with the same mass produces somewhat more energy. This is because the rotating model has a larger radius than the non-rotating one due to the centrifugal acceleration, hence its luminosity and effective temperature are lower.

The fast rotators evolve chemically-homogeneously towards higher luminosities and higher surface temperatures. They generally produce ~5-10 times more ionizing energy than their normally-evolving counterparts of the same mass during the main-sequence lifetime.

The time-integrated fluxes in the HeI and the He II continua are influenced by the mass and the rotation a similar way as those in the Lyman continuum. Consequently, the minimum and maximum time-integrated flux values correspond, respectively, to the lowest- and highest-mass models, at intermediate rotation rates. Table 2.1 gives the minimum and maximum values of the energy and photon numbers emitted by our models in all three continua.

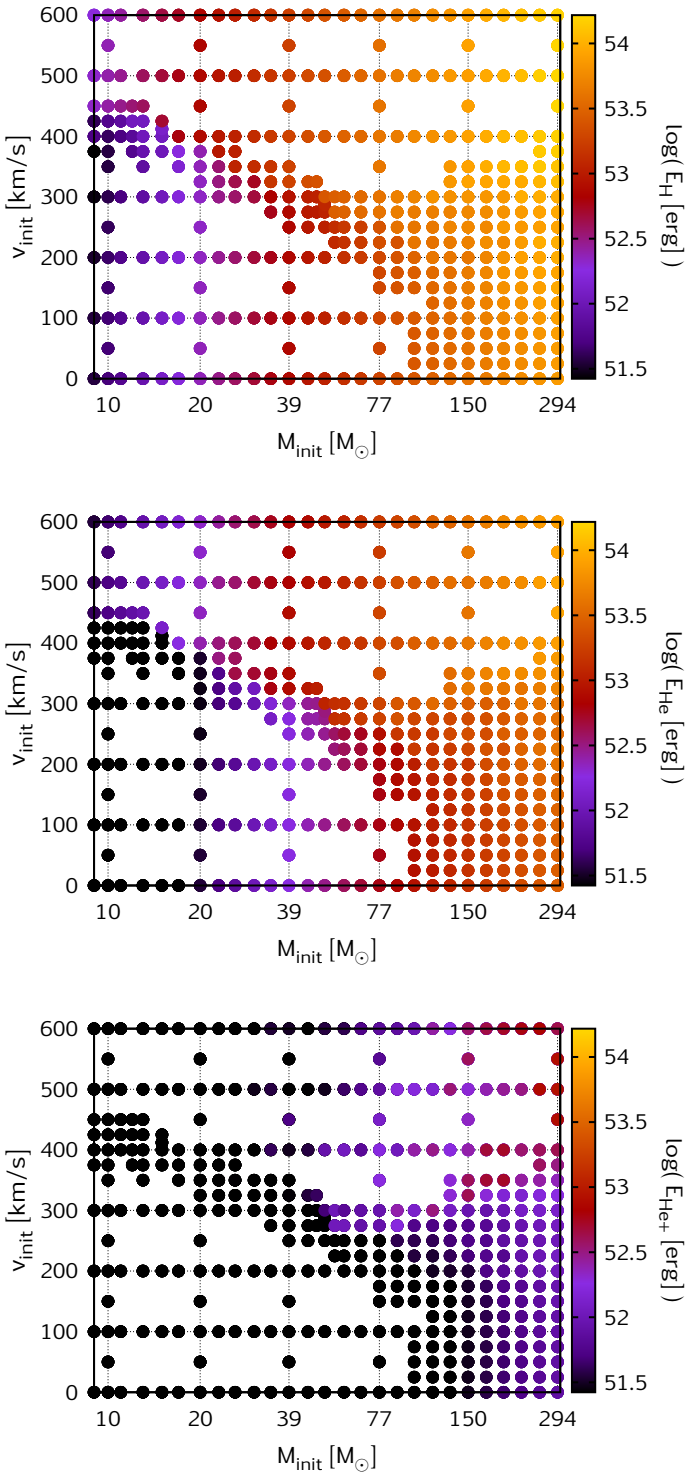

Figure 2.16. *Top:* Ionizing energy emitted by our stellar sequences in the Lyman continuum during their main-sequence lifetime. Each evolutionary sequence of our grid is represented by one dot in this diagram and the total amount of energy emitted in the Lyman continuum (in ergs) is colour coded in a logarithmic scale. *Middle and bottom:* The same as the top figure but for the HeI and He II continua, respectively.

Table 2.1. Minimum and maximum values of time-integrated energy (E) in ergs, time-integrated number (Q) of the ionizing photons and the time average value of the photon numbers per seconds for hydrogen (H), neutral helium (He) and singly ionised helium (He^+) emitted during the main-sequence phase by our stellar evolutionary models (cf. Table 2.3). Black body radiation is assumed. For comparison, the ionizing energy and photon numbers of the Pop III models of Yoon et al. (2012) are shown: these values are systematically higher than those of our corresponding models due to the higher effective temperatures of the metal-free models (see also Fig. 2.17).

	this work	E_{tot} [erg]	Q_{tot}	Q_{avr} [s^{-1}]	*Pop III models*	E_{tot}^{PopIII} [erg]	Q_{tot}^{PopIII}	Q_{avr}^{PopIII} [s^{-1}]
H	9 $M_\odot$-375 km/s	2.65e51	1.00e62	1.21e+47	10 $M_\odot$-0 v_k	1.53e52	4.95e62	6.41e+47
	100 $M_\odot$-500 km/s	4.87e53	1.32e64	1.52e+50	100 $M_\odot$-0.4 v_k	7.31e53	1.66e64	2.48e+50
	294 $M_\odot$-500 km/s	1.49e54	3.89e64	6.75e+50	300 $M_\odot$-0.4 v_k	1.96e54	4.55e64	7.19e+50
He	9 $M_\odot$-375 km/s	9.22e49	2.11e60	2.55e+45	10 $M_\odot$-0 v_k	3.36e51	7.10e61	9.20e+46
	100 $M_\odot$-500 km/s	2.28e53	4.33e63	4.99e+49	100 $M_\odot$-0.4 v_k	4.78e53	8.18e63	7.32e+49
	294 $M_\odot$-500 km/s	7.58e53	1.42e64	2.46e+50	300 $M_\odot$-0.4 v_k	1.24e54	2.15e64	2.92e+50
He^+	9 $M_\odot$-375 km/s	1.81e45	1.98e55	2.39e+40	10 $M_\odot$-0 v_k	1.20e49	1.27e59	1.65e+44
	100 $M_\odot$-500 km/s	9.63e51	9.72e61	1.12e+48	100 $M_\odot$-0.4 v_k	6.24e52	6.03e62	5.39e+48
	294 $M_\odot$-500 km/s	3.93e52	3.95e62	6.85e+48	300 $M_\odot$-0.4 v_k	1.41e53	1.37e63	1.86e+49

2.10.2 Time evolution of the emission

Fig. 2.17 shows the time evolution of the emission from both normal and chemically-homogeneous models with M_{ini} =100 $M_{\odot}$. According to the plot, the emission from the model with NE decreases while that with CHE increases during their main-sequence evolution. This is expected since the model with CHE evolves towards higher luminosities and higher effective temperatures.

The average photon flux in the He II continuum is 2.00×10^{47} s^{-1} for the model with NE and 1.12×10^{48} s^{-1} for the model with CHE during their main-sequence phase. Considering somewhat lower masses, we find that the time-average He II photon flux from the chemically-homogeneous models is higher than that of the normally-evolving models by factors of 9, 12, and 15 at 77 $M_{\odot}$, 51 $M_{\odot}$ and 39 $M_{\odot}$, respectively. The order of magnitude of these ratios implies that the contribution of the models with CHE to the total emitted He II ionizing flux of a low-metallicity galaxy may be significant.

Moreover, Fig. 2.17 demonstrates that towards the end of the main-sequence evolution, the ionizing fluxes of the chemically-homogeneous models can be an order of magnitude larger than those of normally-evolving models. In fact, comparing the peak ionizing He II fluxes from the chemically-homogeneous models to those of the normally-evolving models, we find ratios of 20, 27, 50, and 92 for stars of 100 $M_{\odot}$, 77 $M_{\odot}$, 51 $M_{\odot}$ and 39 $M_{\odot}$, respectively. We therefore expect that ionizing fluxes predicted by starburst models will drastically change when the TWUIN stars are taken into account.

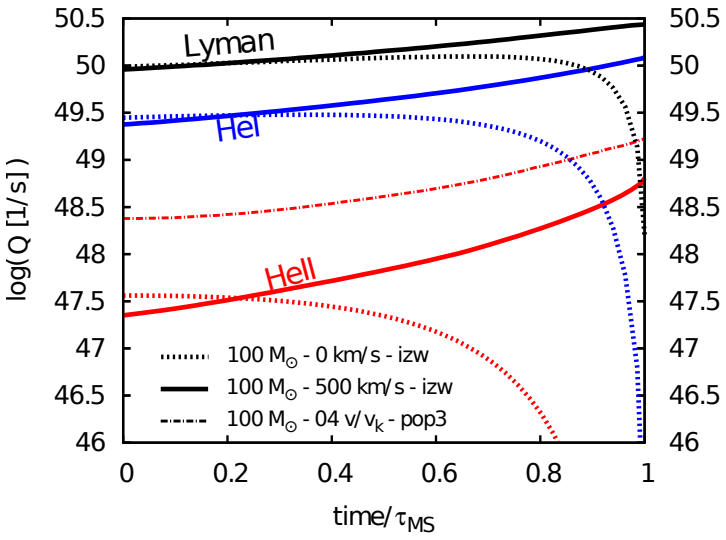

Figure 2.17. Time evolution of the number of the ionizing photons for models with an initial mass of 100 $M_{\odot}$. Photons emitted in the Lyman, HeI and He II continua by a normally-evolving model (without rotation) and a chemically-homogeneously-evolving model (with an initial rotational velocity of 500 km s^{-1}) from our grid are plotted. For comparison, the number of photons emitted in the He II continuum by a chemically-homogeneously-evolving Pop III model from Yoon et al. (2012) with similar initial mass and initial rotational velocity (in units of the critical rotation, which refers to v_{ini} ~520 km s^{-1}) is plotted by the dotted-dashed line. Note that the He II flux of the Pop III model may, however, be overestimated by a factor of three (see text).

For comparison, a corresponding metal-free model with CHE is plotted in Fig. 2.17. The ratio of the time-integrated fluxes of the two models with CHE for the main-sequence lifetime is $E(\gamma_{He^+})^{IZw18}/E(\gamma_{He^+})^{PopIII}$=0.15 in the He II continuum. Table 2.1 compares the time-integrated ionizing energy and photon numbers in all three bands between our sequences and the Pop III sequences. The differences between the metal-poor and metal-free models derive from the latter evolving at systematically higher effective temperatures. Note, however, that the He II fluxes of the metal-free models may be overestimated by a factor of three (see below).

2.10.3 Validity of the approximations

At the considered metallicity, the mass-loss of massive stars is generally sufficiently weak to make the wind transparent in the continuum. As mentioned in Sect. 2.6, only our most massive chemically-homogeneously-evolving models are expected to develop winds with a continuum optical depth of order unity (cf., Fig. 2.8).

Kudritzki (2002) investigated the dependence of the ionizing photon fluxes of low-metallicity massive main-sequence stars on the mass-loss rate. He found the ionizing fluxes in general to be reduced at the highest considered metallicities due to the correspondingly stronger stellar winds. However, below a threshold metallicity, Kudritzki found that the fluxes are not affected by the winds anymore as they become too weak. While in the quoted work, the threshold metallicity is close to the one used in our models, the mass-loss rates adopted by Kudritzki are significantly larger than what is assumed in our work.

For He II ionizing photons, and only for those, Kudritzki found slightly more complex behaviour. At 50 kK and below, he found that the He II flux per cm^2 can increase for stronger winds. However, at the highest effective temperature, 60 kK, this effect was not seen anymore. In fact, the He II flux per cm^2 for the most luminous main-sequence stars at 60 kK is predicted by Kudritzki to be approximately $10^{23.5}$ s^{-1} in the case of both our metallicity and lower values. This value is very close to the black body prediction, as shown in Fig. 2.18.

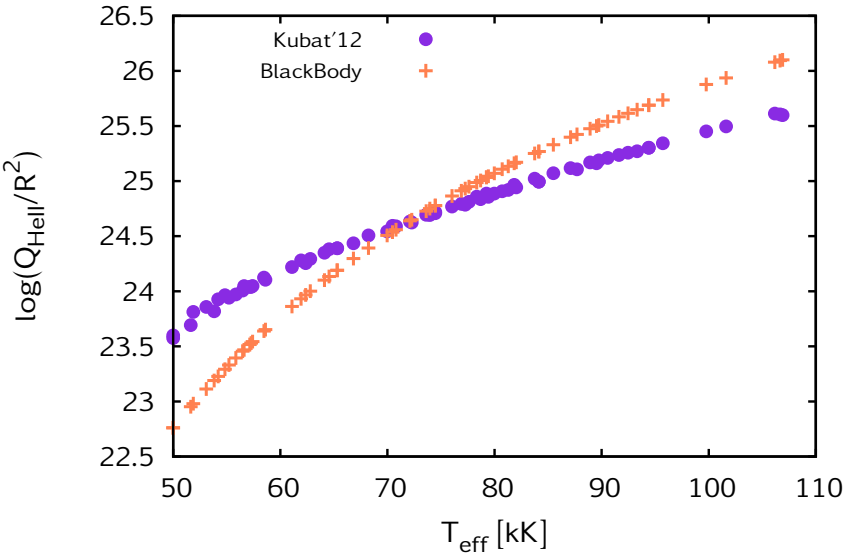

Figure 2.18. Ionizing flux (normalised to one square centimetre of stellar surface) in the He II continuum provided by Kubát (2012) based on non-LTE spectra of metal-free massive stars and ionizing flux values using a black body approximation for the same collection of metal-free massive stars.

Kubát (2012) calculated the ionizing flux of metal-free massive hot stars based on simulated stellar atmospheres, for a large range of effective temperatures. In Fig. 2.18, we show the He II fluxes from Kubát (2012) for a large number of stellar models. As the models cover a wide mass range, Fig. 2.18 demonstrates that gravity effects, which cause the scatter in the plot, are very small.

When comparing Kubat's results to the black body prediction, we note that while our metallicity is different from zero, Kudritzki (2002) finds that the metallicity dependence of the ionizing fluxes at the considered low-metallicity is generally quite weak, as discussed above. We find that in the temperature range of our most massive and hot stellar models, between 60 kK<T_{eff}<85 kK (i.e. where they provide most of the ionizing radiation), Fig. 2.18 shows that the ionizing flux in the He II continuum calculated from the black body approximation matches that calculated from the stellar atmospheres to within $\lesssim$50% (0.3 dex). Although this comparison is limited by the number of stellar spectra provided by Kubát (2012), as well as the difference between the composition of their metal-free models and our metal-poor models, it implies that the ionizing energy coming from our stellar evolutionary models using the black body approximation is indeed a good estimate for their He II ionizing fluxes.

We note that the Pop III models from Yoon et al. (2012) are significantly hotter than our low-metallicity models during core-hydrogen-burning. This results in significantly greater estimates of He II fluxes (almost one order of magnitude larger than those of our models, e.g. Fig. 2.17) as they also used black body models. However, Fig. 2.18 indicates that these hot Pop III models may over-predict the true He II fluxes by a factor of three. At the lower temperatures of our models, this discrepancy is less severe, as indicated by Fig. 2.18. Thus, the step from our low-metallicity calculations to the zero-metallicity models may only increase the He II fluxes by around a factor of three (rather than the factor of ten which one might conclude from inspection of Fig. 2.17).

In summary, the neglect of wind effects and the black body approximation both introduce uncertainties into the predicted ionizing fluxes. However, in the mass and metallicity regime which we consider here, the uncertainty of both effects appears to be within a factor of two. Conceivably, other uncertainties may be larger. Indeed, the mass-loss rates we consider, in particular those for WR stars, may be more uncertain. E.g. Vink et al. (2011), found the mass-loss rate to jump to a steeper relation once the winds become optically thick. This effect, which is observationally confirmed for very luminous Of/WN and WNh stars in the LMC (Bestenlehner et al., 2014), is not implemented into our stellar models. On the other hand, Gräfener and Hamann (2008) and Muijres et al. (2012) predict the winds of the hottest helium-rich stars to become weaker or even to break down for increasing temperature. However, the investigated wind models are largely restricted to effective temperatures below 50 kK, whereas our TWUIN stars reach values of 80 kK, and higher.

Clearly, the ionizing fluxes which we provide are only approximate. Our work demonstrates the need for model atmosphere calculations for very hot stars (50...100 kK) at low (but finite) metallicity. At the same time, self-consistent mass-loss rate predictions are required, to place firmer constraints on the predicted ionizing fluxes.

2.10.4 He II ionizing flux of star-forming dwarf galaxies

As found in the comprehensive study by Shirazi and Brinchmann (2012), a large fraction of star-forming dwarf galaxies display strong He II emission, which is difficult to understand based on previously published evolutionary models of low-metallicity massive stars (cf. also

Sect. 2.11). While WR stars are thought to have the potential to produce He II ionizing photons, most of the He II emitting dwarf galaxies below a certain metallicity do not show WR features in their spectra (Crowther and Hadfield, 2006). We suggest that TWUIN stars (Sect. 2.6) could potentially resolve this discrepancy.

Kehrig et al. (2015b) reported a He II ionizing photon flux, $Q(\mathrm{He\,II})_{\mathrm{obs}} \simeq 1.3{\times}10^{50}$ photons s^{-1} measured by integral field spectroscopy for I Zw 18 . They also suggested that WR stars are not responsible for most of this emission, and speculated about the presence of very massive, metal-free, chemically-homogeneously-evolving stars in this galaxy. Indeed, about 10-15 massive chemically-homogeneously-evolving Pop III stars with fluxes of 10^{49} photons s^{-1} in the He II continuum could emit the amount of ionizing photons observed (Yoon et al., 2012). However, the gas in I Zw 18 is very metal-poor but not primordial, so the presence of actual Pop III stars in I Zw 18 may be debatable.

As we have shown above, our simulations of massive stars with the composition of I Zw 18 predict chemically-homogeneous evolution even for moderately fast rotating stars. Based on the empirical distribution of rotational velocities for O stars in the SMC by Mokiem et al. (2006), up to 20% of the very massive stars could undergo CHE. Possibly, at the ten-times smaller metallicity of I Zw 18 , massive stars rotate even faster.

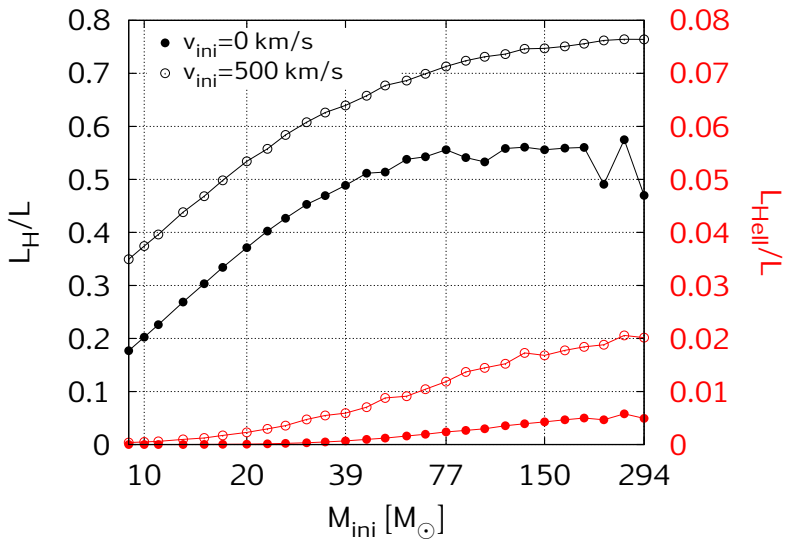

Figure 2.19. Time-averaged luminosity in hydrogen and helium II ionizing photons, relative to the time-averaged total stellar luminosity of our models without rotation and with $v_{\mathrm{ini}} = 500\,\mathrm{km/s}$, as function of the initial stellar mass.

Figure 2.19 shows that the fraction of the stellar luminosity which is emitted as He II ionising photons above $\sim 20\ \mathrm{M}_\odot$ is weakly increasing with mass. This, together with the number of stars of given mass decreasing as $M^{-\alpha}$, with $\alpha \simeq 2.35$, and the mass-luminosity relation $L \sim M^{\beta}$ having an exponent of $\beta \simeq 2.5 \ldots 1.5$ for stars in the mass range $20\ \mathrm{M}_\odot$...$200\ \mathrm{M}_\odot$ (cf. Fig. 17 of Köhler et al., 2015), implies that all mass bins in the considered mass range provide similar contributions to the total He II flux of a stellar generation. Integration over a Salpeter initial mass function (IMF; Salpeter, 1955; Kroupa, 2001) from $0.5\ \mathrm{M}_\odot$ to $500\ \mathrm{M}_\odot$ and assuming a constant star-formation rate of $0.1\ \mathrm{M}_\odot$ (Lebouteiller et al., 2013) giving $300\,000\ \mathrm{M}_\odot$ of stars

within 3 Myr results in a time-averaged He II flux of $1.6 \times 10^{50}\,\mathrm{s}^{-1}$ when 20% of the stars are assumed to undergo chemically-homogeneous evolution. While this simple estimate can not replace proper population synthesis calculations, it indicates that TWUIN stars of finite metallicity may indeed explain the He II flux found for I Zw 18 , especially given the fact that the maximum He II fluxes are about five times higher than the time-averaged values.

As discussed in Sect. 2.6, TWUIN stars have optically-thin ($\tau \lesssim 3$) winds. Therefore, they do not contribute to the broad emission signatures that characterise galaxy spectra with WR stars, but they still emit sufficient radiation to explain the observed He II ionizing photon flux in I Zw 18 . This may imply that chemically-homogeneous evolution, which leads to TWUIN stars in our calculations, is a phenomenon that is indeed happening in nature.

As a consequence of their high temperature and the lack of optically-thick winds, TWUIN stars are expected to radiate at ultraviolet wavelengths. This means that their optical brightness is quite faint, with bolometric corrections estimated from assuming a black body spectrum of the order of $5 \ldots 6^{\mathrm{mag}}$ for effective temperatures in the range $70 \ldots 90$ kK. On the other hand, they may contribute significantly to the observed optical spectra (rest-frame UV) of high-redshift galaxies.

2.10.5 The connection to GRBs, superluminous supernovae and high-z galaxies

Our rapidly-rotating models become TWUIN stars due to quasi-chemically-homogeneous evolution, which was identified as a promising road toward long-duration gamma-ray bursts (GRBs) by Yoon & Langer (2005) and Woosley & Heger (2006). Indeed, our results are consistent with the study of Yoon et al. (2006), who found a very similar threshold rotational velocity for chemically-homogeneous evolution for stars below 60 $M_\odot$ as the present work. While we shall present the post-main-sequence evolution of our models in a forthcoming paper, from our models we can expect a similar ratio of GRBs to supernovae (SNe) of the order of $1\% \ldots 3\%$ as Yoon et al. (2006). This is consistent with the GRB/SN-ratio in the local Universe being significantly smaller (Podsiadlowski et al., 2004) due to the observed preference for GRBs to occur in low-metallicity dwarf galaxies (Langer and Norman, 2006; Niino, 2011). As a consequence, we can consider large He II-emission in low-metallicity star-forming dwarf galaxies (Sect. 2.10.4) as a signpost for upcoming GRBs in the same objects.

Similar to GRBs, the recently discovered hydrogen-poor superluminous supernovae (SLSNe; Quimby et al., 2013) also occur preferentially in low-metallicity dwarf galaxies (Leloudas et al., 2015). While pair-instability explosions (Kozyreva et al., 2014) and massive circumstellar interactions (Moriya et al., 2013; Mackey et al., 2014) have been proposed to explain some of these events, the magnetar model (Thompson et al., 2004; Woosley, 2010) appears currently favoured (Inserra et al., 2013). Within the magnetar model, the enormous luminosities as observed in SLSNe are produced by heating due to the spin-down of a millisecond magnetar. Consequently, again similar to GRBs (Thompson et al., 2004), the progenitor stars need to produce extremely-rapidly-rotating iron cores. Within this scenario, TWUIN stars could also be considered as progenitors of SLSNe. While a quantitative connection requires the investigation of their post-main-sequence evolution, a qualitative connection of SLSNe with low-metallicity dwarf galaxies appears likely in this context.

Recently, Sobral et al. (2015) observed CR7, the most luminous Lyman-α emitter found at $z > 6$. They explained the high Lyman-α and He II emission with a combination of two populations of stars: a 'normal', red stellar population which dominates the mass, and a Pop III population which dominates the nebular emission. While comparing our theoretical

predictions to the observational properties of CR7 falls outside of the scope of present work, we emphasize that our stellar models inherently predict two populations of stars: the normally, redwards-evolving ones with slow rotation, and the chemically-homogeneous, bluewards-evolving ones with fast rotation. This latter type, the TWUIN stars, emits intense ionizing radiation but show no WR features, similar to the supposed Pop III stars. Consequently, two chemically-distinct populations may not be required in CR7, because massive stellar evolution at low metallicity inherently produces the two types of stars observed.

2.11 Comparison to previous results

We discuss the similarities and differences between our stellar models and two grids of models at similar metallicities, one published by Meynet and Maeder (2002) (from now on, MM02) and Ekström et al. (2008), the other by Georgy et al. (2013) (from now on, G+13). Both grids have subsolar initial compositions. The grid from G+13 (with Z=0.002) consists of stellar sequences with initial masses between 9-120 $M_\odot$ and initial rotational velocities of 0 and 0.4 v/v_k (v_k being the critical velocity at the ZAMS). The grid from MM02 (with Z=0.00001) consists of sequences with initial masses between 9-60 $M_\odot$ and initial rotational velocities of 0 and 300 km s^{-1}.

2.11.1 HR diagram

Figure 2.20 shows the HR diagram of the three low-metallicity grids. The ZAMS regions of the grids move towards higher effective temperatures when the metallicity is lower. The ZAMS region of our grid extends to higher luminosities because it contains masses up to 294 $M_\odot$.

The TAMS regions populated by the MM02 and G+13 grids are on the red side of the corresponding ZAMS regions, meaning that all the sequences evolve redwards. In the case of our grid, however, there are two separate TAMS areas corresponding to the normally-evolving and the chemically-homogeneously-evolving sequences. The prediction of chemically-homogeneously-evolving sequences at the TAMS is the first important difference between the previous results and our work.

Another important difference between the three grids derives from the value of the overshooting parameter utilised. The grid with Z=0.00001 was computed without taking overshooting into consideration (Meynet and Maeder, 2002), while the grid with Z=0.002 included an overshooting parameter $\alpha_{\rm over} = 0.1 H_p$ (Georgy et al., 2013). Convective core overshooting gives larger cores, and has been shown to extend the main sequence to lower effective temperatures (Langer and Maeder, 1995). This is why some of the sequences of our grid (with $\alpha_{\rm over} = 0.335 H_p$) finish their main-sequence evolution at lower $T_{\rm eff}$ than the corresponding sequences with Z=0.002.

The broadening of the TAMS of the normally-evolving sequences of our grid at the very high masses is related to the envelope inflation (Sect. 2.5, also see Fig. 2.5). Although the grid with Z=0.002 also shows a broadening around the highest masses (indeed, the non-rotating sequence of the Z=0.002 grid with initial mass of 120 $M_\odot$ finishes the main-sequence evolution at $\log T_{\rm eff} = 4.3$, while the corresponding rotating sequence finishes at $\log T_{\rm eff} = 4.6$), this effect was linked to the efficiency of the stellar wind (Meynet and Maeder, 2002). If the winds are strong and the mass lost during the main-sequence evolution is significant (but not strong enough to remove the hydrogen envelope), the mass fraction of the core increases with respect to the total mass. This increases the ratio of the core mass vs. total mass (similarly to the effect of overshooting) and the stellar models appear more red.

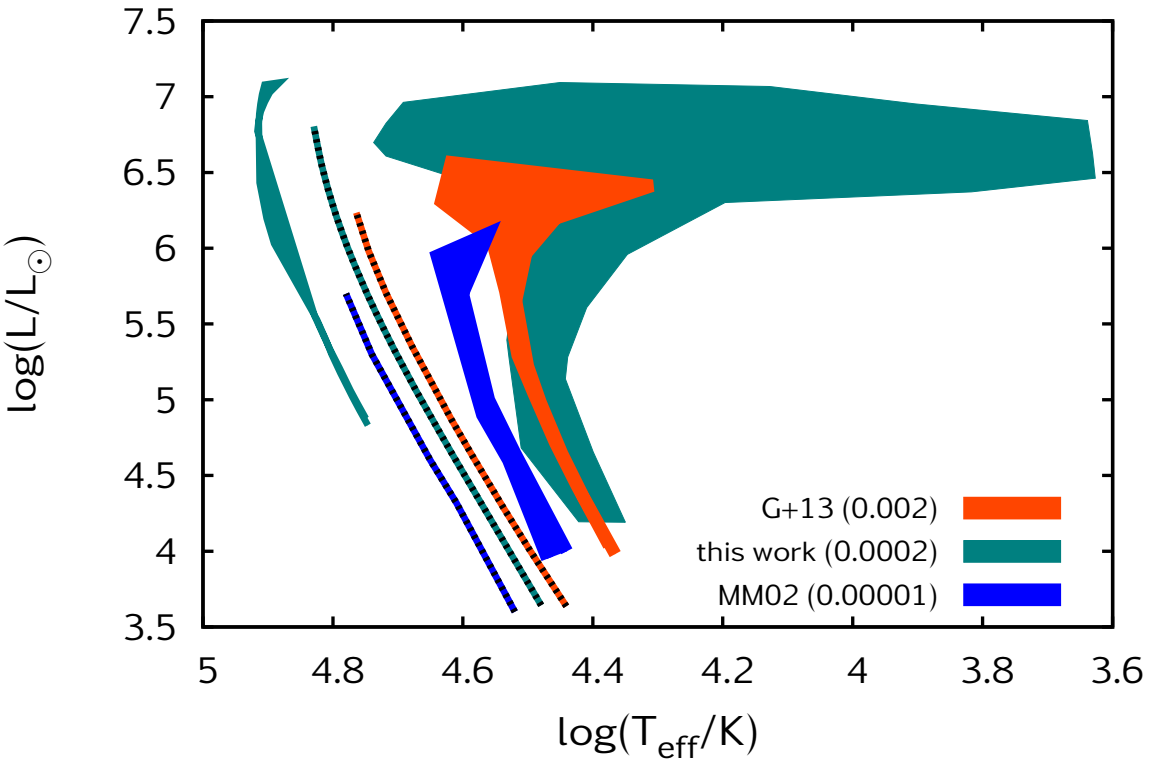

Figure 2.20. HR diagram showing where the stellar sequences of three different grids begin the main-sequence evolution (ZAMS, marked with black dashed lines) and where they finish the main-sequence evolution (TAMS, shaded regions). *G+13*: Georgy et al. (2013); *MM02*: Meynet and Maeder (2002); the initial metallicity of the grids is also indicated by the legend.

2.11.2 Mass-loss history and rotation

Fig. 2.21 compares the mass that is lost during the evolution of the stellar sequences in the three different grids as a function of initial mass and rotation. For the analysis of the mass-loss history of our models, we refer to Sect. 2.8. While the mass-loss rate prescriptions used by MM02 and G+13 are not exactly the same as ours, they nevertheless result in mass-loss rates comparable to those of the prescriptions used here. This is apparent from Fig. 2.21. The mass that is lost during the evolution of stars in the mass range of 9-120 $M_\odot$ is between 0 and 14 $M_\odot$ for models from all three grids, depending strongly on the initial mass.

The non-rotating Z=0.002 sequences lose more mass during the main-sequence lifetime as our non-rotating sequences due to the metallicity dependence of the mass-loss rates. The non-rotating Z=0.00001 sequences end up having similar mass at the end of the helium-burning phase as our non-rotating sequences at the TAMS.

Our fast rotating sequences in Fig. 2.21 evolve chemically-homogeneously and undergo WR-type mass-loss during the last few Myr of the main-sequence evolution. Therefore, although their initial metallicity is lower, they might end up less massive at the TAMS than the rotating Z=0.002 sequences, that do not evolve chemically-homogeneously (Georgy et al., 2013). The rotating Z=0.00001 sequences of 40 and 60 $M_\odot$ lose more mass than the rotating Z=0.002

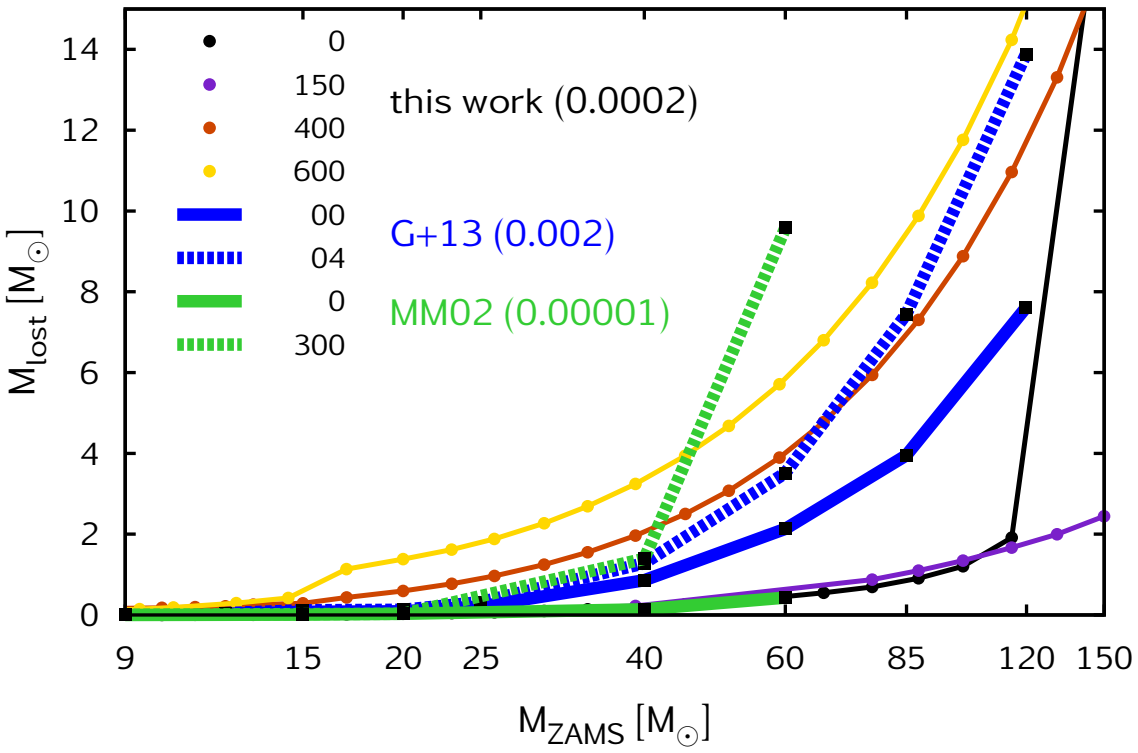

Figure 2.21. Mass lost during the evolution of the stellar sequences in the three grids with different initial compositions. Sequences with four initial rotational rates of our grid, as indicated by the legend with units in km s^{-1}, are shown by connected dots. Sequences of the Z=0.002 grid (Georgy et al., 2013) and the Z=0.00001 grid (Meynet and Maeder, 2002) are shown by black rectangles connected with lines as indicated by the legend with units in v_k and km s^{-1}, respectively. Note that the M_{lost} values of the Z=0.00001 grids correspond to the end of the helium-burning phase and are, therefore, an overestimate of the mass lost during the main sequence. The M_{lost} values of the Z=0.002 and I Zw 18 grids correspond to the end of the main sequence.

sequences of the same masses; and the rotating Z=0.00001 sequence of 60 $M_\odot$ loses even more mass than our chemically-homogeneously-evolving sequences of the same mass. However, this is because the M_{lost} values of the Z=0.00001 grid shown in Fig. 2.21 correspond to the end of helium burning and are, therefore, overestimating the mass lost during their main-sequence evolution.

In Sect. 2.9, we analysed the evolution of the rotational velocity in our models and noted that their behaviour is consistent with the findings of Meynet and Maeder (2002) and Ekström et al. (2008) for their Z=0.00001 models. These authors concluded that the massive ($\gtrsim$30 $M_\odot$) stellar sequences increase their surface rotation due to the strong core-envelope coupling and the low mass-loss rates. Also, if the initial mass function at low metallicity extends up to high-mass stars, as often supposed, rotation is likely to be a major effect in the course of the evolution of massive stars, since many of them are likely to reach high velocities.

Our calculations supports these conclusions since our normally-evolving massive ($\gtrsim$20 $M_\odot$) sequences also increase their surface rotational velocity during the main sequence, as shown

in Sect. 2.9. A quantitative comparison of our models with the Z=0.00001 models is less meaningful because of a limited overlap of the initial parameter space investigated.

2.12 Conclusions

We presented a grid of stellar evolutionary models in the mass range of 9-300 $M_\odot$ with initial rotational velocities between 0-600 km s^{-1}, which is dense enough to be well suited for population-synthesis studies. The initial mass fraction of metals in our models is chosen to be 10% of that found in the SMC, which is probably appropriate for metal-poor blue compact dwarf galaxies such as I Zw 18. We found that our models evolve qualitatively differently compared to models of solar metallicity in several respects. We summarize the most important new results below.

1. **Massive main-sequence stars populate both sides of the ZAMS.** Apart from the normal (i.e. redwards) evolution of the slow rotating models, fast rotation induces chemically-homogeneous evolution in our low-metallicity massive stars. As these objects evolve bluewards from the zero-age main-sequence (cf. Sect. 2.4), we predict core-hydrogen-burning objects to be found on both sides of the ZAMS. This finding might be relevant to explain observations of high-z galaxies such as CR7 (Sobral et al., 2015) which apparently contains two different types of objects: a normal, red stellar population and a hot and luminous stellar population that dominates the ionizing radiation of the galaxy. As we have shown, low-metallicity massive stellar evolution inherently produces both type of objects.

2. **Core-hydrogen-burning cool supergiants**. We find the majority of our massive (>80 $M_\odot$) models evolve into cool supergiants while still burning hydrogen in the core, and spend up to 10% of their life time as such (cf. Sect. 2.5). This evolutionary outcome is a consequence of the low mass-loss rate and the envelope inflation close to the Eddington limit (Sanyal et al., 2015). Although short lived and rare, they may provide an important contribution to the chemical evolution of their environments due to the large amount of nuclearly-processed material that is lost in their slow stellar wind.

3. **Transparent Wind Ultraviolet Intense (TWUIN) stars.** Our fast rotating stars, which may comprise 10...20% of all massive stars, evolve chemically homogeneously and bluewards in the HR diagram during core hydrogen burning (cf. Sect. 2.6). Due to their extremely high effective temperatures, and the expectation that their winds remain optically thin, we show that these TWUIN stars may have very high ionizing fluxes (cf. Sect. 2.10). E.g., their maximum He II ionizing photon flux is about 20 to 100 times larger than that of their non-rotating counterparts (cf. Sect. 2.10.4). We find that the measured He II flux of I Zw 18 (Kehrig et al., 2015b) as well as the weakness or absence of Wolf-Rayet features in I Zw 18 and other low-metallicity dwarf galaxies (Shirazi and Brinchmann, 2012) is compatible with a population of TWUIN stars in these objects.

4. **Increasing surface rotational velocity.** Consistent with previous models of low-metallicity massive stars (cf. Sect. 2.11), our calculations show that the normally evolving models increase their surface rotational velocity during the main-sequence lifetime due to strong core-envelope coupling and low mass-loss rates (cf. Sect. 2.9). Therefore, the rotational

velocity distribution of core-hydrogen-burning massive stars to be observed in low-metallicity environments might be different to that in higher-metallicity environments.

5. **Connection to lGRBs and superluminous SNe.** It has been argued previously that chemically-homogeneous evolution is a promising path towards long-duration gamma-ray bursts (cf., Sect. 2.10.5). Their preference to occur in low-metallicity dwarf galaxies, together with the spectroscopic features of dwarf galaxies mentioned above, provides increasing evidence for chemically-homogeneous evolution indeed occurring at low metallicity. As superluminous supernovae may also require low metallicity and rapid rotation (see Sect. 2.10.5), chemically-homogeneous evolution may also be a factor in these dramatic final explosions and in the evolutionary path that leads to them.

Observations of massive stars in nearby compact dwarf galaxies, of massive-star populations in high-redshift galaxies, or even of stellar explosions in the far Universe can provide promising avenues to expand and improve our knowledge of massive star evolution at low metallicity. Here we provided a complementary view from theoretical models considering the main-sequence evolution, while the post-main-sequence phase will be presented in a forthcoming work. It will thus require further efforts on both sides, observational and theoretical, before we are able to understand low-metallicity massive stars as well as those in our Milky Way, and thus obtain a deeper understanding of metal-poor environments in the Universe.

Table 2.2. Important characteristics of our models. M^i: initial mass. v^i_{rot}: initial rotational velocity. $v^{Y_C=0.28}_{rot}$: rotational velocity at the zero-age main-sequence (defined as Y_C=0.28). τ_{MS}: Main-sequence lifetime. M^f: mass at the end of the calculation. v^f_{rot}: rotational velocity at the end of the calculation. Y^f_C: central mass fraction of helium at the end of the calculation. Y^f_S: surface mass fraction of helium at the end of the calculation; bold face indicates if the last model is chemically-homogeneous (with $Y^f_S \geq 0.7$), i.e. a TWUIN star. $A(C)^f_S$=log[C/H]^f_S+12: surface abundance of carbon (^{12}C) at the end of the calculation. $A(N)^f_S$=log[N/H]^f_S+12: surface abundance of nitrogen (^{14}N) at the end of the calculation. log$L^f/L_\odot$: luminosity at the end of the calculation. T^f_{eff}: effective temperature at the end of the calculation. R^f: radius at the end of the calculation; bold face indicates if the last model is a cool supergiant (with $T^f_{eff} < 12$ kK). Type: evolutionary class as defined in Sect. 2.3.2.

M^i [$M_\odot$]	v^i_{rot} [km s^{-1}]	$v^{Y_C=0.28}_{rot}$ [km s^{-1}]	τ_{MS} [Myr]	M^f [$M_\odot$]	v^f_{rot} [km s^{-1}]	Y^f_C	Y^f_S	$A(C)^f_S$	$A(N)^f_S$	log$L^f/L_\odot$	T^f_{eff} [K]	R^f [$R_\odot$]	Type
10	0	0	19.5	10.0	0	0.98	0.25	6.37	5.50	4.29	24729	7.6	NE
10	500	758	35.3	9.7	635	0.98	**0.96**	6.72	8.31	4.98	57837	3.1	CHE
20	0	0	7.4	20.0	0	0.98	0.25	6.37	5.50	5.09	29910	13.1	NE
20	500	771	11.7	19.1	653	0.98	**0.96**	6.84	8.37	5.55	67287	4.4	CHE
39	0	0	4.0	38.8	0	0.98	0.25	6.37	5.50	5.70	30706	25.2	NE
39	500	747	5.5	36.5	607	0.98	**0.97**	6.93	8.42	6.01	75294	5.9	CHE
77	0	0	2.6	76.3	0	0.98	0.25	6.37	5.50	6.20	23781	74.1	NE
77	500	718	3.3	70.1	546	0.98	**0.97**	6.98	8.44	6.41	80375	8.3	CHE
150	0	0	2.0	147.3	0	0.94	0.25	6.37	5.50	6.59	6786	**1432.3**	NE
150	500	701	2.3	131.7	474	0.98	**0.97**	6.96	8.41	6.76	82236	11.9	CHE
294	0	0	1.8	265.9	0	0.87	0.30	5.88	6.99	6.94	4649	**4580.0**	NE
294	500	691	1.9	247.4	414	0.98	**0.96**	6.86	8.30	7.09	79189	18.6	CHE

See the complete version of this table in the online publication of Szécsi et al. (2015b).

Table 2.3. Time averaged ionizing fluxes (L), and time averaged (Q) and peak photon emission rates ($Q^{\max}$) of the ionizing photons for hydrogen (H), neutral helium (He) and singly ionised helium (He^+) during the main-sequence evolution for each stellar sequence. We emphasize that the given quantities rely on the black body approximation, and refer to Sect. 2.10.3 for a discussion of its validity.

M^i [$M_\odot$]	$v^i_{\rm rot}$ [km s^{-1}]	$L(\gamma_H)$ [erg/s]	$Q(\gamma_H)$ [s^{-1}]	$Q^{\max}(\gamma_H)$ [s^{-1}]	$L(\gamma_{He})$ [erg/s]	$Q(\gamma_{He})$ [s^{-1}]	$Q^{\max}(\gamma_{He})$ [s^{-1}]	$L(\gamma_{He^+})$ [erg/s]	$Q(\gamma_{He^+})$ [s^{-1}]	$Q^{\max}(\gamma_{He^+})$ [s^{-1}]
10	0	7.82E+36	2.85E+47	3.54E+47	4.94E+35	1.11E+46	1.30E+46	4.86E+31	5.28E+41	7.07E+41
10	500	2.18E+37	7.21E+47	6.89E+48	4.34E+36	9.07E+46	1.78E+48	2.88E+34	3.01E+44	1.66E+46
20	0	9.84E+37	3.35E+48	4.20E+48	1.50E+37	3.24E+47	3.80E+47	1.95E+34	2.08E+44	2.83E+44
20	500	1.91E+38	5.91E+48	2.65E+49	5.55E+37	1.13E+48	8.76E+48	8.15E+35	8.40E+45	1.73E+47
39	0	5.99E+38	1.91E+49	2.30E+49	1.45E+38	3.03E+48	3.61E+48	8.39E+35	8.87E+45	1.30E+46
39	500	9.64E+38	2.80E+49	7.50E+49	3.61E+38	7.12E+48	2.85E+49	8.93E+36	9.11E+46	8.76E+47
77	0	2.35E+39	7.14E+49	8.25E+49	7.39E+38	1.49E+49	1.81E+49	1.00E+37	1.04E+47	1.70E+47
77	500	3.61E+39	9.91E+49	1.91E+50	1.61E+39	3.09E+49	7.94E+49	6.00E+37	6.08E+47	3.21E+48
150	0	6.51E+39	1.92E+50	2.27E+50	2.33E+39	4.63E+49	6.10E+49	5.00E+37	5.14E+47	9.87E+47
150	500	1.03E+40	2.73E+50	4.31E+50	5.00E+39	9.43E+49	1.82E+50	2.31E+38	2.32E+48	7.75E+48
294	0	1.38E+40	3.96E+50	5.50E+50	5.30E+39	1.03E+50	1.69E+50	1.45E+38	1.48E+48	3.65E+48
294	500	2.58E+40	6.75E+50	9.34E+50	1.31E+40	2.46E+50	3.92E+50	6.82E+38	6.85E+48	1.64E+49

See the complete version of this table in the online publication of Szécsi et al. (2015b).

Isochrones

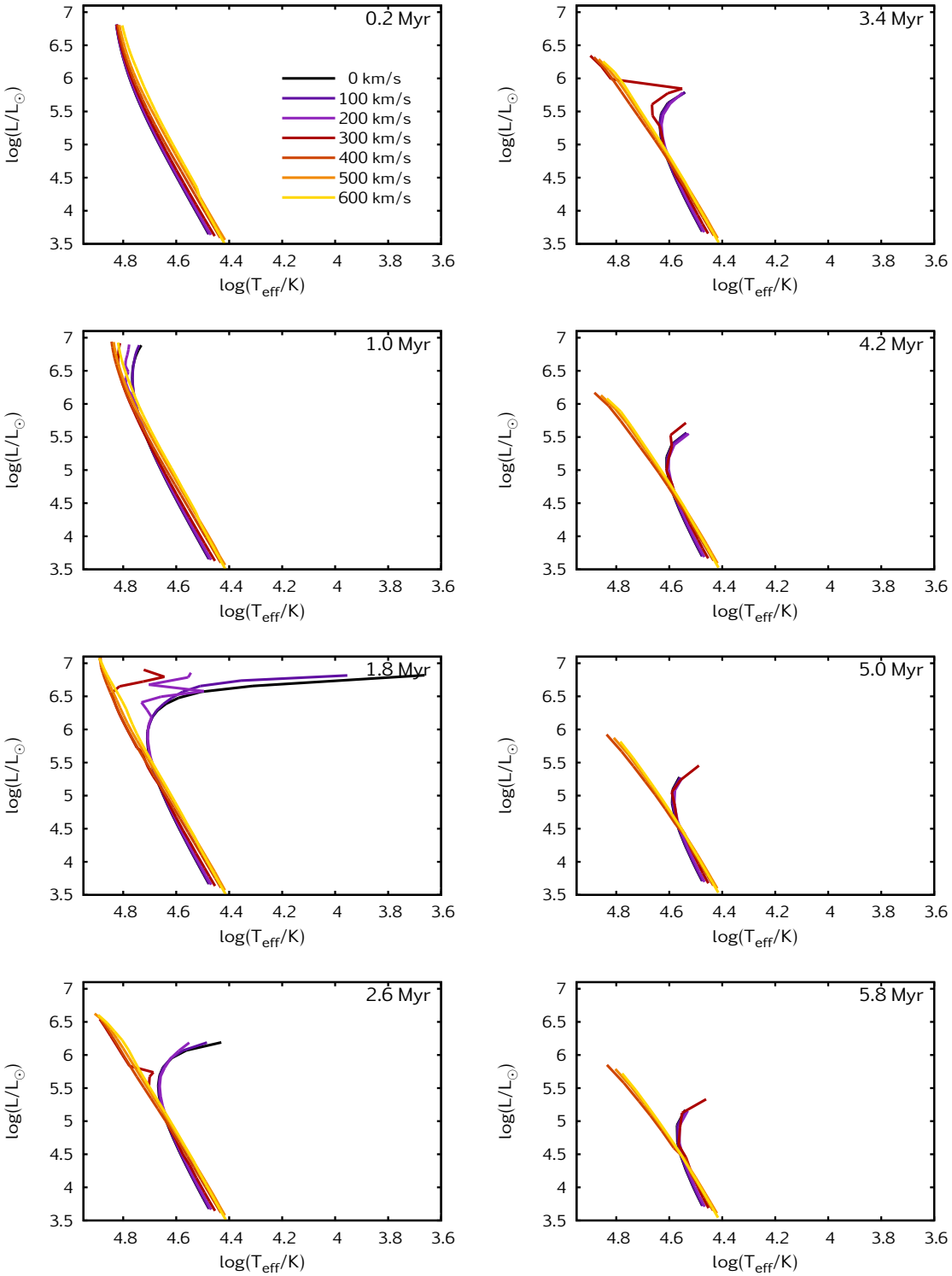

Figure 2.22. Isochrones of different ages of rotating stellar evolutionary models are shown in the HR diagram. The initial surface rotational velocity is chosen in steps of 100 km s^{-1} from non-rotating to 600 km s^{-1}

CHAPTER 3

Supergiants and their shells in young globular clusters

ABSTRACT

Anomalous surface abundances are observed in a fraction of the low-mass stars of galactic globular clusters, that may originate from hot hydrogen burning products ejected by a previous generation of massive stars. We present a scenario in which the second generation of polluted low-mass stars can form in a shell around cool supergiant stars of the young globular cluster.

Simulations of low-metallicity massive stars show that both core-hydrogen burning cool supergiants and hot ionizing stellar sources are expected to be present simulaneously in the young globular clusters. Under these conditions, photoionization confined shells form around the supergiants. We simulated such a shell, investigated its stability and analysed its composition.

We found that the shell is gravitationally unstable on a timescale that is shorter than the lifetime of the supergiant, and the Bonnor-Ebert mass of the overdense regions is low enough to allow star formation. Since the low-mass stellar generation formed in this shell is made up of the material lost from the supergiant, their composition necessarily reflects the composition of the supergiant wind. We show that the wind contains hot hydrogen burning products, and that the shell-stars therefore have the same abundance anomalies that are observed in the second generation stars of globular clusters.

Starforming shells around cool supergiants could form the second generation of low-mass stars in galactic globular clusters. Even without forming a photoionization confined shell, the cool supergiant stars predicted at low-metallicity could contribute to the pollution of the interstellar medium of the cluster from which the second generation was born. Thus, the cool supergiant stars should be regarded as important contributors to the evolution of globular clusters.

D. Szécsi, J. Mackey, N. Langer

To be submitted

3.1 Introduction

Globular clusters (GC) are found in the halo of the Milky Way orbiting around the galactic core. They are generally composed of old, low-mass stars bound together by gravity. The composition of these stars may vary between clusters, but in average, GCs have subsolar metallicity (Z, Gratton et al., 2004). GCs are under intensive investigation for many reasons. Their stars may be as old as the Universe so they could provide constrains on cosmology. Additionally, they are composed of stars at the same distance from the observer so they can be used as natural laboratories of stellar evolution.

One of the most intriguing open questions concerning GCs is the so-called abundance anomalies (Yong et al., 2003; Da Costa et al., 2013). Light element abundances such as O and Na anticorrelate with each other: if O is depleted in a star, then Na is enhanced. The same is observed for the proton-capture isotopes of Mg and Al: if Mg is depleted in a star, then Al is enhanced. The nucleosynthetic processes that can produce an increase in Na and Al with a decrease in O and Mg are the Ne-Na chain and the Mg-Al chain (Burbidge et al., 1957), respectively. These burning chains are side-reactions of the CNO-cycle, the main hydrogen-burning process in *massive* stars. Consequently, there must have been at least one population of massive (and/or intermediate-mass) stars born in the early epochs of the GCs life. These massive stars are already dead, but their nuclear imprint is what we observe today as anomalous abundance patterns in low-mass stars. The question is then: how the pollution happened, i.e. how massive stars lost the amount of nuclearly processed material, and how this material ended up on some of the low-mass stars?

According to the most commonly accepted scenario, the interstellar medium (ISM) had been polluted by hydrogen-burning products from massive stars, and the second generation of stars were born from the polluted ISM (Wünsch et al., 2008; Silich et al., 2010; Palouš et al., 2014). Alternatively, low-mass stars could accrete the ISM during a long pre-main sequence phase (Bastian et al., 2013). In both cases, an astrophysical source – a polluter – is needed. This source, a population of massive or intermediate-mass stars, should only produce hydrogen-burning products (including helium), since no traces of helium burning products or supernova ejecta are observed. Additionally, the polluter should eject the material slowly enough for it to stay inside the gravitational potential well of the GC. This condition excludes fast winds of massive OB stars or Wolf-Rayet stars.

Several astrophysical scenarios were proposed that fulfill the conditions above. Asymptotic giant branch (AGB) stars could eject their hot bottom burning products (Ventura et al., 2001; D'Ercole et al., 2008). Fast rotating massive stars ('spin stars') that are close to the breakup rotation could eject core burning products (Decressin et al., 2007; Tailo et al., 2015). Super-massive (10 000 $M_\odot$) stars could pollute through continuum driven stellar wind (Denissenkov and Hartwick, 2014). In addition, massive binary systems could pollute via non-conservative mass transfer (de Mink et al., 2009).

Here we propose a new scenario: low mass stars could be born in photoionization-confined shells around cool supergiant (SG) stars in the young globular clusters, as shown in Fig. 3.1.

Köhler et al. (2015) and Szécsi et al. (2015b) predict very massive (60-600 $M_\odot$) and long lived SGs. Those long lived SGs are predicted only to exist at low-metallicity, because at solar composition the high mass-loss removes their envelopes and turns them into Wolf–Rayet stars before reaching the SG branch. Moreover, the very massive, metal-poor SGs form *before* the hydrogen is exhausted in the core. Core-hydrogen-burning cool supergiants spend 0.1-0.3 Myr in the SG branch. During this time, they lose a large amount of mass (up to several hundred $M_\odot$

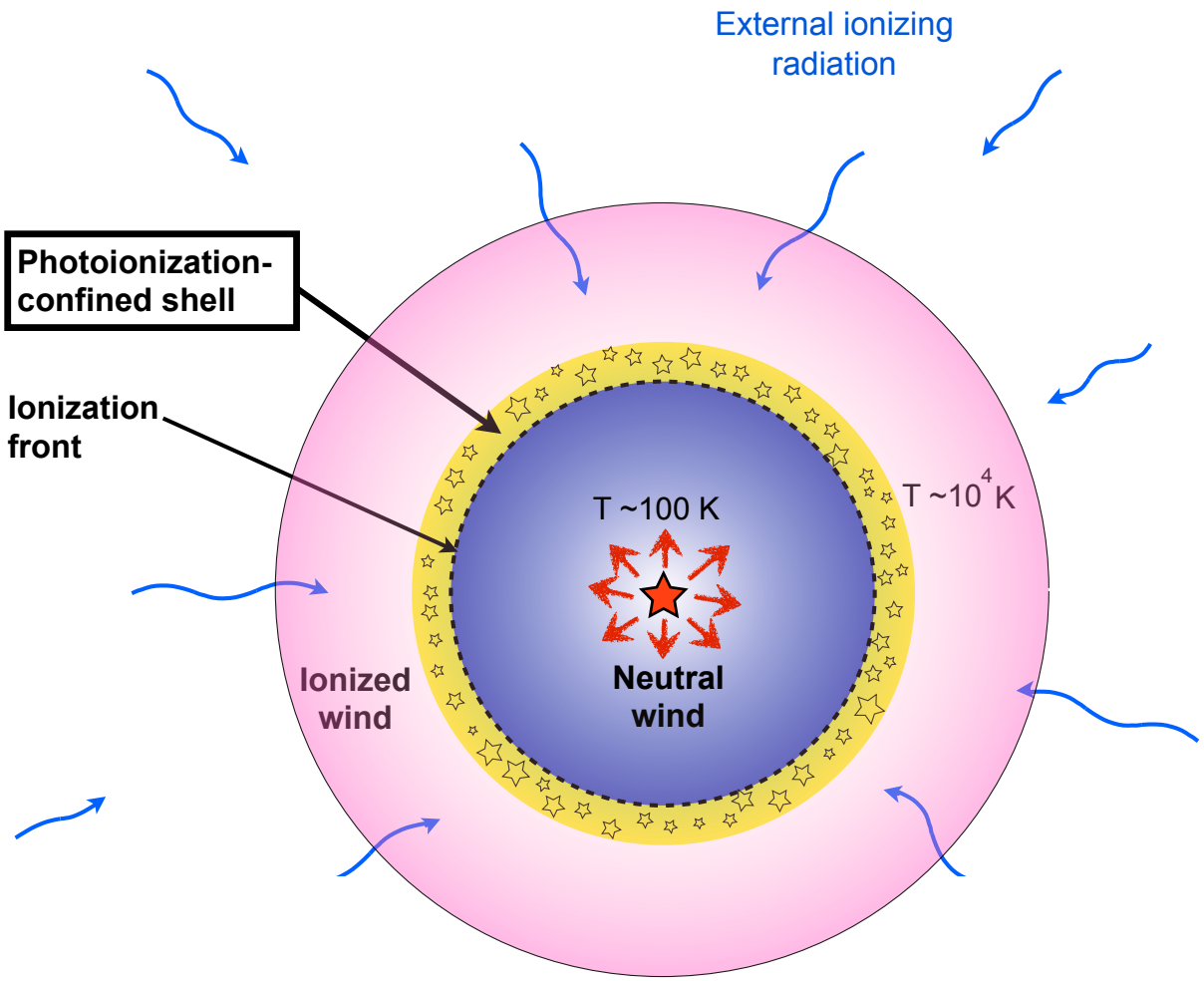

Figure 3.1. Photoionization-confined shell around a core-hydrogen-burning cool supergiant star. The second generation of low mass stars are formed in the shell. This scenario could be common in the first few megayears of the early globular clusters, explaining the pollution of the second generation.

in the case of a 600 $M_\odot$ star). This mass lost in the SG wind has undergone nuclear processing and shows similar abundance variations as those observed in GC stars.

Photoionization-confined shells can be present around cool supergiants at the interface of ionized and neutral material, as shown by Mackey et al. (2014). The shell can contain as much as 35% of the mass lost in the stellar wind. The main condition for a photoionization-confined shell is that there are strong ionizing sources in the surroundings of the SG. This condition may have been fulfilled at the time when galactic globular clusters were born. Evolutionary simulations of low-Z massive stars by Szécsi et al. (2015b) predict that both supergiant stars and compact ionizing sources develop at the same time. The ionizing sources are fast rotating, hot and luminous massive stars that provide a huge amount of photons at short wavelengths. The slowly rotating stars, on the other hand, evolve to be red or cool SGs. Thus, the condition required by Mackey et al. (2014) about SGs and ionizing sources close to each other may have been common in the first few megayears of the GCs' life. Consequently, photoionization-confined shells could be there, too.

This work is organized as follows. In Sect 3.2 we present the evolution of the models that

become core-hydrogen-burning cool SG stars, and discuss the composition of their winds. In Sect. 3.3 we introduce the starforming supergiant shell scenario, and show that in the environment of the young globular clusters, it is possible to form low-mass stars in a supergiant shell from the material ejected by the SG's wind. In Sect. 3.4 we discuss the mass-budget of our scenario, as well as the amount of helium predicted in the second generation. In Sect. 3.5 we summarize the work.

3.2 Supergiants in young GCs

3.2.1 The evolution of core-hydrogen-burning cool SGs

The first generation of stars in the young GCs likely contained massive stars. We see massive stars forming in young massive clusters (YMC) today (Longmore et al., 2014). YMCs are theoretically similar to the young GCs and are thought to become GC-like objects eventually. Furthermore, the massive stars of this first generation must have had the same metallicity that we observe today in the low mass GC stars. Most GC (but not all) have a metallicity in the range of [Fe/H]=−1.5..−2.0 (Gratton et al., 2004). For this reason, the low metallicity ([Fe/H]=−1.7, corresponding to 0.02 $Z_\odot$) massive star simulations of Szécsi et al. (2015b) are used here to model the young GC environment and the first generation of massive and very massive stars.

Massive stars at low Z evolve differently from those at solar Z. Simulations of Szécsi et al. (2015b) predict different evolutionary paths and, consequently, new types of objects present in low Z environments. One of the predictions at low Z are the core-hydrogen-burning cool supergiant stars. These objects start their evolution as O stars, but during their main-sequence phase, they expand due to envelope inflation (Sanyal et al., 2015), and become cool SG stars while still burning hydrogen in their cores. The cool supergiants in general have a convective envelope due to their low ($<10^4$ K) surface temperature. Envelope convection mixes nuclear products from the burning regions (core or shell) to the surface. Thus, the wind of the cool SG stars contains the products of nuclear burning that is happening in the deeper regions of these stars. In case of core-hydrogen-burning cool supergiants, the nuclear burning products in the wind are, necessarily, hot hydrogen burning products.

Core hydrogen burning cool SGs with low metallicity (0.02 $Z_\odot$) are predicted at masses higher than $M_{ini} \gtrsim 80\ M_\odot$. (In the case of LMC metallicity, higher than $M_{ini} \gtrsim 40\ M_\odot$, Köhler et al., 2015). They stay on the SG branch and burn hydrogen for a relatively long time (in some cases, as long as 0.3 Myr, which corresponds to 15% of their main sequence lifetimes). However short this core hydrogen burning SG lifetime is in an absolute sense, these objects have nevertheless a contribution to the chemical evolution of their environments. Such a star could eject several tens, or hundreds, of $M_\odot$ through stellar wind mass-loss, the composition of which material being different from that of the circumstellar gas.

We simulate the cool supergiant phase applying the mass-loss rate prescription by Nieuwenhuijzen and Jager (1990), which is a parametrized version of that by de Jager et al. (1988). The latter has been shown by Mauron and Josselin (2011) to be still applicable in the light of new observations of red supergiants. A metallicity-dependence of the wind is implemented as $\dot{M} \sim Z^{0.85}$ according to Vink et al. (2001). Thus, the mass-loss recipe we use:

$$\log \frac{\dot{M}}{M_\odot \mathrm{yr}^{-1}} = 1.42 \log(L/L_\odot) + 0.16 \log(M/M_\odot) + 0.81 \log(R/R_\odot) - 15 \log(9.6310) + 0.85 \log(Z_{ini}/Z_\odot) \tag{3.1}$$

This formula is in accordance with the results of Mauron and Josselin (2011) who find that the metallicity exponent should be between 0.5 and 1. However, it is important to note that this prescription is based on red SG stars with masses between 8-25 $M_\odot$. Since there is no mass-loss rate observed for SG stars with masses of 150-600 $M_\odot$, we extrapolate Eq. 3.1 up to these masses, pointing out that this approach involves large uncertainties.

Fig. 3.2 shows the Hertzsprung–Russell (HR) diagram of three evolutionary models that become core-hydrogen-burning SG stars during the last few Myr of their main-sequence evolution. The models were taken from Szécsi et al. (2015b), except for the most massive one (M_{ini}=575 $M_\odot$) which was computed for this work.

Our simulation of the model with M_{ini}=575 $M_\odot$ ended before the end of core-hydrogen-burning, with central helium mass fraction of 0.81. We estimate that until core-hydrogen exhaustion, this model needs about 0.28 Myr of further evolution. Altogether, the time it spends as a core-hydrogen-burning cool SG is 0.37 Myr. Based on its main-sequence lifetime of 1.56 Myr and the general trend that massive stars spend 90% of their total life on the main-sequence and 10% on the post-main-sequence, we expect a post-main-sequence lifetime of 0.17 Myr for this model. The mass loss in the SG phase can be as high as 10^{-3} $M_\odot$ yr^{-1}. It is expected that with this high mass-loss, the model loses its whole envelope during its post-main-sequence lifetime. But even if all its hydrogen-rich layers are lost, it will stay cool. According to Köhler et al. (2015, their Fig. 19) the zero-age main-sequence (ZAMS) of pure helium-stars bends toward that of hydrogen-rich stars, crossing it over at ~300 $M_\odot$ in the case of models with subsolar (SMC and LMC) composition. Although the exact mass where the crossover of the two ZAMS-lines happens at our sub-SMC metallicity needs to be investigated in the future, the model with M_{ini}=575 $M_\odot$ (and a total mass of 491 $M_\odot$ at the end of our simulation) is most probably above it. Therefore, we do not expect this model to become a hot Wolf–Rayet star after its envelope is lost, but instead to stay cool, and become a helium-rich SG during the remaining evolution.

The model with M_{ini}=257 $M_\odot$ from Szécsi et al. (2015b) was followed during its post-main-sequence evolution. This model is undergoing core-helium-burning and has a central helium mass fraction of 0.73 in the last computed model. It spends 0.26 Myr as a core-hydrogen-burning cool SG, and is expected to spend 0.25 Myr as a core-helium-burning object. The mass-loss rate is $2.9{\cdot}10^{-4}$ $M_\odot$ yr^{-1} in the last computed model. Supposing that this mass-loss rate stays constant until the end of its post-main-sequence lifetime, this model will end up having only 140 $M_\odot$. It remains an open question if this model, having lost its hydrogen-rich envelope, would stay cool or would become a hot Wolf–Rayet star. To decide, one would need either to follow the rest of its evolution, or to establish a mass-limit where the helium-ZAMS and the hydrogen-ZAMS cross, but both of these tasks fall outside of the scope of current work. However, given all the uncertainties concerning the mass-loss rates of actual supergiant stars at this mass, it may be that the model never loses its envelope because the real mass-loss rate is lower than assumed here.

The model with M_{ini}=150 $M_\odot$ has finished core-helium-burning in our simulation. It spends 0.07 Myr as a core-hydrogen-burning cool SG (during which time its surface does not become cooler than 19 000 K; its largest radius is 182 $R_\odot$) and another 0.30 Myr as a core-*helium*-burning red supergiant (with a surface temperature of ~4250 K and a radius of ~4000 $R_\odot$). It has a final mass of 118 $M_\odot$, and the mass-loss rate in the last computed model is $8.0{\cdot}10^{-5}$ $M_\odot$ yr^{-1}. Since core-helium-burning is finished in this model, we know its final surface temperature, as well as its envelope composition: it is a red supergiant at the end of its life, and it has an envelope of about 25 $M_\odot$ which is composed of 49.02% hydrogen, 50.96% helium and 0.02%

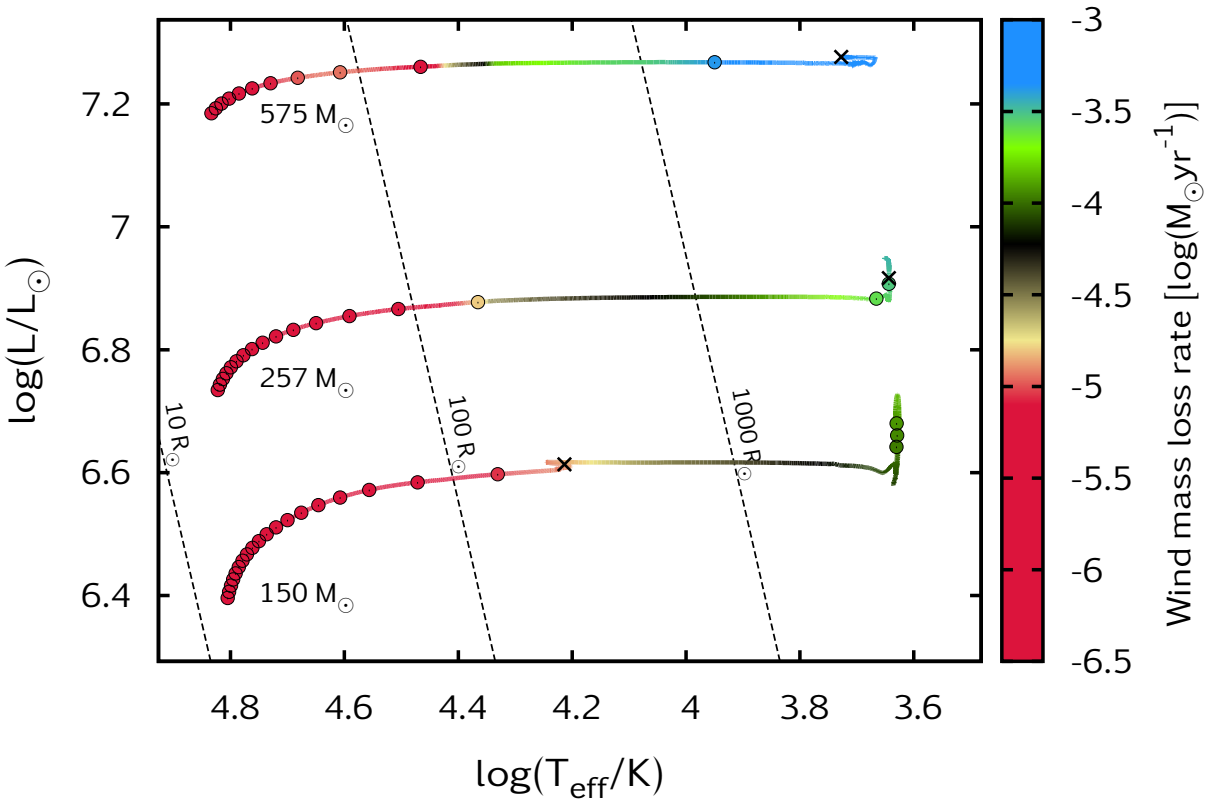

Figure 3.2. HR diagram of three evolutionary models that become core hydrogen burning SG stars with initial masses of 150, 257 and 575 $M_\odot$. Dots in the tracks mark every 10^5 years of evolution. Crosses mark the end of the main sequence evolution. Theoretical mass loss rates are colour coded. The tracks are taken from Szécsi et al. (2015b).

metals. Thus, we know for sure that it stays cool during all its life (while about the two more massive models discussed above, we could not be sure). Moreover, we find no helium-burning side-products on its surface. The reason for this is that the size of the convective core during helium-burning is smaller than that during hydrogen-burning, and the convective envelope of the red supergiant never reaches the layers of the helium-burning. It only mixes the ashes from core-hydrogen-burning and, during the post-main-sequence phase, shell-hydrogen-burning to the surface. As the observed composition of GC stars show no traces of helium-burning products either, we suggest that this SG model, having finished its post-main-sequence evolution while ejecting about 30 $M_\odot$ of material polluted with hot hydrogen burning products, is a potential source of the pollution in the young GCs.

3.2.2 Composition of the SG wind

Core-hydrogen-burning cool SGs have a convective envelope that mixes the hydrogen-burning products from the interior to the surface. The strong stellar wind then removes the surface layers. To calculate the composition of the ejecta, we need to sum over the surface composition of the evolutionary models. Fig. 3.3 shows the surface Na abundance as a function of the surface O abundance of the three models presented above (in Fig. 3.2). During their SG phase, the surface composition of our models cover the area where the most extremely polluted

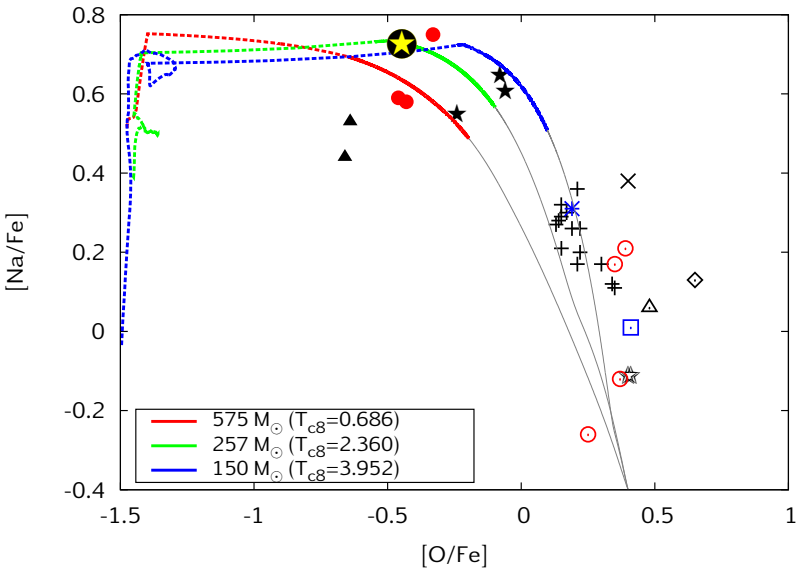

Figure 3.3. Theoretical predictions of the wind composition (i.e. surface Na abundance as a function of the surface O abundance, in solar Fe units) of three stellar models that become core hydrogen burning SGs are plotted with lines. The grey part of the lines correspond to surface compositions at $T_{eff}>10^4$ K (i.e. the evolution before reaching the SG branch), while the coloured part of the lines mean surface composition at $T_{eff}<10^4$ K (i.e. on the SG branch). When the lines become dashed, they represent the composition of the envelope in the last computed model (i.e. deeper layers that could still be lost if the mass-loss rate was higher than assumed here). The evolutionary calculations ended at the core temperatures, T_{c8}, given in the legend (units in 10^8 K). The big black-yellow star-symbol marks the position of a star predicted to form in the shell, as explained in Sect. 3.3.4. Observational data of the surface composition of GC stars (ω Cen red, NGC 6752 black and M 4 blue) are plotted with dots of different colours and shapes, following Yong et al. (2003), Da Costa et al. (2013) and Denissenkov and Hartwick (2014). Open symbols mark the 'primordial' population of stars, that is, those without pollution. Filled symbols mark the 'extremely' polluted population of stars. Crosses mark the 'intermediate' population stars, that is, those with some but not extreme pollution. For details of the observations and the properties of these categories, we refer to Yong et al. (2003) and Da Costa et al. (2013).

population of GC stars are found. This means that if low-mass stars form from the material lost by the SG directly (i.e. without mixing the ejecta with pristine gas), this second generation of low-mass stars would be observed as part of the extremely polluted population (cf. Sect. 3.3.4). In case, however, if the material lost via the slow SG wind is mixed with non-polluted gas, the second generation of low-mass stars could possibly reflect the composition of the so-called intermediate population (i.e. those stars that show some traces of pollution, compared to a not-polluted, primordial population, as explained by Da Costa et al., 2013).

Since the mass-loss rates of our models are uncertain, it is worth to investigate how a higher mass-loss rate would influence the ejecta composition. Therefore, we also plotted the composition of the envelope in the last model in Fig. 3.3. With a higher mass-loss rate (or, in the case of the two most massive models, during the remaining evolutionary time), deeper layers could be lost in the wind, contributing to the extremely polluted generation with very low O (>-1) and very high Na ($\sim$0.7). Deep inside the envelope, the Na abundance drops suddenly because the high temperatures ($\gtrsim 0.8\cdot10^8$ K) destroy the Na.

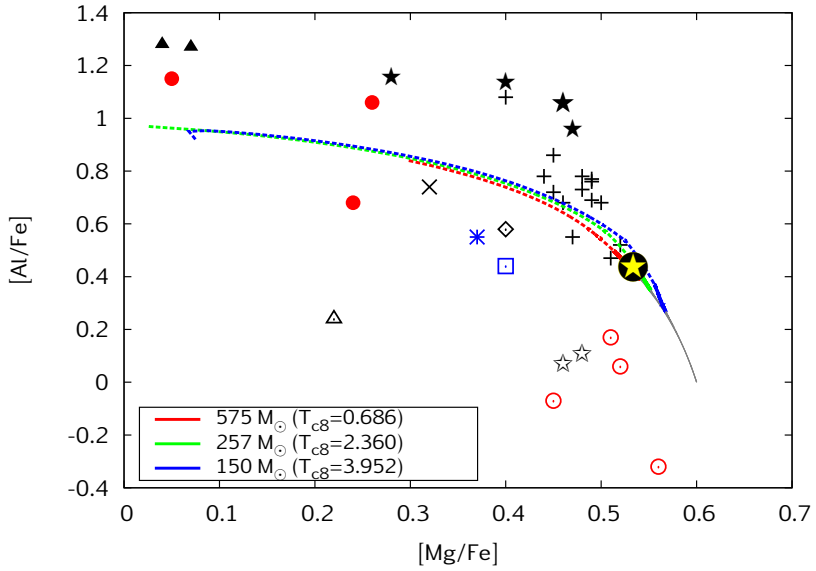

Figure 3.4. The same as Fig. 3.3 but for Mg and Al.

The Mg-Al surface abundances of our models are shown in Fig. 3.4. The surface Mg and Al abundances cover only a small fraction of all the observed variations in these elements. However, loosing deeper layers of the envelope could explain the whole observed ranges of Mg and Al variations.

As mentioned earlier, the surface composition of our models is only a vague indication of which abundance values can be expected through the SG wind pollution. To predict the composition of the ejecta and thus the composition of the second generation of low-mass stars, we need to sum over the surface composition of the evolutionary models. This is done in Sect. 3.3.4 – in the context of the starforming shell scenario, which is introduced below.

3.3 Starforming supergiant shells

3.3.1 Conditions in young GCs

Apart from the core-hydrogen-burning cool SGs, another important prediction by Szécsi et al. (2015b) is that the fast rotating massive stars become hot, compact and bright during all their lives. These objects, called Transparent Wind UV-Intense (TWUIN) stars, have similar surface properties to those of Wolf–Rayet stars, but differ from them in that their stellar winds are optically thin (hence the name). Nonetheless, TWUIN stars produce a huge amount of ionizing radiation during their lifetimes.

In the young GC environment, we expect that both type of low-metallicity objects, core-hydrogen-burning cool SGs and hot, ionizing TWUIN stars were present in the close vicinity of each other. Supposing that the SG stars are surrounded by an isotropic ionizing-radiation field emitted by the TWUIN stars, the SG wind structure changes significantly, giving rise to a dense, spherical region around the SG star called the photoionization-confined shell.

3.3.2 Photoionization confined shells around cool SGs

Mackey et al. (2014) developed a model in which the SG wind is photoionized by radiation from external sources. This model could explain the static shell observed around Betelgeuse, a nearby red SG star. According to their calculations, pressure from the photoionized wind generates a standing shock in the neutral part of the wind and forms an almost static, photoionization-confined shell. The shell traps up to 35% of all mass lost during the red SG phase, confining this gas close to the central object until its final supernova explosion.

We carried out simulations of a shell around a low-Z very massive SG star that undergoes core hydrogen burning. We use the PION code with spherical symmetry (Mackey, 2012) to simulate an evolving stellar wind that is photoionized by external radiation. The supposed source of the ionizing radiation are the fast-rotating TWUIN stars that could exist in the first generation of massive stars in the young GCs, creating an isotopic radiation field that surrounds the SG star. The simulations follow Mackey et al. (2014) except that we include stellar evolution and we use non-equilibrium heating and cooling rates for the gas thermal physics (as in Mackey et al., 2015). The stellar wind flows through the inner boundary of the grid with properties taken from a low-Z stellar evolution model with M_{ini}=257 $M_\odot$ from Szécsi et al. (2015b). This evolutionary model has an initial rotational velocity of 100 km s^{-1} and mass loss in the SG phase of about $10^{-3.5}$ $M_\odot$ yr^{-1}.

The wind is initially cold (200 K; this has no effect on the results because the wind is highly supersonic). The wind velocity is calculated from the escape velocity following Eldridge et al. (2006), except that we set the red SG wind velocity to be $v_\infty = 0.1 v_{esc}$ for $T_{eff} < 4500$ K. The above modification gives a minimum value of $v_\infty \approx 12$ km s^{-1}. The simulations are run with a total metallicity of 0.0002 and surface abundance mass fractions X=0.5 and Y=0.4998, similar to the surface abundances in the low-Z stellar model (Szécsi et al., 2015b). The winds are exposed to an ionizing photon flux of $F_\gamma = 10^{13}$ cm^{-2} s^{-1}.

The formation of the shell in the simulation depends on the thermal physics of the shocked wind (which must be able to cool into a dense and cold layer); this is rather uncertain because we have no constraints on dust formation in such low-metallicity red SGs. We use atomic line cooling (Wolfire et al., 2003) as implemented in Mackey et al. (2013), scaled to the metallicity of the stellar wind.

Fig. 3.5 shows the structure of the shell. The shell formed at a radius $r \approx 0.02$ pc (6×10^{16} cm) from the red supergiant, and shows the classic structure of a radiative shock: (i) an initial density jump at the shock of a factor of ≈ 4 with associated jumps in temperature and velocity according to the Rankine-Hugoniot jump conditions; (ii) a cooling region where the temperature decreases with r, the density increases, and the velocity decreases; and (iii) a cold dense layer. The cold layer is bounded on the outside by the ionization front, at which radius the stellar wind is heated to $\approx 12\,000$ K. A thermally driven wind accelerates outwards from the ionization front. We find that at the metallicity of the SG, the atomic cooling simulation produces a shell with density $\rho \approx 2 \times 10^{-16}$ g cm^{-3} and temperature $T \approx 50$ K.

The shell mass, M_{shell}, is plotted as a function of time in Fig. 3.6. It grows to $M_{shell} \approx 14$ $M_\odot$ by the end of the simulation. The Bonner-Ebert mass (i.e. the mass limit of the overdense region, above which the material collapses into a proto-star), M_{BE}, and the minimum unstable wavelength λ_{min} are also plotted in Fig. 3.6. They are discussed in the next section.

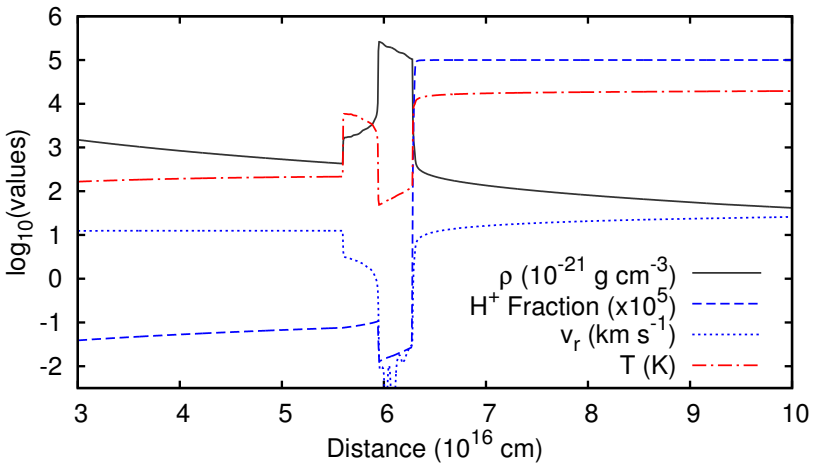

Figure 3.5. Density, temperature, velocity, and ionization fraction for the simulation of the photoionization confined shell around a core hydrogen burning supergiant with initial mass of 257 $M_\odot$. The snapshot is taken at the end of the stellar evolution calculation, when the star has an age of 1.88 Myr, at which time the shell mass is 14 $M_\odot$.

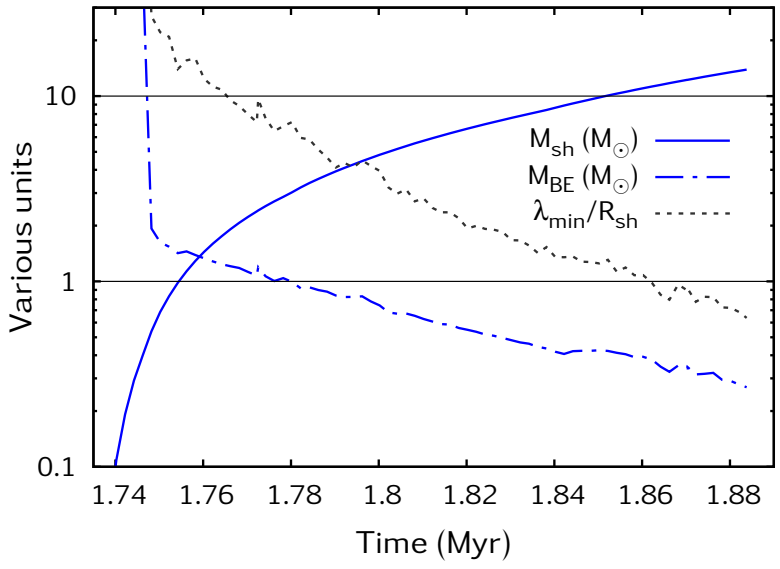

Figure 3.6. Shell mass, $M_{\rm sh}$, as a function of time since the star's birth (solid blue line), compared to the Bonner-Ebert mass $M_{\rm BE}$ at the densest point in the shell (dot-dashed blue line). The dashed black line shows the minimum unstable wavelength in units of the shell radius.

3.3.3 Gravitational instabilities in the shell

For the second generation of low mass stars to form in the photoionization-confined shell, the shell should be gravitationally unstable. We follow Elmegreen (1998, see their Eqs. 2.12-2.14) who describes the stability of a shocked sheet of gas (see also Doroshkevich et al., 1980; Vishniac, 1983). The dispersion relation (Eq. 2.13) gives the condition that perturbations with wavelength λ ($k = 2\pi/\lambda$) are unstable ($\omega^2 > 0$) if

$$\lambda \geq \frac{c^2}{G\sigma} = \frac{P}{G\sigma\rho} \tag{3.2}$$

where c^2 is the isothermal sound speed squared, $c^2 = P/\rho$ (P being the total pressure and ρ the density), and σ is the column density through the shell. This condition needs to be fulfilled by the shell in order to become gravitationally unstable. We define $\lambda_{\rm min}$ to be the wavelength at which this inequality is an equality.

In our simulation, the shell thickness is $l = 0.36 \cdot 10^{16}$ cm, $\rho = 2.65 \cdot 10^{-16}$ g cm^{-3} dense and its pressure is $P = 5.89 \cdot 10^{-7}$ dyne cm^{-2}. For this shell, the above condition gives a perturbation wavelength $\lambda \geq 3.4 \cdot 10^{16}$ cm.

An overdense region should have a diameter of $\lambda/2$. For our spherical shells, we should restrict $\lambda/2$ to be significantly less than the radius of curvature, so that the unstable part of the shell looks more like a flat sheet than a sphere. The shell is at radius $\sim$6.2$\cdot$10^{16} cm (0.02 pc). The angular size of the overdense region is thus 1.7/6.2 which is much less than one radian (about 16 degrees), so curvature effects can be neglected. Fig. 3.6 shows that $\lambda_{\rm min}/2R_{\rm sh} \approx 0.33$ at the end of the simulation, similar to the estimate above.

The Bonnor-Ebert mass for this dense region is

$$M_{\rm BE} = 1.18 \frac{c^4}{P^{1/2} G^{3/2}} = 0.2 \ {\rm M}_\odot, \tag{3.3}$$

meaning that if the dense region contains more mass than this, it would collapse into a stellar core. The mass of the dense region depends on its geometry, but with a density of $\rho = 2.65 \cdot 10^{-16}$ g cm^{-3} and a length scale of $\lambda/2 \approx 1.7 \cdot 10^{16}$ cm, it is around 2-3 M$_\odot$. We see from Fig. 3.6 that the shell contains a mass $M_{\rm sh} \approx 50 M_{\rm BE}$ at the end of the simulation. The stability analysis shows that the shell does not become unstable until it contains $> 20 M_{\rm BE}$ because the mass is distributed in a shell and not in a spherical cloud. We conclude therefore, that the thermodynamic conditions in the shell allow for gravitational instability, and that potentially many low mass stars may form from a single shell.

Additionally, the growth timescale of the perturbation should be less than a few times 10^5 years (lifetime of the SG star). Using Eqs. 2.12 and 2.14 from Elmegreen (1998), we get 3100 and 2.2$\cdot$10^4 years, respectively. These timescales are indeed significantly shorter than the life of the SG star with shell.

Once gravitational instability sets in, the collapse timescale is very short because the shell already has a very high density, much larger than dense cores in molecular clouds. Three-dimensional simulations are required to follow the gravitational collapse, so we cannot predict the final masses of the stars that will form. They may be larger than $M_{\rm BE}$ because the shell is constantly replenished from the red SG mass loss, and this could accrete onto collapsing cores. We can be sure, however, that we will not have a typical initial mass function, but rather it will be dominated by stars with less than one-solar mass, and the probability of forming massive

stars is expected to be extremely small.

3.3.4 Composition of the stars in the shell

The low-mass stars formed in the shell necessarily reflect the composition of the SG wind which is polluted by hot hydrogen burning products. To compute the composition of the shell-stars, we assume that the wind that leaves the SG star goes directly to the shell, and the material inside the shell is homogeneously mixed. Figs. 3.3 and 3.4 show the composition of a star formed inside the shell simulated around the M_{ini}=257 $M_{\odot}$ supergiant.

The abundances of Na and O of the shell-stars are compatible with the surface composition observed in the extremely polluted generation. The abundances of Mg and Al of our shell stars are compatible with the intermediate population. To fit more extreme abundances of Mg and Al, deeper layers of the SG star should be lost (represented by the dashed lines in Fig. 3.4). This could still happen during the post-main-sequence evolution of the SG model which would last for an additional 0.17 Myr (not simulated).

The shell stars have a helium mass fraction of Y_{sh}=0.48. We discuss the issue of the observed helium abundance of GC stars in Sect. 3.4.2.

3.4 Discussion

3.4.1 Mass budget

Any scenarios that aim to explain the abundance anomalies observed in GCs need to account for the mass that is contained in the first as well as in the second generation of stars. The three most popular of the polluter sources (AGB stars, spin stars, massive binaries), when only one of them is taken into consideration, fail to explain the amount of stellar mass that we observe with polluted composition. These scenarios suppose that the polluted material stays inside the gravitational potential well of the cluster, preferably accumulating near the center. Here the polluted material and the pristine material mix and form the second stellar generation. This would explain why we observe not just the primordial and extreme abundances but everything in between (see Figs. 3.3 and 3.4).

But for a second generation to be as numerous as the first generation, one needs much more polluted material than one of these sources can provide (de Mink et al., 2009). Therefore, it is possible that more then one source is present, or even that all the suggested sources play together (Bastian et al., 2013).

In our scenario, the mass budget constrain is the following: the second generation that is born inside the shell should contain as much mass as the first generation of low mass stars (0.1-0.8 $M_{\odot}$) born normally. This first generation of low mass stars observed represents ~35% of the stellar mass initially present in the cluster assuming a Kroupa (2001) initial mass function (IMF) between 0.1-1000 $M_{\odot}$. Even if all the mass contained in stars between 60-1000 $M_{\odot}$ would be lost through the SG wind and would swallowed into the second generation stars formed in the shell (which is clearly a very weak constrain), this mass accounts for only 12% of the initial stellar mass of the cluster. One simple way around this problem is to assume a top-heavy IMF, which indeed have been favoured for massive clusters recently (Ciardi et al., 2003; Dabringhausen et al., 2009).

3.4.2 Helium spread in different clusters

In some globular clusters, there are extremely helium-rich stars. For example, ~15% of the stars in NGC 2808 show helium abundance of Y~0.4, as inferred from their main-sequence multiplicity (Piotto et al., 2007; D'Antona and Ventura, 2007), as well as from spectroscopic measurements (Marino et al., 2014). Other GCs, however, have less extreme helium variations (Bastian et al., 2015; Dotter et al., 2015).

The most extreme values cannot be reproduced by AGB stars (Karakas et al., 2006). All the other polluter sources (massive binaries, spin stars, supermassive stars) have a general problem reproducing the required light element variations when the helium spread is a constraint, as shown by Bastian et al. (2015). Our simulated shell-stars (the surface composition of which is represented by the black-yellow symbol in Figs. 3.3 and 3.4) have a helium mass fraction of Y_{sh}=0.48. This can explain the most extreme helium abundances observed.

The fact that only some GCs are observed to have large helium spread may indicate, in the context of our scenario, that these clusters were the ones where the rather delicate process of shell-star formation could happen. This process is considered delicate because it requires several astrophysical effects to play together: that sufficiently dense and long-lived photoionization-confined shells form isotropically around very massive SG stars, so that gravitational instabilities could develop and the second generation of shell-stars could form from the shell. The conditions that are needed for this process might be only present in some GCs, preferably in the ones with (1) high cluster mass, so that massive and very massive stars can form; (2) dense inner regions, where the IMF is top-heavy, so very massive SGs can form; and (3) broad rotational velocity distribution, because the TWUIN stars that produce the ionizing radiation are fast rotators. Under these conditions, the starforming shell scenario could potentially produce a second population of stars with a helium mass fraction of Y~0.4. The total mass of this population would be, depending strongly on the IMF and the efficiency of the shell-formation process, around 12% of the cluster mass (cf. Sect. 3.4.1).

3.5 Conclusions

We propose starforming shells around cool supergiants as a possible way to form the second generation of low-mass stars in galactic globular clusters. Photoionization confined shells around core-hydrogen-burning cool supergiant stars may have been common in the young GCs. We have simulated such a shell and found that it could be dense enough to become gravitationally unstable. The new generation of low mass stars that would be formed in the shells should have an initial composition that reflects that of the supergiant's stellar wind, i.e. polluted by hot hydrogen burning products. Moreover, the shell-stars are predicted to have a surface helium mass fraction of $Y_{sh} \sim 0.4$, a value indeed observed in some, but not all GCs.

Even without forming a photoionization confined shell, the cool supergiant stars predicted at low-Z could contribute to the three sources discussed above in polluting the interstellar gas. The winds of these cool objects are slow enough to stay inside the gravitational potential well of the GC and, together with the ejecta of AGB stars, spin stars and massive binaries, make up the material in the cluster center which the second generation of stars is born from (or polluted by). Either way, with or without the starforming shell, the cool supergiant stars may be important contributors to the chemical changes happening in the young GCs.

CHAPTER 4

Final fate of hot massive stars in I Zwicky 18

ABSTRACT

Hot and very hot massive stars with weak winds have been recently predicted to exist in low-metallicity dwarf galaxies such as I Zw 18. These stars, called Transparent Wind Ultraviolet Intense (TWUIN) stars, have optically thin winds during their main-sequence lifetimes while being extremely hot and bright. Their presence is proposed to explain the unusually high ionizing radiation observed in low-metallicity environments. We aim to investigate the post-main-sequence evolution and the possible final fates of the TWUIN stars from a theoretical perspective, providing predictions that can be tested by observations of metal-poor environments.

TWUIN stars are the outcome of massive (9-300 $M_\odot$), fast rotating (v_{ini}>275 km s^{-1}) stellar evolutionary models at the initial metallicity of Z=0.0002 ([Fe/H]=−1.7). We simulated the evolution of TWUIN stars during core-helium-burning and beyond.

During their post-main-sequence lifetimes, the winds of the most massive models are predicted to become optically thick: these objects might be observed as Wolf–Rayet stars. The winds of the models below 30 $M_\odot$ are, however, still transparent during these evolved phases. We call these newly predicted objects stars of type TN and type TC – that is, TWUIN stars with similar surface abundances to those of Wolf–Rayet stars of type WN and type WC. We show that a theoretical population of massive stars in I Zw 18 is able to self-consistently explain both the high photoionization, both the small number of WC stars observed in this galaxy. The models are predicted to explode as superluminous supernovae in either the pair-instability, the pulsational-pair-instability or the magnetar scenario, and some of them are predicted to produce long-duration gamma-ray bursts.

TWUIN stars may be responsible for the unusually high photoionization in metal-poor environments such as dwarf galaxies, and may produce certain types of superluminous supernovae and gamma-ray bursts.

D. Szécsi, N. Langer, Frank Tramper, Takashi Moriya

To be submitted

4.1 Introduction

Massive star evolution taking place in astrophysical environments consisting almost entirely of hydrogen and helium – in other words, metal-poor environments – is responsible for some of the most intriguing and energetic cosmic phenomena, including supernovae and gamma-ray bursts.

Szécsi et al. (2015b, Chapter 2 of this thesis, from now on: Sz15) computed evolutionary models of core hydrogen burning massive stars with a composition of the compact dwarf galaxy I Zw 18, considering rotation. They found that even moderately fast rotators undergo efficient mixing induced by rotation resulting in quasi-chemically homogeneous evolution. Their homogeneously evolving models reach effective temperatures of up to 90 kK during core hydrogen burning. This, together with their moderate mass-loss rates, make them Transparent Wind Ultraviolet INtense stars (TWUIN star). Sz15 showed that the expected number of TWUIN stars can explain the observed He II ionizing photon flux of I Zw 18.

Here we present the further evolution (during core-helium-burning and beyond) of these TWUIN star models. We investigate their mass-loss histories, rotational velocities and wind opacity, as well as their surface compositions, and based on these quantities we classify them further as TWUIN stars or as Wolf–Rayet (WR) stars of different types. The amount of ionizing radiation they emit is discussed, and their final fates are predicted. As a complementary study, we present another set of models computed using an alternative mass-loss prescription, and discuss the predictions of this alternative set of models.

This work is organized as follows. Sect. 4.2 summarizes the physical assumptions applied for the post-main-sequence evolution of our models. Sect. 4.3 presents the 14 stellar models, and Sect. 4.4 their rotational and mass-loss history. Sect. 4.5 discusses their surface composition and classifies them as TWUIN stars or WR stars of different types. Sect. 4.6 predicts the amount of ionizing radiation they emit during their post-main-sequence evolution and compares it to that during their main-sequence lifetimes. Sect. 4.7 speculates about the possible final fates that our models will experience after their evolution ends. Sect. 4.8 presents an alternative set of models that has been computed with a higher mass-loss rate. These alternative models are compared to the original models, and the differences are discussed. Sect. 4.9 summarizes the results and discusses their implications.

4.2 Physical assumptions

The physical assumption applied for the main-sequence evoltution of our models has been descussed in Sz15. Here we summarize the physical assumptions applied for the computation of the post-main-sequence lifetime.

The same one-dimensional hydrodynamic binary evolutionary code (BEC) is used to compute the post-main-sequence evolution of the rotating single stellar evolutionary sequences of Sz15. BEC solves the five stellar structure equations using the implicit Henyey method. It contains detailed state-of-the-art treatment of rotation, magnetic fields, angular momentum transport and mass-loss.

To be consistent with Sz15, we identify our models with the initial mass and initial surface rotational velocity, the same way as Sz15 did. However, note that the models lose mass during their main-sequence evolution, therefore the mass and the rotational velocity which the post-main-sequence evolution starts with are different from the initial values. We refer to Table 4.1,

as well as to Table B.1 of Sz15, which gives these values at the end of the main-sequence (i.e. the terminal-age main-sequence or TAMS, defined as the evolutionary age when the helium mass fraction in the core first reaches 0.98).

The initial composition of our models is consistent with the observed composition of the stars in the starforming dwarf galaxy I Zw 18. The metallicity of this galaxy and, consequently, that of our models corresponds to Z=0.0002.

Mass-loss of massive stars influences their evolution significantly even at this low metallicity. We use the prescription of Hamann et al. (1995) for the winds of our post-main sequence models:

$$\log \frac{\dot{M}}{M_{\odot}\mathrm{yr}^{-1}} = 1.5\log(L/L_{\odot}) - 2.85X_{\mathrm{surf}} - 12.95 + 0.85\log(Z_{\mathrm{ini}}/Z_{\odot}) \tag{4.1}$$

This expression is given in Eq. 2 of Hamann et al. (1995), but has been reduced by a factor of 10 as suggested by Yoon et al. (2006). The reduction by 10 gives a mass-loss rate comparable to the commonly adopted one by Nugis and Lamers (2000) (see Fig. 1 of Yoon, 2015). For the dependence on the surface hydrogen mass fraction, X_{surf}, see the steepness of the fit in Fig. 7 of Hamann et al. (1995). The prescription is applied together with a metallicity dependence of $\dot{M} \sim Z^{0.85}$ following Vink et al. (2001).

The radiation driven mass-loss prescription in Eq. 4.1, however, is modified for those stellar models that rotate close to the critical breakup limit (including their Eddington-factors). In this case, a rotationally induced mass-loss is implemented, following Langer (1997) and Yoon and Langer (2005), also see Sect. 2.3 of Szécsi et al. (2015b). This prescription provides a mechanically driven mass-loss, the main source of which is not the surface properties of the model but the centrifugal acceleration.

4.3 Our models

We follow the post-main-sequence evolution of 14 stellar models of Sz15 (Z=0.0002), as listed in Table 4.1. These models were chosen to cover the hot side of the Hertzsprung–Russell (HR) diagram where chemically homogeneous evolution takes place, as shown in Fig. 4.1. Their initial masses are in the range of 13-257 $M_{\odot}$, corresponding to TAMS masses (i.e. helium-core masses) of 12.7-218 $M_{\odot}$.

The models are fast rotators (between v_{ini}=275-600 km s^{-1}), therefore undergo strong rotational mixing. As a consequence, they evolve chemically-homogeneously and stay compact and hot during their main-sequence lifetime. At the TAMS, their surface consists almost entirely of helium. Since the optical depth in their wind is in the order of unity, they are called Transparent Wind Ultraviolet INtense stars during core-hydrogen burning.

During their post-main-sequence lifetime, our models evolve to very high effective temperatures (~150 kK). Some of them stay TWUIN stars, while others become WR stars, as explained in Sect 4.5.

Table 4.1 summarizes the evolution of our models during the post-main-sequence. Column 9 gives information on how evolved the model is when the computation was stopped (also see the line colours in the HR diagram in Fig. 4.1). From the 14 models presented here, 12 have finished core-helium-burning, and 10 have finished core-carbon burning at the end of the computation.

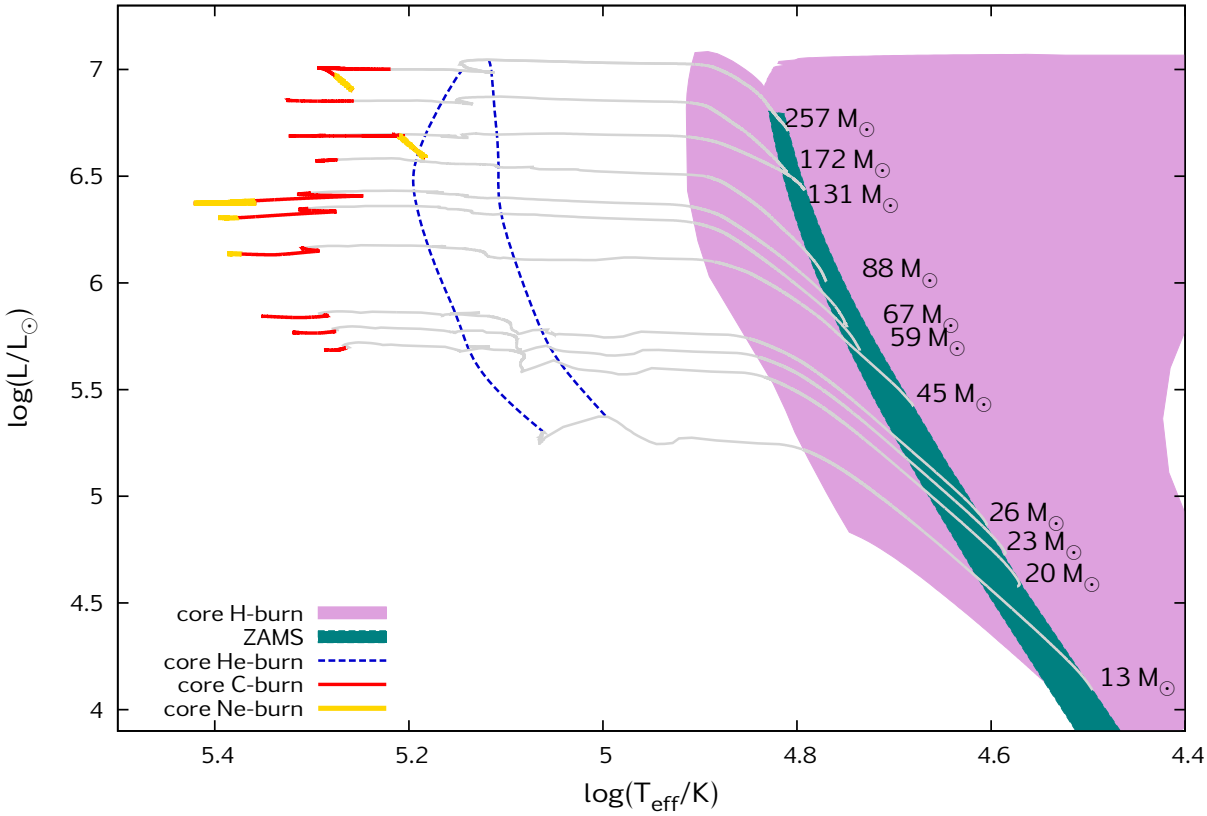

Figure 4.1. Evolutionary tracks in the HR diagram for fast rotating models with initial masses between 13-257 $M_\odot$ (see labels) with a composition of Z=0.0002. The lighter (purple) shading identifies the region in which all models of the grid of Sz15 undergo core hydrogen burning. The darker (green) shading identifies the zero-age main-sequence. Our models burn helium in their cores in the region enclosed by the dashed, blue lines. When the energy released by core-carbon-burning exceeds that of core-helium-burning, we mark the sequence with red line. When the central temperature reaches $1.6{\cdot}10^9$ K, which is the nominal temperature for neon burning, we mark the sequence with yellow. (Note that the computation of some of the models has been stopped before entering the core-neon-burning phase, cf. Table 4.1). (Models with 26 $M_\odot$–350 km s^{-1}, 67 $M_\odot$–300 km s^{-1} and 77 $M_\odot$–350 km s^{-1} are not shown here for clarity, since they would be overplotted by other tracks.)

Table 4.1. *Masses at different evolutionary stages.* Properties of 14 stellar models of Sz15, referred to with their initial mass (M_{ini}) and initial surface rotational velocity (v_{ini}), which have been followed beyond core-hydrogen exhaustion until the evolutionary stage given in the last column. Stellar and core masses at different evolutionary stages of these models are listed (units in $M_\odot$). $M_{TAMS}^{He\text{-}core}$: total stellar mass at the terminal-age main-sequence, that is, the mass of the helium-core (since the models are homogeneous during the main-sequence). $M_{He\text{-}exh}^{total}$: total stellar mass at helium-exhaustion from the core. $M_{He\text{-}exh}^{CO\text{-}core}$: core mass at helium-exhaustion from the core (i.e. CO-core mass); not equal to $M_{He\text{-}exh}^{total}$ since the models are not always evolving homogeneously during core-helium-burning. $M_{C\text{-}exh}^{total}$: total stellar mass at core-carbon-exhaustion. M_{End}: total stellar mass at the end of the computation. 'End': the end point of the model sequence (YB: core-helium-burning, YE: central helium-exhaustion, CB: core-carbon-burning, CE: central carbon-exhaustion, NB: core-neon-burning).

M_{ini} [$M_\odot$]	v_{ini} [km s^{-1}]	$M_{TAMS}^{He\text{-}core}$	$M_{He\text{-}exh}^{total}$	$M_{He\text{-}exh}^{CO\text{-}core}$	$M_{C\text{-}exh}^{total}$	M_{End}	End
13	450	12.7	-	-	-	11.2	YB
20	450	19.3	16.6	13.4	15.7	15.7	CE
23	500	21.9	18.7	15.4	17.7	17.7	CE
26	350	25.1	-	-	-	22.8	YB
26	500	24.7	21.0	17.6	19.9	19.9	CE
45	500	41.9	35.1	32.5	33.8	33.8	NB
59	300	55.7	48.5	44.1	47.2	47.2	NB
67	275	63.2	55.0	50.6	53.9	53.9	NB
67	300	63.0	54.6	52.7	53.6	53.6	NB
77	500	70.1	57.9	56.0	-	57.3	CB
88	275	83.0	72.2	68.0	-	71.5	CB
131	600	113.9	90.9	87.4	90.9	89.7	NB
172	350	153.6	124.1	122.2	124.1	123.0	CE
257	500	218.1	168.0	166.8	167.9	166.5	NB

4.4 Rotation and mass-loss history

At the metallicity of our stellar models, mass-loss during the main-sequence is not effective enough to spin these fast rotating models down. As shown by Sz15 (see their Fig. 14), TWUIN stars still rotate fast (~350-650 km s^{-1}) at TAMS. Here we discuss how much mass and angular momentum these models lose during their post-main-sequence evolution.

Fig. 4.2 shows the HR diagram of our models with the mass-loss rate colour coded. The mass-loss rate scales with the total mass of the models: during core helium burning, models with M_{ini}=13..26 $M_\odot$ lose mass with a rate of $\sim 5 \cdot 10^{-6}$ $M_\odot$ yr^{-1}; those with M_{ini}=45..88 $M_\odot$ lose mass with a rate of $\sim 2 \cdot 10^{-5}$ $M_\odot$ yr^{-1}; and our most massive models with M_{ini}=131..257 $M_\odot$ lose mass with a rate of as high as $\sim 10^{-3}$ $M_\odot$ yr^{-1}.

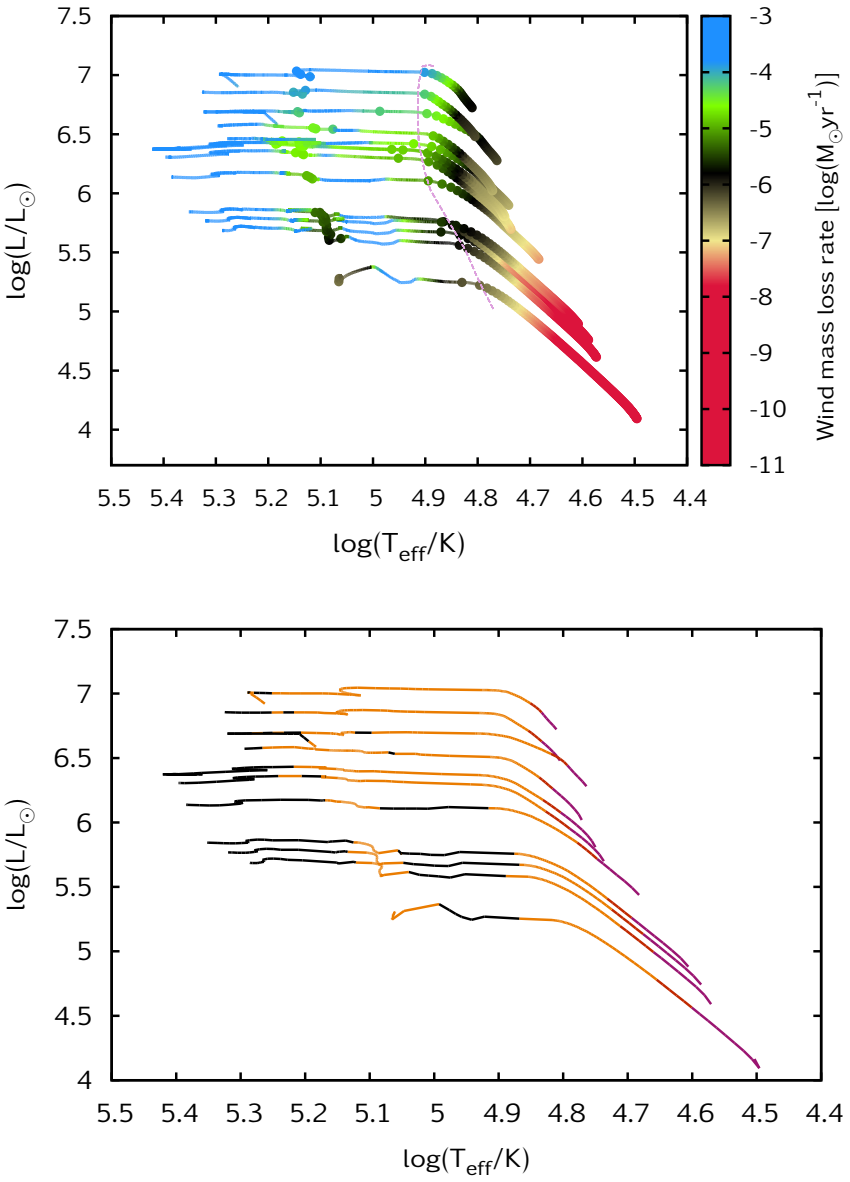

Figure 4.2. *Top:* HR diagram showing the mass-loss rates of our models colour coded. Dots mark every 10^5 yr of evolution, a purple dashed line marks the TAMS. *Bottom:* HR diagram showing the type of mass-loss prescription used for the models. Orange lines: radiation-driven mass-loss (as given in Eq. 4.1). Black lines: rotationally-induced mass-loss (following Langer, 1997, as explained in Sect. 4.2). (The purple-coloured phases during the main-sequence evolution of our models were computed using the mass-loss prescription for O-stars by Vink et al., 2000, as explained in Sz15.)

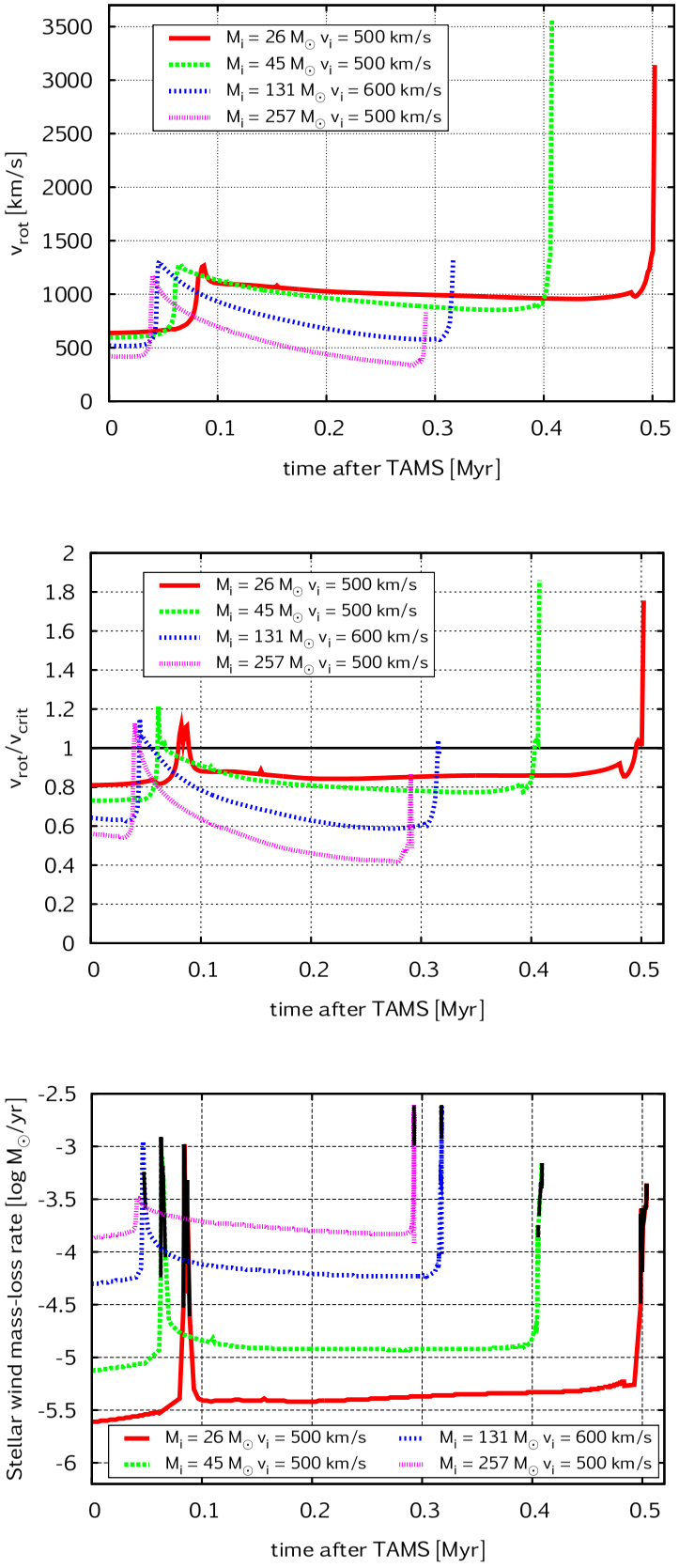

Figure 4.3. *Top:* Time evolution of the surface rotational velocity during the post-main-sequence phase of some of our models. The spin-up events between 0.04–0.09 Myr correspond to the core-contraction due to hydrogen-exhaustion, while the spin-up events at the end of the evolution are caused by the core-contraction due to helium-exhaustion carbon-exhaustion. *Middle:* Time evolution of the ratio of the surface rotational velocity to the Keplerian critical velocity. When the ratio exceeds one, a mechanically driven stellar wind is applied (cf. Sect. 4.2). This leads to enhanced mass-loss, which removes angular momentum and, in the case of the spin-up events between 0.04-0.09 Myr, spins the models down below v_{rot}/v_{crit}=1. *Bottom:* Time evolution of the mass-loss rate. The rotationally enhanced mass-loss rate is marked by black.

Fig. 4.3 shows the time evolution of the surface rotation and that of the mass-loss rate in some of our models. Due to the overall contraction at core-hydrogen-exhaustion, the models spin up and reach the Keplerian critical rotation. When this happens, a rotationally induced mass-loss prescription is applied, which removes both mass and angular momentum, so the models spin down below the critical rotation. During the long phase of core-helium-burning, they gradually lose mass and angular momentum. The second spin-up after core-helium-exhaustion makes the models reach the critical rotation again. Our computations were stopped shortly after that, but as discussed in Sect. 4.7.1, we expect that the models with M_{ini}=26 $M_\odot$ and M_{ini}=45 $M_\odot$ will not spin down significantly during their remaining evolution until the iron-core forms, and that their cores will collapse into fast-rotating black holes.

4.5 WR stars and TWUIN stars

4.5.1 WR classes

WR stars have been classified by several authors based on both observational and theoretical conditions (e.g. Hamann et al., 1995; Vink and Koter, 2005; Eldridge et al., 2006; Yoon et al., 2006; Georgy et al., 2012; Bestenlehner et al., 2014; Groh et al., 2014; Tramper et al., 2015). From a theoretical point of view, the WR class of a stellar model can be predicted most reliably by computing the spectrum of the model in question (see e.g. Groh et al., 2014). However, computing the spectra of our models falls outside of the scope of our current work. Therefore, we rely on a definition of the WR classes which takes only the surface abundances into account. Following Georgy et al. (2012), a WR star is of type WNL if the hydrogen mass fraction at the surface is higher than a few percent (we choose this limit to be 1%. Note that Georgy et al., 2012, uses the value of 10^{-5}; however, this seems too strict a condition, as this low amount of hydrogen would not be observable). If the surface hydrogen drops below this value, the star is further classified as WNE, WC, WO or WNC the following way:

- WNL: hydrogen mass fraction at the surface is higher than 1%;
- WNE: hydrogen mass fraction at the surface is lower than 1%, and the mass fraction of carbon at the surface is lower than that of nitrogen;
- WNC: hydrogen mass fraction at the surface is lower than 1%, and the mass fraction of carbon is higher than that of nitrogen;
- WC: hydrogen mass fraction at the surface is lower than 1%, the mass fraction of carbon at the surface is higher than that of nitrogen, and the ratio of (C+O)/He at the surface is between 0.03 and 1;
- WO: hydrogen mass fraction at the surface is lower than 1%, the mass fraction of carbon at the surface is higher than that of nitrogen, and the ratio of (C+O)/He at the surface is above 1.

This classification was developed for solar-metallicity stellar models. At solar metallicity, models do not follow chemically homogeneous evolution, but evolve towards low T_{eff} during their main-sequence lifetimes. They become WR stars only after the main-sequence, due to the loss of their whole envelopes via strong mass-loss. Our low-metallicity models, however, follow an entirely different evolutionary path (as explained by Sz15): they evolve directly towards the

Table 4.2. *Rotation and angular momentum.* Surface rotational velocity (v) and total angular momentum inside the stellar model (J) are listed for different evolutionary stages (such as the terminal-age main-sequence, core-helium-exhaustion and the end of the computation). Additionally, the average specific angular momentum ($\bar{j}$) inside the inner 3 $M_\odot$ and inside the inner 1.4 $M_\odot$ of the model's core at the end of the computation are given. When the model has a CO-core at the end of the computation, also the average specific angular momentum inside the CO-core is given.

M_{ini}	v_{ini}	v_{TAMS}	$v_{He\text{-}exh}$	$v_{C\text{-}exh}$	v_{End}	J_{TAMS}	$J_{He\text{-}exh}$	J_{End}	$\bar{j}^{3M_\odot}_{End}$	$\bar{j}^{1.4M_\odot}_{End}$	$\bar{j}^{CO\text{-}core}_{End}$
$[M_\odot]$	[km s^{-1}]	[km s^{-1}]	[km s^{-1}]	[km s^{-1}]	[km s^{-1}]	[erg s^{-1}]	[erg s^{-1}]	[erg s^{-1}]	[erg s^{-1}]	[cm^2 s^{-1}]	[cm^2 s^{-1}]
13	450	620	-	-	763	2.6e+52	-	8.5e+51	8.1e+16	4.5e+16	-
20	450	612	1046	2209	2582	4.9e+52	1.3e+52	5.6e+51	1.1e+16	6.0e+15	8.6e+16
23	500	645	1052	2368	2857	6.2e+52	1.5e+52	7.0e+51	1.3e+16	6.9e+15	1.1e+17
26	350	482	-	-	941	6.1e+52	-	2.7e+52	7.1e+16	4.1e+16	-
26	500	637	1039	2571	3155	7.4e+52	1.7e+52	9.0e+51	1.4e+16	7.7e+15	1.4e+17
45	500	596	920	2724	3564	1.6e+53	3.2e+52	2.1e+52	1.5e+16	8.7e+15	2.5e+17
59	300	392	813	2966	3411	1.7e+53	4.5e+52	3.2e+52	1.5e+16	8.4e+15	2.6e+17
67	275	360	757	3254	2851	1.8e+53	5.0e+52	3.7e+52	1.5e+16	8.4e+15	2.7e+17
67	300	385	719	2463	3483	1.9e+53	5.0e+52	3.7e+52	1.4e+16	8.6e+15	3.1e+17
77	500	546	711	-	1285	3.1e+53	5.5e+52	4.7e+52	2.3e+16	1.3e+16	4.0e+17
88	275	379	547	-	1377	2.7e+53	5.4e+52	4.6e+52	1.2e+16	7.1e+15	2.6e+17
131	600	520	615	1924	1330	6.0e+53	7.7e+52	6.4e+52	1.2e+16	6.5e+15	3.4e+17
172	350	376	470	1243	1221	6.5e+53	8.6e+52	7.4e+52	8.5e+15	4.5e+15	3.0e+17
257	500	422	370	833	833	1.2e+54	9.5e+52	8.2e+52	6.0e+15	3.5e+15	2.5e+17

WR branch in the HR-diagram, overgoing a phase during the main-sequence when their winds are transparent (TWUIN stars). Therefore, we need to pay attention to the wind optical depth in addition to the surface composition when classifying our models.

In order to predict if a model is a TWUIN star or a WR star, we estimate the optical depth in the wind following Sz15, who used the estimate given by Langer (1989):

$$\tau(R) = \frac{\kappa \dot{M}}{4\pi R(v_\infty - v_0)} \ln \frac{v_\infty}{v_0}, \tag{4.2}$$

where R designates the radius of the stellar model without taking the wind into account. This equation is derived from a β-velocity law with β=1. In that, we use the electron scattering opacity $\kappa = \sigma(1+X)$, σ being the Thomson scattering cross-section, an expansion velocity of v_0=20 km s^{-1} at the surface of the stellar model, and a terminal wind velocity of $v_\infty = \sqrt{\frac{GM}{R}}$.

If the wind optical depth is above unity, the effective temperature and the radius of the model needs to be corrected for this thick wind. Following Langer (1989), these corrections can be estimated as:

$$R^{corr} = R + \frac{3}{2}\frac{\kappa \dot{M}}{4\pi R v_\infty} R \tag{4.3}$$

and

$$T_{\rm eff}^{corr} = T_{\rm eff}\left(\frac{R}{R^{corr}}\right)^{1/2}. \tag{4.4}$$

Models in the initial mass range of 131-257 M$_\odot$ have an estimated wind optical depth greater than 5 during core-helium-burning, while those in the mass range of 45-88 M$_\odot$ have $2 < \tau < 5$, and those in the mass range of 13-26 M$_\odot$ have $\tau \approx 1$ (see Sects. 4.5.2–4.5.4 for details). Thus, our less massive models are TWUIN stars during their post-main-sequence lifetimes, while our most massive models are WR stars.

4.5.2 WR stars of type WN and type WC

Fig. 4.4 shows the time evolution of the estimated wind optical depth in the model with M$_{\rm ini}$=257 M$_\odot$ and v$_{\rm ini}$=500 km s^{-1}.

The two peaks at 0.04 Myr and 0.28 Myr (after reaching the TAMS) are caused by the high mass-loss due to the rotationally-enhanced wind. At 0.04 Myr, hydrogen is exhausted from the core, and the model contracts to reach helium-burning temperatures. Therefore, it spins up to close to the critical rotation, which leads to an enhanced mass-loss (cf. the second Y-axis of the same figure which shows the time evolution of the total stellar mass of the model). At 0.28 Myr, contraction and spin-up is happening again since helium is exhausted in the core.

Apart from these two peaks, however, the model has an estimated wind optical depth of around 9 during core-helium-burning. Therefore, this model is predicted to be a WR star (and not a TWUIN star).

Fig. 4.5 shows the time evolution of the surface composition of the same model. In the first ~0.06 Myr after the TAMS, the surface of the model consists entirely of helium (>98%), with some hydrogen still left. This composition is consistent with the WR class WNL. Hydrogen drops below 1% only at 0.05 Myr, after which the model is classified as a WNE star (with a surface C/N ratio below 1). For a very short phase at around 0.114 Myr, the carbon fraction at the surface exceeds the nitrogen fraction. During this short phase, the model is classified as a WNC star. At ~0.118 Myr after the TAMS, the surface helium fraction drops, while the surface

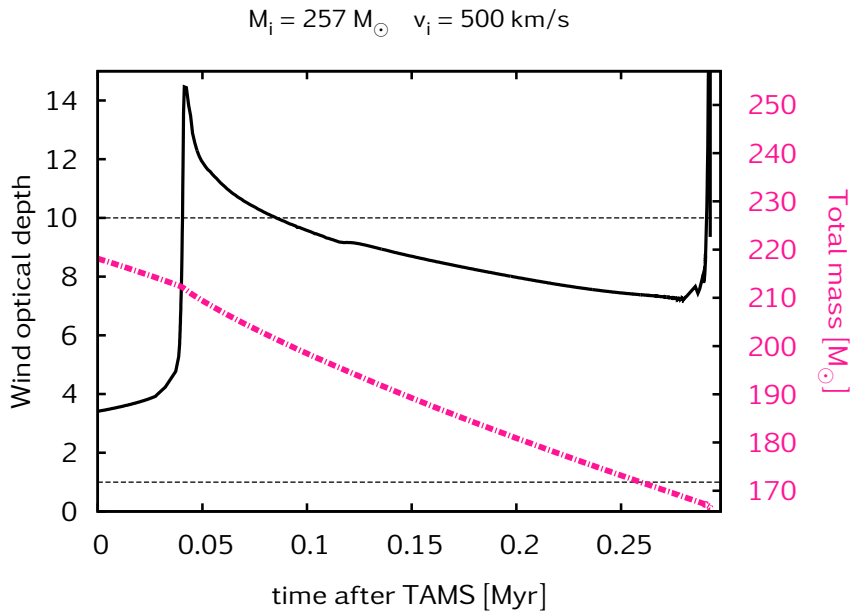

Figure 4.4. Time evolution of the optical depth in the wind (black straight line, Y-axis on the left) and that of the total mass (red dash-dotted line, Y-axis on the right) of the stellar model with M_{ini}=257 $M_\odot$ and v_{ini}=500 km s^{-1}. The wind optical depth, τ, is estimated by Eq. (4.2). The levels of τ=1 and τ=10 are shown with dashed lines. The peak at 0.04 Myr is caused by the rotationally-enhanced stellar wind which follows the contraction due to hydrogen-exhaustion from the core and the consequent spin-up of the model. The other peak at 0.28 Myr is caused by the same effect at helium-exhaustion from the core. The red-coloured Y-axis on the right indicates the total mass of the stellar model, shown by thick straight red line.

carbon and, later on, the oxygen fraction too, increase, fulfilling the condition for a WC star. Both carbon and oxygen are produced by core-helium-burning.

At ~0.22 Myr, the ratio (C+O)/He at the surface reaches 1, so based on the criterium above, the model is classified as WO. However, a more realistic classification would require to create atmosphere models for several points during the evolution. Groh et al. (2014) did this for their evolutionary models, and found that the models' spectra become WO type shortly (~10^4 years) before core collapse, i.e. *after* core-helium exhaustion. This result agrees with the conclusions of Tramper et al. (2015), who computed evolutionary models to match the observed WO properties.

Tramper et al. (2015) needed to apply a rather high mass-loss rate for the models to reproduce the observations (in fact, they needed a low clumping factor, so that the model mass-loss matches the observed unclumped mass-loss rate). See for instance Fig. 11 (and Appendix D) in Tramper et al. (2015). From this they concluded that it is the high surface temperature, achieved due to the contraction after core-helium-exhaustion, that makes a star a WO, not a difference in abundance. Additionally, the (C+O)/He ratio is naturally higher in them than in most – but not all – WC stars because they are in a very late stage of evolution. From their models, one would expect WC stars with similar surface abundances as observed in the WOs, because the abundance does not change very much during the very short time in which the star migrates to the hot WO regime in the HR-diagram.

Note that only 3 of the 6 single WO stars observed agree with (C+O)/He > 1, the others still

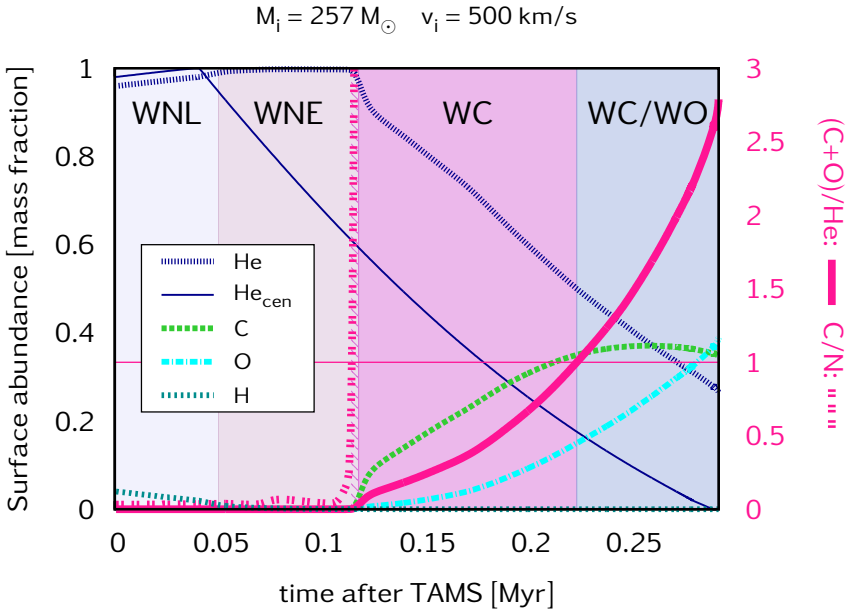

Figure 4.5. Time evolution of surface properties of the model with M_{ini}=257 $M_\odot$ and v_{ini}=500 km s^{-1}. The Y-axis on the left hand side gives the mass fraction of hydrogen, helium, carbon and oxygen at the surface, as well as that of helium in the center, as indicated by the key legend. The TAMS is defined by the helium mass fraction in the core reaching 0.98: core-helium-burning starts at ~0.04 Myr after the TAMS and proceeds for about 0.2 Myr. The hydrogen mass-fraction at the surface drops below 1% at 0.06 Mry after the TAMS, until which point the model is predicted to be WNL star, after that a WNE star. The Y-axis on the right hand side gives the ratio of (C+O)/He at the surface, represented by the red thick line. When this ratio is between 0.03 and 1, the model is predicted to be a WC type star; when this ratio is above 1, it is technically classified as a WO (but see the text for why it might be still observed as a WC). The Y-axis on the right hand side also shows the ratio of C/N at the surface, which is represented by the dot-dotted thick line of the same red colour. When the C/N ratio rises above 1 (dashed region between the WNE and WC phases), the model is classified as a WNC star.

have higher He abundances. To be in line with the observed properties of WO stars (Tramper et al., 2015), we include the additional criterium that WO stars need to have T_{eff}>140 kK. With this definition, our models become WO type stars usually after central helium-exhaustion. This definition of WO is also supported by the results of Groh et al. (2014), who found that the WO spectral type only arises at the end of the evolution, and that the difference between WC and WO stars results mainly from the differences in T_{eff} and $\dot{M}$, and not from the surface oxygen abundance.

Our other models in the initial mass range of 131-257 $M_\odot$ also have an estimated wind optical depth greater than 5 during core-helium-burning, and their surface composition is similar to the case of the 257 $M_\odot$ model, see Fig. 4.13. Table 4.3 gives the lifetimes they spend as WN and WC stars.

4.5.3 He-burning TWUIN stars of type TN and type TC

Fig. 4.6 shows the time evolution of the estimated wind optical depth in the model with M_{ini}=20 $M_\odot$ and v_{ini}=450 km s^{-1}.

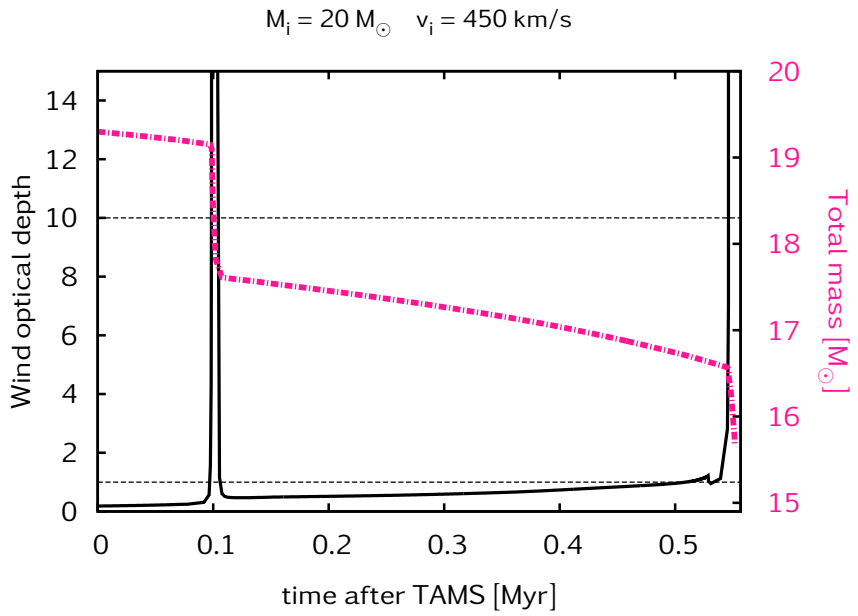

Figure 4.6. Time evolution of the optical depth in the wind (black straight line, Y-axis on the left) and that of the total mass (red dash-dotted line, Y-axis on the right) of the stellar model with M_{ini}=20 $M_\odot$ and v_{ini}=450 km s^{-1}. The wind optical depth, τ, is estimated by Eq. (4.2). The levels of τ=1 and τ=10 are shown with dashed lines. The peaks at 0.1 Myr and 0.53 Myr are caused by the rotationally-enhanced stellar wind which follows the contraction due to hydrogen-exhaustion and helium-exhaustion from the core, respectively, and the consequent spin-ups of the model. The red-coloured Y-axis on the right indicates the total mass of the stellar model, shown by thick straight red line.

The two peaks at 0.1 Myr and 0.55 Myr (after reaching the TAMS), again, are caused by the high mass-loss due to the rotational-enhanced wind, as explained in the previous section. Apart from the two peaks, the model has an estimated wind optical depth of less than 1 during core-helium-burning. Therefore, this model is predicted to be a TWUIN star during core-helium burning.

Fig. 4.7 shows the time evolution of the surface composition of the same model. In this model, hydrogen drops below 1% after 0.1 Myr, until which the model would be classified as a WNL star if the wind was thick. After this, the surface composition is consistent with the definition of the WNE and WC classes. Note however, that this is a TWUIN star with thin wind: therefore, we classify the corresponding phases as TNL, TNE and TC. Additionally, between the TNE and TC phases, the carbon fraction at the surface exceeds the nitrogen fraction, which is the nominal condition for a WNC star – in our transparent-wind case, a TNC star.

This classification of TWUIN stars as TNL, TNE, TNC and TC is purely theoretical and relies on only the predicted surface composition of our evolutionary models. In order to predict how their spectrum would look like, one needs to perform a simulation of their atmospheres, which will be done in a future study. Here we only highlight their possible existence based on our evolutionary computations.

Note that although we only investigate the post-main-sequence evolution of these models here, the TWUIN star models presented by Sz15 during the main-sequence should be, based on the discussion above, assigned to the class TNL.

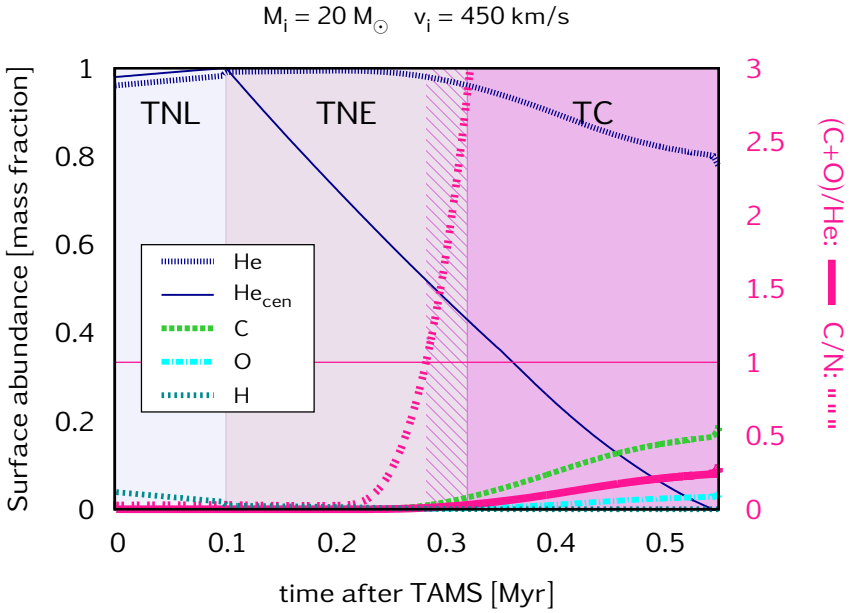

Figure 4.7. Time evolution of surface properties of the model with M_{ini}=20 $M_\odot$ and v_{ini}=450 km s^{-1}. The Y-axis on the left hand side gives the mass fraction of hydrogen, helium, carbon and oxygen at the surface, as well as that of helium in the center, as indicated by the key legend. The TAMS is defined by the helium mass fraction in the core reaching 0.98: core-helium-burning starts at ~0.1 Myr after the TAMS and proceeds for about 0.45 Myr. The hydrogen mass-fraction at the surface drops below 1% at 0.1 Myr after the TAMS, until which point the model is predicted to be TNL star – that is, a TWUIN star with some surface hydrogen. The Y-axis on the right hand side gives the ratio of (C+O)/He at the surface, represented by the red thick straight line. After 0.32 Myr, this ratio is between 0.03 and 1, therefore the model is predicted to be a TC type star – that is, a TWUIN star with similar surface abundances to a WC star. The Y-axis on the right hand side also shows the ratio of C/N at the surface, which is represented by the dot-dotted thick line of the same red colour. When the C/N ratio rises above 1 (dashed region between the TNE and TC phases), the model is classified as a TNC star.

Our post-main-sequence models in the initial mass range of 13-26 $M_\odot$ have $\tau \approx 1$: they are similar to the case of the 20 $M_\odot$ model (see Table 4.3 and Fig. 4.10). We found that, based on the surface composition condition of (C+O)/He>1, none of our models would become TWUIN stars of TO type. The condition of (C+O)/He>1 is only fulfilled in our most massive models because of their higher mass-loss rates; but the high mass-loss also contributes to a higher wind optical depth. TO type stars could only be predicted by models with even stronger internal mixing than ours, during the post-main-sequence evolution.

4.5.4 Other WR models

Our models in the initial mass range of 45-88 $M_\odot$ are TWUIN stars of type TNL during their main-sequence lifetimes, but have $2 < \tau < 5$ during the post-main-sequence phase, so here we classify them as WR stars as follows. Note however, that a more reliable classification would require the modelling of their atmospheres, which falls outside the scope of current work.

Figs. 4.10-4.13 depict the surface properties of these models. The models with M_{ini}=45 and 59 $M_\odot$, as well as that with M_{ini}=67 $M_\odot$–v_{ini}=275 km s^{-1}, are TWUIN stars of type TNL during

the first few 10 000 years of their post-main-sequence lifetimes, but become WR stars of WNE, WNC and WC after this. The models with M_{ini}=67 $M_\odot$–v_{ini}=300 km s^{-1} and M_{ini}=77 $M_\odot$, however, develop and keep a helium-rich envelope after core-hydrogen-exhaustion. These models are classified as WNE stars during all their core-helium-burning phase. The model with M_{ini}=88 $M_\odot$ even keeps some (about 3-9%) hydrogen on its surface, so it is classified as a WNL type star during almost all of its post-main-sequence evolution, except for the less 50 000 years when it becomes a WC type star.

Table 4.3 summarizes their radii at different epochs, as well as the lifetime they spend as WR stars. In the following, we discuss the ionizing radiation and the number of WC stars predicted in I Zw 18 in Sect. 4.6.

4.6 Ionizing photons

Ionizing radiation emitted by our low-metallicity main-sequence models have been discussed by Sz15. They used the black body approximation to predict the amount of ionizing photons radiated by a population of massive stars and compared it to observations of I Zw 18. They found that this galaxy's very high He II flux can be attributed to main-sequence TWUIN stars predicted at this low metallicity. In particular, they predicted a total He II photon rate of $1.6{\cdot}10^{50}$ s^{-1}. This rate was calculated with assuming a Salpeter initial mass function, and a rotational velocity distribution where 20% of all massive stars evolve chemically homogeneously. The stellar mass present in I Zw 18 was taken to be 300 000 $M_\odot$[1] and a constant star formation rate of 0.1 $M_\odot$ yr^{-1} (Lebouteiller et al., 2013) was applied that lasts for 3 Myr.

Here we follow their approach of using the black body approximation to predict the contribution of our post-main-sequence models to the total ionizing radiation of a massive stellar population in I Zw 18. Tables 4.4–4.6 present the number of ionizing photons that our models emit during their main-sequence as well as their post-main-sequence lifetimes. Since the observational comparison presented by Sz15 was done for photons in the He II continuum, in the following we only discuss the contribution of our models to the He II continuum.

The ionizing flux is a function of the surface temperature and the radius of the stellar model. Both quantities are, however, influenced by the wind optical depth (Langer, 1989), which itself depends on the strength of mass-loss (see Eq. 4.2). As seen in Fig. 4.8, models with M_{ini}=13..26 $M_\odot$ have optically thin ($\tau \simeq 1$) winds during core-helium-burning; those with M_{ini}=45..88 $M_\odot$ have $\tau \approx$ 2..3; and our most massive models with M_{ini}=131..257 $M_\odot$ have $\tau \approx$ 5..9. The optical depth in the wind increases above 10 only during the short restructuring episodes at the end of every burning phase (cf. Figs. 4.4 and 4.6).

Fig. 4.9 shows the photon emission rate of our models in the He II continuum. The second diagram in Fig. 4.9 presents the photon rate computed by using corrected values of T_{eff} and the stellar radius, given by Eqs. 4.3 and 4.4. The correction was applied to take the wind optical depth into account. Consequently, where the wind optical depth is high, the He II photon rate is lower compared to the not-corrected values on the first panel in Fig. 4.9 . The corrected stellar tracks evolve to low surface temperatures during the short spin-up episodes at the end of every burning phase; however, the long-lasting phase of core-helium-burning (marked by

[1] The irregular dwarf galaxy I Zw 18 has two large clusters, a north-western cluster and a south-eastern cluster. Note that here, when we talk about I Zw18, we always undertand the north-western cluster, as this is the one that, according to Kehrig et al. (2015b), is responsible for both the He II ionization and the WR star population. The total mass of the north-wester cluster is taken to be 300 000 $M_\odot$ in Kehrig et al. (2015b).

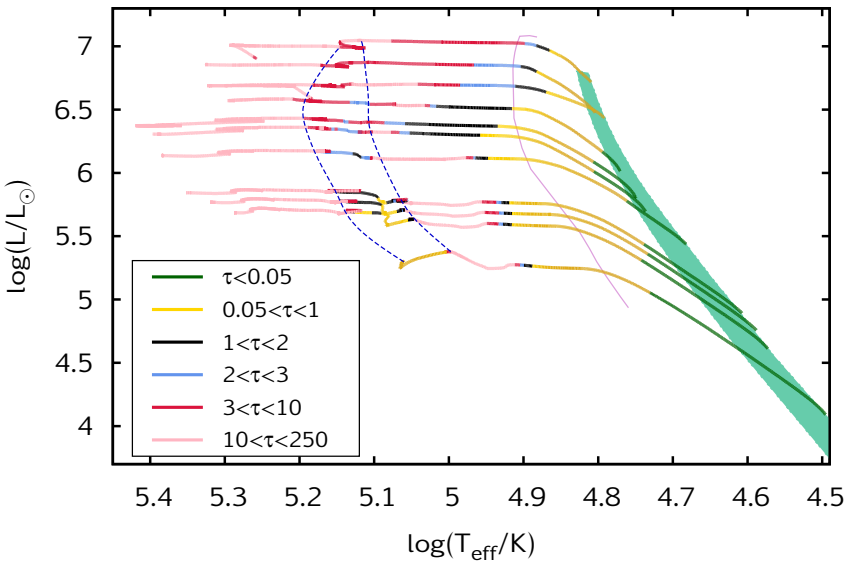

Figure 4.8. HR diagram showing the post-main-sequence phase of our models: colouring indicates the wind optical depth τ according to Eq.(4.2). The thick green area marks the ZAMS, the solid, purple line marks the end of core-hydrogen-burning, while core-helium-burning phases are enclosed into the region between the blue, dashed lines.

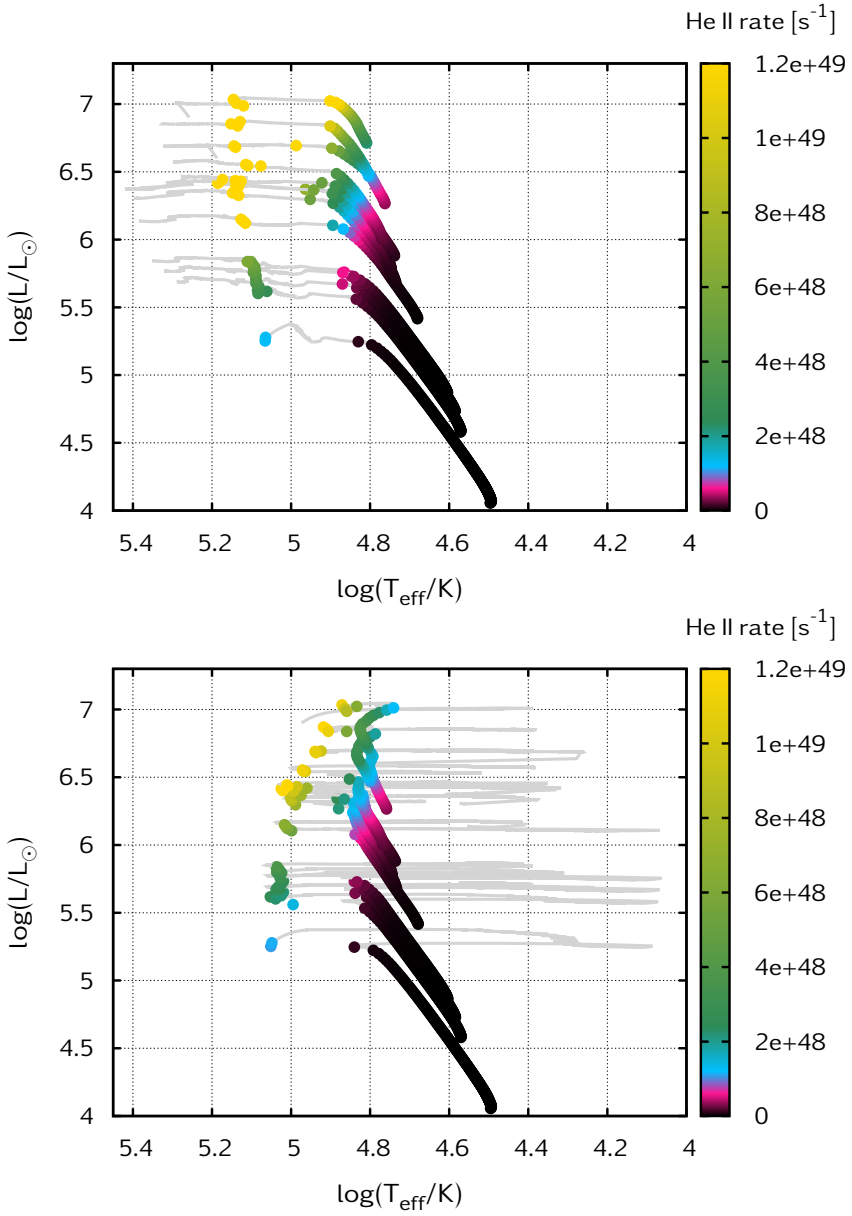

Figure 4.9. *Top:* HR diagram showing both the main-sequence and the post-main-sequence phases of our models. Dots represent every 10^5 yr of evolution. The colouring of the dots indicate the photon emission rate in the He II continuum (based on the black body approximation). The stellar tracks themselves are shown by gray lines.
Bottom: The same as above, but values of T_{eff} and the stellar radius are corrected for the wind optical depth (as given by Eqs. 4.4 and 4.3, cf. Fig. 4.8).

Table 4.3. *Radii and lifetimes of our models.* In columns 3-6, stellar radii at different ages (such as the terminal-age main-sequence, core-helium-exhaustion, core-carbon-exhaustion and the end of the computation) are given in units of $R_\odot$ for the models indicated by columns 1-2. The time that the models spend as different type of WR stars (such as WNL, WNE, WNC, WC or WO) and different type of TWUIN stars (such as TNL, TNE, TNC or TC) are shown in columns 9-13 (units in years), while the type itself is given in column 8. Asterisk marks the values that are lower limits in the case the evolution was stopped before reaching the given phase, see also Table 4.1. Note that our models below M_{ini}=100 $M_\odot$ are TWUIN stars of type TNL during their main-sequence lifetimes (given in column 6). About their main-sequence phase, see Sz15.

M_{ini} [$M_\odot$]	v_{ini} [km s^{-1}]	R_{TAMS}	$R_{He\text{-}exh}$	$R_{C\text{-}exh}$	R_{End}	τ^{MS}	type	$\tau^{T/WNL}$	$\tau^{T/WNE}$	$\tau^{T/WNC}$	$\tau^{T/WC}$	τ^{WO}
13	450	3.5	-	-	1.1	1.97e7	T	1.48e5	2.42e5*	-	-	-
20	450	4.3	1.3	0.7	0.6	1.04e7	T	1.02e5	1.83e5	3.77e4	2.30e5	0.00
23	500	4.7	1.4	0.7	0.6	8.82e6	T	9.21e4	1.51e5	4.03e4	2.39e5	0.00
26	350	4.7	-	-	1.7	7.27e6	T	1.04e5	1.37e5*	-	-	-
26	500	4.9	1.4	0.7	0.6	7.60e6	T	8.50e4	1.35e5	3.75e4	2.46e5	0.00
45	500	6.4	1.9	1.0	0.7	4.39e6	W	6.35e4	8.42e4	3.85e4	2.22e5	9.03e2
59	300	7.1	2.3	1.3	0.8	3.44e6	W	8.94e4	6.85e4	2.44e4	1.83e5	2.15e2
67	275	7.6	2.5	1.4	1.0	3.15e6	W	1.01e5	5.92e4	2.18e4	1.71e5	0.00
67	300	7.6	2.3	1.4	0.8	3.16e6	W	8.49e4	2.65e5	0.00	0.00	0.00
77	500	8.3	2.3	-	1.6	2.98e6	W	5.25e4	2.94e5	7.00e1	0.00	-
88	275	9.7	2.8	-	1.6	2.68e6	W	2.98e5	0.00	1.44e4	3.12e4	-
131	600	11.0	3.5	3.5	2.8	2.30e6	W	4.65e4	5.27e4	2.77e4	1.60e5	3.06e4
172	350	13.3	4.5	4.5	2.0	2.01e6	W	7.25e4	9.17e4	2.30e3	8.64e4	4.90e4
257	500	16.8	5.9	6.0	2.9	1.80e6	W	5.03e4	6.46e4	3.25e3	1.06e5	6.87e4

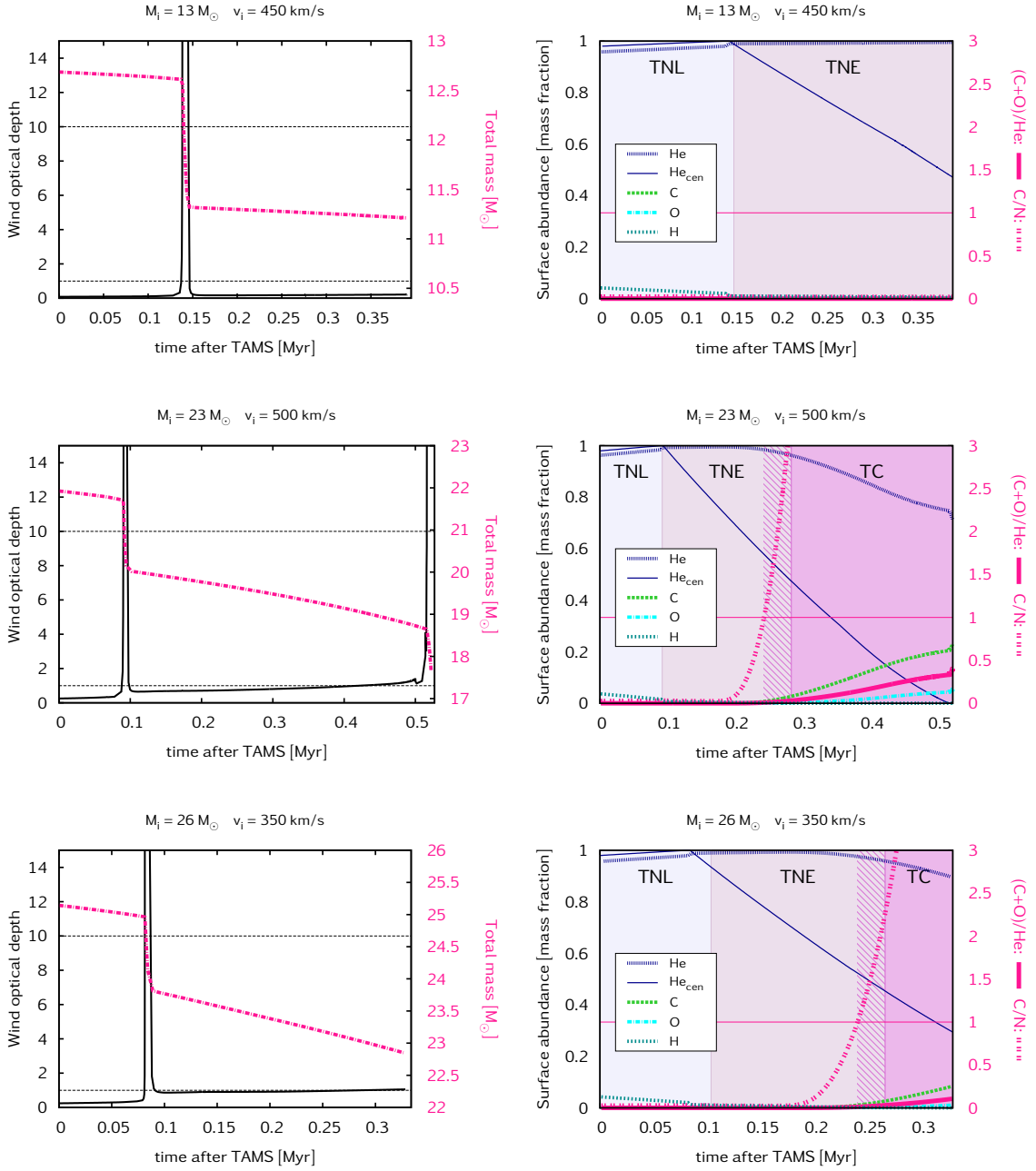

Figure 4.10. *Left:* Time evolution of the optical depth (black solid line, Y-axis on the left) and of the total mass (red dash-dotted line, Y-axis on the right) of the stellar models indicated by the title of every figure. The optical depth, τ, is estimated by Eq. (4.2). The levels of τ=1 and τ=10 are marked with dashed lines. Cf. Figs. 4.4-4.7 for details. *Right:* Time evolution of surface properties of the models indicated by the title of every figure. The Y-axis on the left hand side gives the mass fraction of hydrogen, helium, carbon and oxygen at the surface, as well as that of helium in the center, as indicated by the key legend. The Y-axis on the right hand side gives the ratio of (C+O)/He at the surface, represented by the red thick straight line, and that of C/N, represented by red dot-dotted line. For explanation of the classification, see Sect. 4.5.

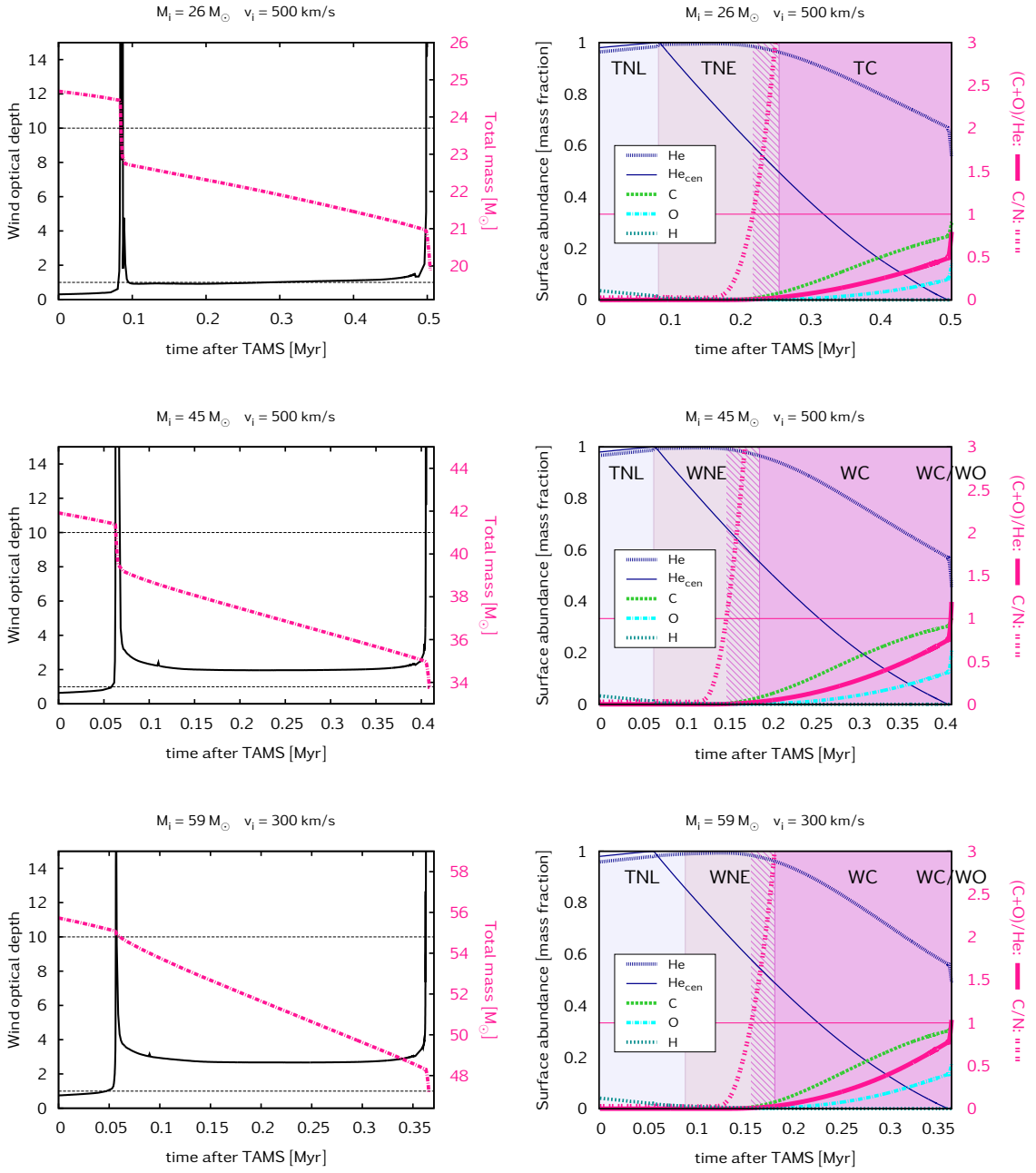

Figure 4.11. The same as Fig. 4.10, but for other models, as indicated by the title of every figure.

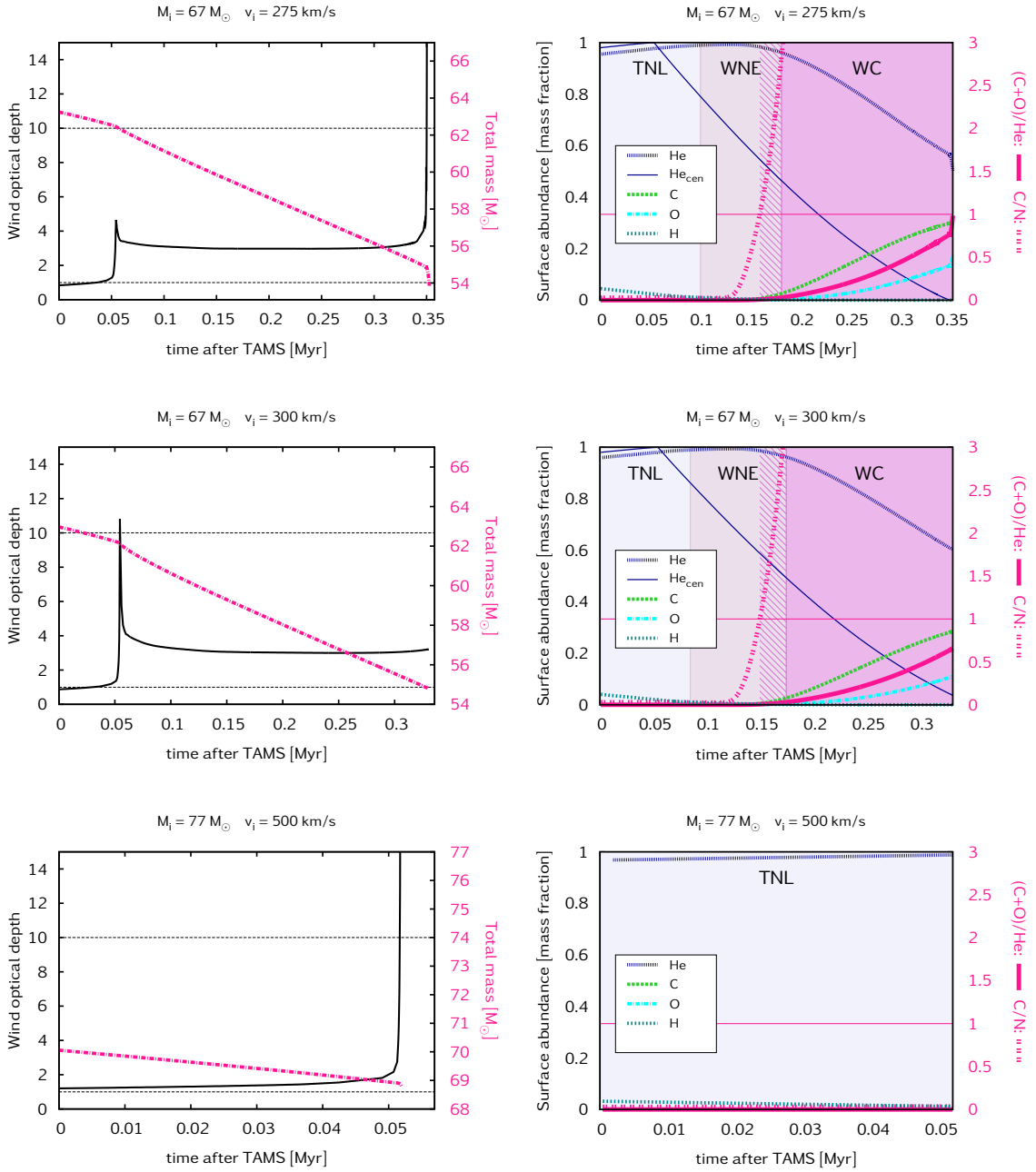

Figure 4.12. The same as Fig. 4.10, but for other models, as indicated by the title of every figure.

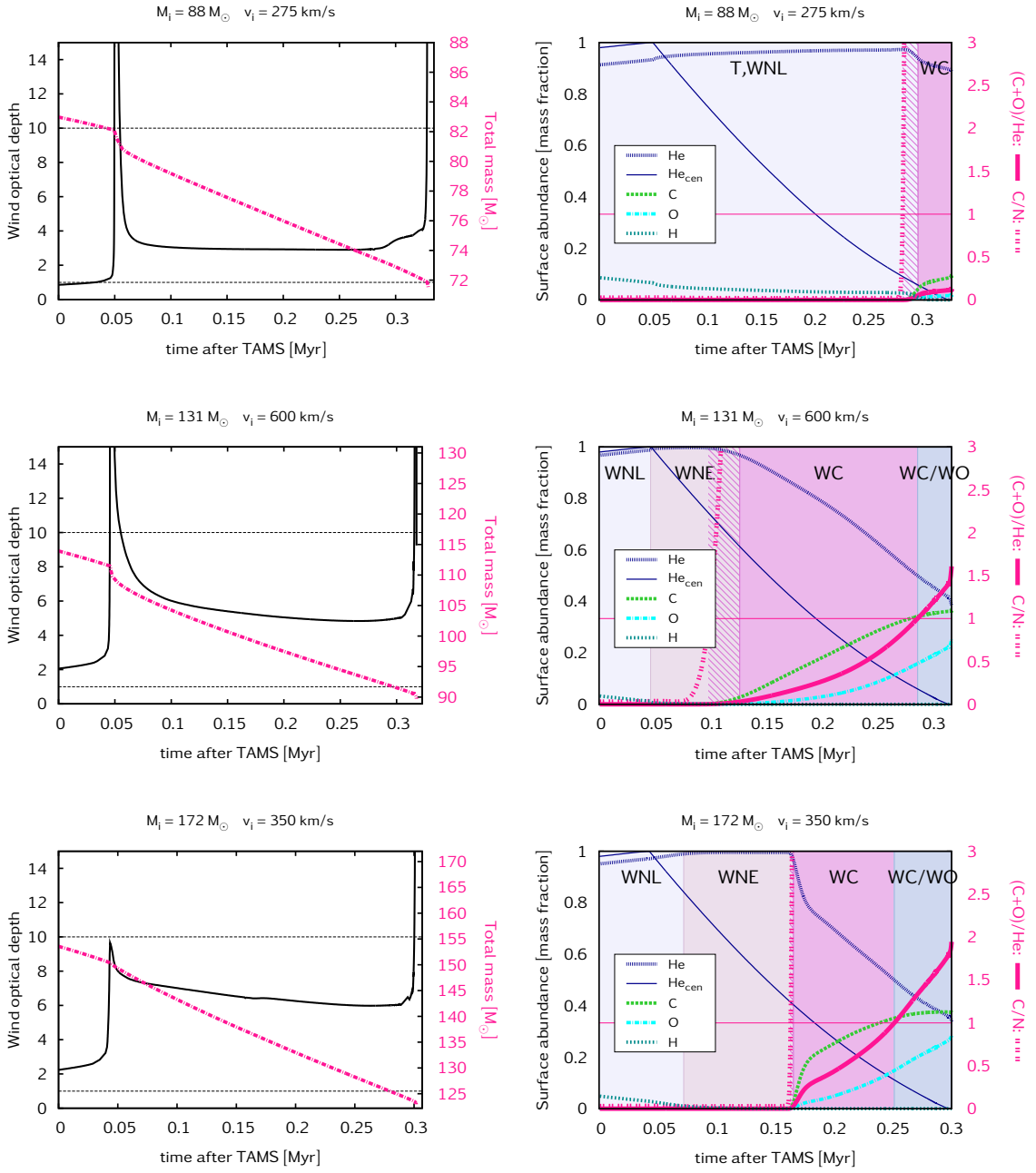

Figure 4.13. The same as Fig. 4.10, but for other models, as indicated by the title of every figure.

Table 4.4. *Lymann continuum.* Time-averaged rate (Q) and peak rate (Q^{max}) of the ionizing photons in the Lymann continuum during the main-sequence (MS) and the post-main-sequence (p.MS) evolution for each stellar sequence. Both the values that are not corrected for the wind optical-depth and the values that are corrected for the wind optical-depth (marked with *corr*) are tabulated. (Note that Sz15 gave not-corrected values for the main-sequence evolution of their models.) The last four columns have the following meaning. The ionizing photon rate during the whole evolution is marked with Q^{total}, and calculated by: $Q^{total}=(1-\frac{\tau^{p.MS}}{\tau^{MS}})\cdot Q^{MS}+\frac{\tau^{p.MS}}{\tau^{MS}}\cdot Q^{p.MS}$, where τ means the lifetime of the model in the given evolutionary phase (as given in Table 4.3). Q^{total}_{corr} is calculated the same way, but using the corrected flux values. The total ionizing photon rates are compared to those during the main-sequence and the post-main-sequence, both in the not-corrected and the corrected case, in the last four columns. Asterisks mark the sequences that have not finished core-helium-burning. We emphasize that the given quantities rely on the black body approximation, and refer to Sz15 for a discussion of its validity.

M^i-v^i_{rot} [$M_\odot$-km/s]	Q^{MS} [s^{-1}]	$Q^{p.MS}$ [s^{-1}]	Q^{MS}_{corr} [s^{-1}]	$Q^{p.MS}_{corr}$ [s^{-1}]	$Q^{max,MS}$ [s^{-1}]	$Q^{max,p.MS}$ [s^{-1}]	$Q^{max,MS}_{corr}$ [s^{-1}]	$Q^{max,p.MS}_{corr}$ [s^{-1}]	Q^{total}/Q^{MS}	$Q^{total}_{corr}/Q^{MS}_{corr}$	$Q^{p.MS}/Q^{total}$	$Q^{p.MS}_{corr}/Q^{total}_{corr}$
13-450*	1.75E+48	1.27E+49	1.75E+48	1.34E+49	1.18E+49	1.35E+49	1.18E+49	1.36E+49	1.11*	1.13*	6.51*	6.80*
20-450	6.03E+48	2.85E+49	6.03E+48	2.96E+49	2.61E+49	3.11E+49	2.61E+49	3.35E+49	1.20	1.21	3.95	4.07
23-500	8.48E+48	3.49E+49	8.48E+48	3.61E+49	3.39E+49	3.70E+49	3.39E+49	4.03E+49	1.16	1.17	3.55	3.65
26-350*	1.27E+49	4.33E+49	1.27E+49	4.54E+49	4.44E+49	4.44E+49	4.14E+49	4.78E+49	1.09*	1.09*	3.12*	3.27*
26-500	1.14E+49	4.18E+49	1.14E+49	4.44E+49	4.11E+49	4.40E+49	4.11E+49	4.80E+49	1.16	1.18	3.17	3.31
45-500	3.74E+49	8.88E+49	3.72E+49	9.67E+49	9.23E+49	9.80E+49	9.21E+49	1.00E+50	1.11	1.13	2.13	2.29
59-300	6.66E+49	1.36E+50	6.65E+49	1.53E+50	1.42E+50	1.48E+50	1.43E+50	1.59E+50	1.11	1.14	1.84	2.02
67-275	8.30E+49	1.62E+50	8.30E+49	1.86E+50	1.69E+50	1.75E+50	1.70E+50	1.92E+50	1.11	1.15	1.75	1.95
67-300	8.26E+49	1.56E+50	8.26E+49	1.80E+50	1.68E+50	1.75E+50	1.68E+50	1.84E+50	1.11	1.14	1.71	1.91
77-500	9.91E+49	1.77E+50	9.88E+49	1.95E+50	1.91E+50	2.00E+50	1.91E+50	1.98E+50	1.10	1.12	1.62	1.76
88-275	1.29E+50	2.32E+50	1.29E+50	2.64E+50	2.36E+50	2.36E+50	2.36E+50	2.64E+50	1.09	1.11	1.66	1.85
131-600	2.20E+50	3.17E+50	2.19E+50	3.70E+50	3.63E+50	3.63E+50	3.58E+50	3.75E+50	1.05	1.09	1.37	1.55
172-350	3.43E+50	4.33E+50	3.42E+50	5.49E+50	5.28E+50	5.28E+50	5.31E+50	5.66E+50	1.04	1.08	1.22	1.48
257-500	5.73E+50	6.23E+50	5.65E+50	7.92E+50	8.09E+50	8.09E+50	8.11E+50	8.34E+50	1.01	1.06	1.07	1.32

Table 4.5. *He I continuum.* Time-averaged rate (Q) and peak rate (Q^{max}) of the ionizing photons in the He I continuum during the main-sequence (MS) and the post-main-sequence (p.MS) evolution for each stellar sequence. Both the values that are not corrected for the wind optical-depth and the values that are corrected for the wind optical-depth (marked with *corr*) are tabulated. (Note that Sz15 gave not-corrected values for the main-sequence evolution of their models.) The last four columns have the following meaning. The ionizing photon rate during the whole evolution is marked with Q^{total}, and calculated by: $Q^{total}=(1-\frac{\tau^{p.MS}}{\tau^{MS}})\cdot Q^{MS}+\frac{\tau^{p.MS}}{\tau^{MS}}\cdot Q^{p.MS}$, where τ means the lifetime of the model in the given evolutionary phase (as given in Table 4.3). Q^{total}_{corr} is calculated the same way, but using the corrected flux values. The total ionizing photon rates are compared to those during the main-sequence and the post-main-sequence, both in the not-corrected and the corrected case, in the last four columns. Asterisks mark the sequences that have not finished core-helium-burning. We emphasize that the given quantities rely on the black body approximation, and refer to Sz15 for a discussion of its validity.

M^i-v^i_{rot} [$M_\odot$-km/s]	Q^{MS} [s^{-1}]	$Q^{p.MS}$ [s^{-1}]	Q^{MS}_{corr} [s^{-1}]	$Q^{p.MS}_{corr}$ [s^{-1}]	$Q^{max,MS}$ [s^{-1}]	$Q^{max,p.MS}$ [s^{-1}]	$Q^{max,MS}_{corr}$ [s^{-1}]	$Q^{max,p.MS}_{corr}$ [s^{-1}]	Q^{total} / Q^{MS}	Q^{total}_{corr} / Q^{MS}_{corr}	$Q^{p.MS}$ / Q^{total}	$Q^{p.MS}_{corr}$ / Q^{total}_{corr}
13-450*	2.65E+47	6.01E+48	2.65E+47	5.93E+48	3.37E+48	7.98E+48	3.30E+48	7.91E+48	1.40*	1.40*	16.20*	16.03*
20-450	1.17E+48	1.69E+49	1.16E+48	1.72E+49	8.60E+48	2.02E+49	8.40E+48	1.95E+49	1.71	1.73	8.45	8.56
23-500	1.75E+48	2.08E+49	1.72E+48	2.12E+49	1.18E+49	2.43E+49	1.20E+49	2.34E+49	1.56	1.58	7.62	7.79
26-350*	3.07E+48	2.76E+49	3.12E+48	2.72E+49	1.71E+49	2.93E+49	2.35E+49	2.85E+49	1.30*	1.29*	6.90*	6.75*
26-500	2.49E+48	2.54E+49	2.44E+48	2.55E+49	1.47E+49	2.93E+49	1.42E+49	2.84E+49	1.55	1.56	6.60	6.69
45-500	9.97E+48	5.47E+49	9.64E+48	5.39E+49	3.60E+49	6.02E+49	3.25E+49	5.73E+49	1.37	1.39	3.99	4.02
59-300	2.08E+49	8.72E+49	2.01E+49	8.40E+49	6.00E+49	9.39E+49	5.77E+49	8.81E+49	1.35	1.34	3.11	3.11
67-275	2.65E+49	1.05E+50	2.57E+49	9.98E+49	7.19E+49	1.12E+50	6.95E+49	1.06E+50	1.35	1.34	2.93	2.89
67-300	2.65E+49	1.02E+50	2.56E+49	9.88E+49	7.11E+49	1.09E+50	6.51E+49	1.07E+50	1.34	1.34	2.88	2.88
77-500	3.09E+49	1.09E+50	2.89E+49	1.06E+50	7.94E+49	1.17E+50	6.46E+49	1.12E+50	1.32	1.34	2.68	2.75
88-275	4.28E+49	1.51E+50	4.08E+49	1.34E+50	9.71E+49	1.53E+50	8.75E+49	1.37E+50	1.26	1.24	2.79	2.65
131-600	7.17E+49	2.02E+50	6.34E+49	1.74E+50	1.55E+50	2.09E+50	1.08E+50	1.77E+50	1.22	1.21	2.30	2.26
172-350	1.25E+50	3.06E+50	1.12E+50	2.43E+50	2.28E+50	3.17E+50	2.01E+50	2.56E+50	1.20	1.16	2.04	1.87
257-500	2.09E+50	4.33E+50	1.76E+50	3.06E+50	3.49E+50	4.60E+50	2.82E+50	3.29E+50	1.17	1.11	1.77	1.56

Table 4.6. *He II continuum.* Time-averaged rate (Q) and peak rate (Q^{max}) of the ionizing photons in the He II continuum during the main-sequence (MS) and the post-main-sequence (p.MS) evolution for each stellar sequence. Both the values that are not corrected for the wind optical-depth and the values that are corrected for the wind optical-depth (marked with *corr*) are tabulated. (Note that Sz15 gave not-corrected values for the main-sequence evolution of their models.) The last four columns have the following meaning. The ionizing photon rate during the whole evolution is marked with Q^{total}, and calculated by: $Q^{total}=(1-\frac{\tau^{p.MS}}{\tau^{MS}})\cdot Q^{MS}+\frac{\tau^{p.MS}}{\tau^{MS}}\cdot Q^{p.MS}$, where τ means the lifetime of the model in the given evolutionary phase (as given in Table 4.3). Q^{total}_{corr} is calculated the same way, but using the corrected flux values. The total ionizing photon rates are compared to those during the main-sequence and the post-main-sequence, both in the not-corrected and the corrected case, in the last four columns. Asterisks mark the sequences that have not finished core-helium-burning. We emphasize that the given quantities rely on the black body approximation, and refer to Sz15 for a discussion of its validity.

M^i-v^i_{rot} [$M_\odot$-km/s]	Q^{MS} [s^{-1}]	$Q^{p.MS}$ [s^{-1}]	Q^{MS}_{corr} [s^{-1}]	$Q^{p.MS}_{corr}$ [s^{-1}]	$Q^{max,MS}$ [s^{-1}]	$Q^{max,p.MS}$ [s^{-1}]	$Q^{max,MS}_{corr}$ [s^{-1}]	$Q^{max,p.MS}_{corr}$ [s^{-1}]	Q^{total}/Q^{MS}	$Q^{total}_{corr}/Q^{MS}_{corr}$	$Q^{p.MS}/Q^{total}$	$Q^{p.MS}_{corr}/Q^{total}_{corr}$
13-450*	1.23E+45	6.56E+47	1.18E+45	6.00E+47	4.20E+46	1.27E+48	3.89E+46	1.14E+48	10.81*	10.42*	49.32*	48.78*
20-450	8.76E+45	2.69E+48	8.26E+45	2.16E+48	1.67E+47	3.69E+48	1.53E+47	2.55E+48	17.12	14.77	17.93	17.70
23-500	1.52E+46	3.39E+48	1.43E+46	2.66E+48	2.70E+47	4.61E+48	2.88E+47	2.89E+48	12.37	10.49	18.03	17.73
26-350*	3.88E+46	5.36E+48	6.66E+46	3.59E+48	5.51E+47	5.74E+48	2.93E+48	3.82E+48	6.19*	3.00*	22.33*	17.95*
26-500	2.39E+46	4.31E+48	2.14E+46	3.25E+48	3.67E+47	6.03E+48	3.26E+47	3.74E+48	11.67	10.00	15.45	15.19
45-500	1.42E+47	9.95E+48	1.13E+47	6.02E+48	1.19E+48	1.34E+49	7.80E+47	6.67E+48	6.80	5.39	10.31	9.89
59-300	4.28E+47	1.77E+49	3.59E+47	8.49E+48	2.56E+48	2.32E+49	2.15E+48	9.21E+48	5.35	3.45	7.73	6.85
67-275	5.68E+47	2.26E+49	4.73E+47	9.86E+48	3.13E+48	3.21E+49	2.68E+48	1.10E+49	5.60	3.36	7.11	6.20
67-300	5.76E+47	2.19E+49	4.59E+47	1.07E+49	3.08E+48	3.20E+49	2.10E+48	1.31E+49	5.38	3.64	7.06	6.41
77-500	6.08E+47	2.27E+49	4.20E+47	1.04E+49	3.21E+48	3.25E+49	1.37E+48	1.25E+49	5.56	3.98	6.72	6.23
88-275	9.49E+47	2.93E+49	7.38E+47	1.09E+49	3.82E+48	3.20E+49	2.46E+48	1.14E+49	4.13	2.44	7.47	6.06
131-600	1.57E+48	3.93E+49	8.47E+47	1.07E+49	6.82E+48	5.07E+49	1.61E+48	1.15E+49	3.95	2.43	6.34	5.19
172-350	3.57E+48	7.22E+49	2.26E+48	1.23E+49	1.05E+49	7.66E+49	6.08E+48	1.37E+49	3.70	1.62	5.47	3.35
257-500	5.91E+48	1.02E+50	3.01E+48	9.82E+48	1.61E+49	1.13E+50	6.46E+48	1.12E+49	3.54	1.35	4.88	2.41

the coloured dots) is spent at $\log(T_{eff}/K) \approx 4.8..5.1$ even when the correction is applied.

The last four columns of Table 4.6 show how much more photons are emitted over the total lifetime of a model than during the main-sequence phase in the He II continuum. These columns serve to revise the estimate presented by Sz15 of the total ionization emitted by a stellar population in I Zw 18, which only took the main-sequence phase of these stars into account[2]. We include the correction for the wind optical depth, as this plays an important role during the post-main-sequence evolution of our models with optically thick winds. Using the same assumptions as Sz15 (a Salpeter initial mass function, a rotational velocity distribution where 20% of all massive stars evolve chemically homogeneously, a constant star formation rate of 0.1 $M_\odot$ yr^{-1} that lasts for 3 Myr and thus produces a total stellar mass of 300 000 $M_\odot$) but taking also the post-main-sequence phases into account with corrections for the wind optical depth, we get a total photon number rate of $1.42 \cdot 10^{50}$ s^{-1} in the He II continuum for a massive stellar population in I Zw 18. Although this photon rate matches the observed rate $Q^{obs}=1.3 \cdot 10^{50}$ s^{-1} within ten percent, we can now take a step further, as Kehrig et al. (2015b) also established the number of WC stars observed in I Zw 18.

4.6.1 The number of WC stars in I Zw 18

According to Kehrig et al. (2015b) who measured the luminosity of carbon emission lines in I Zw 18, the number of WC stars present in this galaxy is about 9. With the main-sequence models of Sz15, it was impossible to check the numbers of WC stars in a simulated population, as none of the models evolve to be a WC type star during core-hydrogen-burning. Including the post-main-sequece phases, however, makes it possible to predict the number of WC stars in our simulations.

Using the assumptions listed above, a 3 Myr long starburst that procudes a He II photon rate of $1.42 \cdot 10^{50}$ s^{-1} predicts only 2 WC stars. The reason for this is that in 3 Myr, only our very massive models reach the post-main-sequence phase (see column 7 of Table 4.3). This excludes the post-main-sequence evolution of our M_{ini}=45, 59 and 67 $M_\odot$ models, which could produce several WC stars (see their evolutionary behaviours in Fig. 4.11). To include these models, we did the same calculations for a starburst that lasts for 5.3 Myr (the lifetime of the M_{ini}=45 $M_\odot$ model). This way, we found a He II photon rate of $2.75 \cdot 10^{50}$ s^{-1} and 12 WC stars. These numbers are higher than observed, but note that the total mass of the simulated population is 530 000 $M_\odot$ in this case, which is clearly not realistic. There are several ways out, however, as there is no guarantee that the star formation rate was constant in the past. As a very simple estimate, if we assume a lower (constant) star formation rate than currently observed, say 0.06 $M_\odot$ yr^{-1} instead of 0.1 $M_\odot$ yr^{-1}, we get a 5.3 Myr old cluster with 300 000 $M_\odot$ total mass, a He II photon rate of $1.65 \cdot 10^{50}$ s^{-1} and 8 WC stars.

It will be a part of a future study to investigate how the star formation history shapes our predictions of the He II photon rate and the number of WC stars. These simple estimates above show, however, that our models are able to explain both the He II flux and the number of WC stars consistently, with some necessary assumptions about the star formation history. As discussed by Sz15 referring to the He II photon rate, several authors suggest that the very high He II photon rate observed in I Zw 18 means that there are hot, bright, He II-emitting,

[2] The photon rate estimation by Sz15 did not correct for the wind optical depth, resulting $1.6 \cdot 10^{50}$ s^{-1} in the He II continuum. However, their most massive models reach $\tau \sim 2..3$ during the last 70% of their main-sequence lifetimes. Correcting for the wind optical depth, the main-sequence phase of the models predicts a photon rate of $1.0 \cdot 10^{50}$ s^{-1}.

metal-free Pop III stars present in the galaxy (Heap et al., 2015; Kehrig et al., 2015b). According to our models, however, there is no need to assume the presence of Pop III stars in I Zw 18, as low-metallicity massive stellar evolution produces both TWUIN stars and WR stars, and is therefore able to explain the observed properties of this galaxy self-consistently.

Apart from the star formation history, there are two further uncertainties involved into the estimates given above. First, the ratio of homogeneously evolving stars to normally evolving stars has been assumed to be 20% (based on the measurements by Mokiem et al., 2006, of SMC massive stars). Since there is no observational statistics of the rotational velocity distribution of massive stars at the metallicity of I Zw 18, this ratio of TWUIN vs. normal stars is uncertain. Second, as discussed in Sect. 4.8, the mass-loss rate applied for these hot stellar models is also uncertain. Since mass-loss directly influences massive stellar evolution, the surface properties of the models and, consequently, the ionizing photon flux may change significantly if we use another mass-loss rate prescription. To demonstrate this, we apply an alternative mass-loss rate to compute the same set of models in Sect. 4.8, and show how the results differ (in Tables 4.12–4.14).

Our analysis only takes the fast rotating, chemically homogeneously evolving population of I Zw 18 into account when estimating the total flux emitted by this galaxy. Sz15 showed that, during their main-sequence lifetimes, the normally evolving stellar population do not provide a significant contribution to the total flux. As for their post-main-sequence lifetimes, we expect that the ionizing emission of the normally-evolving models is also not significant. Since they evolve to be cool supergiant stars (and do not become WR stars, as opposed to similar stars at solar metallicity) during their post-main-sequence lifetimes, their contribution to the total flux during this evolutionary phase is still negligible. Furthermore, close binary interaction may produce TWUIN stars as well. A population of TWUIN stars of binary origin may change the prediction of the total flux, and will be taken into account in a future study.

4.7 Explosions

In this section, we discuss the final fates that our low-metallicity massive stellar models undergo. We start the discussion with the models that are long-duration gamma-ray burst (lGRB) progenitors, then investigate the possibility of the magnetar-powered superluminous supernova (SLSN) production by some of our models. After this, we present the models that undergo pair-instability. Finally, we combine all this information and predict what kind of the explosion and remnant we expect from every model.

4.7.1 Gamma-ray bursts

Collapsars

If a stellar model forms an iron-core, nuclear fusion cannot maintain its hydrostatic stability anymore. The star collapses and falls in due to gravity. In case a neutron-star forms in the center, it is possible that the outer layers bounce back from the surface of the neutron star and produce a (core-collapse type) supernova explosion. In case, however, the core is compact enough to form a black hole directly, the supernova is said to 'fail' and the outer layers fall into the black hole (e.g. MacFadyen and Woosley, 1999). A 'failed' supernova may lead to the formation of a long-duration GRB if the progenitor star was rotating fast. This is called the collapsar scenario of the lGRBs.

Chemically-homogeneously evolving single stellar models have been proposed to be long-duration gamma-ray burst progenitors, since they may fulfill the collapsar criterion: their fast-rotating cores can retain significant amount of angular momentum until the moment of the collapse, so an accretion disc forms around the central black hole. This set-up, called a collapsar, is thought to lead to a lGRB explosion (Yoon and Langer, 2005; Woosley and Heger, 2006). To decide if a given stellar model is a collapsar progenitor or not, the angular momentum distribution of the stellar model needs to be compared to the critical angular momentum corresponding to the last stable orbit around a Kerr-black-hole (Yoon and Langer, 2005; Woosley and Heger, 2006). In case the angular momentum of the star is higher than that of the last stable orbit, an accretion-disc can be maintained after the core-collapse, and two jets, facilitating the gamma-ray production, can form. Our models in the mass-range of 13-133 $M_\odot$ fulfill the angular momentum criterion. This, however, does not necessarily mean that they all produce lGRBs, as discussed below.

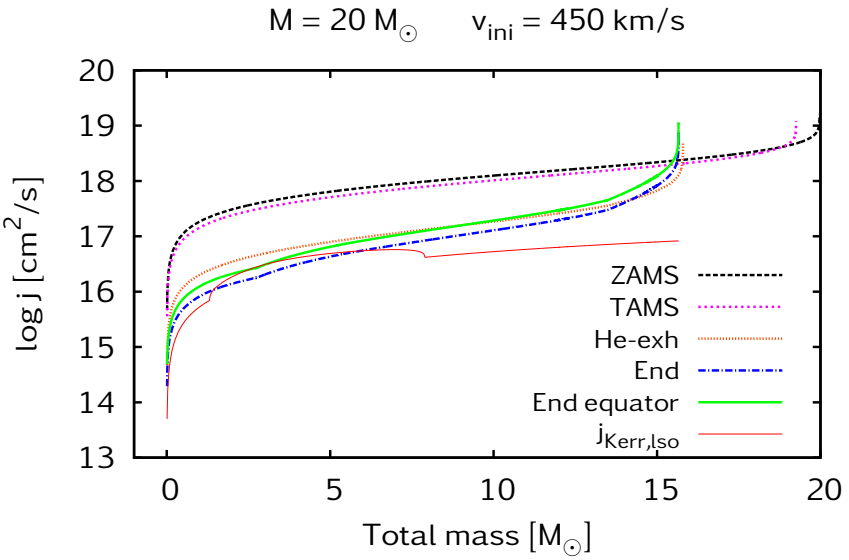

Figure 4.14. Distribution of the specific angular momentum inside the stellar model with M_{ini}=20 $M_\odot$ and v_{ini}=450 km s^{-1}. Models corresponding to four evolutionary stages are plotted: the zero-age main-sequence (ZAMS), the terminal-age main-sequence (TAMS), the end of core-helium-burning (He-exhaustion) and the end of the calculation at core-carbon-exhaustion (End). Since the model is not spherical due to fast rotation, and since the accretion disc supporting the collapsar-formation should form around the equator, the angular momentum at the equator is plotted for the end of the calculation (End equator). The specific angular momentum corresponding to the last stable orbit (lso) around a rotating Kerr-black-hole is represented by the line marked with $j_{Kerr,lso}$. This model fulfills the angular momentum constrain of the collapsar scenario, as significant parts of the stellar core retain enough angular momentum to form an accretion disc around the central black hole.

Fig. 4.14 shows the angular momentum distribution in the final model with an initial mass of 20 $M_\odot$. It does fulfill the above criterion: not only the material around the equator is above the critical limit, but most of the stellar model is. This model has a CO-core of 13.55 $M_\odot$ at the end of the computation, as seen in Fig. 4.15. The core contains a total angular mometum of $5.6{\cdot}10^{51}$ erg·s. The temperature in the core is $9.5{\cdot}10^{8}$ K, which means that there is carbon-burning going on. In the remaining time until the iron-core formation and core-collapse, which

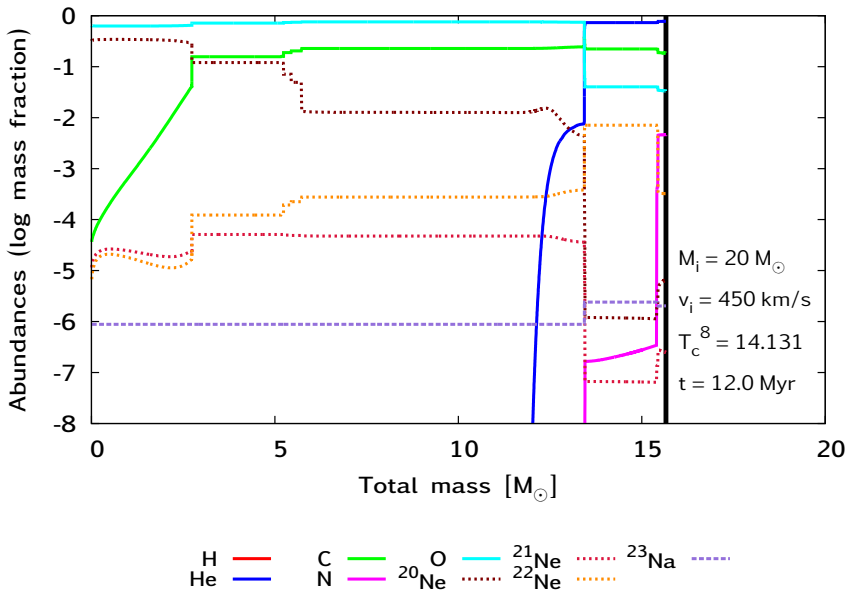

Figure 4.15. Composition of the last computed model of the sequence with M_{ini}=20 $M_\odot$ and v_{ini}=450 km s^{-1}. Isotopes of the elements indicated by the key legend are shown with coloured lines (except for hydrogen since the model is hydrogen-deficient at this late evolutionary stage). Vertical black line marks the surface. The core temperature is $1.4{\cdot}10^9$ K, and has exhausted from the core (see green line). The total mass of the CO-core is 13.55 $M_\odot$.

is around 3 yr, the mass-loss and the consequent angular momentum loss are 0.0009 $M_\odot$ and $3{\cdot}10^{49}$ erg·s, respectively (with the mass-loss rate of $3.05{\cdot}10^{-4}$ $M_\odot$ yr^{-1}, rotational velocity of 2582 km s^{-1} and radius of 0.62 $R_\odot$ in the last computed model, cf. Tables 4.1 and 4.3). Since the angular momentum to be lost until the iron core formation is not significant (two orders of magnitude lower than the total amount of angular momentum in the last computed model), the angular momentum distribution at the moment of the core-collapse can be fairly estimated by that at the onset of carbon-burning.

Our other models in the initial mass-range of 13-131 $M_\odot$ behave similarly to that shown in Figs. 4.14 and 4.15. Table 4.2 provides information on their rotational velocity and their total angular momentum at several evolutionary stages. We present the plots of their angular momentum distribution in Figs. 4.16–4.17. The models with initial masses of 13-131 $M_\odot$ all rotate faster than the critical limit for collapsar formation.

However, starting with the model of M_{ini}=59 $M_\odot$, some parts of the stellar core of our most massive models enter the regime of pair-instability. As we shall show in Sect. 4.7.4, the models in the initial mass range of M_{ini}=59 $M_\odot$–M_{ini}=77 $M_\odot$ are predicted to undergo pulsational pair-instability, which means that although they do eventually form an iron-core, they may lose their high angular momentum due to pulsation-induced mass-loss. As for the more massive models, they are predicted to explode as a pair-instability supernovae *before* a hydrostatic iron-core could even form. Therefore, the most massive collapsar progenitor amongst our models is the one with M_{ini}=45 $M_\odot$.

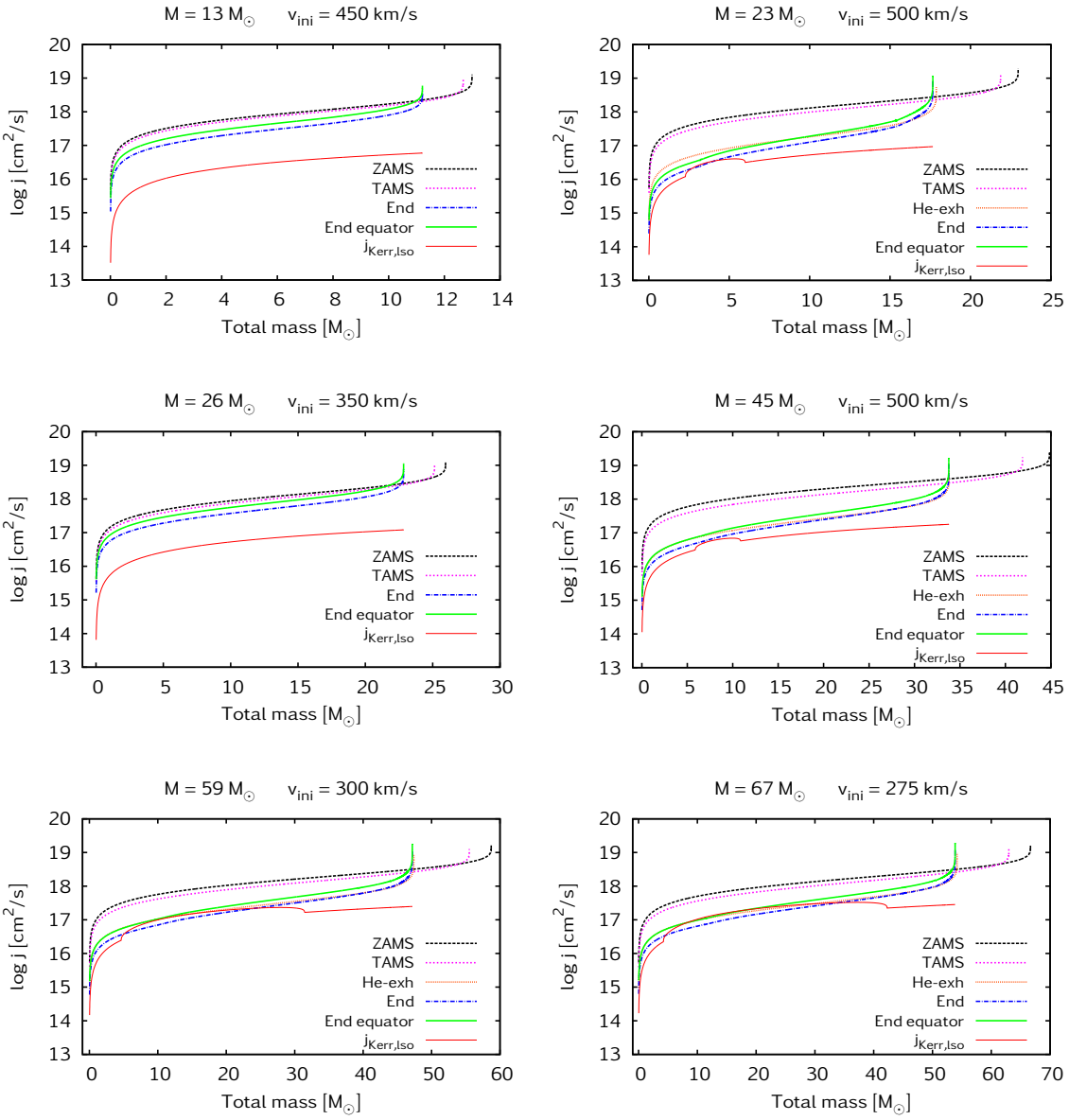

Figure 4.16. Distribution of the specific angular momentum inside the stellar models indicated by the title of every figure. Models corresponding to four evolutionary stages are plotted: the zero-age main-sequence (ZAMS), the terminal-age main-sequence (TAMS), the end of core-helium-burning (He-exhaustion) and the end of the calculation (End). Since the models are not spherical due to fast rotation, and since the accretion disc supporting the collapsar-formation should form around the equator, also the angular momentum at the equator is plotted for the end of the calculation (End equator). The specific angular momentum corresponding to the last stable orbit (lso) around a rotating Kerr-black-hole is represented by the line marked with $j_{Kerr,lso}$. For details, see Sect. 4.7.1.

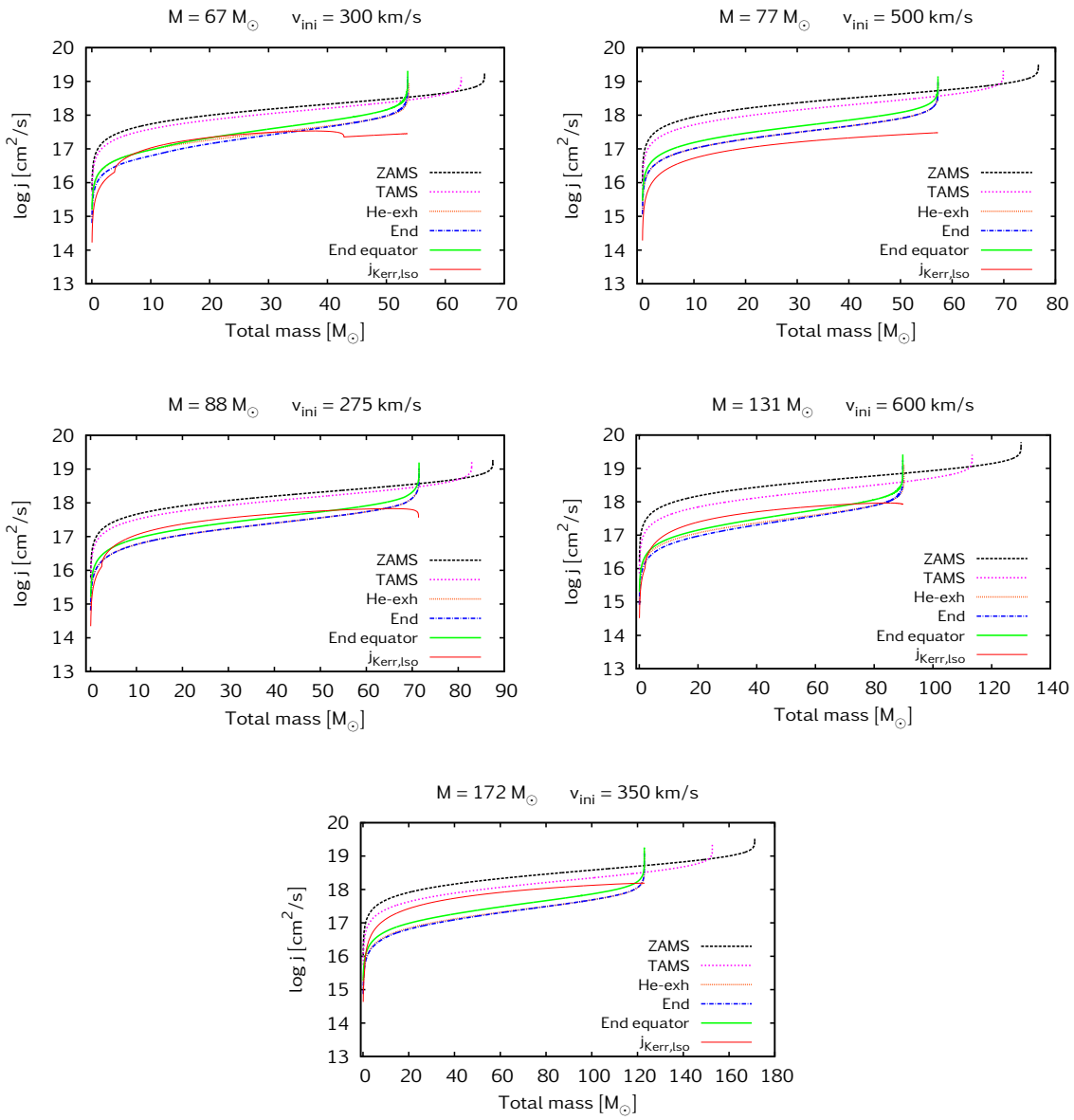

Figure 4.17. The same as Fig. 4.16, but for another models as indicated by the title of every figure.

Magnetars

Another promising scenario for the origin of long-duration GRBs is the proto-magnetar model. As opposed to the collapsar scenario where the central object is a black hole, the magnetar model supposes a fast rotating, magnetized proto-neutron-star as the powering engine of the jet (Metzger et al., 2011). For this to happen in our model, their supernova explosion should not 'fail', but produce a successful outgoing shock and a (rotating) neutron star in the center (MacFadyen and Woosley, 1999; MacFadyen et al., 2001). In the context of our models, it is possible that they form lGRBs via the proto-magnetar model.

It is not straightforward to decide whether our models destined to become 'failed' supernovae and collapsars, or successful supernovae and magnetars, since our simulations have been stopped before an iron-core formed. We will come back to this question in Sect. 4.7.3. It is indeed an important question, not necessarily from the point of view of lGRB formation (after all, both scenarios predict lGRBs), but from the point of view of superluminous supernovae, as explained below.

4.7.2 Superluminous supernovae

SLSNe are supernovae which are extremely bright compared to all other types of supernovae. While a regular supernova event typically have a peak luminosity of 10^{43} erg s^{-1}, SLSNe exceed the value of 10^{44} erg s^{-1} (Gal-Yam, 2012). Based on observational properties, three main types are identified amongst them: type II, type R and type I, from which the last two can be discussed in terms of our models as possible progenitors. SLSN type II, which have distinct features of a hydrogen-rich envelope, cannot be discussed in terms of our models. The reason for this is that our models have no hydrogen envelope, so the SLSN they would possibly produce would not show any trace of hydrogen.

In the case of SLSN type R, R stands for radioactive. During the expansion of the massive ejecta, the radioactive decay chain $^{56}Ni \rightarrow {}^{56}Co \rightarrow {}^{56}Fe$ deposits energy into the expanding material which converts it into optical radiation. The peak luminosity of the supernova lightcurve is proportional to the amount of radioactive ^{56}Ni available. After the peak, there is a 'tail' seen in the lightcurve, the steepness of which follows the theoretical decay rate of ^{56}Co. To power such a luminous event, about 5 $M_\odot$ of ^{56}Ni is needed, which have been shown theoretically to be produced by pair-instability induced explosions of very massive stars (Woosley et al., 2007; Quimby et al., 2013; Kozyreva et al., 2014; Gal-Yam, 2012). As some of our models undergo pair-instability, we will explore the possibility that they form SLSNe of type R in Sect. 4.7.4.

In the case of SLSN type I, the decline of the tail is substantially faster than implied from radioactive cobalt decay (Gal-Yam, 2012). It has been suggested that the type I lightcurve is the result of the interaction with expanding shells of hydrogen-free material ejected by the pulsational pair-instability; we discuss our models that undergo the pulsational pair-instability criterion in. Sect. 4.7.4. However, another promising model has been proposed, in which the lightcurve is powered by an internal engine: the spin-down of a magnetar.

Magnetar-powered SLSNe

Hydrogen-poor superluminous supernovae of type I (Quimby et al., 2013) occur preferentially in low-metallicity dwarf galaxies (Leloudas et al., 2015). While pair-instability explosions (Kozyreva et al., 2014) and massive circumstellar interactions (Moriya et al., 2013; Mackey

et al., 2014) have been proposed to explain some of these events, the magnetar-powered internal engine model (Thompson et al., 2004; Woosley, 2010) appears currently favoured (Kasen and Bildsten, 2010; Dessart et al., 2012; Inserra et al., 2013; Nicholl et al., 2013). In the magnetar scenario, the enormous luminosities as observed in SLSNe are produced by heating due to the spin-down of a millisecond magnetar, which deposits its rotational energy into the the explosion. Consequently, the progenitor stars need to produce extremely-rapidly-rotating iron cores. This condition is fulfilled by our TWUIN star models.

Inserra et al. (2013) gives a list of estimated magnetar initial spins for SLSNe (their Table 4). These values are typically a few milliseconds. Assuming a neutron star radius of 10 km, this spin corresponds to the specific angular momentum of ~1e15-1e16 cm^2 s^{-1}: the central part of the star becoming a neutron star (within ~1.4 $M_\odot$) needs to have this specific angular momentum. We list the specific angular momentum inside the inner 1.4 $M_\odot$ of our models in Table 4.2. As these values fall in the range required for millisecond magnetars, we expect that some of our TWUIN star models could also be considered as progenitors of SLSNe.

Although there are suggestions that accretion to black hole can power SLSNe (e.g. Dexter and Kasen, 2013), in the magnetar-powered scenario we need to keep a neutron star at the center to power SLSNe. Since we need to avoid making a black hole, our most massive model of M_{ini}=257 $M_\odot$, which has 166 $M_\odot$ at the end of its evolution, is clearly excluded as a candidate, no matter how high the angular momentum inside its innermost 1.4 $M_\odot$ is. The same is true for all of our very massive models as well. Given that the typical ejecta mass estimated for SLSNe is ~1-10 $M_\odot$ (see e.g. Table 3 of Nicholl et al., 2015), only our less massive models can be successful candidates. The model with M_{ini}=13 $M_\odot$, for example, has a total stellar mass of 11 $M_\odot$ at the end of our computation (at which point it is still burning helium in the core, the core helium mass fraction in the last computed model being 0.47; cf. Table 4.1). This model has a transparent wind during core-helium-burning (type TNE, as seen in Sect. 4.5), and a small mass-loss rate ($5{\cdot}10^{-7}$ $M_\odot$ yr^{-1}), so significant spin-down is not expected during the remaining evolution. This model is, based on the considerations above, a possible candidate for a magnetar-powered SLSN. Note that according to Sect. 4.7.1, this model was also a candidate for a lGRB. To decide which of these two explosions will happen, we need further considerations, as discussed in Sect. 4.7.3.

As for our other models that are not too massive, like the one with M_{ini}=20 $M_\odot$ with a total stellar mass of 15.7 $M_\odot$ at the end of carbon-burning, or the ones with M_{ini}=26 $M_\odot$ (Table 4.1), it is still feasible that a neutron star would form if there is enough material ejected, as suggested by Table 3 of Nicholl et al. (2015) in which ejecta masses as high as 14, 22 and even 31 $M_\odot$ are presented as well. (These high values, however, have very large error bars. Within these large error bars, even our models with as high initial mass as M_{ini}=77 $M_\odot$ would be possible candidates for a magnetar-powered SLSN. Given the large error bars in the observational ejecta values at this high mass, we do not consider models more massive than 30 $M_\odot$ as possible magnetar progenitors.)

4.7.3 SLSN or GRB?

As mentioned in Sect. 4.7.1, the question if our models produce failed or successful supernova explosions need to be decided in order to predict their final fates. Since magnetars are theorized to be the central engines of lGRBs as well as the power source behind some SLSNe, it is now crutial to decide if our models produce black holes directly after the core-collapse (and thus a lGRB in the collapsar scenario) or form rapidly rotating neutron stars (and thus a lGRB in the

proto-magnetar scenario or a magnetar-powered SLSN).

One way to decide if our stellar models are candidates for magnetars or for collapsars, is to look into the 'compactness' of the progenitor models in the moment of the core-collapse (O'Connor and Ott, 2011). The so-called compactness parameter is a dimensionless parameter that gives a robust prediction on the evolution of the model towards the black hole formation, i.e. whether it explodes as a supernova or fails. The systematics of supernova explosions were investigated as a function of the compactness parameter by O'Connor and Ott (2011) and Ugliano et al. (2012) who both found that a small value ($\lesssim$0.4) of the compactness parameter is needed for a successful explosion.

Although the compactness of the core is just one indicator, it might give us a valuable information on the final fate: if we expect a successful SN explosion based on the compactness, with the rotational rate of our models we are likely to produce a magnetar. If, on the other hand, the SN explosion seems to fail, we probably have a black hole formation and the collapsar scenario is likely to work.

For the proper calculation of the compactness parameter we would need to evolve our models until the iron-core collapse. However, we might still be able to make use of our models the following way. Sukhbold and Woosley (2014) recently investigated how the compactness parameter depends on the main-sequence masses, as well as on the CO-core masses of the progenitors. They found that for WR type stars and other stars that have no large hydrogen/helium-rich envelopes (such as our homogeneously evolving TWUIN stars) the CO-core mass is a sufficiently good indicator of the pre-supernova structure. According to their Fig. 27, which gives the compactness parameter as a function of the CO-core masses for low-metallicity stellar models, a star with a CO-core of 10 $M_{\odot}$ (such as our model with M_{ini}=13 $M_{\odot}$) has a compactness parameter of 0.5, while that with a CO-core of 13 $M_{\odot}$ (such as our model with M_{ini}=20 $M_{\odot}$) has a compactness parameter of 0.6, and that with a CO-core of 18 $M_{\odot}$ (such as our model with M_{ini}=26 $M_{\odot}$) has a compactness parameter of 0.4. Therefore, although quite arbitrarily given all the uncertainties concerning the connection between the CO-core mass and the compactness parameter as discussed by Sukhbold and Woosley (2014), we expect that our models with M_{ini}=26 $M_{\odot}$ form magnetars, while our models less massive and more massive than that form collapsars.

The collapsar formation leads to lGRB since the angular momentum of these models is high, as discussed in Sect. 4.7.1. As for the magnetar formation, some further considerations are needed. Whether we have a lGRB or a SLSN from magnetars depends on the magnetic field strength of the magnetar. If the initial magnetic field strength is more than ~1e15 G, the spin-down timescale is less than ~100 s and we can expect a lGRB. If it is ~1e14 G, we expect a SLSN because they need a continuous energy injection (~10 days). There are also suggestions that, in the intermediate magnetic field range, we may have both lGRB and SLSN (Metzger et al., 2015). Recently, one ultra-long GRB is found with a very luminous SN component (Greiner et al., 2015), and they suggest that both are powered by magnetars (although the SN component is not in the SLSN range, but it is still brighter than other SNe associated with lGRBs). Therefore, in case a magnetar is the central object, we cannot exclude the possibility of finding a lGRBs associated with a SLSN. Table 4.8 summarizes the theoretically predicted final fates and remnants for every one of our models.

4.7.4 Pair-instability

The upper mass limit for a collapsar or magnetar formation, and thus for the lGRB formation, can be determined by one of two conditions. One of these two conditions is that the progenitor needs to have high angular momentum to form an accretion disc. This condition was already seen to be fulfilled by our models in Sect. 4.7.1. The other condition is that, independently from the question of angular momentum, an iron-core needs to form. This second condition might be not fulfilled in the models that undergo pair-instability.

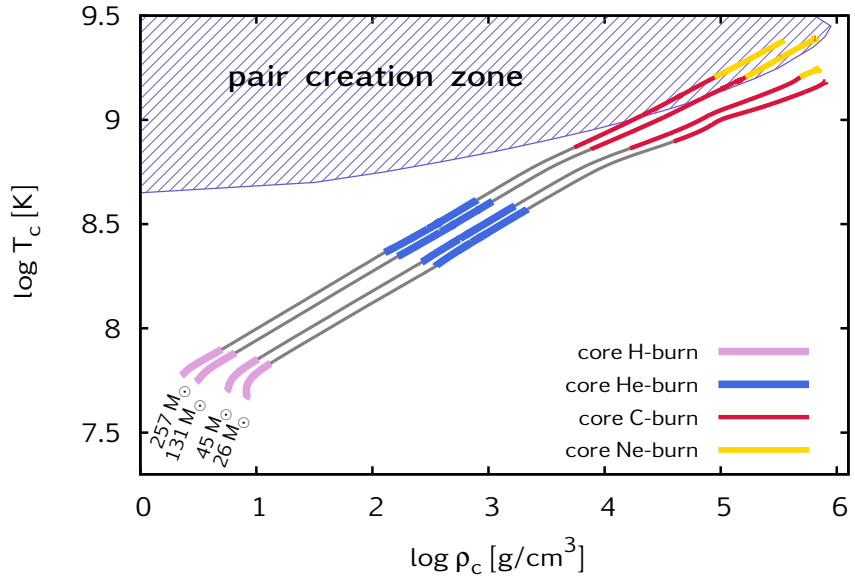

Figure 4.18. Central density vs. central temperature diagram for some of our models (initial masses indicated by the labels). Different burning stages are indicated by colours. Our most massive models enter the pair creation zone, i.e. their central layers become unstable. Cf. Table 4.7.

The cores of very massive stellar models at low-metallicity undergo pair-instability (Burbidge et al., 1957; Langer, 1991; Heger et al., 2003; Langer et al., 2007; Yoon et al., 2012; Kozyreva et al., 2014). At a certain temperature and density ($T \gtrsim 10^9$ K and $\rho \gtrsim 10^5$ g cm^{-3}, see the shaded area in Fig. 4.18), the photons released by the nuclear fusion create pairs of an electron and a positron. The number of photons therefore drops and the stability of the stellar model, maintained by the balance between its self-gravity and the radiation pressure of the photons, is compromized.

If the core is not stable anymore due to the pair-instability, one of the following three things can happen (Heger and Woosley, 2002; Woosley et al., 2007; Chatzopoulos and Wheeler, 2012).[3]

(1) *Direct fall-in.* In case of very massive cores (above a non-rotating helium-core mass of ~133 $M_\odot$), the star collapses directly into a black hole without an explosion.

(2) *PISN explosion.* In case of less massive cores, the collapse would be stopped and reversed by the nuclear energy release of explosive oxygen burning. In this case, a pair-instability supernova (PISN) event would happen, which disrupts the whole star leaving no remnant. The

[3] The helium-core mass limits given here were established by Heger and Woosley (2002) for non-rotating models, but note that all the values given above were confirmed by the oxygen-core mass of rotating, homogeneously evolving, metal-free and mass-loss-free models of Chatzopoulos and Wheeler (2012).

brightness of such a supernova depends strongly on the amount of nickel synthesized (Herzig et al., 1990; Dessart et al., 2013), but according to the deep analysis of PISN lightcurves by Kasen et al. (2011), some PISNe should be observable out to large distances.

(3) *Pulsational PISN explosion.* For even less massive cores (below a helium-core mass of ~64 $M_\odot$) the instability results in violent pulsations, not in a complete disruption. As a consequence of the pulsations, the star expels some of its outer layers and thus regains its stability and continues its hydrostatic evolution until an iron-core forms. The expelled layers may collide with each other and thus produce a so called pulsational pair-instability supernova (pPISN, Woosley et al., 2007). As discussed by Sukhbold and Woosley (2016), the collisions of the layers expelled by stars in the mass range $M^{\text{He-core}}$=50–55 $M_\odot$ might produce luminosities as high as 10^{44} erg s^{-1}, but for lower and higher masses, the resulting event is predicted to be quite faint and probably not observable.

If the PISN disrupts the star right after oxygen burning, an iron core never forms, so neither a collapsar, nor a magnetar can form, and a lGRB never happens. In case, however, if one or more pulsational pair-instability events take place, the evolution might proceed to an iron core formation, so a collapsar or magnetar might still form. The actual outcome of this type of evolution would depend strongly on how much mass is lost during the pulsations, and if the remaining angular momentum in the iron-core is still enough to form a fast rotating central object. The possibility of a scenario in which a pPISN is followed by a lGRB needs to be investigated in the future with simulations of such a model, as well as with observational evidences for a SN event followed by a lGRB in about 10 years (cf. the caption of Fig. 2 of Woosley et al., 2007). If the model spins down considerably during the pulsations, then supernovae of type Ib or Ic (that is, core-collapse supernovae coming from compact stars with no hydrogen- or helium-rich envelope, respectively) are expected from these models.

Our models with M_{ini}>50 $M_\odot$ have some parts (not necessarily the center) that enters the instability region. Table 4.7 lists their core temperatures and core densities.

The model with M_{ini}=257 $M_\odot$

We resolved the post-helium-burning evolution of one of our very massive models with refined timesteps. This model with M_{ini}=257 $M_\odot$ is presented here.

Fig. 4.19 shows the part of the model with M_{ini}=257 $M_\odot$ that entered the instability zone. In the last computed model, 76% of all the stellar mass is effected. As a result, the model is collapsing with a total kinetic energy of $4.15{\cdot}10^{51}$ erg, cf. Fig. 4.20.

The top panel in Fig. 4.20 shows the infall velocity of several mass shells of the stellar model. The bottom panel shows the time evolution of the radius for the same shells. In the last computed model, the total stellar mass (166 $M_\odot$) is confined inside a radius of 2.9 $R_\odot$, while 90% of all mass is confined inside a small region with the size of 0.2 $R_\odot$. The gravitational potential energy of the star is, therefore, very high, $3.86{\cdot}10^{53}$ erg.

As seen before in Fig. 4.3, this model is spinning up at the end of our computation. However, according to Fig 4.21, its specific angular momentum distribution is one order of magnitude lower than that needed for the accretion disc around the central object. This model therefore does not fulfill the collapsar scenario (cf. Sect. 4.7.1). Moreover, its total rotational energy is only $2{\cdot}10^{50}$ erg, three orders of magnitude lower than its total gravitational potential energy. Thus, rotation has an effectively insignificant contribution to the collapse in this case.

In the last computed model, the core temperature is $26.1{\cdot}10^8$ K. At this temperature, neon burning occurs, as seen in Fig. 4.22: the abundance of the ^{20}Ne isotope is decreasing towards

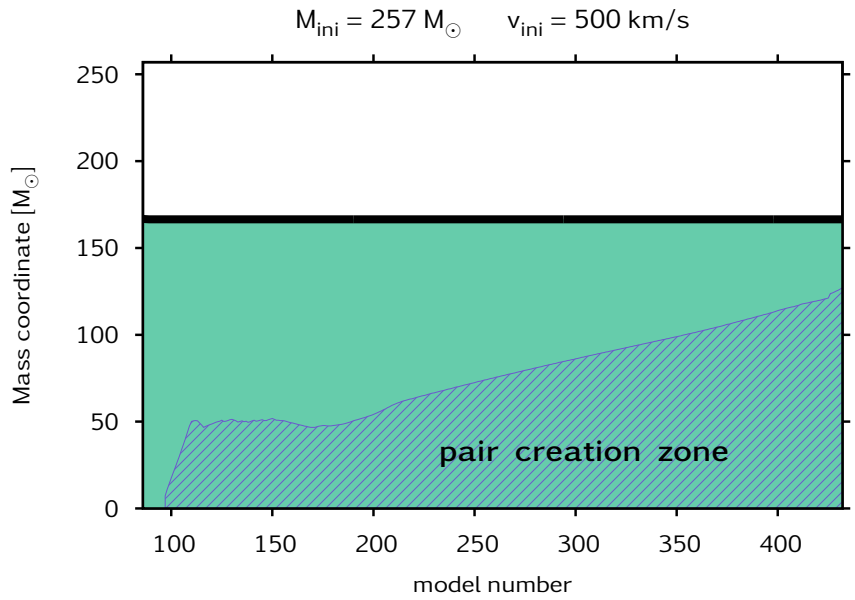

Figure 4.19. Pair-instability in the model with M_{ini}=257 $M_\odot$ and v_{ini}=500 km s^{-1}. The thick black line marks the surface of the star. The X-axis is analogous to time between core-helium-exhaustion (which happens at 2.236 Myr) and the end of the computation, with the later phases stretched to show how the pair-instability region, marked by the blue dashed region, evolves. In the last computed model, 76% of the total mass is effected by the pair-instability.

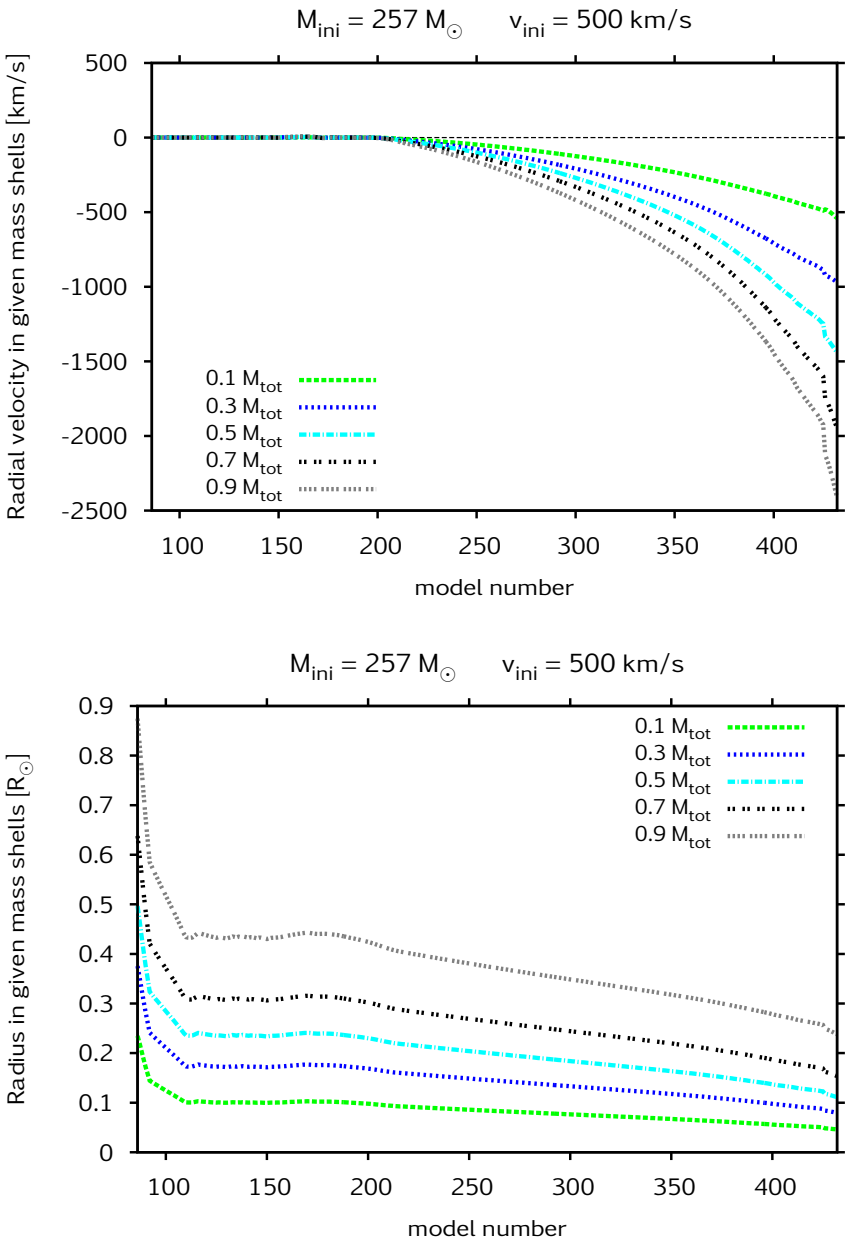

Figure 4.20. Velocities and radii versus time (represented by the model number, which is analogous to time between core-helium-exhaustion and the end of the computation) for selected mass zones (see the key legend) in the model with M_{ini}=257 $M_{\odot}$ and v_{ini}=500 km s^{-1}.

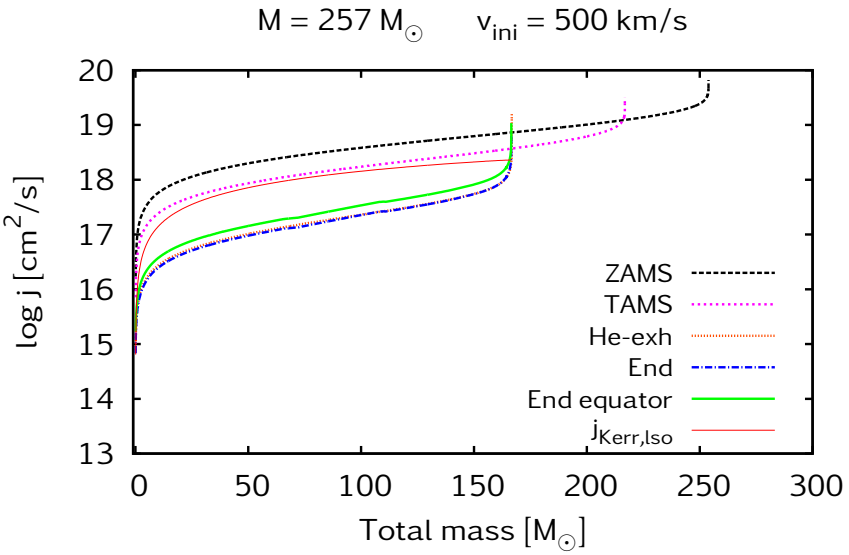

Figure 4.21. Distribution of the specific angular momentum inside the stellar model with M_{ini}=257 $M_\odot$ and v_{ini}=500 km s^{-1}. Models corresponding to four evolutionary stages are plotted: the zero-age main-sequence (ZAMS), the terminal-age main-sequence (TAMS), the end of core-helium-burning (He-exhaustion) and the end of the calculation (End). Since the model is not spherical due to fast rotation, and since the accretion disc supporting the collapsar-formation should form around the equator, the angular momentum at the equator is plotted for the end of the calculation (End equator). The specific angular momentum corresponding to the last stable orbit (lso) around a rotating Kerr-black-hole is represented by the line marked with $j_{Kerr,lso}$. This model does not fulfill the angular momentum constrain of the collapsar scenario, as the star does not keep enough angular momentum to form an accretion disc around the central black hole.

Table 4.7. *Energetics of the last computed models.* Only models that are found to undergo pair-instability are listed, i.e. those that are less massive than 40 $M_\odot$ at the end of our computations, as well as those that have not evolved until core-carbon-exhaustion, are not listed. The maximum temperature and the maximum density in the core of the last computed model of the sequences listed in columns 1-2 are given in columns 3 and 4. Column 5 gives the percentage of the total mass that is influenced by the instability in the last computed model (cf. Fig. 4.19). Columns 6-14 have the following meaning. E_{grav}: gravitational potential energy. E_{rot}: rotational kinetic energy. E_{therm}: thermal energy inside the stellar model. E_{kin}: kinetic energy along radial directions (not taking rotational kinetic energy into account). E_{total}: total energy of the stellar model, calculated as $E_{therm}-E_{grav}+E_{rot}-E_{kin}$. $E_{^{16}O}$: estimated nuclear energy release in case all the ^{16}O inside the model is burned explosively. $E_{^{12}C}$, $E_{^{20}Ne}$: same for ^{12}C and for ^{20}Ne.

M_{ini} [$M_\odot$]	v_{ini} [km s^{-1}]	T_c^{max} [10^8 K]	ρ_c^{max} [log g cm^{-3}]	unstable	E_{grav} [erg]	E_{rot} [erg]	E_{therm} [erg]	E_{kin} [erg]	E_{total} [erg]	$E_{^{16}O}$ [erg]	$E_{^{12}C}$ [erg]	$E_{^{20}Ne}$ [erg]
59	300	18.79	5.81	34%	4.00e+52	1.87e+50	3.51e+52	5.29e+42	-4.71e+51	1.18e+52	9.31e+50	9.10e+50
67	275	19.58	5.81	41%	5.04e+52	2.11e+50	4.50e+52	1.84e+41	-5.19e+51	1.36e+52	9.99e+50	1.07e+51
67	300	20.21	5.92	40%	5.00e+52	2.03e+50	4.46e+52	8.38e+43	-5.20e+51	1.36e+52	9.98e+50	1.03e+51
131	600	24.74	5.82	69%	1.43e+53	3.81e+50	1.36e+53	3.82e+50	-7.00e+51	2.32e+52	1.40e+51	1.81e+51
172	350	14.00	4.87	31%	1.28e+53	9.51e+49	1.18e+53	4.00e+43	-9.90e+51	3.15e+52	1.84e+51	3.23e+51
257	500	26.11	5.55	76%	3.86e+53	2.06e+50	3.75e+53	4.15e+51	-1.49e+52	4.26e+52	1.78e+51	4.33e+51

the innermost layers. Oxygen has just ignited and has not burned in significant amount to make a visible effect in Fig. 4.22. The figure also shows that this model consists almost entirely of oxygen (while the surface consists of oxygen, carbon, and some helium, cf. Sect. 4.5.2). The total oxygen-mass (^{16}O) of this model is 129 $M_\odot$.

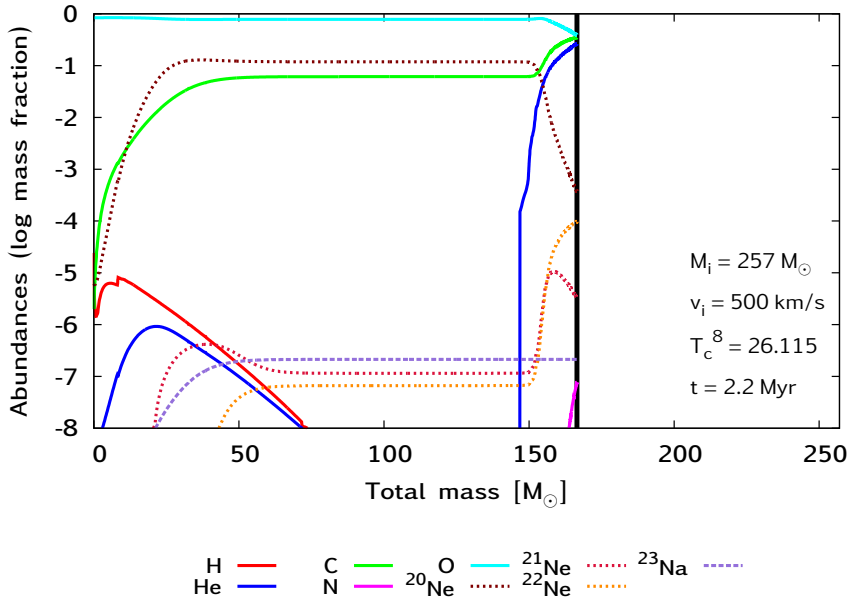

Figure 4.22. Composition of the last computed model of the sequence with M_{ini}=257 $M_\odot$ and v_{ini}=500 km s^{-1}. Isotopes of the elements indicated by the key legend are shown with coloured lines. Vertical black line marks the surface. The core temperature is $2.6{\cdot}10^9$ K, and there is neon burning in the core (see the brown dotted line representing ^{20}Ne). The total mass of the CO-core (which is practically the total mass of the star) is 166 $M_\odot$. The total mass of the ^{16}O isotope in this model is 129 $M_\odot$.

Our simulation stops here. However, as the infall continues, the core would reach even higher temperatures and oxygen would burn. If all the oxygen that is available burns explosively, this would produce a total nuclear energy release of, approximately, $4.26{\cdot}10^{52}$ erg. (The nuclear energy release by burning the remaining carbon and neon are approximately $1.7{\cdot}10^{51}$ erg and $3{\cdot}10^{51}$ erg, respectively.) In the meantime, the total binding energy of the star would grow due to the infall.

Based on the current stage of our computation, it is not possible to predict how exactly this model will end its life. In case the nuclear energy that is released during the explosive oxygen burning is enough to overcome the actual binding energy of the collapsing star at any point during the remaining evolution, then the collapse might be stopped and reversed. In this case, a pair-instability supernova is produced, that disrupts the star entirely leaving no remant. On the other hand, if the star becomes too bound – so that the nuclear energy release is not enough to overcome all its gravitational potential energy at this evolutionary phase when the star is very compact –, then the collapse will continue and a black hole of about 166 $M_\odot$ will form.

Previous simulations of pair-instable stellar models Heger and Woosley (2002) showed that in case of metal-free, non-rotating models, the mass of the helium-core needs to be between $64 \lesssim M^{He-core}/M_\odot \lesssim 133$ for a PISN event to happen (while for helium-core masses of $40 \lesssim M^{He-core}/M_\odot \lesssim 64$, a pulsational PISN event happens). Note that the models of Heger

and Woosley (2002) were initially metal-free (and therefore have been computed omitting mass-loss), while our models have low-metallicity and mass-loss is included, which means that our models are less massive at the onset of the pair-instability than those of Heger and Woosley (2002) with the same helium-core mass. Chatzopoulos and Wheeler (2012) studied the oxygen-core mass of rotating, homogeneously evolving, metal-free and mass-loss-free models, and their results confirm the mass limits given by Heger and Woosley (2002). Based on these limits, we expect that our model with M_{ini}=257 $M_\odot$, which has a helium-core of $M_{TAMS}^{He-core}$=218 $M_\odot$ and a still very high CO-core mass of 167 $M_\odot$, will fall into a black hole without an explosion.

Other models entering the pair-instability zone

Apart from the model with M_{ini}=257 $M_\odot$ presented above, the cores of some of our very massive models also enter the pair-instability regions, as Table 4.7 shows. These models have also just started to collapse when our computation ended. To predict their final fates, we would need to follow their evolution throughout the whole collapse, which falls outside the scope of the current study. Relying on the helium-core mass-limits of Heger and Woosley (2002) again, and taking the contribution of the mass-loss at our finite metallicity into account with comparing their CO-core masses to the helium-core masses of the metal-free models, our models between initial masses of M_{ini}=59 $M_\odot$–M_{ini}=77 $M_\odot$ would produce pPISN, and those between M_{ini}=88 $M_\odot$–M_{ini}=172 $M_\odot$ would produce PISN, while our most massive model, the one with M_{ini}=257 $M_\odot$ presented above, would fall into a black hole directly (cf. Tables 4.1 and 4.8).

4.7.5 The predicted final fates

Table 4.8 summarizes our models and their predicted final fates and remnants. The models less massive than M_{ini}=50 $M_\odot$ avoid the pair-instability, and thus they will develop a fast-rotating iron-core. In case the supernova is successful (cf. Sect. 4.7.3), a magnetar might form that can power a superluminous supernova explosion or a long-duration gamma-ray burst. In case the supernova fails, the collapsar scenario is possible to happen, and the outcome is a long-duration gamma-ray burst.

The models more massive than M_{ini}=50 $M_\odot$ become pair-instable. Based on their core masses, they either produce a pair-instability supernova or a pulsational pair-instability supernova. As discussed in Sect. 4.7.4, the observational properties of such supernovae depend strongly on the detailed evolutionary properties of the progenitors, as well as on the atmospheric properties of the exploding model (including the interaction with pulsationally ejected layers). Thus, predicting the type of event they likely produce falls outside the scope of current work. Nonetheless, PISNe and pPISNe have been proposed to be responsible for some of the superluminous supernovae observed (Woosley et al., 2007; Quimby et al., 2013; Kozyreva et al., 2014; Gal-Yam, 2012, but cf. Sect. 4.7.2). Recently, Sukhbold and Woosley (2016) predicted that models in the narrow helium-core mass range of 50-55 $M_\odot$ are likely to account for superluminous supernova explosions via pulsational pair-instability, which might make our models with M_{ini}=67 $M_\odot$ (with CO-core masses of 50.6–52.7 $M_\odot$) potential SLSN progenitors in the pPISN scenario. However, further investigations are needed in the direction of simulating the post-carbon-burning evolution and the explosion of our models in order to draw a line between them and any observed supernova.

Table 4.8. *Final fate predictions.* Columns 1 and 2 lists the models' initial parameters, column 3 shows the mass of the CO-core at core-helium-exhaustion. In case the model has not reached this phase, the He-core size at the TAMS is given in column 3 (marked by asterisk, cf. Table 4.1). Column 4 and 5 give the final fate predictions and the type of remnant, respectively. For the discussion of the collapsar scenario, see Sect. 4.7.1, for the magnetar scenario, see Sects. 4.7.1 and 4.7.2. For the explanation of the PISN and pPISN events, see Sect. 4.7.4.

M_{ini} [$M_\odot$]	v_{ini} [km s^{-1}]	$M_{He\text{-}exh}^{CO\text{-}core}$ [$M_\odot$]	theoretical scenario (observable event)	remnant
13	450	12.7*	collapsar (lGRB)	black hole
20	450	13.4	collapsar (lGRB)	black hole
23	500	15.4	collapsar (lGRB)	black hole
26	350	25.1*	magnetar (SLSN type I and/or lGRB)	neutron star
26	500	17.6	magnetar (SLSN type I and/or lGRB)	neutron star
45	500	32.5	collapsar (lGRB)	black hole
59	300	44.1	pPISN	black hole
67	275	50.6	pPISN	black hole
67	300	52.7	pPISN	black hole
77	500	56.0	pPISN	black hole
88	275	68.0	PISN	no remnant
131	600	87.4	PISN	no remnant
172	350	122.2	PISN	no remnant
257	500	166.8	direct fall-in	black hole

4.8 An alternative set of models

The mass-loss rates of WR stars are, despite many efforts, not well known. On one hand, this is due to the rarity of observable WR stars and, on the other hand, due to the extreme physical conditions in their atmospheres (Lamers and Cassinelli, 1999). Moreover, the mass-loss rates of TWUIN stars are not known at all, since these objects are, at this point, only theoretical predictions. However, mass-loss can have crucial influences on the evolution of a massive stellar model: the more mass is removed, the less massive the model is in the next timestep of the simulation; and a less massive model may evolve differently.

Here we present an alternative set of models, which is compared to the original set of models presented above. The only difference between the original and the alternative set of models is the mass-loss rate prescription. The original set of models is computed using the mass-loss rate prescription of Hamann et al. (1995, with some modifications, as explained in Sect. 4.2). The alternative set of models is computed with an additional mass-loss-enhancement as follows.

When the sum of the carbon, nitrogen and oxygen mass fractions, Z_{CNO}, at the surface exceeds the initial metal abundances, Z_{metal}, the mass loss rate is enhanced with a factor that scales linearly with Z_{CNO} (Yoon et al., 2006) according to the following expression:

$$\dot{M}_{\rm enh} = \dot{M} \cdot \left(1 + 19 \frac{Z_{CNO} - Z_{metal}}{1 - Z_{metal}}\right) \tag{4.5}$$

where $\dot{M}$ is the mass-loss rate given by Eq. 4.1. The condition Z_{CNO}>Z_{metal} requires a very efficient mixing (so the nuclear burning products can be mixed between the core and the surface), and is fulfilled in our models during core-helium-burning. The physical motivation of this additional increase is that it takes the effect of the CNO enhancement at the surface into consideration. According to Vink and Koter (2005), at very low metallicity, optically thick lines due to carbon, nitrogen and oxygen at the surface may gain relative importance over the contribution of optically thin iron lines.

However, the linear approach in Eq. 4.5 to take the CNO-enhancement of the surface into account is overestimating the mass-loss (Yoon, 2015 – private communication). Thus, this mass-loss enhancement is not implemented into our original set of models discussed in Sects. 4.2–4.7. It is nonetheless worth to investigate how our models would evolve if this mass-loss enhancement were used for the following reasons. The models presented by Yoon et al. (2006) were computed with this additional enhancement (Szécsi et al., 2014). To be consistent with past results, therefore, computing models with the same physical assumptions is beneficial.

Additionally, computing our models with this alternative mass-loss rate is not only useful in terms of consistency with previous results, but also since it is a straightforward way to test the effects of using high mass-loss rates on our models. Although we expect that it is our original set of models that fits to reality, it is of academic interest to discuss alternative theories, especially when it comes to such an uncertain physical ingredient as the mass-loss. In this section, therefore, we provide the same analysis as before, but for the alternative set of models, that is, models computed with the mass-loss enhancement described by Eq. 4.5.

Fig. 4.23 shows the HR diagram of the alternative models, and Figs. 4.24-4.37 present the same plots as before, but for the alternative models – with the captions noting the differences to the original models.

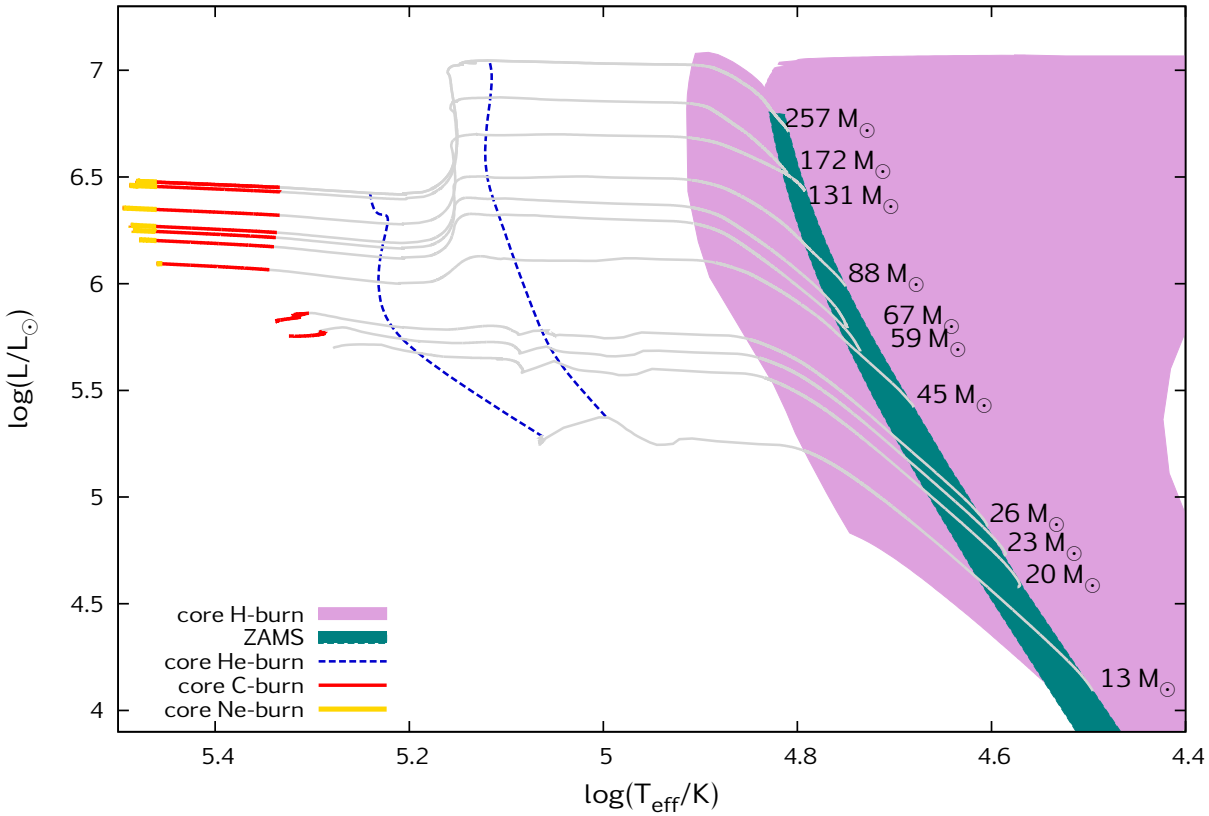

Figure 4.23. Same as Fig. 4.1, but for the alternative set of models. The higher mass-loss rate in this alternative set makes our most massive models lose more than twice as much mass as in the original set. Therefore, their surface luminosity drops (at around $\log(T_{eff}/K)\sim5.17$) and they continue their evolution with this lower luminosity of $\log(L/L_{\odot})\sim6.2$–6.5 (as opposed to $\log(L/L_{\odot})\sim6.3$–7 in the case of the original set of models). On the other hand, they evolve to higher T_{eff} than the original set, reaching $\log(T_{eff}/K)$ values as high as 5.49 (309 kK).

Table 4.9. *Masses at different evolutionary stages.* Same as Table 4.1 but for the alternative set of models. While the ratio of the mass lost during the post-main-sequence to the mass at the TAMS varies between 10% and 24% in the original models, that in the alternative models varies between 14 and 75%.

M_{ini} [$M_\odot$]	v_{ini} [km s^{-1}]	$M_{TAMS}^{He\text{-}core}$	$M_{He\text{-}exh}^{total}$	$M_{He\text{-}exh}^{CO\text{-}core}$	$M_{C\text{-}exh}^{total}$	M_{End}	evolved until
13	450	12.7	-	-	-	11.2	YB
20	450	19.3	15.5	13.1	-	15.2	CB
23	500	21.9	17.1	14.9	16.8	16.8	CE
26	350	25.1	19.7	17.9	19.4	19.4	NB
26	500	24.7	18.7	16.6	18.4	18.4	NB
45	500	41.9	26.5	25.6	25.6	25.6	NB
59	300	55.7	32.5	31.2	31.2	31.2	NB
67	275	63.2	35.3	33.9	33.9	33.9	NB
67	300	63.0	54.6	52.7	-	53.6	CB
77	500	70.1	57.9	56.0	56.8	56.8	NB
88	275	83.0	70.4	68.0	69.4	69.4	CE
131	600	113.9	43.5	41.5	41.5	41.5	NB
172	350	153.6	54.5	51.5	54.5	51.5	NB
257	500	218.1	57.0	53.7	56.9	53.7	NB

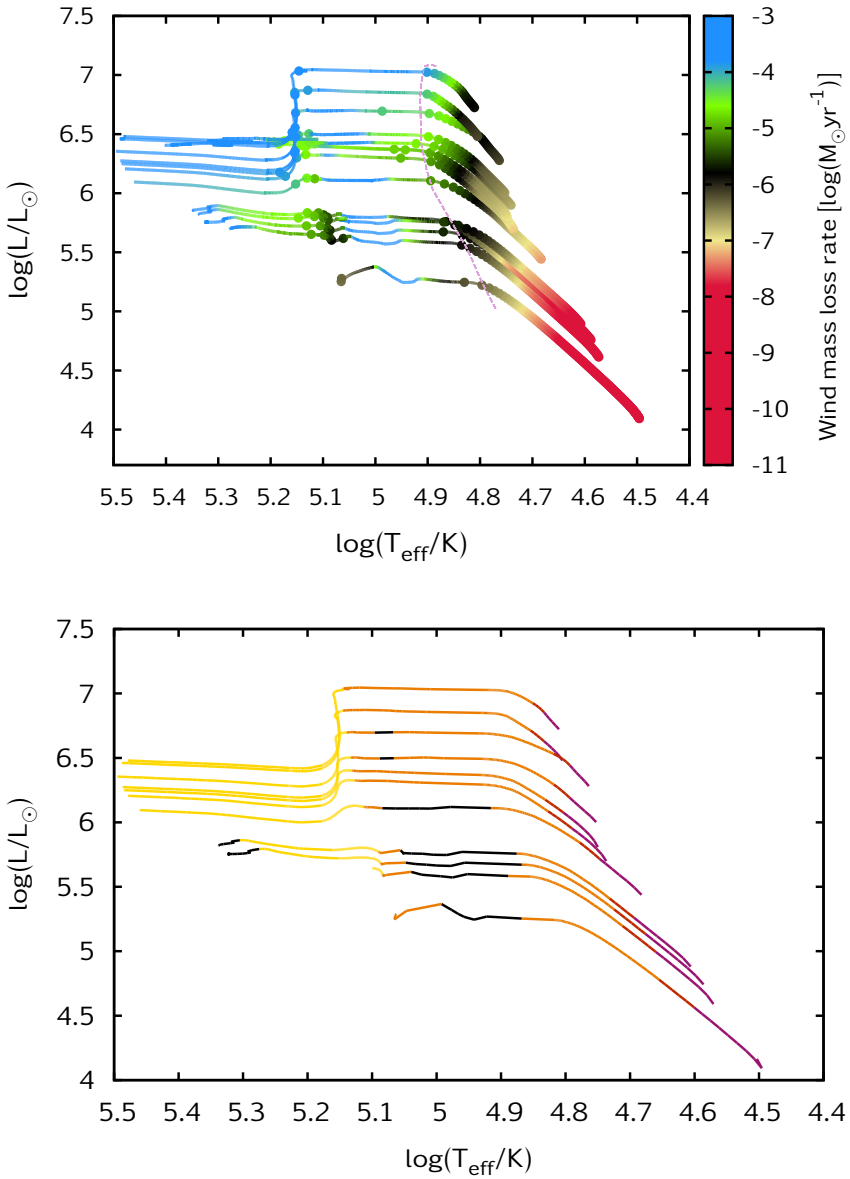

Figure 4.24. Same as Fig. 4.2 but for the alternative set of models. In the bottom figure, yellow lines mark the alternative mass-loss prescription. This prescription leads to higher mass-loss rates during core-helium-burning, especially during the second half of the core-helium-burning lifetime, as explained in the caption of Fig. 4.25.

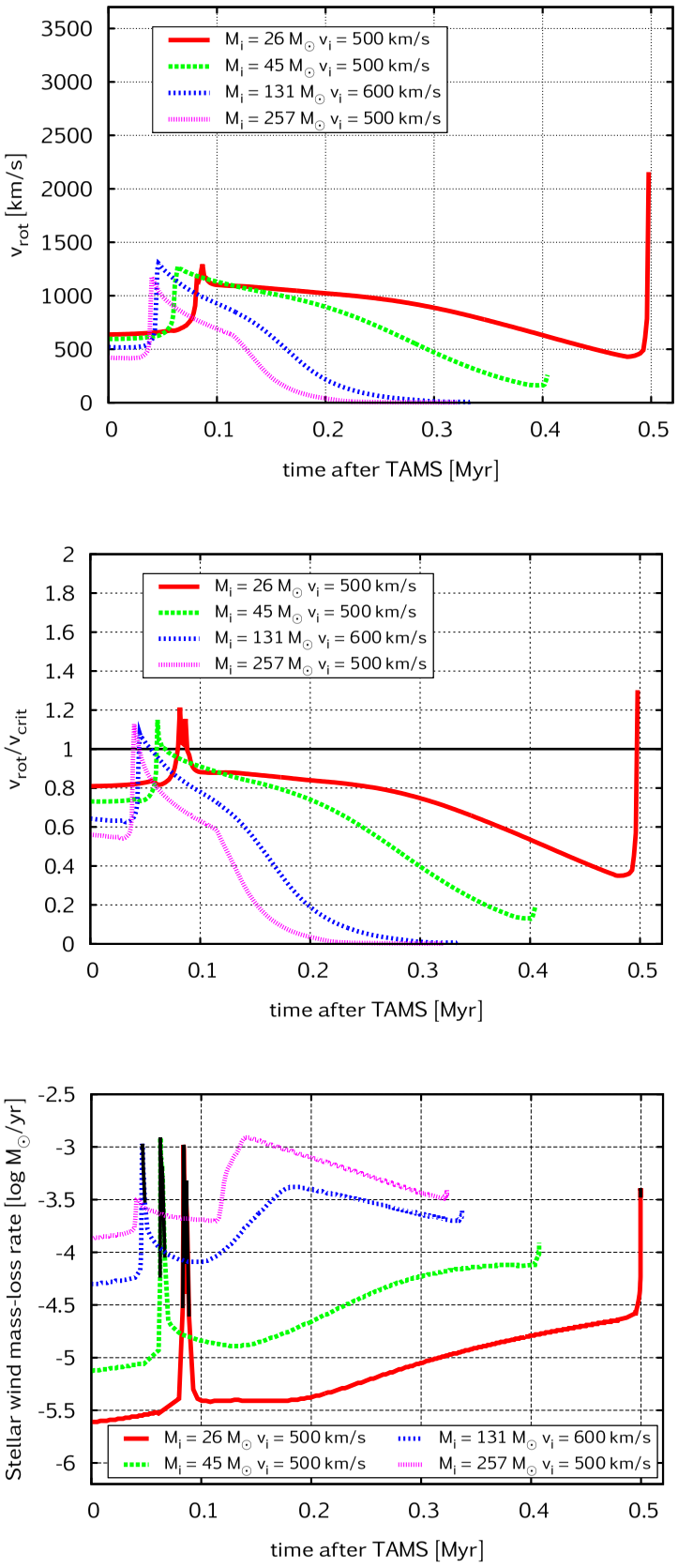

Figure 4.25. Same as Fig. 4.3 but for the alternative set of models. The time-evolution of the rotational velocity starts to differ significantly in the second half of the core-helium-burning lifetime of the alternative models. This is because at this point, the surface enhancement of carbon, nitrogen and oxygen, which drives the alternative mass-loss, becomes significant. As a result, the models start to lose mass in a very rapid process: the more deep layers are exposed, the higher the C, N and O abundances in the surface and, therefore, the higher the mass-loss rate, which in turn exposes even deeper layers, and so on. The most massive models spin down to almost zero due to this enhanced mass-loss, and even the less massive models finish their evolution with lower rotational velocity then those in the original set. However, the models in the initial mass-range of 13-26 $M_\odot$ still rotate fast at the end of their evolutions so that a collapsar or a magnetar can be produced.

Table 4.10. *Rotation and angular momentum.* Same as Table 4.2 but for the alternative set of models. The models in the initial mass-range of 13-26 $M_\odot$ still keep rotating fast at the end of their core-carbon-burning lifetimes so they are still possible progenitors of lGRBs in the collapsar scenario or SLSNe in the magnetar scenario (cf. the original models in Sect. 4.7.3).

M_{ini}	v_{ini}	v_{TAMS}	$v_{He\text{-}exh}$	$v_{C\text{-}exh}$	v_{End}	J_{TAMS}	$J_{He\text{-}exh}$	J_{End}	$\bar{j}^{3M_\odot}_{End}$	$\bar{j}^{1.4M_\odot}_{End}$	$\bar{j}^{CO\text{-}core}_{End}$
$[M_\odot]$	$[km\ s^{-1}]$	$[km\ s^{-1}]$	$[km\ s^{-1}]$	$[km\ s^{-1}]$	$[km\ s^{-1}]$	$[erg\ s^{-1}]$	$[erg\ s^{-1}]$	$[erg\ s^{-1}]$	$[erg\ s^{-1}]$	$[cm^2\ s^{-1}]$	$[cm^2\ s^{-1}]$
13	450	620	-	-	739	2.6e+52	-	8.6e+51	8.5e+16	4.7e+16	-
20	450	612	622	-	1573	4.9e+52	7.4e+51	5.4e+51	2.1e+16	1.1e+16	1.1e+17
23	500	645	520	2202	2471	6.2e+52	7.3e+51	5.8e+51	1.3e+16	6.8e+15	1.3e+17
26	350	482	435	2023	2223	6.1e+52	7.5e+51	6.2e+51	1.2e+16	6.5e+15	1.2e+17
26	500	637	440	2032	2157	7.4e+52	7.1e+51	5.9e+51	1.2e+16	6.5e+15	1.4e+17
45	500	596	162	529	610	1.6e+53	4.3e+51	3.3e+51	5.5e+15	2.9e+15	6.6e+16
59	300	392	77	222	255	1.7e+53	2.8e+51	2.1e+51	2.6e+15	1.5e+15	3.3e+16
67	275	360	56	151	175	1.8e+53	2.3e+51	1.7e+51	2.0e+15	1.1e+15	2.5e+16
67	300	385	715	-	2018	1.9e+53	5.0e+52	3.7e+52	1.6e+16	8.9e+15	3.2e+17
77	500	546	711	3653	3572	3.1e+53	5.5e+52	4.2e+52	1.5e+16	8.6e+15	3.7e+17
88	275	379	417	1838	1717	2.7e+53	4.2e+52	3.5e+52	1.0e+16	5.8e+15	2.3e+17
131	600	520	8	24	34	6.0e+53	1.0e+51	8.4e+50	7.9e+14	4.6e+14	1.0e+16
172	350	376	4	14	20	6.5e+53	1.2e+51	9.7e+50	6.4e+14	3.8e+14	9.4e+15
257	500	422	3	8	10	1.2e+54	9.6e+50	8.1e+50	5.1e+14	3.0e+14	7.5e+15

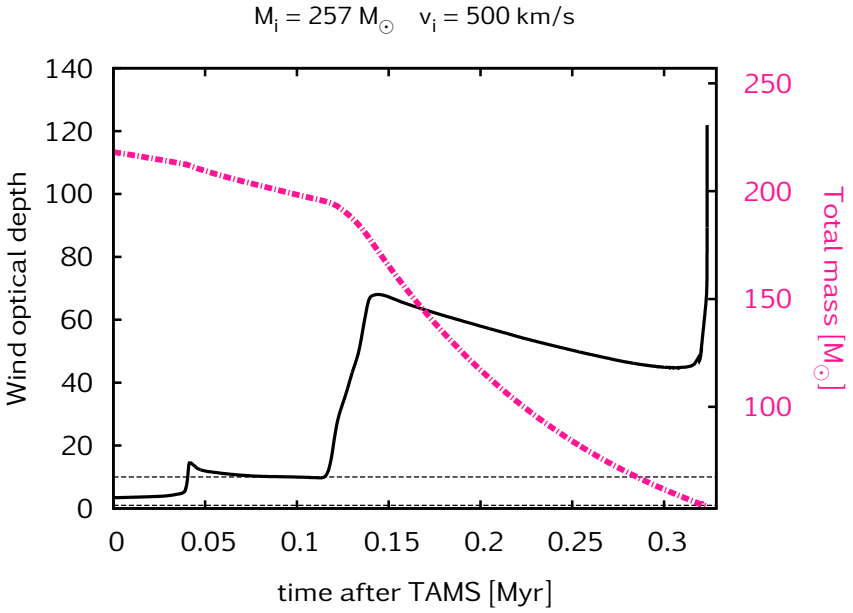

Figure 4.26. Same as Fig. 4.4 but for the model with the alternative mass-loss rate. As the mass-loss becomes higher due to the surface enhancement of CNO at ~0.11 Myr, the wind optical depth increases to 70 and the stellar mass decreases rapidly. The model ends up having a total stellar mass of only 54 $M_\odot$ at the end of its evolution (compared to the final stellar mass of 166 $M_\odot$ in the original model).

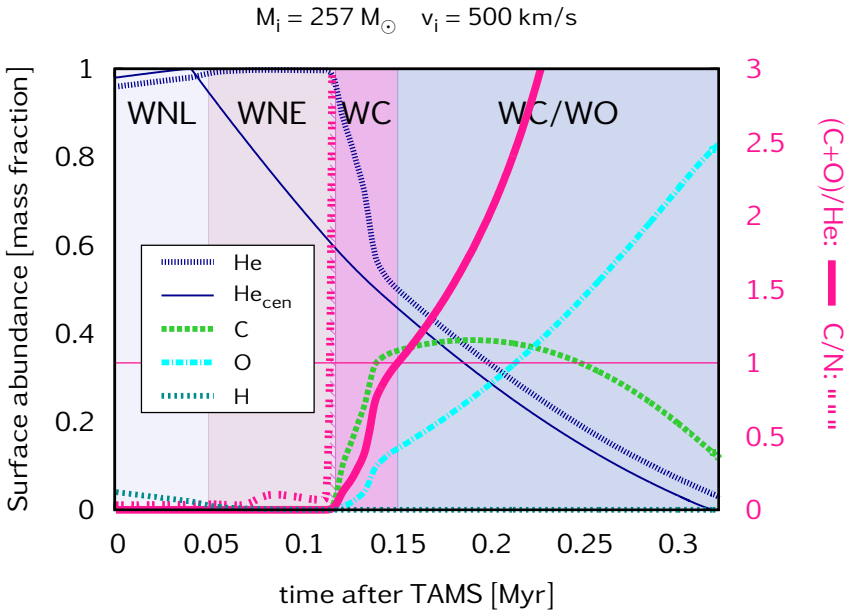

Figure 4.27. Same as Fig. 4.5 but for the model with the alternative mass-loss rate. Since the mass-loss is higher in the case of the alternative model, deeper layers of the star are exposed, as compared to the original model. This results in higher surface abundances of carbon and oxygen in expense of that of helium, which means that the WC type phase (as defined by the (C+O)/He ratio being between 0.03 and 1) is short, while the WO type phase becomes longer. Note also that as a consequence of the reduced stellar mass, the alternative model lives longer than the original one.

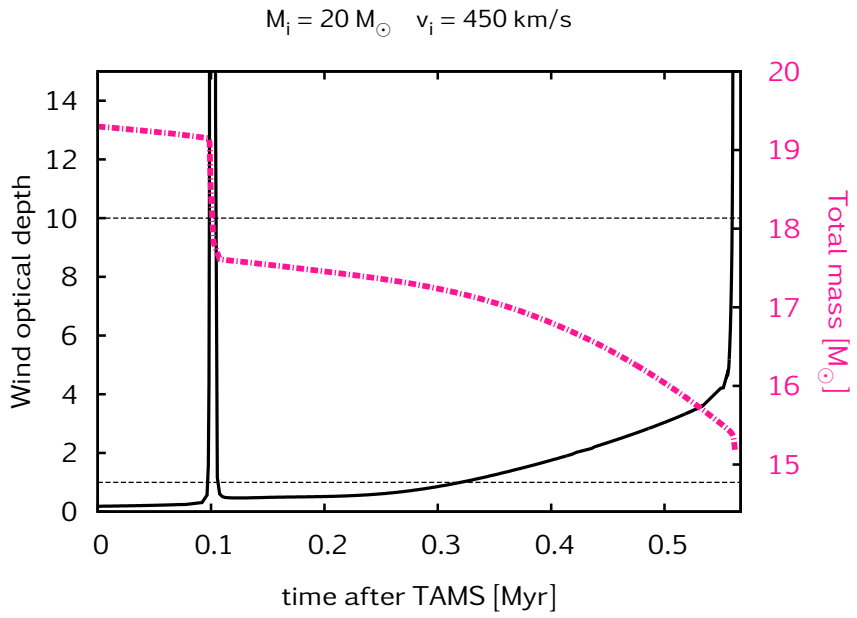

Figure 4.28. Same as Fig. 4.6 but for the model with the alternative mass-loss rate. While the original model has transparent wind during its core-helium-burning lifetime, the alternative model's wind becomes optically thick during the second half of the core-helium-burning lifetime due to the increased mass-loss.

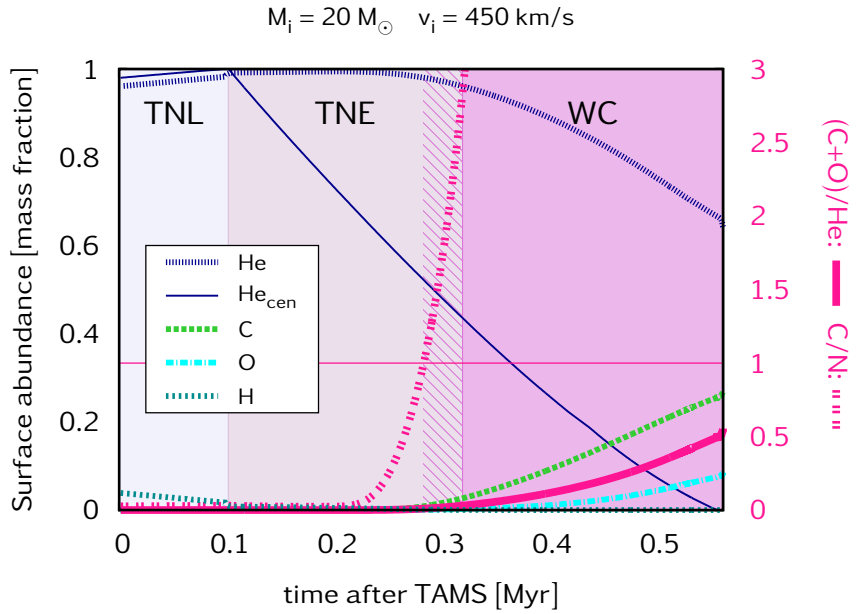

Figure 4.29. Same as Fig. 4.7 but for the model with the alternative mass-loss rate. While the original model has transparent wind during its core-helium-burning lifetime, the alternative model's wind becomes optically thick during the second half of the core-helium-burning lifetime due to the increased mass-loss. Therefore, it becomes a WC type star after 0.32 Myr (as opposed to the original model, where it was a TC type star during this evolutionary phase).

Table 4.11. *Radii and lifetimes of our models.* Same as Table 4.3 but for the alternative set of models.

M_{ini} [$M_\odot$]	v_{ini} [km s^{-1}]	R_{TAMS}	$R_{He\text{-}exh}$	$R_{C\text{-}exh}$	R_{End}	τ^{MS}	type	$\tau^{T/WNL}$	$\tau^{T/WNE}$	τ^{WNC}	τ^{WC}	τ^{WO}
13	450	3.5	-	-	1.1	1.97e7	T	1.48e5	2.42e5*	-	-	-
20	450	4.3	1.3	0.7	0.6	1.04e7	T	1.02e5	1.83e5	3.77e4	2.30e5	0.00
23	500	4.7	1.4	0.7	0.6	8.82e6	T	9.21e4	1.51e5	4.03e4	2.39e5	0.00
26	350	4.7	-	-	1.7	7.27e6	T	1.04e5	1.37e5*	-	-	-
26	500	4.9	1.4	0.7	0.6	7.60e6	T	8.50e4	1.35e5	3.75e4	2.46e5	0.00
45	500	6.4	1.9	1.0	0.7	4.39e6	W	6.35e4	8.42e4	3.85e4	2.22e5	9.03e2
59	300	7.1	2.3	1.3	0.8	3.44e6	W	8.94e4	6.85e4	2.44e4	1.83e5	2.15e2
67	275	7.6	2.5	1.4	1.0	3.15e6	W	1.01e5	5.92e4	2.18e4	1.71e5	0.00
67	300	7.6	2.3	1.4	0.8	3.16e6	W	8.49e4	2.65e5	0.00	0.00	0.00
77	500	8.3	2.3	-	1.6	2.98e6	W	5.25e4	2.94e5	7.00e1	0.00	-
88	275	9.7	2.8	-	1.6	2.68e6	W	2.98e5	0.00	1.44e4	3.12e4	-
131	600	11.0	3.5	3.5	2.8	2.30e6	W	4.65e4	5.27e4	2.77e4	1.60e5	3.06e4
172	350	13.3	4.5	4.5	2.0	2.01e6	W	7.25e4	9.17e4	2.30e3	8.64e4	4.90e4
257	500	16.8	5.9	6.0	2.9	1.80e6	W	5.03e4	6.46e4	3.25e3	1.06e5	6.87e4

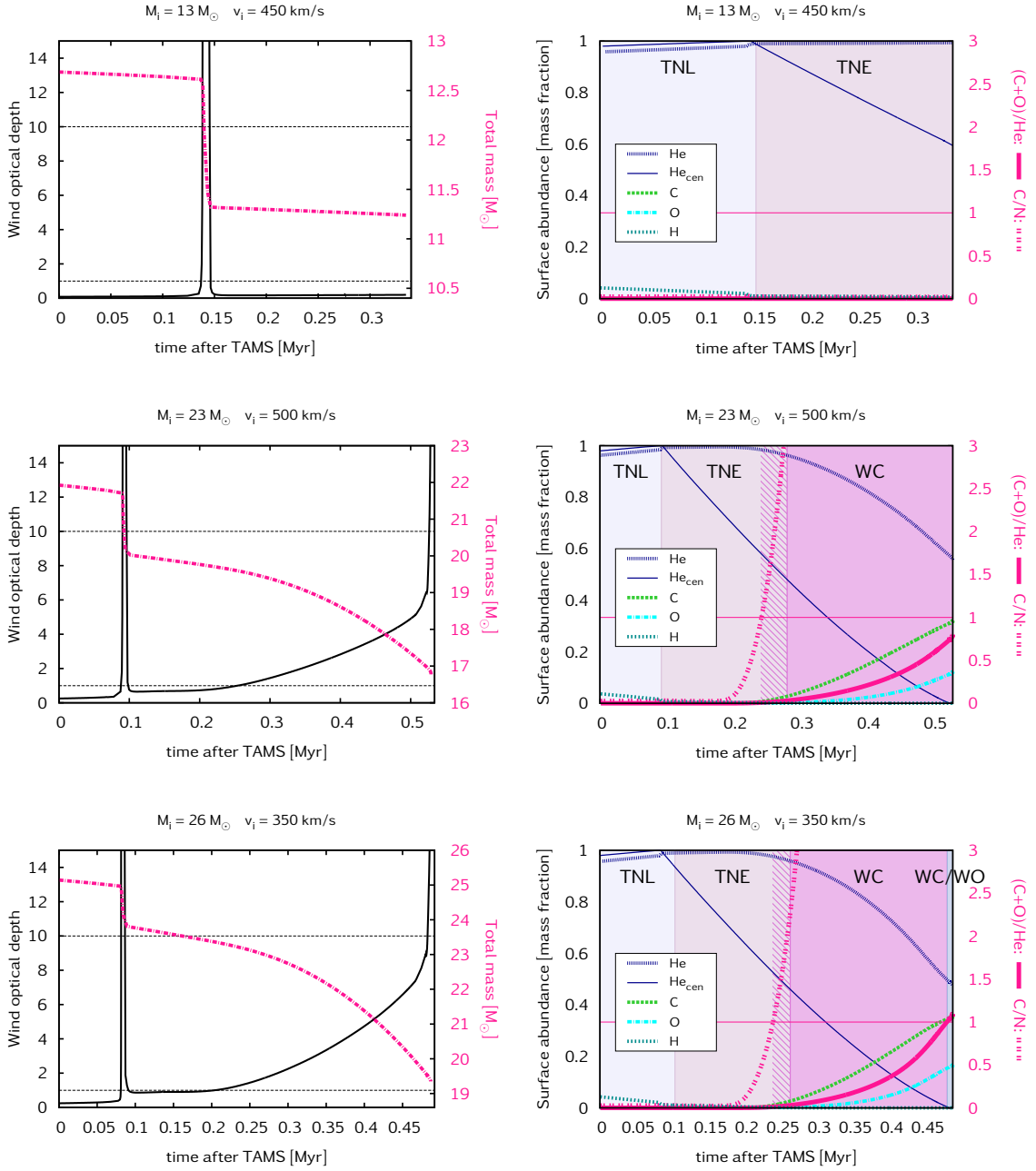

Figure 4.30. Same as Fig. 4.10 but for the set of alternative models. For our less massive models in the alternative set, the TC type stars become WC type stars (with thick winds) at around half of the core-helium-burning lifetime due to strong mass-loss. As for our most massive models in Figs. 4.31-4.33, the surface oxygen mass fraction increases to values as high as 0.6-0.8. Interestingly, we find some of our models with $M_{ini}/M_{\odot} \sim 67$-$77$ staying WNL type stars during all their core-helium-burning lifetimes (cf. Yoon et al., 2006). For a further discussion, see the captions of Figs. 4.26, 4.27, 4.28 and 4.29.

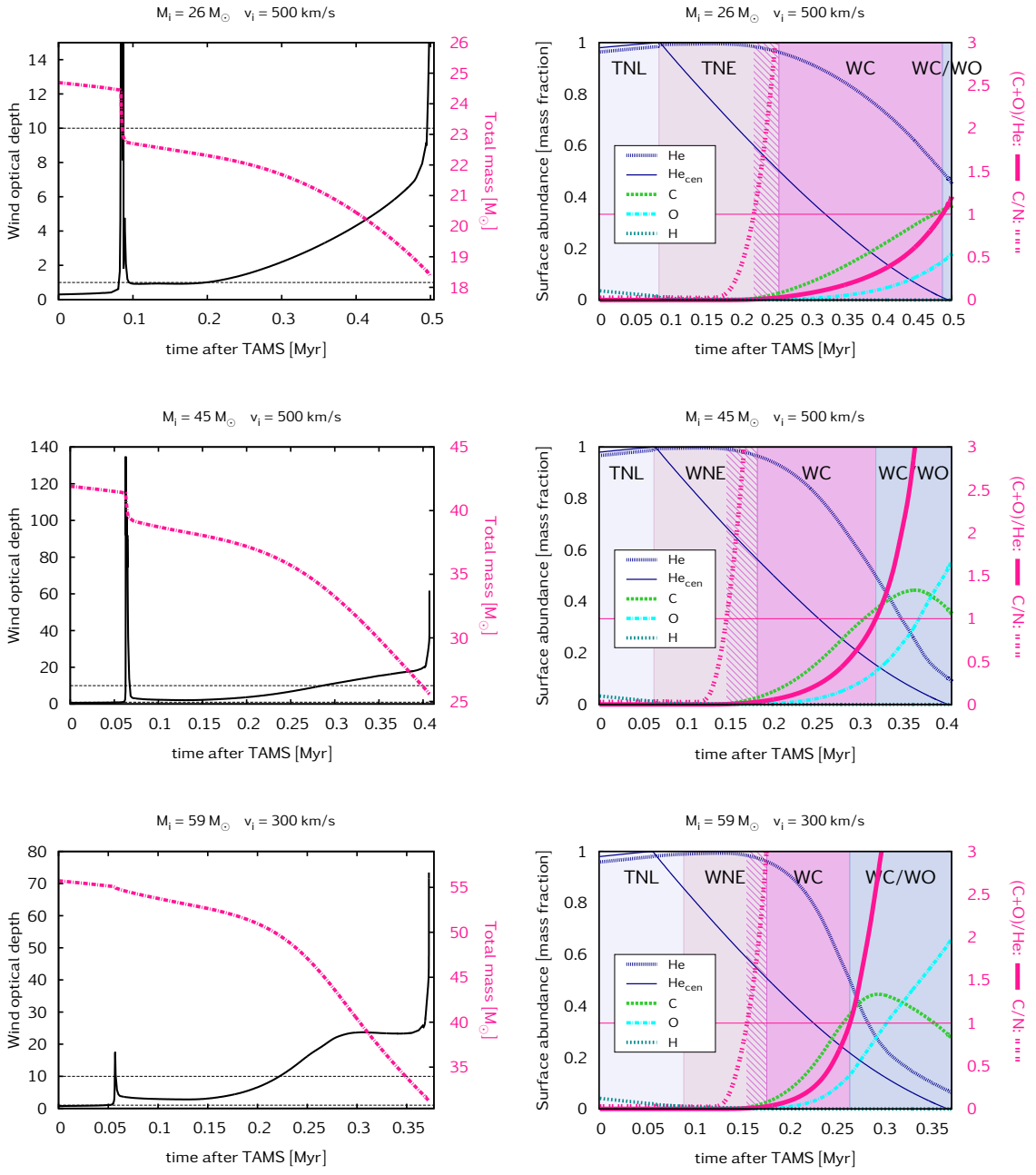

Figure 4.31. Same as Fig. 4.30, but for other models of the alternative set, as indicated by the title of every figure.

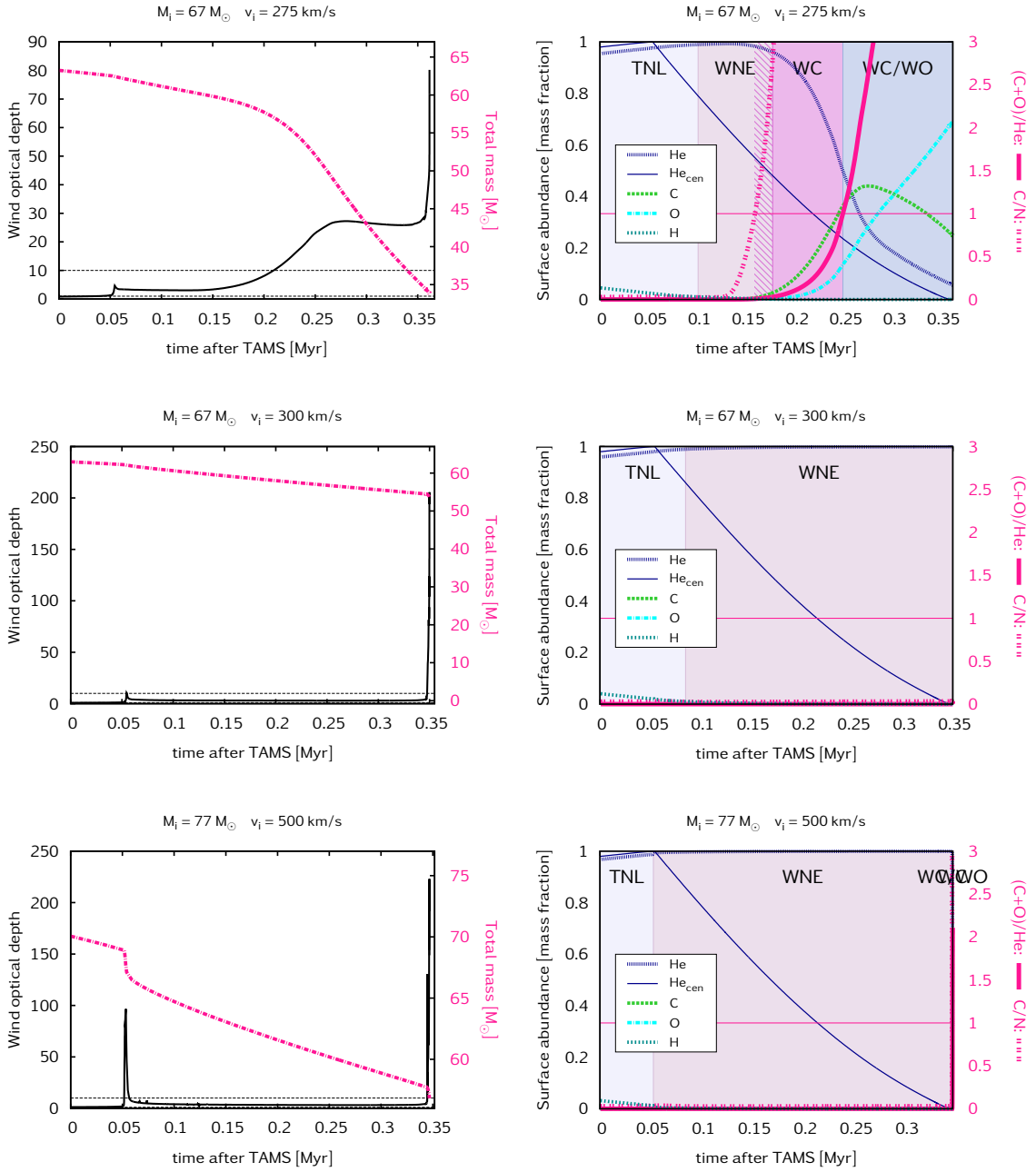

Figure 4.32. Same as Fig. 4.30, but for other models of the alternative set, as indicated by the title of every figure. The models with M_{ini}=67 $M_\odot$–v_{ini}=300 km s^{-1} and M_{ini}=77 $M_\odot$ (as well as that with M_{ini}=88 $M_\odot$ in Fig. 4.33) do not change their evolutionary behavior even when the alternative mass-loss is applied, since their surface is never enriched by helium-burning products such as carbon, nitrogen and oxygen (cf. Sect. 4.5.4). Consequently, they do not lose more mass than the corresponding models in the original set, and their final fate predictions are also not changed.

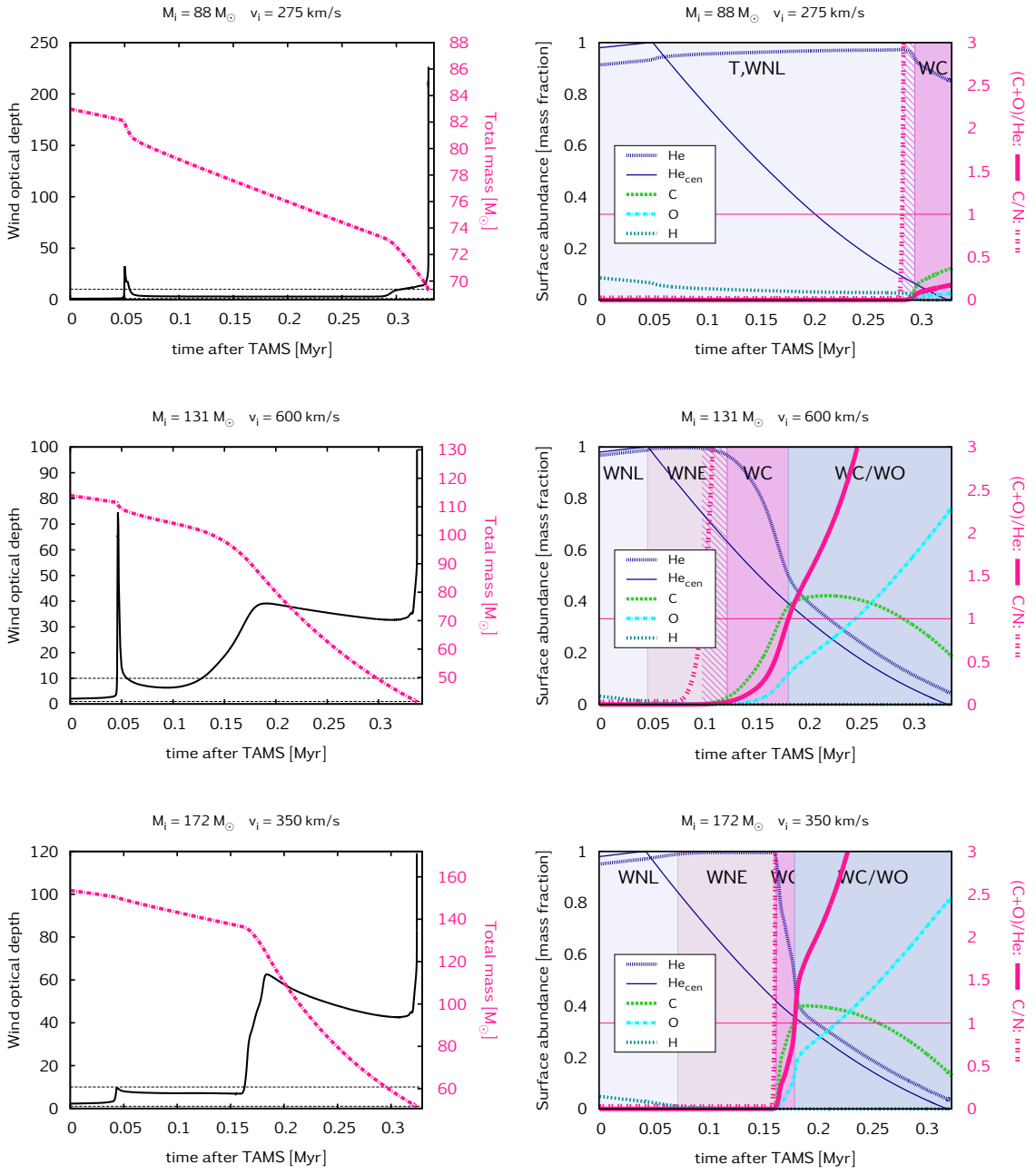

Figure 4.33. Same as Fig. 4.30, but for other models of the alternative set, as indicated by the title of every figure.

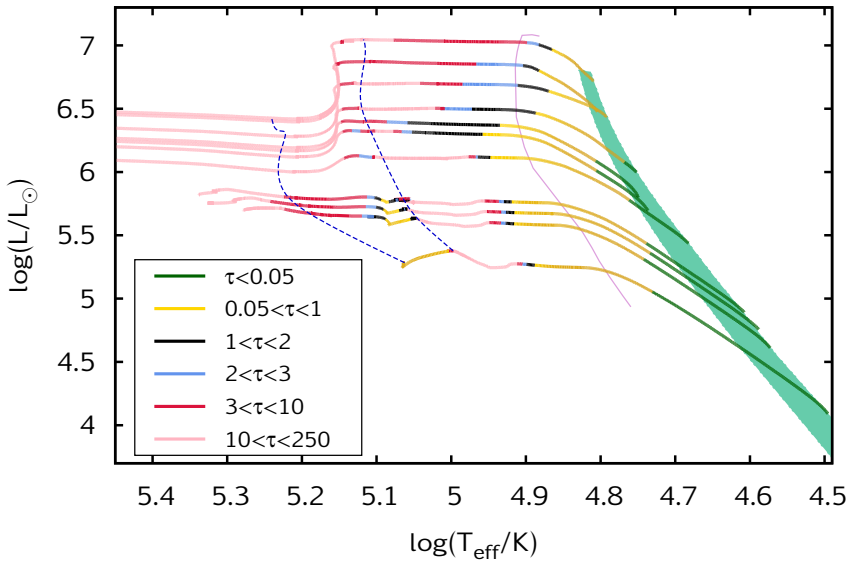

Figure 4.34. Same as Fig. 4.8 but for the alternative set of models. The wind optical depth becomes higher than in the original set of models, especially during the second half of their core-helium-burning lifetimes, due to the incresed mass-loss rate. Our models in the initial mass-range of 20-26 $M_{\odot}$ become WR stars with optically thick winds with the alternative mass-loss rate (as opposed to the original set, in which they are TWUIN stars during all their core-helium-burning lifetimes). But our most massive models increase their wind optical depth as well, with τ values well above 10.

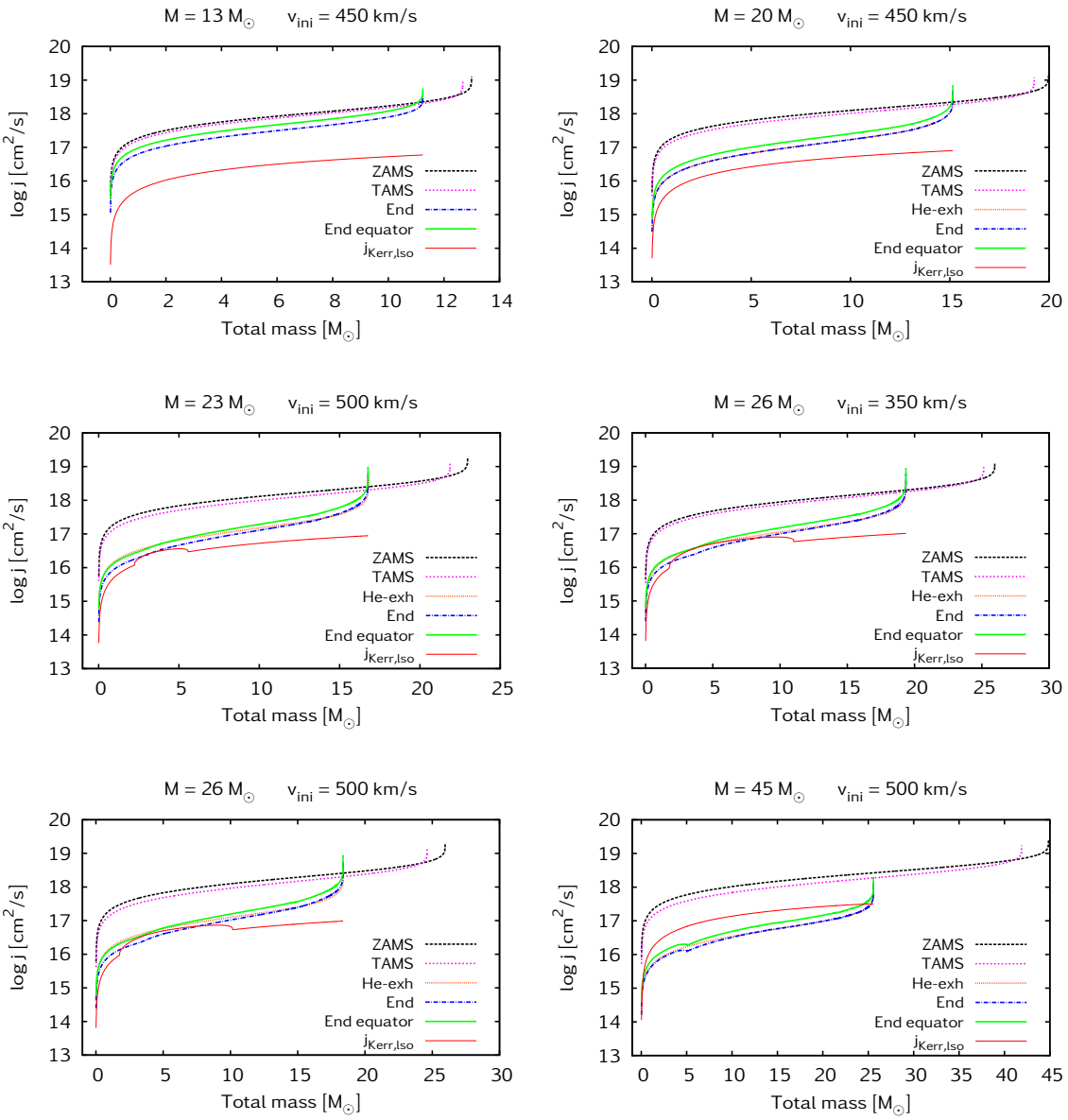

Figure 4.35. Same as Fig. 4.16 but for the alternative set of models. Although the mass-loss rates are higher than in the original models, the alternative models in the initial mass-range of 13-26 $M_\odot$, as well as some models in the range of 67-77 $M_\odot$ still keep rotating fast at the end of their core-carbon-burning lifetimes so they are possible progenitors of lGRBs in the collapsar scenario (for details, see Sect. 4.7.1) or SLSNe in the magnetar scenario (for details, see Sect. 4.7.2). .

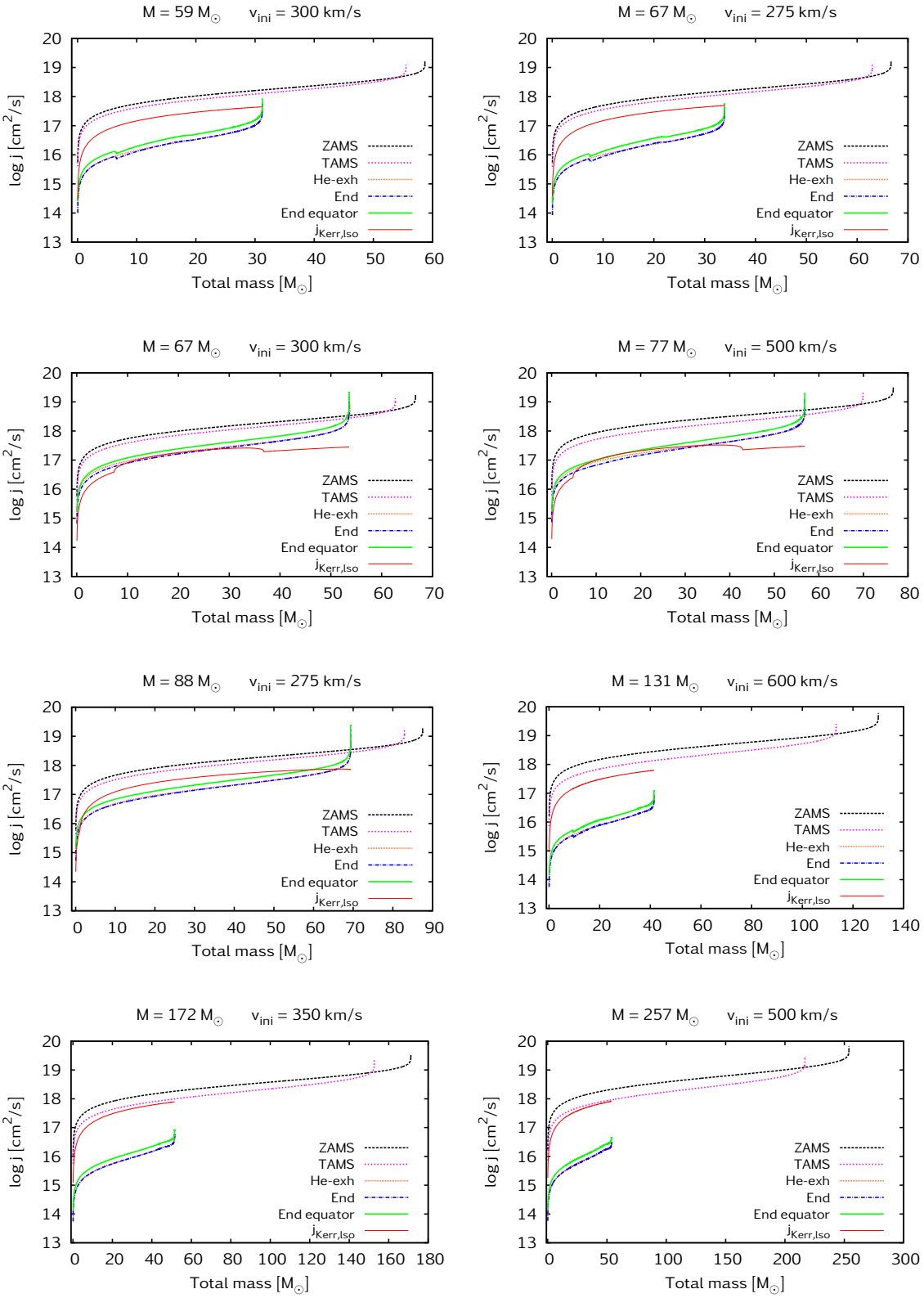

Figure 4.36. The same as Fig. 4.16, but for another models as indicated by the title of every figure. For discussion, see the caption of that figure.

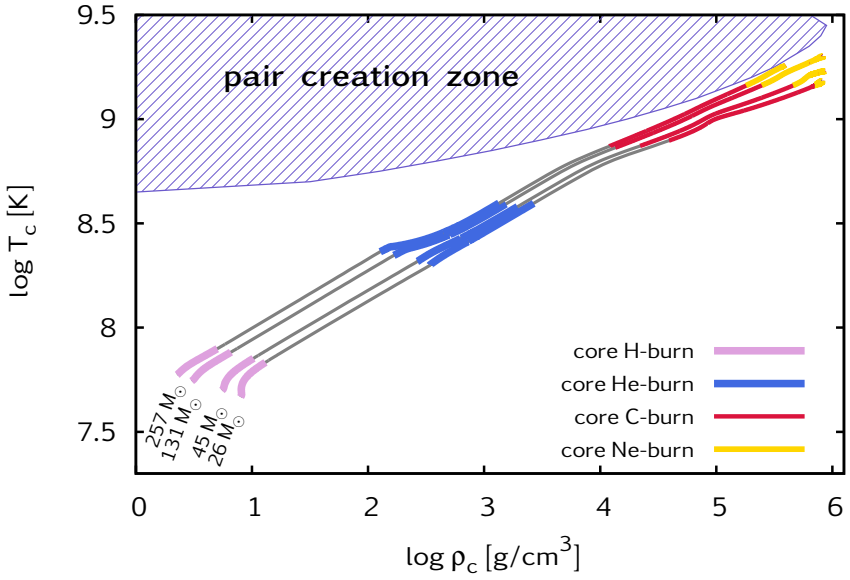

Figure 4.37. Same as Fig. 4.18 but for the alternative set of models. Due to the high mass-loss, the models evolve with a lower stellar mass as compared to the original set of models during core-helium-burning. As a consequence, their cores avoid entering the pair-instability zone. This has consequences for the predicted final fates, as even our most massive model can avoid the direct collapse. For all the models above the initial mass of 50 $M_{\odot}$, some parts of the star still enter the pair-instability region (but not the very core). Given that their CO-core masses are below 57 $M_{\odot}$, they may produce pPISN events (cf. Sect. 4.7.4).

Table 4.12. *Alternative set of models. Lymann continuum.* Time-averaged rate (Q) and peak rate (Q^{max}) of the ionizing photons in the Lymann continuum during the main-sequence (MS) and the post-main-sequence (p.MS) evolution for each stellar sequence. Both the values that are not corrected for the wind optical-depth and the values that are corrected for the wind optical-depth (marked with *corr*) are tabulated. (Note that Sz15 gave not-corrected values for the main-sequence evolution of their models.) The last four columns have the following meaning. The ionizing photon rate during the whole evolution is marked with Q^{total}, and calculated by: $Q^{total}=(1-\frac{\tau^{p.MS}}{\tau^{MS}})\cdot Q^{MS}+\frac{\tau^{p.MS}}{\tau^{MS}}\cdot Q^{p.MS}$, where τ means the lifetime of the model in the given evolutionary phase (as given in Table 4.3). Q^{total}_{corr} is calculated the same way, but using the corrected flux values. The total ionizing photon rates are compared to those during the main-sequence and the post-main-sequence, both in the not-corrected and the corrected case, in the last four columns. Asterisks mark the sequences that have not finished core-helium-burning. We emphasize that the given quantities rely on the black body approximation, and refer to Sz15 for a discussion of its validity.

M^i-v^i_{rot} [$M_\odot$-km/s]	Q^{MS} [s^{-1}]	$Q^{p.MS}$ [s^{-1}]	Q^{MS}_{corr} [s^{-1}]	$Q^{p.MS}_{corr}$ [s^{-1}]	$Q^{max,MS}$ [s^{-1}]	$Q^{max,p.MS}$ [s^{-1}]	$Q^{max,MS}_{corr}$ [s^{-1}]	$Q^{max,p.MS}_{corr}$ [s^{-1}]	Q^{total}/Q^{MS}	$Q^{total}_{corr}/Q^{MS}_{corr}$	$Q^{p.MS}/Q^{total}$	$Q^{p.MS}_{corr}/Q^{total}_{corr}$
13-450*	1.75E+48	1.27E+49	1.75E+48	1.34E+49	1.18E+49	1.35E+49	1.18E+49	1.36E+49	1.11*	1.13*	6.51*	6.80*
20-450	6.03E+48	2.80E+49	6.03E+48	3.01E+49	2.61E+49	2.85E+49	2.61E+49	3.33E+49	1.19	1.21	3.89	4.12
23-500	8.48E+48	3.36E+49	8.48E+48	3.68E+49	3.39E+49	3.63E+49	3.39E+49	3.99E+49	1.15	1.17	3.44	3.71
26-350*	1.27E+49	4.28E+49	1.27E+49	4.83E+49	4.44E+49	4.44E+49	4.14E+49	5.19E+49	1.12*	1.14*	3.01*	3.33*
26-500	1.14E+49	3.99E+49	1.14E+49	4.50E+49	4.11E+49	4.40E+49	4.11E+49	4.86E+49	1.15	1.18	3.05	3.36
45-500	3.74E+49	8.40E+49	3.72E+49	9.67E+49	9.23E+49	9.80E+49	9.21E+49	1.02E+50	1.10	1.13	2.03	2.29
59-300	6.66E+49	1.19E+50	6.65E+49	1.35E+50	1.42E+50	1.48E+50	1.43E+50	1.57E+50	1.09	1.11	1.65	1.83
67-275	8.30E+49	1.39E+50	8.30E+49	1.54E+50	1.69E+50	1.75E+50	1.70E+50	1.74E+50	1.08	1.10	1.55	1.68
67-300	8.26E+49	1.57E+50	8.26E+49	1.80E+50	1.68E+50	1.75E+50	1.68E+50	1.83E+50	1.11	1.14	1.72	1.91
77-500	9.91E+49	1.77E+50	9.88E+49	1.95E+50	1.91E+50	2.00E+50	1.91E+50	1.98E+50	1.10	1.12	1.62	1.76
88-275	1.29E+50	2.32E+50	1.29E+50	2.64E+50	2.36E+50	2.36E+50	2.36E+50	2.64E+50	1.09	1.11	1.66	1.85
131-600	2.20E+50	2.75E+50	2.19E+50	2.85E+50	3.63E+50	3.63E+50	3.58E+50	3.81E+50	1.03	1.04	1.21	1.26
172-350	3.43E+50	3.59E+50	3.42E+50	3.80E+50	5.28E+50	5.28E+50	5.31E+50	5.69E+50	1.01	1.01	1.04	1.10
257-500	5.73E+50	4.12E+50	5.65E+50	3.38E+50	8.09E+50	8.09E+50	8.11E+50	8.11E+50	0.96	0.94	0.75	0.64

Table 4.13. *Alternative set of models. He I continuum.* Time-averaged rate (Q) and peak rate (Q^{max}) of the ionizing photons in the He I continuum during the main-sequence (MS) and the post-main-sequence (p.MS) evolution for each stellar sequence. Both the values that are not corrected for the wind optical-depth and the values that are corrected for the wind optical-depth (marked with *corr*) are tabulated. (Note that Sz15 gave not-corrected values for the main-sequence evolution of their models.) The last four columns have the following meaning. The ionizing photon rate during the whole evolution is marked with Q^{total}, and calculated by: $Q^{total}=(1-\frac{\tau^{p.MS}}{\tau^{MS}})\cdot Q^{MS}+\frac{\tau^{p.MS}}{\tau^{MS}}\cdot Q^{p.MS}$, where τ means the lifetime of the model in the given evolutionary phase (as given in Table 4.3). Q^{total}_{corr} is calculated the same way, but using the corrected flux values. The total ionizing photon rates are compared to those during the main-sequence and the post-main-sequence, both in the not-corrected and the corrected case, in the last four columns. Asterisks mark the sequences that have not finished core-helium-burning. We emphasize that the given quantities rely on the black body approximation, and refer to Sz15 for a discussion of its validity.

M^i-v^i_{rot} [$M_\odot$-km/s]	Q^{MS} [s^{-1}]	$Q^{p.MS}$ [s^{-1}]	Q^{MS}_{corr} [s^{-1}]	$Q^{p.MS}_{corr}$ [s^{-1}]	$Q^{max,MS}$ [s^{-1}]	$Q^{max,p.MS}$ [s^{-1}]	$Q^{max,MS}_{corr}$ [s^{-1}]	$Q^{max,p.MS}_{corr}$ [s^{-1}]	Q^{total}/ Q^{MS}	Q^{total}_{corr}/ Q^{MS}_{corr}	$Q^{p.MS}$/ Q^{total}	$Q^{p.MS}_{corr}$/ Q^{total}_{corr}
13-450*	2.65E+47	6.01E+48	2.65E+47	5.93E+48	3.37E+48	7.98E+48	3.30E+48	7.96E+48	1.40*	1.40*	16.20*	16.03*
20-450	1.17E+48	1.67E+49	1.16E+48	1.64E+49	8.60E+48	1.91E+49	8.40E+48	1.73E+49	1.70	1.70	8.39	8.32
23-500	1.75E+48	2.03E+49	1.72E+48	1.95E+49	1.18E+49	2.26E+49	1.20E+49	1.97E+49	1.54	1.53	7.52	7.41
26-350*	3.07E+48	2.78E+49	3.12E+48	2.52E+49	1.71E+49	2.91E+49	2.35E+49	2.59E+49	1.40*	1.36*	6.45*	5.96*
26-500	2.49E+48	2.42E+49	2.44E+48	2.24E+49	1.47E+49	2.71E+49	1.42E+49	2.37E+49	1.52	1.49	6.40	6.17
45-500	9.97E+48	5.15E+49	9.64E+48	3.80E+49	3.60E+49	5.72E+49	3.25E+49	5.07E+49	1.35	1.24	3.81	3.17
59-300	2.08E+49	7.69E+49	2.01E+49	4.36E+49	6.00E+49	9.04E+49	5.77E+49	7.66E+49	1.29	1.12	2.86	1.93
67-275	2.65E+49	8.95E+49	2.57E+49	4.59E+49	7.19E+49	1.08E+50	6.95E+49	9.07E+49	1.28	1.09	2.63	1.63
67-300	2.65E+49	1.02E+50	2.56E+49	9.89E+49	7.11E+49	1.09E+50	6.51E+49	1.06E+50	1.34	1.34	2.88	2.88
77-500	3.09E+49	1.09E+50	2.89E+49	1.06E+50	7.94E+49	1.17E+50	6.46E+49	1.12E+50	1.32	1.34	2.68	2.75
88-275	4.28E+49	1.51E+50	4.08E+49	1.34E+50	9.71E+49	1.53E+50	8.75E+49	1.37E+50	1.26	1.24	2.79	2.65
131-600	7.17E+49	1.74E+50	6.34E+49	7.29E+49	1.55E+50	2.03E+50	1.08E+50	1.42E+50	1.17	1.02	2.07	1.13
172-350	1.25E+50	2.54E+50	1.12E+50	1.06E+50	2.28E+50	3.17E+50	2.01E+50	2.50E+50	1.14	0.99	1.78	0.95
257-500	2.09E+50	2.96E+50	1.76E+50	3.17E+49	3.49E+50	4.60E+50	2.82E+50	2.82E+50	1.07	0.88	1.33	0.21

Table 4.14. *Alternative set of models. He II continuum.* Time-averaged rate (Q) and peak rate (Q^{max}) of the ionizing photons in the He II continuum during the main-sequence (MS) and the post-main-sequence (p.MS) evolution for each stellar sequence. Both the values that are not corrected for the wind optical-depth and the values that are corrected for the wind optical-depth (marked with *corr*) are tabulated. (Note that Sz15 gave not-corrected values for the main-sequence evolution of their models.) The last four columns have the following meaning. The ionizing photon rate during the whole evolution is marked with Q^{total}, and calculated by: $Q^{total}=(1-\frac{\tau^{p.MS}}{\tau^{MS}})\cdot Q^{MS}+\frac{\tau^{p.MS}}{\tau^{MS}}\cdot Q^{p.MS}$, where τ means the lifetime of the model in the given evolutionary phase (as given in Table 4.3). Q^{total}_{corr} is calculated the same way, but using the corrected flux values. The total ionizing photon rates are compared to those during the main-sequence and the post-main-sequence, both in the not-corrected and the corrected case, in the last four columns. Asterisks mark the sequences that have not finished core-helium-burning. We emphasize that the given quantities rely on the black body approximation, and refer to Sz15 for a discussion of its validity.

M^i-v^i_{rot} [$M_\odot$-km/s]	Q^{MS} [s^{-1}]	$Q^{p.MS}$ [s^{-1}]	Q^{MS}_{corr} [s^{-1}]	$Q^{p.MS}_{corr}$ [s^{-1}]	$Q^{max,MS}$ [s^{-1}]	$Q^{max,p.MS}$ [s^{-1}]	$Q^{max,MS}_{corr}$ [s^{-1}]	$Q^{max,p.MS}_{corr}$ [s^{-1}]	Q^{total}/ Q^{MS}	Q^{total}_{corr}/ Q^{MS}_{corr}	$Q^{p.MS}$/ Q^{total}	$Q^{p.MS}_{corr}$/ Q^{total}_{corr}
13-450*	1.23E+45	6.56E+47	1.18E+45	6.17E+47	4.20E+46	1.27E+48	3.89E+46	1.21E+48	10.81*	10.68*	49.32*	48.97*
20-450	8.76E+45	2.83E+48	8.26E+45	1.71E+48	1.67E+47	4.18E+48	1.53E+47	2.55E+48	18.04	11.89	17.91	17.41
23-500	1.52E+46	3.58E+48	1.43E+46	1.82E+48	2.70E+47	5.17E+48	2.88E+47	2.61E+48	13.03	7.48	18.08	17.01
26-350*	3.88E+46	5.72E+48	6.66E+46	2.15E+48	5.51E+47	6.60E+48	2.93E+48	3.39E+48	8.38*	2.57*	17.60*	12.57*
26-500	2.39E+46	4.50E+48	2.14E+46	1.82E+48	3.67E+47	6.46E+48	3.26E+47	2.93E+48	12.18	6.03	15.46	14.11
45-500	1.42E+47	9.87E+48	1.13E+47	2.08E+48	1.19E+48	1.30E+49	7.80E+47	5.16E+48	6.75	2.46	10.30	7.48
59-300	4.28E+47	1.58E+49	3.59E+47	1.89E+48	2.56E+48	2.11E+49	2.15E+48	6.76E+48	4.88	1.46	7.56	3.61
67-275	5.68E+47	1.88E+49	4.73E+47	2.08E+48	3.13E+48	2.54E+49	2.68E+48	7.81E+48	4.81	1.40	6.89	3.14
67-300	5.76E+47	2.18E+49	4.59E+47	1.07E+49	3.08E+48	3.19E+49	2.10E+48	1.31E+49	5.36	3.64	7.06	6.41
77-500	6.08E+47	2.27E+49	4.20E+47	1.04E+49	3.21E+48	3.25E+49	1.37E+48	1.25E+49	5.56	3.98	6.72	6.23
88-275	9.49E+47	2.93E+49	7.38E+47	1.09E+49	3.82E+48	3.20E+49	2.46E+48	1.14E+49	4.13	2.44	7.47	6.06
131-600	1.57E+48	3.39E+49	8.47E+47	1.43E+48	6.82E+48	5.14E+49	1.61E+48	4.10E+48	3.53	1.09	6.12	1.56
172-350	3.57E+48	6.23E+49	2.26E+48	4.02E+48	1.05E+49	7.71E+49	6.08E+48	1.21E+49	3.31	1.11	5.28	1.60
257-500	5.91E+48	7.41E+49	3.01E+48	0.00E+00	1.61E+49	1.13E+50	6.46E+48	6.46E+48	2.79	0.84	4.49	0.00

Table 4.15. *Energetics of the last computed models.* The same as Table 4.7 but for the alternative set of models. Only models that are found to undergo pair-instability are listed, i.e. those that are less massive than 40 $M_\odot$ at the end of our computations, as well as those that have not evolved until core-carbon-exhaustion, are not listed.

M_{ini} [$M_\odot$]	v_{ini} [km s^{-1}]	T_c^{max} [10^8 K]	ρ_c^{max} [log g cm^{-3}]	unstable	E_{grav} [erg]	E_{rot} [erg]	E_{therm} [erg]	E_{kin} [erg]	E_{total} [erg]	$E_{^{16}O}$ [erg]	$E_{^{12}C}$ [erg]	$E_{^{20}Ne}$ [erg]
77	500	19.57	5.79	42%	5.45e+52	2.45e+50	4.88e+52	1.89e+43	-5.46e+51	1.44e+52	1.10e+51	1.15e+51
88	275	13.96	5.10	21%	5.49e+52	6.60e+49	4.88e+52	3.69e+41	-6.03e+51	1.80e+52	1.26e+51	1.38e+51
131	600	20.04	5.92	38%	3.58e+52	2.17e+47	3.16e+52	4.36e+41	-4.20e+51	1.13e+52	5.48e+50	7.98e+50
172	350	18.99	5.70	41%	4.74e+52	1.75e+47	4.24e+52	1.45e+44	-5.00e+51	1.41e+52	5.76e+50	1.10e+51
257	500	18.16	5.60	39%	4.85e+52	1.05e+47	4.33e+52	3.87e+43	-5.20e+51	1.47e+52	5.74e+50	1.21e+51

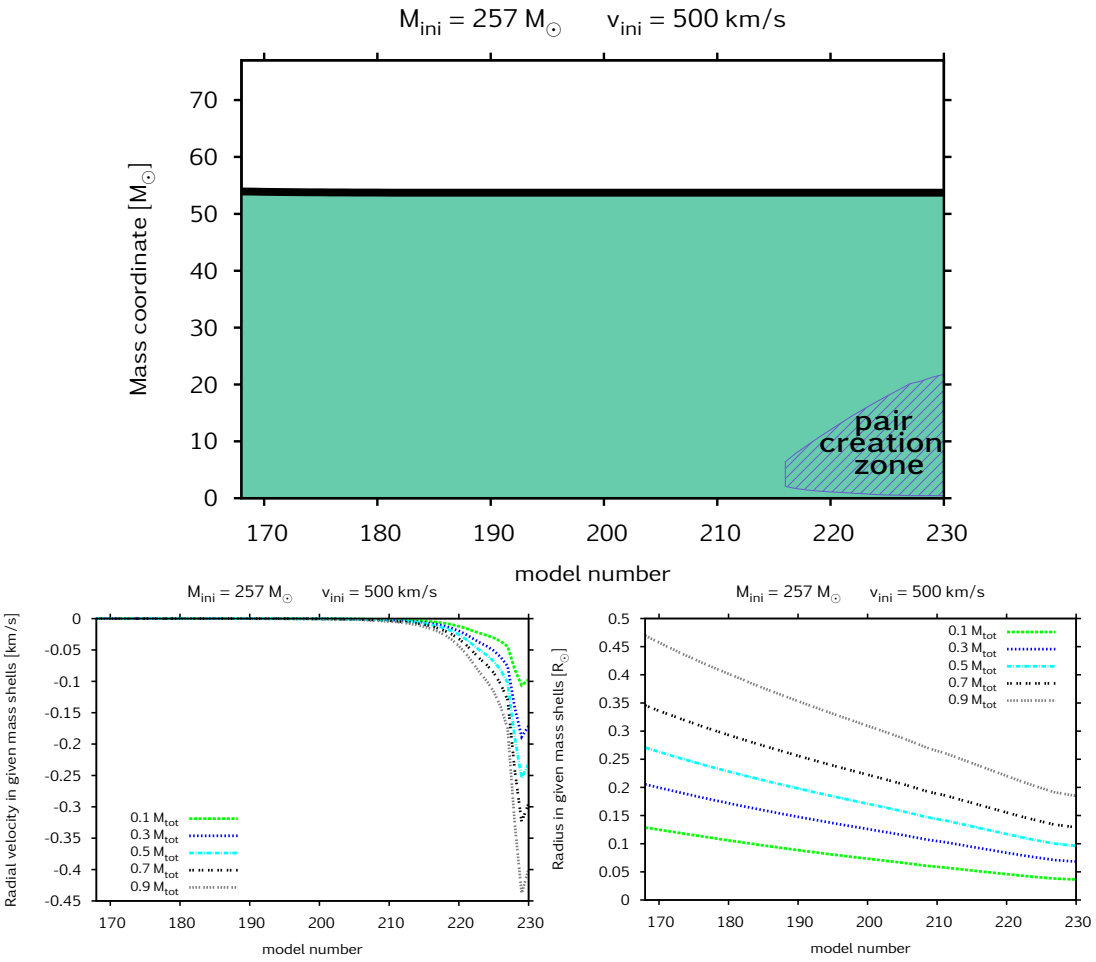

Figure 4.38. Same as Fig. 4.19 and Fig. 4.20 but for the model with the alternative mass-loss rate. The most striking difference between the original and the alternative model is the total stellar mass being 166 $M_\odot$ and 54 $M_\odot$, respectively. The alternative model, while some parts of it become pair-instable, is not predicted to fall into a black hole directly like the original model. Instead, it may produce pPISN event.

The most important differences between the original and the alternative set of models are the following.

I The higher mass-loss rate in the alternative set makes our most massive models (those above 45 $M_\odot$ initially) in this set lose more than twice as much mass during their post-main-sequence lifetimes as do the corresponding models in the original set. While the ratio of the mass lost to the mass at the TAMS varies between 10% and 24% in the original models (see Table 4.1), that in the alternative models varies between 14 and 75% (see Table 4.9).

II The surface luminosities of the most massive alternative models drop (at around $\log(T_{\rm eff}/K) \sim 5.17$) and they continue their evolution with this lower luminosity of $\log(L/L_\odot)\sim$6.2–6.5 (as opposed to $\log(L/L_\odot)\sim$6.3–7 in the case of the original set of models). On the other hand, they evolve to higher $T_{\rm eff}$ than the original set, reaching $\log(T_{\rm eff}/K)$ values as high as 5.49 (300 kK, cf. Fig. 4.23).

III The time-evolution of the rotational velocity of the alternative models starts to differ significantly from that of the original models in the second half of the core-helium-burning lifetime, as seen in Fig. 4.25. This is because at this point, the surface mass-fractions of C, N and O, that drive the alternative mass-loss, become very high (cf. Fig. 4.24 and Figs. 4.30-4.33). As a result, the models start to lose mass rapidly: the deeper layers are exposed, the higher the C, N and O abundances at the surface are and, therefore, the higher the mass-loss rate, which in turn exposes even deeper layers, and so on. The most massive models spin down to almost zero due to this enhanced mass-loss, and even the less massive models finish their evolution with lower rotational velocity then those in the original set (Table 4.10).

IV The wind optical depth of the alternative models becomes higher than that of the corresponding models in the original set, especially during the second half of their core-helium-burning lifetimes (Fig. 4.34). This is due to the increased mass-loss rate. As Figs. 4.30-4.31 show, our alternative models in the initial mass-range of 20-26 $M_\odot$ become WR stars with optically thick winds (as opposed to the original models in the same mass-range, which stay TWUIN stars during all their core-helium-burning lifetimes).

V As for the surface composition, deeper layers of the alternative models are exposed (Figs. 4.30-4.33), as compared to the original models. This results in higher surface abundances of carbon and oxygen at the expense of that of helium in the models above 45 $M_\odot$, which means that the WC phase (as defined by the (C+O)/He ratio being below 1) is very short, while the WO phase becomes longer. Some models show an extremely high surface oxygen abundance (as high as 0.8 at the end of the core-helium-burning lifetime, Fig. 4.27).

VI We give the ionizing photon emission rates of the alternative models in Tables 4.12-4.14. These models produce less He II photons than the original set of models. For the assumptions listed in Sect. 4.6, the original set of models predict a He II photon rate of $1.65{\cdot}10^{50}$ s^{-1} and 8 WC stars, while the alternative set of models predict these values to be $1.06{\cdot}10^{50}$ s^{-1} and 5, respectively.

VII The alternative models in the initial mass-range of 13-26 $M_\odot$ still rotate fast at the end of their evolutions so that a collapsar or a magnetar can be produced. The alternative mass-loss rate, however, makes a large difference in the final fate predictions of our models in the initial mass-range of 45-257 $M_\odot$. Our most massive model with M_{ini}=257 $M_\odot$ ends its life with only 57 $M_\odot$, and is predicted to produce a pPISN (as opposed to the original case where it is as massive as 166 $M_\odot$ at the end of its life and is predicted to fall into a black hole directly). A similar small final mass is found in the models with M_{ini}=131 and 172 $M_\odot$, so they also produce pPISNe (as opposed to the original cases where they produce PISNe). As for the models with M_{ini}=45 and 59 $M_\odot$, as well as for that with M_{ini}=67 $M_\odot$–v_{ini}=275 km s^{-1}, their final mass is lower than the pPISN limit, but also their angular momentum is lower than the critical limit for collapsar formation. These models are therefore predicted to produce supernovae of type Ic (without traces of both hydrogen and helium).

VIII The models with M_{ini}=67 $M_\odot$–v_{ini}=300 km s^{-1} and M_{ini}=77 $M_\odot$ as well as that with M_{ini}=88 $M_\odot$, do not change their evolutionary behavior even when the alternative mass-loss is applied, since their surface is never enriched by helium-burning products such as carbon, nitrogen and oxygen (cf. Sect. 4.5.4). Consequently, they do not lose more mass than the corresponding models in the original set, and their final fate predictions are also not changed. Indeed, the only model in the alternative set that we find to become a PISN is the one with M_{ini}=88 $M_\odot$, in which the conditions for the alternative mass-loss prescription are never fulfilled. Table 4.16 summarizes the final fate predictions of the alternative models.

Table 4.16. *Final fate predictions.* The same as Table 4.8 but for the alternative set of models. See remark VII and VIII for the discussion of these predictions.

M_{ini} [$M_\odot$]	v_{ini} [km s^{-1}]	$M_{He\text{-}exh}^{CO\text{-}core}$ [$M_\odot$]	theoretical scenario (observable event)	remnant
13	450	12.7*	collapsar (lGRB)	black hole
20	450	13.1	collapsar (lGRB)	black hole
23	500	14.9	collapsar (lGRB)	black hole
26	350	17.9	magnetar (SLSN type I and/or lGRB)	neutron star
26	500	16.6	magnetar (SLSN type I and/or lGRB)	neutron star
45	500	25.6	core-collapse (SN type Ic)	black hole
59	300	31.2	core-collapse (SN type Ic)	black hole
67	275	33.9	core-collapse (SN type Ic)	black hole
67	300	52.7	pPISN	black hole
77	500	56.0	pPISN	black hole
88	275	68.0	PISN	no remnant
131	600	41.5	pPISN	black hole
172	350	51.5	pPISN	black hole
257	500	57.0	pPISN	black hole

4.9 Conclusions

We followed the computation of 14 TWUIN star models of Sz15 during their post-main-sequence lifetimes. We analyzed their surface properties and predicted the ionizing flux they emit during core-helium-burning, and speculated about their possible final fates as superluminous supernovae or gamma-ray bursts. We summarize the most important new results below.

1 **New types of TWUIN stars: type TNE, type TNC and type TC.** The models are shown to have increased carbon and oxygen at the surface due to the very efficient mixing of nuclear burning products during the second half of core-helium-burning. In case these objects have optically thick winds, we would observe them as WR stars of type WNL, WNE and WC. In case, however, a model with increased surface carbon and oxygen still have transparent wind, that makes it a new type of object predicted at low-metallicity. This happens for models with initial masses of 13-26 $M_{\odot}$. We call these new types of stars TWUIN stars of type TNL, TNE and TC.

2 **High ionizing-photon emission and a small WR population.** We find that taking the post-main-sequence phase of our models into account, and correcting for the wind optical depth, a population of low-metallicity massive stars is predicted to produce a He II photon rate of $1.65{\cdot}10^{50}$ s^{-1} and 8 WC stars, the observed values in I Zw 18 being $1.3{\cdot}10^{50}$ s^{-1} and 9, respectively. Although our estimate involves several assumptions (e.g. about the star formation rate and the rotational velocity distribution of low-metallicity massive stars), these results are nonetheless of great importance. It has been theorized that there are metal-free Population III stars in I Zw 18, contributing to the ionizing radiation but not to the WR-emission. However, as our study shows, there is no need to assume any Pop III stars to be present, since low-metallicity massive stellar evolution *self-consistently* explains the high photoionization and the small number of WC stars in I Zw 18.

3 **Final explosions as lGRBs, magnetar-powered SLSNe, pPISNe and PISNe.** After core-helium-exhaustion, the carbon-oxygen cores of our stellar models retain significant amount of angular momentum. Therefore, the fast rotating models with initial masses of 13-23 $M_{\odot}$ could produce collapsars and thus lead to the production of long-duration gamma-ray bursts, while the models with initial mass of 26 $M_{\odot}$ are predicted to become magnetar-powered superluminous supernovae or long-duration gamma-ray bursts in the proto-magnetar scenario. Our very massive models with initial masses of 50-172 $M_{\odot}$, on the other hand, undergo pair-instability, which leads to either pulsational pair-instability supernova events, or a pair-instability supernova explosion. Our most massive model with an initial mass of 257 $M_{\odot}$ however does not explode, but falls into a black hole directly.

4 **Mass-loss may influence the evolutionary outcomes and the final fate predictions significantly.** As the mass-loss is one of the most uncertain quantities influencing the behaviour of our stellar models, we investigated its contribution to shaping the post-main-sequence evolution and final fate predictions. We found that using an alternative mass-loss rate (which is higher than the original), some of our results are altered. The alternative models are not predicted to become TWUIN stars of type TNE, nor TC. Instead, these alternative models are predicted to become Wolf–Rayet stars of type WNE

and WC. Moreover, our most massive models with the alternative mass-loss rate show extremely high surface oxygen mass fraction (0.6-0.8) during the second half of their core-helium-burning lifetimes. As for the ionizing photon emission, since the alternative models evolve at lower surface luminosities, they produce 2/3 times less ionizing photons in the He II continuum and less WC stars than the original models. The final fate predictions of the alternative set of models are also different from that of the original set, since the initially most massive models lose 50-75% of their mass during core-helium-burning. This makes all our alternative models in the initial mass range of 45-257 $M_{\odot}$ finish their evolution in the small final mass range of 25-68 $M_{\odot}$, so some of them are predicted to produce supernovae of type Ic, some of them a pPISN event. – Although we expect that it is our original set of models that fits to reality, the differences between the predictions of the two set of models make it clear that there is an imperative need of reliable mass-loss rate prescriptions of hot and very hot massive stars of low-metallicity. Further efforts are required from both observational and theoretical research in the direction of the winds of very hot massive stars in order to understand real stellar populations in low-metallicity environments such as those in compact dwarf galaxies or those in the early Universe.

CHAPTER 5

Conclusions

Based on the following publications:

D. Szécsi, N. Langer, D. Sanyal, C.J. Evans, J. Bestenlehner, F. Raucq
Do rapidly-rotating massive stars at low metallicity form WR stars?
Published by: Wolf-Rayet Stars: Proceedings of an International Workshop held in Potsdam, Germany, 1–5 June 2015. Edited by Wolf-Rainer Hamann, Andreas Sander, Helge Todt. Universitätsverlag Potsdam, 2015., p.189-192

D. Szécsi, J. Mackey, N. Langer
Core Hydrogen Burning Red Supergiants in the Young Globular Clusters
Conference talk: Stellar Behemots – Red supergiants across the local Universe. IAU General Assembly 2015 Focus Meeting 16 (3-5 August 2015, Honolulu, Hawaii)

5.1 Matching theory to observations

Massive stars are rare. Apart from a few exceptions such as Betelgeuse, most stars that we see on the night-sky are low-mass stars. The reason for this is twofold. On one hand, the star-formation process favours low-mass stars over massive stars. On the other hand, the total lifetime of a star is a function of its mass: the lower the mass, the longer the star lives. Thus, we need to look for special places of the Milky Way, such as young star-forming clusters, in order to observe massive stars at solar metallicity in large number (cf. the discussion in Sects. 1.2 and 1.6.1).

Low-metallicity massive stars are even more difficult to find. Although they must have played an important role in the early Universe as part of the first few stellar generations, today we can hardly observe them directly – especially not in large numbers.

However, there are at least two indirect ways we can compare our theoretical predictions to observations. One involves core-hydrogen-burning supergiant stars and globular clusters, and the other involves TWUIN stars and dwarf galaxies. Before summarizing these two methods (in Sects. 5.3 and 5.4, respectively), we give a short overview of how stellar evolution proceeds at low-metallicity (in Sect. 5.2). At the end, we summarize the most important conclusions of this thesis (in Sect. 5.5) and propose several ways to continue the investigation of the metal-poor Universe with the help of our models (in Sect. 5.6).

5.2 Stellar evolution at low Z

Massive stars at very low metallicity (1/50 $Z_{\odot}$) evolve differently than those at solar metallicity (Meynet and Maeder, 2002; Brott et al., 2011; Yoon et al., 2012; Yusof et al., 2013). We have computed low-Z stellar evolutionary models in the mass range of 9-300 $M_{\odot}$ and with initial rotational velocities between 0-600 km/s (Szécsi et al., 2015b). Fig. 5.1 shows a representative sample of the computed tracks in the Hertzsprung–Russell (HR) diagram.

The slow rotators (< 200 km/s) follow the normal evolutionary path which proceeds redwards from the zero-age main-sequence. After core-hydrogen burning, these stars develop a distinct core-envelope structure (i.e. no enhanced mixing between the core and the surface), burn helium on the red-supergiant branch and would explode as Type IIp supernovae (Langer, 2012; Yoon et al., 2012; Szécsi et al., 2015b). The most massive slow rotators constitute a special type of object predicted only at low-metallicity, the core-hydrogen-burning supergiant stars.

On the other hand, the fast rotators (> 300 km/s) evolve bluewards from the ZAMS, and undergo chemically-homogeneous evolution. In this case, the mixing timescale is significantly shorter than the main-sequence lifetime of these stars, so the nuclear burning products are mixed throughout the star. These stars stay compact and hot, spending their post-main-sequence lifetimes as fast rotating helium stars. Some of them would, according to the collapsar scenario, explode as long-duration gamma-ray bursts (Yoon and Langer, 2005; Woosley and Heger, 2006; Yoon et al., 2006; Brott et al., 2011; Szécsi et al., 2015b). Since their winds are optically thin, we call these objects Transparent Wind UV-INtense stars, or TWUIN stars.

5.3 Core-hydrogen-burning cool supergiant stars

Core-hydrogen-burning cool supergiant stars are recently predicted to exist in low-metallicity environments (Köhler et al., 2015; Sanyal et al., 2015; Szécsi et al., 2015b). Although they

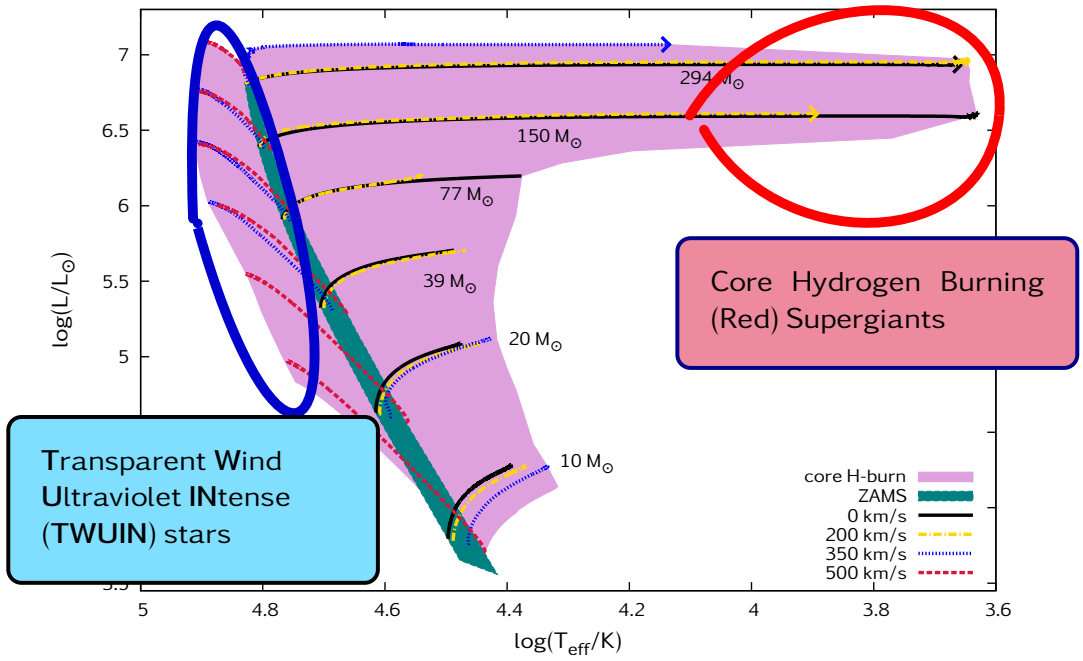

Figure 5.1. Evolutionary tracks in the HR diagram during the core-hydrogen-burning phase for models with initial masses between 10-294 $M_\odot$ (see labels) and several initial rotational velocities (see key legend) with an initial composition of 1/50 $Z_\odot$ (cf. Fig. 2.5 and Szécsi et al., 2015b). Highlighted are two special types of object found only at this low metallicity.

have not been identified directly in any observed sample of low-metallicity massive stars, their presence may have contributed to the chemical evolution of globular clusters.

The first stellar generation in galactic globular clusters contained massive low-metallicity stars (Charbonnel et al., 2014). We modelled the evolution of this massive stellar population and found that such stars with masses 100-600 $M_\odot$, if rotating slower than ~300 km s^{-1} initially, evolve into cool supergiants (Szécsi et al., 2015b). These stars spend not only the core-helium-burning phase but even the last few 10^5 years of the core-hydrogen-burning phase on the supergiant branch. Due to the presence of hot massive stars (TWUIN stars) in the cluster at the same time, we showed that the supergiant wind may be trapped into photoionization-confined shells around these objects (Mackey et al., 2014). We simulated the shell formation around one of our core-hydrogen-burning cool supergiant models and find the shell to become gravitationally unstable (Chapter 3).

We proposed a scenario in which these supergiant shells are responsible for the formation of the second generation low-mass stars with anomalous surface abundances in globular clusters. Since the shell is gravitationally unstable on a timescale that is shorter than the lifetime of the supergiant, and since the Jeans masses of the overdense regions is low enough to allow star formation, we propose that the second generation could be formed around the supergiant, in the photoionization-confined shell. Since the shell is made up of the material lost from the supergiant, the composition of the new stars would necessarily reflects the composition of the supergiant wind. Shell-stars are shown to have similar abundance anomalies to those that are observed in the second generation stars of globular clusters.

Even without forming a photoionization-confined shell, the core-hydrogen-burning cool

supergiant stars predicted at low-metallicity could contribute to the pollution of stars in globular clusters. Their presence in the first generation of massive stars in globular clusters needs to be taken into consideration, in order to fully understand how these old clusters evolved in the past.

5.4 Transparent Wind UV-Intense (TWUIN) stars

5.4.1 TWUIN stars are not WR stars

Chemically-homogeneously-evolving stars were so far understood to be Wolf–Rayet type stars during their main-sequence evolution based on their position in the HR diagram (on the hot side of the ZAMS) and their surface composition (enhanced helium abundance). However, WR stars have optically thick winds which lead to emission line dominated spectra, so in order to decide if chemically-homogeneously-evolving stars are WR stars or not, one needs to analyse their wind properties.

We have estimated the optical depth τ of the wind for the chemically-homogeneously-evolving stars in our simulations. During most of their main-sequence lifetimes, these stellar models have *optically-thin winds* (i.e. $\tau \lesssim 1$). Therefore, they are not expected to show the broad emission lines in their spectra that characterize WR-type stars. On the other hand, they have luminosities up to 10^7 $L_\odot$ and surface temperatures up to 80 kK. Therefore, they emit intense UV radiation and photoionize their surroundings. To highlight that these hot stars with weak winds would look different from classical WR stars, we call them Transparent Wind Ultraviolet INtense (TWUIN) stars.

TWUIN stars are rapidly-rotating, main-sequence stars which are undergoing chemically-homogeneous evolution and have $\tau \lesssim 1$, predicted by our stellar simulations with low-Z ($1/50\ Z_\odot \simeq 1/10\ Z_{SMC}$). Based on the empirical distribution of rotational velocities for O stars in the Small Magellanic Cloud (SMC) by Mokiem et al. (2006), we expect that at least 10%, but possibly more, of the massive stars in a given starburst would be influenced by chemically-homogeneous evolution in such a low-metallicity environment.

5.4.2 Ionizing photons in I Zw 18

I Zw 18 is a blue compact dwarf galaxy (Legrand et al., 1997; Aloisi et al., 1999; Y. I. Izotov et al., 1999; Schaerer et al., 1999a; Shirazi and Brinchmann, 2012; Kehrig et al., 2013) with very low metal content (12+log(O/H)=7.17 $\rightarrow$ $Z_{IZw18} \simeq 1/50\ Z_\odot$ Lebouteiller et al., 2013). Kehrig et al. (2015b) observed I Zw 18 and found an unusually high ionizing flux emission in the He II continuum. The mesured He II flux, $Q(\text{He II})^{obs} \approx 10^{50}$ s^{-1}, could not be attributed to the rather small WR stellar population in this galaxy (Crowther and Hadfield, 2006). Kehrig et al. (2015b) therefore proposed that Pop III stars could be responsible for the corresponding ionizing radiation (see also Heap et al., 2015). However, while the gas in I Zw 18 is very metal poor, it is not primordial, so the presence of Pop III stars in I Zw 18 is debatable.

In our simulations, the fast rotators evolve chemically homogeneously and become TWUIN stars during their main-sequence lifetime. According to Fig. 5.2, the hottest and most luminous of the TWUIN stars ($\sim$300 $M_\odot$) produce a He II ionizing flux of the order of 10^{49} photons s^{-1}. This means that the total He II flux, $Q(\text{He II})^{obs}$ observed in I Zw 18 could be produced by just a few very massive TWUIN stars.

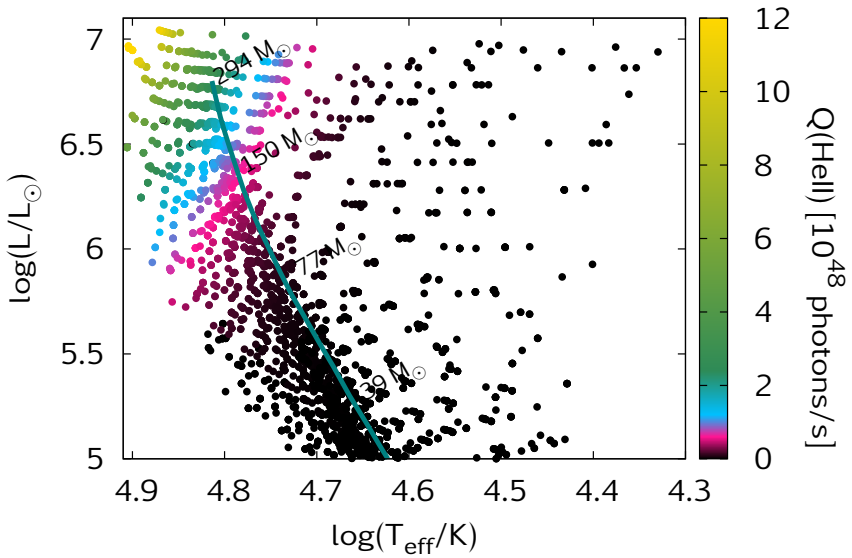

Figure 5.2. HR diagram of our low-Z stellar models (both, slow and fast rotators). The dots correspond to equal timesteps of 10^5 yr. The thick green line marks the zero-age main-sequence (ZAMS). The colouring represents the photon number rate in the He II continuum produced by our models, based on the black body approximation (cf. Szécsi et al., 2015b). TWUIN stars are left from the ZAMS; the most massive of them emit as many as 10^{49} He II ionizing photons per second.

It may be more likely that the observed ionizing flux is produced by TWUIN stars of ~100 $M_\odot$, which emit a He II ionizing flux of about $5{\times}10^{48}$ photons s^{-1}. Consequently, about 20 such stars could explain the observations. Given that the star formation rate for I Zw 18 is about 0.1 $M_\odot$ yr^{-1} (Lebouteiller et al., 2013), this number of TWUIN star appears quite plausible (Szécsi et al., 2015b).

5.4.3 The post-MS phase

The most massive TWUIN stars are expected to spend their post-main-sequence evolution as WR stars with optically-thick winds, see Chapter 4. This finding is in accordance with our interpretation of the observations of I Zw 18: while during core hydrogen burning these models are in the TWUIN star phase, but during their post-main-sequence lifetime they would constitute the small WR population found in the galaxy. Indeed, we found that including their post-main-sequence phase, a population of low-metallicity massive stars is predicted to produce a He II photon rate of $1.65{\cdot}10^{50}$ s^{-1} and 8 WC stars, the observed values in I Zw 18 being $1.3{\cdot}10^{50}$ s^{-1} and 9, respectively. Additionally, we found in Chapter 4 that our models with initial masses of 13-23 $M_\odot$ could produce collapsars and thus lead to the production of long-duration gamma-ray bursts.

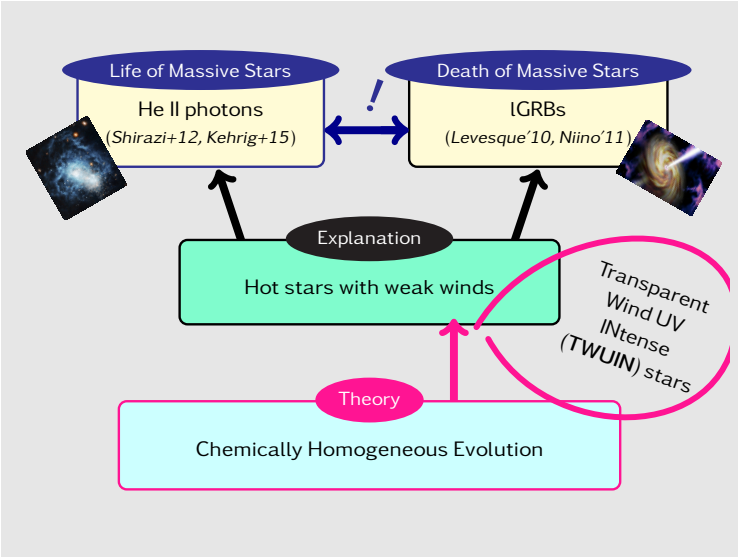

Figure 5.3. One of the most important takeaway message is that He II emission may imply upcoming lGRBs. We have shown that there exists a strong theoretical connection between two distinct observational phenomena: the He II emission of dwarf galaxies and the long-duration gamma-ray bursts. In our theoretical understanding, these two phenomena are both produced by the same object: low-metallicity hot stars with weak winds. We call these hot stars TWUIN stars, and point out that they are predicted to be different from classical Wolf–Rayet stars. TWUIN stars are the outcome of chemically homogeneous stellar evolution. We predict that the high HeII flux observed in dwarf galaxies is possibly a signpost for upcoming lGRBs in these galaxies.

5.5 Takeaway messages

5.5.1 He II emission may imply upcoming lGRBs

We have presented stellar evolutionary predictions for massive stars at the composition of the dwarf galaxy I Zw 18. We found that the main-sequence stars populate both sides of the ZAMS. Our fast rotating stars, which may comprise more than 10% of all massive stars, evolve chemically homogeneously and bluewards in the HR diagram. We call them TWUIN stars and note that they are not WR stars in the classical sense. Due to their extremely high effective temperatures and the optically-thin winds, TWUIN stars have very high ionizing fluxes. We argue that the measured He II flux of I Zw 18 as well as weakness of Wolf-Rayet features is compatible with a population of TWUIN stars in this galaxy.

The TWUIN stars, which have weak winds because of their low metal content, are possible lGRB progenitors, as they do not lose enough angular momentum in the wind. Our conclusion is that the high He II flux observed in dwarf galaxies can be a signpost for upcoming lGRBs in these objects (Fig. 5.3). Additionally, the observed high HeII flux may argue that chemically-homogeneous evolution, which leads to the TWUIN stars, is indeed happening in nature.

5.5.2 Our models: to interpret observations of the metal-poor Universe

We used our set of low-metallicity massive star models not only to interpret observations of star-bursting dwarf galaxies, but also observations of another low-metallicity environment in the local Universe: globular clusters. We showed that understanding the evolutionary behaviour of massive stars at low-metallicity can lead us to identify possible contributors to the chemical evolution of these clusters. In particular, we suggest that core-hydrogen-burning cool supergiants could be responsible for the abundance anomalies observed in globular cluster stars. Supergiants have not been considered as polluters in globular clusters so far, mainly because there have been no systematic studies conducted on their evolutionary behaviour at low-metallicity. We expect that one of the most important future applications of our models is to study their contribution to globular cluster evolution in detail.

Similarly, our simulations could be used to interpret observations of high-redshift galaxies, since their metallicities are also known to be quite low. It is possible that recent observations, for example, the Lyman-α emitter CR7 found at $z > 6$ (Sobral et al., 2015) – which has been theorized to contain two populations of massive stars, a cool, metal-poor one and an ionizing, metal-free one – could also be explained by our models as containing only one population of massive stars. As we established that a population of low-metallicity massive stars show two distinct types of evolution, the 'normal', redward evolution and the chemically-homogeneous, blueward evolution, there is no need anymore to assume the presence of metal-free Population III stars as source of the ionizing radiation in metal-poor environments, such as the early Universe. TWUIN stars may be responsible for that.

5.6 Outlook and future research

5.6.1 Massive binary simulations

Although only the evolution of isolated *single* stars were considered in this thesis, the majority of massive stars form in close binary systems, where the two stars interact with each other during their lives (Chini et al., 2012; Sana et al., 2012). Massive binaries at low-metallicity are an important field of research for several reasons. The interaction can drastically affect their evolution (Eldridge et al., 2008; Eldridge et al., 2011) and produce certain types of supernova events (such as Type IIb, Langer, 2012). As part of the hypothetical first generation of massive stars in globular clusters, low-metallicity massive binaries may have contributed in polluting the second generation of cluster stars (Bastian et al., 2013; Charbonnel et al., 2014). Furthermore, massive stars in binary systems are fast rotators: their evolutionary behaviours might be similar to that of fast rotating massive single stars (Maeder and Meynet, 2000; Meynet and Maeder, 2005; Szécsi et al., 2015b), the evolution of which have been shown to lead to TWUIN stars. And last but not least, compact object binary mergers, which are the remnants of massive star binaries, are thought to be responsible for short-duration GRBs (Berger, 2014). Since all these astrophysical scenarios should be explored comprehensively from a theoretical point-of-view, this research on low-metallicity massive single stars needs to be complemented with one on low-metallicity massive binary stars.

Since the evolutionary behaviour of each binary system depends strongly on the initial parameters (i.e. masses, mass ratios and periods, de Mink et al., 2009), such a study should explore a broad initial parameter space. Once the models are ready, a synthetic population of low-metallicity massive stars, where binarity plays an important role, should be created

and analyzed. The aim is to identify and describe the possible evolutionary behaviours and outcomes (including TWUIN stars, different types of supernovae and GRBs) that such a theoretical population would predict. Then, the predictions should be compared to observational results of low-metallicity environments, namely the early Universe, dwarf galaxies and globular clusters (Evans et al., 2014; Jaskot and Oey, 2014; Evans et al., 2015; Kehrig et al., 2015b; Piotto et al., 2015). It is expected to find new and surprising links between phenomena that have been thought to be independent from each other, but in fact could be the outcome of the same astrophysical source, massive binaries at low-metallicity.

5.6.2 GRBs through cosmic time

As one of the main conclusions of this thesis is that there is a strong theoretical connection between GRBs and stellar evolution at low-metallicity, this connection should be further elaborated quantitatively. Using the measurements of recent space-instruments, including the satellites Fermi, Swift and INTEGRAL (Foley et al., 2008; Vianello et al., 2009; Butler et al., 2010; Gruber et al., 2014; Horváth et al., 2014; Lien et al., 2014; Balázs et al., 2015; Bagoly et al., 2015), as well as available information on the host-galaxies (Le Floc'h et al., 2003; Thöne et al., 2014; Perley et al., 2015; Krühler et al., 2015; Schaerer et al., 2015) and GRB-afterglows (Kawai et al., 2006; Hartoog et al., 2015), the number of GRBs predicted by simulations of Yoon et al. (2006) should be compared to the observations, taking the low-metallicity binary models into account, the computation of which has been suggested previously. In light of the results of this thesis – namely, that the extremely high photoionizing flux observed in low-metallicity galaxies is possibly a signpost for upcoming GRB events (Szécsi et al., 2015b) – this comparison seems to be the reasonable next step. As many of the host-galaxies are observed at high-redshift, this project also has direct connections to cosmology (Yoon et al., 2006; Szécsi et al., 2014; Wang et al., 2015).

5.6.3 Spectra of lGRB progenitors

It is of great importance that the mass-loss of hot massive stars be better understood. One way for this is to model the spectra of the progenitors of long-duration GRBs during both the main-sequence phase (as TWUIN stars) and the post-main-sequence phase (as low-metallicity Wolf–Rayet stars). The evolutionary calculations predict them to be extremely hot objects with peculiar composition (Szécsi et al., 2015b; Szécsi et al., 2015a). However, there exist no such stellar spectra in the literature so far, since the presence of these objects in starsburst dwarf galaxies has been only recently considered (Kehrig et al., 2015b; Szécsi and Langer, 2015; Kehrig et al., 2015a). Spectral simulations could link TWUIN stars to the observed spectra of their host galaxies (Shirazi and Brinchmann, 2012; Groh et al., 2014; Kehrig et al., 2015b; Safranek-Shrader et al., 2016), a comparison which could not only provide information on the actual stellar properties of long-duration GRB progenitors, but also could constrain massive stellar evolution at low-metallicity.

5.6.4 Observing dwarf galaxies

Although the results of this thesis revealed that massive stellar evolution at low-metallicity leads to exciting new predictions, we also highlighted several uncertain components of our theory, the most important being the mass-loss rate of hot stars. These uncertainties and

assumptions can be eliminated with detailed and focused observational diagnostics targeted directly at low-metallicity massive-star populations. Such populations can be found in compact dwarf galaxies. Therefore, we suggest that observing these actively starforming, bright and metal-poor congregations of stars are one of our best chances to fill the gaps in the theory, and thus take the next step towards an understanding of metal-poor environments such as the early Universe.

Bibliography

Abbott, B. P. et al. (2016a). "Astrophysical Implications of the Binary Black Hole Merger GW150914". In: *The Astrophysical Journal Letters* 818.2, p. L22. URL: http://stacks.iop.org/2041-8205/818/i=2/a=L22 (cit. on p. 15).

Abbott, B. P. et al. (2016b). "Observation of Gravitational Waves from a Binary Black Hole Merger". In: *Physical Review Letters* 116.6, 061102, p. 061102 (cit. on p. 15).

Abel, T., G.L. Bryan and M.L. Norman (2002). In: *Science* 295, p. 93 (cit. on p. 20).

Abraham, R. G. et al. (1996). "The Morphologies of Distant Galaxies. II. Classifications from the Hubble Space Telescope Medium Deep Survey". In: *ApJS* 107, p. 1 (cit. on p. 3).

Aloisi, A., M. Tosi and L. Greggio (1999). In: *ApJ* 118, pp. 302–322 (cit. on pp. 4, 21, 150).

Aloisi, A. et al. (2003). "Abundances in the Neutral Interstellar Medium of I Zw 18 from Far Ultraviolet Spectroscopic Explorer Observations". In: *ApJ* 595, pp. 760–778 (cit. on p. 23).

Aloisi, A. et al. (2007). "I Zw 18 Revisited with HST ACS and Cepheids: New Distance and Age". In: *ApJ* 667, pp. L151–L154 (cit. on pp. 4, 32).

Amorín, R. O., E. Pérez-Montero and J. M. Vílchez (2010). "On the Oxygen and Nitrogen Chemical Abundances and the Evolution of the "Green Pea" Galaxies". In: *ApJ* 715, pp. L128–L132. DOI: 10.1088/2041-8205/715/2/L128. arXiv: 1004.4910 (cit. on p. 6).

Annibali, F. et al. (2013). "The Star Formation History of the Very Metal-poor Blue Compact Dwarf I Zw 18 from HST/ACS Data". In: *AJ* 146, 144, p. 144 (cit. on pp. 4, 21).

Arcavi, I. et al. (2010). "Core-collapse Supernovae from the Palomar Transient Factory: Indications for a Different Population in Dwarf Galaxies". In: *ApJ* 721, pp. 777–784 (cit. on p. 20).

Asplund, M., N. Grevesse, A. J. Sauval and P. Scott (2009). "The Chemical Composition of the Sun". In: *ARA&A* 47, pp. 481–522 (cit. on pp. 2, 23).

Bagoly, Z., I. Racz, L. Gyorgy Balazs, V. Toth and I. Horvath (2015). "Spatial distribution of GRB and large scale structure of the Universe". In: *IAU General Assembly* 22, p. 57425 (cit. on pp. 12, 154).

Bagoly, Z. et al. (2003). "Gamma photometric redshifts for long gamma-ray bursts". In: *A&A* 398, pp. 919–925 (cit. on p. 11).

Balázs, L. G., A. Mészáros, I. Horváth and R. Vavrek (1999). "An intrinsic anisotropy in the angular distribution of gamma-ray bursts". In: *A&AS* 138, pp. 417–418 (cit. on p. 11).

Balázs, L. G. et al. (2015). "A giant ring-like structure at 0.78 z 0.86 displayed by GRBs". In: *MNRAS* 452, pp. 2236–2246 (cit. on pp. 12, 20, 154).

Bastian, N., I. Cabrera-Ziri and M. Salaris (2015). "A general abundance problem for all self-enrichment scenarios for the origin of multiple populations in globular clusters". In: *MNRAS* 449, pp. 3333–3346. DOI: 10.1093/mnras/stv543. arXiv: 1503.03071 (cit. on p. 75).

Bastian, N. et al. (2013). "Early disc accretion as the origin of abundance anomalies in globular clusters". In: *MNRAS* 436, pp. 2398–2411 (cit. on pp. 5, 21, 33, 64, 74, 153).

Beers, T. C. and N. Christlieb (2005). "The Discovery and Analysis of Very Metal-Poor Stars in the Galaxy". In: *ARA&A* 43, pp. 531–580 (cit. on pp. 6, 20).
Berger, E. (2014). "Short-Duration Gamma-Ray Bursts". In: *ARA&A* 52, pp. 43–105 (cit. on pp. 12, 15, 153).
Bestenlehner, J. M. et al. (2014). "The VLT-FLAMES Tarantula Survey. XVII. Physical and wind properties of massive stars at the top of the main sequence". In: *A&A* 570, A38, A38 (cit. on pp. 51, 84).
Böhm-Vitense, E. (1958). "Über die Wasserstoffkonvektionszone in Sternen verschiedener Effektivtemperaturen und Leuchtkräfte. Mit 5 Textabbildungen". In: *ZAp* 46, p. 108 (cit. on p. 24).
Bromm, V. and R. B. Larson (2004). "The First Stars". In: *ARA&A* 42, pp. 79–118 (cit. on p. 20).
Brott, I. et al. (2011). "Rotating massive main-sequence stars. I. Grids of evolutionary models and isochrones". In: *A&A* 530, A115, A115 (cit. on pp. 2, 11, 20–24, 30, 45, 148).
Burbidge, E. M., G. R. Burbidge, W. A. Fowler and F. Hoyle (1957). "Synthesis of the Elements in Stars". In: *Reviews of Modern Physics* 29, pp. 547–650 (cit. on pp. 13, 64, 111).
Butler, N. R., J. S. Bloom and D. Poznanski (2010). "The Cosmic Rate, Luminosity Function, and Intrinsic Correlations of Long Gamma-Ray Bursts". In: *ApJ* 711, pp. 495–516 (cit. on pp. 12, 154).
Cantiello, M., S.-C. Yoon, N. Langer and M. Livio (2007). "Binary star progenitors of long gamma-ray bursts". In: *A&A* 465, pp. L29–L33 (cit. on p. 28).
Caretta (2010). In: *A&A* 516, A55 (cit. on pp. 20, 33).
Carretta, E., R. G. Gratton, S. Lucatello, A. Bragaglia and P. Bonifacio (2005). "Abundances of C, N, O in slightly evolved stars in the globular clusters NGC 6397, NGC 6752 and 47 Tuc". In: *A&A* 433, pp. 597–611 (cit. on p. 20).
Castro, N. et al. (2014). "The spectroscopic Hertzsprung-Russell diagram of Galactic massive stars". In: *A&A* 570, p. L13 (cit. on p. 24).
Chabrier, G., P. Hennebelle and S. Charlot (2014). "Variations of the Stellar Initial Mass Function in the Progenitors of Massive Early-type Galaxies and in Extreme Starburst Environments". In: *ApJ* 796, 75, p. 75 (cit. on p. 25).
Chaisson, E. and S. McMillan (2004). *Astronomy: A Beginner's Guide to the Universe* (cit. on p. 5).
Charbonnel, C., W. Chantereau, M. Krause, F. Primas and Y. Wang (2014). "Are there any first-generation stars in globular clusters today?" In: *A&A* 569, L6, p. L6 (cit. on pp. 149, 153).
Chatzopoulos, E. and J. C. Wheeler (2012). "Effects of Rotation on the Minimum Mass of Primordial Progenitors of Pair-instability Supernovae". In: *ApJ* 748, 42, p. 42 (cit. on pp. 111, 118).
Chiappini, C. et al. (2011). "Imprints of fast-rotating massive stars in the Galactic Bulge". In: *Nature* 472, pp. 454–457 (cit. on p. 27).
Chini, R., V. H. Hoffmeister, A. Nasseri, O. Stahl and H. Zinnecker (2012). "A spectroscopic survey on the multiplicity of high-mass stars". In: *MNRAS* 424, pp. 1925–1929 (cit. on pp. 15, 21, 153).
Ciardi, B., A. Ferrara and S. D. M. White (2003). "Early reionization by the first galaxies". In: *MNRAS* 344, pp. L7–L11 (cit. on pp. 25, 74).
Crowther, P. A. and L. J. Hadfield (2006). "Reduced Wolf-Rayet line luminosities at low metallicity". In: *A&A* 449, pp. 711–722 (cit. on pp. 52, 150).

Crowther, P. A. et al. (2010). "The R136 star cluster hosts several stars whose individual masses greatly exceed the accepted 150M_{solar} stellar mass limit". In: *MNRAS* 408, pp. 731–751 (cit. on p. 25).

Cucchiara, A. et al. (2011). "A Photometric Redshift of z ˜ 9.4 for GRB 090429B". In: *ApJ* 736, 7, p. 7 (cit. on p. 3).

Cunha, M. S. et al. (2007). "Asteroseismology and interferometry". In: *A&A Rev.* 14, pp. 217–360 (cit. on p. 6).

Da Costa, G. S., J. E. Norris and D. Yong (2013). "Magnesium Isotope Ratios in omega Centauri Red Giants". In: *ApJ* 769, 8, p. 8 (cit. on pp. 5, 64, 69).

Dabringhausen, J., P. Kroupa and H. Baumgardt (2009). "A top-heavy stellar initial mass function in starbursts as an explanation for the high mass-to-light ratios of ultra-compact dwarf galaxies". In: *MNRAS* 394, pp. 1529–1543 (cit. on pp. 25, 74).

D'Antona, F. and P. Ventura (2007). "A model for globular cluster extreme anomalies". In: *MNRAS* 379, pp. 1431–1441 (cit. on p. 75).

– (2010). In: *Proceedings IAU Symposium* No.268 (cit. on p. 20).

de Jager, C., H. Nieuwenhuijzen and K. A. van der Hucht (1988). "Mass loss rates in the Hertzsprung-Russell diagram". In: *A&AS* 72, pp. 259–289 (cit. on pp. 25, 66).

de Mink, S. E., N. Langer, R. G. Izzard, H. Sana and A. de Koter (2013). "The Rotation Rates of Massive Stars: The Role of Binary Interaction through Tides, Mass Transfer, and Mergers". In: *ApJ* 764, 166, p. 166 (cit. on pp. 21, 39).

de Mink, S. E., O. R. Pols, N. Langer and R. G. Izzard (2009). "Massive binaries as the source of abundance anomalies in globular clusters". In: *A&A* 507, pp. L1–L4 (cit. on pp. 15, 21, 64, 74, 153).

de Mink, S. E., H. Sana, N. Langer, R. G. Izzard and F. R. N. Schneider (2014). "The Incidence of Stellar Mergers and Mass Gainers among Massive Stars". In: *ApJ* 782, 7, p. 7 (cit. on p. 21).

Decressin, T., G. Meynet, C. Charbonnel, N. Prantzos and S. Ekström (2007). "Fast rotating massive stars and the origin of the abundance patterns in galactic globular clusters". In: *A&A* 464, pp. 1029–1044 (cit. on pp. 21, 27, 43, 64).

D'Elia, V. et al. (2015). "SN 2013dx associated with GRB 130702A: a detailed photometric and spectroscopic monitoring and a study of the environment". In: *A&A* 577, A116, A116 (cit. on p. 12).

Denissenkov, P.A. and F.D.A Hartwick (2014). In: *MNRAS* 437.L21 (cit. on pp. 20, 64, 69).

D'Ercole, A., E. Vesperini, F. D'Antona, S. L. W. McMillan and S. Recchi (2008). "Formation and dynamical evolution of multiple stellar generations in globular clusters". In: *MNRAS* 391, pp. 825–843 (cit. on p. 64).

Dessart, L., D. J. Hillier, R. Waldman, E. Livne and S. Blondin (2012). "Superluminous supernovae: 56Ni power versus magnetar radiation". In: *MNRAS* 426, pp. L76–L80 (cit. on p. 109).

Dessart, L., R. Waldman, E. Livne, D. J. Hillier and S. Blondin (2013). "Radiative properties of pair-instability supernova explosions". In: *MNRAS* 428, pp. 3227–3251 (cit. on p. 112).

Dexter, J. and D. Kasen (2013). "Supernova Light Curves Powered by Fallback Accretion". In: *ApJ* 772, 30, p. 30 (cit. on p. 109).

Dodelson, S. (2003). *Modern cosmology* (cit. on p. 2).

Dominik, M. et al. (2012). "Double Compact Objects. I. The Significance of the Common Envelope on Merger Rates". In: *ApJ* 759, 52, p. 52 (cit. on p. 15).

Doroshkevich, A. G. et al. (1980). "Two-dimensional simulation of the gravitational system dynamics and formation of the large-scale structure of the universe". In: *MNRAS* 192, pp. 321–337 (cit. on p. 73).

Dotter, A. et al. (2015). "Stellar models of multiple populations in globular clusters - I. The main sequence of NGC 6752". In: *MNRAS* 446, pp. 1641–1656 (cit. on p. 75).

Dufton, P. L. et al. (2013). "The VLT-FLAMES Tarantula Survey. X. Evidence for a bimodal distribution of rotational velocities for the single early B-type stars". In: *A&A* 550, A109, A109 (cit. on p. 21).

Ekström, S., C. Georgy, G. Meynet, A. Maeder and A. Granada (2011). "Massive stellar models: rotational evolution, metallicity effects". In: *IAU Symposium*. Ed. by C. Neiner, G. Wade, G. Meynet and G. Peters. Vol. 272. IAU Symposium, pp. 62–72 (cit. on pp. 11, 22).

Ekström, S., G. Meynet, A. Maeder and F. Barblan (2008). "Evolution towards the critical limit and the origin of Be stars". In: *A&A* 478, pp. 467–485. DOI: 10.1051/0004-6361:20078095 (cit. on pp. 21, 39, 40, 54, 56).

Eldridge, J. J., F. Genet, F. Daigne and R. Mochkovitch (2006). "The circumstellar environment of Wolf-Rayet stars and gamma-ray burst afterglows". In: *MNRAS* 367, pp. 186–200 (cit. on pp. 71, 84).

Eldridge, J. J., R. G. Izzard and C. A. Tout (2008). "The effect of massive binaries on stellar populations and supernova progenitors". In: *MNRAS* 384, pp. 1109–1118 (cit. on pp. 15, 21, 153).

Eldridge, J. J., N. Langer and C. A. Tout (2011). "Runaway stars as progenitors of supernovae and gamma-ray bursts". In: *MNRAS* 414, pp. 3501–3520 (cit. on pp. 15, 21, 153).

Eldridge, J. J. and E. R. Stanway (2012). "The effect of stellar evolution uncertainties on the rest-frame ultraviolet stellar lines of C IV and He II in high-redshift Lyman-break galaxies". In: *MNRAS* 419, pp. 479–489 (cit. on p. 28).

Elmegreen, B. G. (1998). "Observations and Theory of Dynamical Triggers for Star Formation". In: *Origins*. Ed. by C. E. Woodward, J. M. Shull and H. A. Thronson Jr. Vol. 148. Astronomical Society of the Pacific Conference Series, p. 150. eprint: astro-ph/9712352 (cit. on p. 73).

Espinosa Lara, F. and M. Rieutord (2013). "Self-consistent 2D models of fast-rotating early-type stars". In: *A&A* 552, A35, A35 (cit. on p. 27).

Evans, C. J. et al. (2014). "Science case and requirements for the MOSAIC concept for a multi-object spectrograph for the European Extremely Large Telescope". In: *SPIE Conference Series*. Vol. 9147, p. 96 (cit. on p. 154).

Evans, C. J. et al. (2015). "The VLT-FLAMES Tarantula Survey. XVIII. Classifications and radial velocities of the B-type stars". In: *A&A* 574, A13, A13 (cit. on p. 154).

Foley, S., S. McGlynn, L. Hanlon, S. McBreen and B. McBreen (2008). "Global characteristics of GRBs observed with INTEGRAL and the inferred large population of low-luminosity GRBs". In: *A&A* 484, pp. 143–157 (cit. on pp. 12, 154).

Frebel, A. et al. (2005). "Nucleosynthetic signatures of the first stars". In: *Nature* 434, pp. 871–873 (cit. on p. 20).

Friis, M. et al. (2015). "The warm, the excited, and the molecular gas: GRB 121024A shining through its star-forming galaxy". In: *MNRAS* 451, pp. 167–183 (cit. on p. 12).

Fryer, C. L., S. E. Woosley and A. Heger (2001). "Pair-Instability Supernovae, Gravity Waves, and Gamma-Ray Transients". In: *ApJ* 550, pp. 372–382 (cit. on p. 13).

Fryer, C.L. (2004). *Stellar Collapse*. Kluwer Academic Publishers. (cit. on p. 10).

Gal-Yam, A. (2012). "Luminous Supernovae". In: *Science* 337, pp. 927– (cit. on pp. 13, 108, 118).

Georgy, C., G. Meynet, R. Walder, D. Folini and A. Maeder (2009). "The different progenitors of type Ib, Ic SNe, and of GRB". In: *A&A* 502, pp. 611–622 (cit. on p. 20).
Georgy, C. et al. (2012). "Grids of stellar models with rotation. II. WR populations and supernovae/GRB progenitors at Z = 0.014". In: *A&A* 542, A29, A29 (cit. on pp. 21, 84).
Georgy, C. et al. (2013). "Grids of stellar models with rotation. III. Models from 0.8 to 120 Ms at a metallicity Z = 0.002". In: *A&A* 558, A103 (cit. on pp. 54–56).
Gräfener, G. and W.-R. Hamann (2008). "Mass loss from late-type WN stars and its Z-dependence. Very massive stars approaching the Eddington limit". In: *A&A* 482, pp. 945–960 (cit. on p. 51).
Gräfener, G., J.S. Vink, A. de Koter and N. Langer (2011). "The Eddington factor as the key to understand the winds of the most massive stars. Evidence for a Γ-dependence of Wolf-Rayet type mass loss". In: *A&A* 535, A56, A56 (cit. on p. 25).
Graham, J. F. and A. S. Fruchter (2013). "The Metal Aversion of Long-duration Gamma-Ray Bursts". In: *ApJ* 774, 119, p. 119 (cit. on pp. 13, 20).
Gratton, R. G., C. Sneden and E. Carretta (2004). "Abundance Variations Within Globular Clusters". In: *ARA&A* 42, pp. 385–440 (cit. on pp. 5, 64, 66).
Gratton, R. G. et al. (2001). "The O-Na and Mg-Al anticorrelations in turn-off and early subgiants in globular clusters". In: *A&A* 369, pp. 87–98 (cit. on p. 20).
Greif, T. H., S. C. O. Glover, V. Bromm and R. S. Klessen (2010). "The First Galaxies: Chemical Enrichment, Mixing, and Star Formation". In: *ApJ* 716, pp. 510–520 (cit. on pp. 3, 20).
Greiner, J. et al. (2015). "A very luminous magnetar-powered supernova associated with an ultra-long gamma-ray burst". In: *Nature* 523, pp. 189–192 (cit. on p. 110).
Grevesse, N., A. Noels and A. J. Sauval (1996). "Standard Abundances". In: *Cosmic Abundances*. Ed. by S. S. Holt and G. Sonneborn. Vol. 99. Astronomical Society of the Pacific Conference Series, p. 117 (cit. on p. 24).
Groenewegen, M. A. T., G. C. Sloan, I. Soszyński and E. A. Petersen (2009). "Luminosities and mass-loss rates of SMC and LMC AGB stars and red supergiants". In: *A&A* 506, pp. 1277–1296 (cit. on p. 24).
Groh, J. H., G. Meynet, S. Ekström and C. Georgy (2014). "The evolution of massive stars and their spectra. I. A non-rotating 60 Ms star from the zero-age main sequence to the pre-supernova stage". In: *A&A* 564, A30, A30 (cit. on pp. 84, 87, 88, 154).
Groh, J. H., G. Meynet, C. Georgy and S. Ekström (2013). "Fundamental properties of core-collapse supernova and GRB progenitors: predicting the look of massive stars before death". In: *A&A* 558, A131, A131 (cit. on pp. 7, 9, 11).
Gruber, D. et al. (2014). "The Fermi GBM Gamma-Ray Burst Spectral Catalog: Four Years of Data". In: *ApJS* 211, 12, p. 12 (cit. on pp. 12, 154).
Hamann, W.-R., L. Koesterke and U. Wessolowski (1995). In: *A&A* 299, pp. 151–162 (cit. on pp. 25, 79, 84, 120).
Hartoog, O. E. et al. (2015). "VLT/X-Shooter spectroscopy of the afterglow of the Swift GRB 130606A. Chemical abundances and reionisation at z ˜ 6". In: *A&A* 580, A139, A139 (cit. on pp. 12, 154).
Heap, S., J.-C. Bouret and I. Hubeny (2015). "Population III Stars in I Zw 18". In: *ArXiv e-print 1504.02742* (cit. on pp. 4, 21, 103, 150).
Heger, A., C. L. Fryer, S. E. Woosley, N. Langer and D. H. Hartmann (2003). "How Massive Single Stars End Their Life". In: *ApJ* 591, pp. 288–300 (cit. on pp. 13, 111).
Heger, A. and N. Langer (2000). In: *ApJ* 544, p. 1016 (cit. on pp. 22, 24).

Heger, A., N. Langer and S. E. Woosley (2000). "Presupernova Evolution of Rotating Massive Stars. I. Numerical Method and Evolution of the Internal Stellar Structure". In: *ApJ* 528, pp. 368–396 (cit. on pp. 21, 22, 24).
Heger, A. and S. E. Woosley (2002). "The Nucleosynthetic Signature of Population III". In: *ApJ* 567, pp. 532–543 (cit. on pp. 13, 111, 117, 118).
– (2010). In: *ApJ* 724, p. 341 (cit. on p. 20).
Heger, A., S. E. Woosley and H. C. Spruit (2005). "Presupernova Evolution of Differentially Rotating Massive Stars Including Magnetic Fields". In: *ApJ* 626, pp. 350–363 (cit. on p. 24).
Herzig, K., M. F. El Eid, K. J. Fricke and N. Langer (1990). "Theoretical light curves for exploding massive Wolf-Rayet stars". In: *A&A* 233, pp. 462–473 (cit. on p. 112).
Hirschi, R., G. Meynet and A. Maeder (2005). "Stellar evolution with rotation. XIII. Predicted GRB rates at various Z". In: *A&A* 443, pp. 581–591 (cit. on pp. 20, 21).
Horváth, I., L. G. Balázs, Z. Bagoly, F. Ryde and A. Mészáros (2006). "A new definition of the intermediate group of gamma-ray bursts". In: *A&A* 447, pp. 23–30 (cit. on p. 12).
Horváth, I., J. Hakkila and Z. Bagoly (2014). "Possible structure in the GRB sky distribution at redshift two". In: *A&A* 561, L12, p. L12 (cit. on pp. 12, 20, 154).
Horváth, I. et al. (2010). "Detailed Classification of Swift 's Gamma-ray Bursts". In: *ApJ* 713, pp. 552–557 (cit. on p. 12).
Hosokawa, T., N. Yoshida, K. Omukai and H. W. Yorke (2012). "Protostellar Feedback and Final Mass of the Second-generation Primordial Stars". In: *ApJ* 760, L37, p. L37. DOI: 10.1088/2041-8205/760/2/L37. arXiv: 1210.3035 [astro-ph.CO] (cit. on pp. 3, 20).
Huang, W., D. R. Gies and M. V. McSwain (2010). "A Stellar Rotation Census of B Stars: From ZAMS to TAMS". In: *ApJ* 722, pp. 605–619 (cit. on p. 21).
Hunter, D.A. and H.A. Thronson (1995). In: *ApJ* 452, pp. 238–252 (cit. on pp. 4, 21).
Hunter, I. et al. (2007). "The VLT-FLAMES survey of massive stars: surface chemical compositions of B-type stars in the Magellanic Clouds". In: *A&A* 466, pp. 277–300 (cit. on p. 23).
Hunter, I. et al. (2008). "The VLT-FLAMES survey of massive stars: atmospheric parameters and rotational velocity distributions for B-type stars in the Magellanic Clouds". In: *A&A* 479, pp. 541–555 (cit. on p. 24).
Iglesias, C. A. and F. J. Rogers (1996). "Updated Opal Opacities". In: *ApJ* 464, p. 943 (cit. on p. 24).
Inserra, C. et al. (2013). "Super-luminous Type Ic Supernovae: Catching a Magnetar by the Tail". In: *ApJ* 770, p. 128 (cit. on pp. 53, 109).
Ivanova, N. et al. (2013). "Common envelope evolution: where we stand and how we can move forward". In: *A&A Rev.* 21, 59, p. 59 (cit. on p. 15).
Izotov, Y. I., C. B. Foltz, R. F. Green, N. G. Guseva and T. X. Thuan (1997). "I Zw 18: A New Wolf-Rayet Galaxy". In: *ApJ* 487, pp. L37–L40 (cit. on p. 4).
Izotov, Y. I. et al. (1999). "Is I Zw 18 a young galaxy?" In: *ArXiv Astrophysics e-prints*. eprint: astro-ph/9907082 (cit. on pp. 22, 150).
Izotov, Y.I. and T.X. Thuan (2002). In: *ApJ* 567.875 (cit. on pp. 4, 21).
– (2004). In: *ApJ* 616, pp. 768–782 (cit. on pp. 4, 21).
Jaskot, A. E. and M. S. Oey (2014). "Linking Lyα and Low-ionization Transitions at Low Optical Depth". In: *ApJ* 791, L19, p. L19. DOI: 10.1088/2041-8205/791/2/L19. arXiv: 1406.4413 (cit. on pp. 6, 154).

Karakas, A. I., Y. Fenner, A. Sills, S. W. Campbell and J. C. Lattanzio (2006). "The Chemical Evolution of Helium in Globular Clusters: Implications for the Self-Pollution Scenario". In: *ApJ* 652, pp. 1240–1245 (cit. on p. 75).

Kasen, D. and L. Bildsten (2010). "Supernova Light Curves Powered by Young Magnetars". In: *ApJ* 717, pp. 245–249 (cit. on p. 109).

Kasen, D., S. E. Woosley and A. Heger (2011). "Pair Instability Supernovae: Light Curves, Spectra, and Shock Breakout". In: *ApJ* 734, 102, p. 102 (cit. on p. 112).

Kawai, N. et al. (2006). "An optical spectrum of the afterglow of a Gamma-ray burst at a redshift of z = 6.295". In: *Nature* 440, pp. 184–186 (cit. on pp. 12, 154).

Kehrig, C. et al. (2013). "Uncovering multiple Wolf-Rayet star clusters and the ionized ISM in Mrk 178: the closest metal-poor Wolf-Rayet H II galaxy". In: *MNRAS* 432, pp. 2731–2745 (cit. on pp. 4, 21, 150).

Kehrig, C. et al. (2015a). "PopIII-star siblings in IZw18 and WRs in metal-poor galaxies unveiled from integral field spectroscopy". In: *ArXiv e-prints*. arXiv: 1509.06285 (cit. on p. 154).

Kehrig, C. et al. (2015b). "The Extended He II lambda4686-emitting Region in IZw 18 Unveiled: Clues for Peculiar Ionizing Sources". In: *ApJ* 801, L28, p. L28 (cit. on pp. 4, 21, 52, 57, 91, 102, 103, 150, 154).

Keller, S. C. et al. (2014). "A single low-energy, iron-poor supernova as the source of metals in the star SMSS J031300.36-670839.3". In: *Nature* 506, pp. 463–466 (cit. on pp. 6, 20).

Kippenhahn, R. and A. Weigert (1990). *Stellar Structure and Evolution*. Springer (cit. on p. 7).

Köhler, K. et al. (2015). "The evolution of rotating very massive stars with LMC composition". In: *A&A* 573, A71, A71 (cit. on pp. 31, 36, 37, 39, 44, 52, 64, 66, 67, 148).

Kozyreva, A., S. Blinnikov, N. Langer and S.-C. Yoon (2014). "Observational properties of low-redshift pair instability supernovae". In: *A&A* 565, A70, A70 (cit. on pp. 13, 20, 53, 108, 111, 118).

Kroupa, P. (2001). "On the variation of the initial mass function". In: *MNRAS* 322, pp. 231–246 (cit. on pp. 52, 74).

Krtička, J., S. P. Owocki and G. Meynet (2011). "Mass and angular momentum loss via decretion disks". In: *A&A* 527, A84, A84 (cit. on p. 27).

Krühler, T. et al. (2015). "GRB hosts through cosmic time. VLT/X-Shooter emission-line spectroscopy of 96 Gamma-ray-burst-selected galaxies at 0.1 z 3.6". In: *A&A* 581, A125, A125 (cit. on pp. 12, 154).

Kubát, J. (2012). "Spherically Symmetric NLTE Model Atmospheres of Hot Hydrogen-Helium First Stars". In: *ApJS* 203, 20, p. 20 (cit. on pp. 50, 51).

Kudritzki, R. P. (2002). "Line-driven Winds, Ionizing Fluxes, and Ultraviolet Spectra of Hot Stars at Extremely Low Metallicity. I. Very Massive O Stars". In: *ApJ* 577, pp. 389–408 (cit. on pp. 50, 51).

Kudritzki, R. P., A. Pauldrach and J. Puls (1987). "Radiation driven winds of hot luminous stars. II - Wind models for O-stars in the Magellanic Clouds". In: *A&A* 173, pp. 293–298 (cit. on p. 22).

Kunth, D. and G. Östlin (2000). "The most metal-poor galaxies". In: *A&A Rev.* 10, pp. 1–79. DOI: 10.1007/s001590000005. eprint: astro-ph/9911094 (cit. on p. 4).

Lamers, H.J.G.L.M. and J.P. Cassinelli (1999). *Introduction to Stellar Winds*. Cambridge University Press (cit. on pp. 14, 120).

Langer, N. (1989). "Standard models of Wolf-Rayet stars". In: *A&A* 210, pp. 93–113 (cit. on pp. 33, 86, 91).

– (1991). In: *A&A* 252, p. 669 (cit. on pp. 13, 24, 111).

Langer, N. (1997). In: *Luminous Blue Variables: Massive Stars in Transition. ASP Conference Series. Ed. A.Nota, H.Lamers.* 120, p. 83 (cit. on pp. 25, 79, 82).
– (1998). "Coupled mass and angular momentum loss of massive main sequence stars". In: *A&A* 329, pp. 551–558 (cit. on pp. 29, 39).
– (2012). "Presupernova Evolution of Massive Single and Binary Stars". In: *ARA&A* 50, pp. 107–164 (cit. on pp. 10, 15, 21, 148, 153).
Langer, N., K. J. Fricke and D. Sugimoto (1983). In: *A&A* 126, p. 207 (cit. on p. 24).
Langer, N. and A. Maeder (1995). In: *A&A* 295, p. 685 (cit. on p. 54).
Langer, N. and C. A. Norman (2006). "On the Collapsar Model of Long Gamma-Ray Bursts: Constraints from Cosmic Metallicity Evolution". In: *ApJ* 638, pp. L63–L66 (cit. on p. 53).
Langer, N. et al. (2007). "Pair creation supernovae at low and high redshift". In: *A&A* 475, pp. L19–L23 (cit. on pp. 13, 20, 111).
Le Floc'h, E. et al. (2003). "Are the hosts of gamma-ray bursts sub-luminous and blue galaxies?" In: *A&A* 400, pp. 499–510 (cit. on pp. 12, 154).
Lebouteiller, V., S. Heap, I. Hubeny and D. Kunth (2013). "Chemical enrichment and physical conditions in I Zw 18". In: *A&A* 553, A16, A16 (cit. on pp. 4, 22, 23, 52, 91, 150, 151).
Lecavelier des Etangs, A. et al. (2004). "FUSE observations of the H I interstellar gas of I Zw 18". In: *A&A* 413, pp. 131–137 (cit. on p. 23).
Lee, Young Sun, Takuma Suda, Timothy C. Beers and Richard J. Stancliffe (2014). "Carbon-enhanced Metal-poor Stars in SDSS/SEGUE. II. Comparison of CEMP-star Frequencies with Binary Population-synthesis Models". In: *ApJ* 788.2, p. 131 (cit. on p. 20).
Legrand, F., D. Kunth, J.-R. Roy, J. M. Mas-Hesse and J. R. Walsh (1997). "Detection of WR stars in the metal-poor starburst galaxy IZw 18." In: *A&A* 326, pp. L17–L20 (cit. on pp. 21, 150).
Leloudas, G. et al. (2015). "Spectroscopy of superluminous supernova host galaxies. A preference of hydrogen-poor events for extreme emission line galaxies". In: *MNRAS* 449, pp. 917–932 (cit. on pp. 53, 108).
Levesque, E. M., L. J. Kewley, E. Berger and H. J. Zahid (2010). "The Host Galaxies of Gamma-ray Bursts. II. A Mass-metallicity Relation for Long-duration Gamma-ray Burst Host Galaxies". In: *AJ* 140, pp. 1557–1566 (cit. on pp. 13, 20).
Lien, A. et al. (2014). "The Third Swift Burst Alert Telescope Gamma-Ray Burst Catalog". In: *Proceedings of Swift: 10 Years of Discovery*, p. 38 (cit. on pp. 12, 154).
Lipunov, V. M., K. A. Postnov and M. E. Prokhorov (1997). "An independent estimate of the cosmological distance to GRB970228 and GRB970508". In: *ArXiv Astrophysics e-prints*. eprint: astro-ph/9703181 (cit. on p. 11).
Longmore, S. N. et al. (2014). "The Formation and Early Evolution of Young Massive Clusters". In: *Protostars and Planets VI*, pp. 291–314 (cit. on pp. 20, 66).
Lunnan, R. et al. (2013). "PS1-10bzj: A Fast, Hydrogen-poor Superluminous Supernova in a Metal-poor Host Galaxy". In: *ApJ* 771, p. 97 (cit. on p. 20).
MacFadyen, A. I. and S. E. Woosley (1999). In: *ApJ* 524, p. 262 (cit. on pp. 20, 103, 108).
MacFadyen, A. I., S. E. Woosley and A. Heger (2001). "Supernovae, Jets, and Collapsars". In: *ApJ* 550, pp. 410–425 (cit. on p. 108).
Mackey, J. (2012). "Accuracy and efficiency of raytracing photoionisation algorithms". In: *A&A* 539, A147, A147 (cit. on p. 71).
Mackey, J., N. Castro, L. Fossati and N. Langer (2015). "About W26". In: *A&A* submitted (cit. on p. 71).
Mackey, J., N. Langer and V. V. Gvaramadze (2013). "Dynamics of H II regions around exiled O stars". In: *MNRAS* 436, pp. 859–880 (cit. on p. 71).

Mackey, J. et al. (2014). "Interacting supernovae from photoionization-confined shells around red supergiant stars". In: *Nature* 512, pp. 282–285 (cit. on pp. 53, 65, 71, 108, 149).
Maeder, A. (1987). In: *A&A* 178.159-169 (cit. on pp. 28, 30).
Maeder, A. and G. Meynet (2000). "The Evolution of Rotating Stars". In: *ARA&A* 38, pp. 143–190 (cit. on pp. 21, 153).
Marchant, P., N. Langer, P. Podsiadlowski, T. Tauris and T. Moriya (2016). "A new route towards merging massive black holes". In: *ArXiv e-prints*. arXiv: 1601.03718 (cit. on pp. 15, 16).
Marigo, P., C. Chiosi and R.-P. Kudritzki (2003). "Zero-metallicity stars. II. Evolution of very massive objects with mass loss". In: *A&A* 399, pp. 617–630 (cit. on p. 32).
Marino, A. F. et al. (2014). "Helium enhanced stars and multiple populations along the horizontal branch of NGC 2808: direct spectroscopic measurements". In: *MNRAS* 437, pp. 1609–1627 (cit. on p. 75).
Martins, F., E. Depagne, D. Russeil and L. Mahy (2013). "Evidence of quasi-chemically homogeneous evolution of massive stars up to solar metallicity". In: *A&A* 554, A23, A23 (cit. on p. 28).
Mathews, G. J., T. Kajino and T. Shima (2005). "Big bang nucleosynthesis with a new neutron lifetime". In: *Phys. Rev. D* 71.2 (cit. on pp. 3, 20).
Mauron, N. and E. Josselin (2011). In: *A&A* 526.A156 (cit. on pp. 25, 66, 67).
McEvoy, C. M. et al. (2015). "The VLT-FLAMES Tarantula Survey. XIX. B-type supergiants: Atmospheric parameters and nitrogen abundances to investigate the role of binarity and the width of the main sequence". In: *A&A* 575, A70, A70 (cit. on p. 24).
Mészáros, A., Z. Bagoly, I. Horváth, L. G. Balázs and R. Vavrek (2000). "A Remarkable Angular Distribution of the Intermediate Subclass of Gamma-Ray Bursts". In: *ApJ* 539, pp. 98–101 (cit. on p. 12).
Metzger, B. D., D. Giannios, T. A. Thompson, N. Bucciantini and E. Quataert (2011). "The protomagnetar model for gamma-ray bursts". In: *MNRAS* 413, pp. 2031–2056 (cit. on p. 108).
Metzger, B. D., B. Margalit, D. Kasen and E. Quataert (2015). "The diversity of transients from magnetar birth in core collapse supernovae". In: *MNRAS* 454, pp. 3311–3316 (cit. on p. 110).
Meynet, G. and A. Maeder (2000). "Stellar evolution with rotation. V. Changes in all the outputs of massive star models". In: *A&A* 361, pp. 101–120 (cit. on p. 21).
– (2002). "Stellar evolution with rotation. VIII. Models at Z = 10^{-5} and CNO yields for early galactic evolution". In: *A&A* 390, pp. 561–583 (cit. on pp. 20, 40, 54–56, 148).
– (2005). "Stellar evolution with rotation. XI. Wolf-Rayet star populations at different metallicities". In: *A&A* 429, pp. 581–598 (cit. on pp. 20, 153).
– (2007). "Wind anisotropies and GRB progenitors". In: *A&A* 464, pp. L11–L15 (cit. on p. 28).
Modjaz, M. et al. (2011). "Progenitor Diagnostics for Stripped Core-collapse Supernovae: Measured Metallicities at Explosion Sites". In: *ApJ* 731, L4, p. L4 (cit. on pp. 13, 20).
Mokiem, M. R. et al. (2006). "The VLT-FLAMES survey of massive stars: mass loss and rotation of early-type stars in the SMC". In: *A&A* 456, pp. 1131–1151 (cit. on pp. 52, 103, 150).
Mokiem, M. R. et al. (2007). "The empirical metallicity dependence of the mass-loss rate of O- and early B-type stars". In: *A&A* 473, pp. 603–614 (cit. on pp. 20, 22).
Moriya, T. J. and N. Langer (2015). "Pulsations of red supergiant pair-instability supernova progenitors leading to extreme mass loss". In: *A&A* 573, A18 (cit. on p. 32).
Moriya, T. J. et al. (2013). "Light-curve modelling of superluminous supernova 2006gy: collision between supernova ejecta and a dense circumstellar medium". In: *MNRAS* 428, pp. 1020–1035 (cit. on pp. 53, 108).

Muijres, L. E., J.S. Vink, A. de Koter, P. E. Müller and N. Langer (2012). "Predictions for mass-loss rates and terminal wind velocities of massive O-type stars". In: *A&A* 537, A37, A37 (cit. on p. 51).
Müller, P. E. and J.S. Vink (2014). "Rotating massive O stars with non-spherical 2D winds". In: *A&A* 564, A57, A57 (cit. on pp. 25, 43).
Nicholl, M. et al. (2013). "Slowly fading super-luminous supernovae that are not pair-instability explosions". In: *Nature* 502, pp. 346–349 (cit. on p. 109).
Nicholl, M. et al. (2015). "On the diversity of superluminous supernovae: ejected mass as the dominant factor". In: *MNRAS* 452, pp. 3869–3893 (cit. on p. 109).
Nicholls, D. C. et al. (2014). "Metal-poor Dwarf Galaxies in the SIGRID Galaxy Sample. I. H II Region Observations and Chemical Abundances". In: *ApJ* 786, 155, p. 155 (cit. on p. 22).
Nieuwenhuijzen, H. and C. de Jager (1990). In: *A&A* 231, pp. 134–136 (cit. on pp. 24, 66).
Niino, Y. (2011). "Revisiting the metallicity of long-duration gamma-ray burst host galaxies: the role of chemical inhomogeneity within galaxies". In: *MNRAS* 417, pp. 567–572 (cit. on p. 53).
Nugis, T. and H.J.G.L.M. Lamers (2000). "Mass-loss rates of Wolf-Rayet stars as a function of stellar parameters". In: *A&A* 360, pp. 227–244 (cit. on pp. 25, 79).
O'Connor, E. and C. D. Ott (2011). "Black Hole Formation in Failing Core-Collapse Supernovae". In: *ApJ* 730, 70, p. 70 (cit. on p. 110).
Palouš, J., R. Wünsch and G. Tenorio-Tagle (2014). "On the Onset of Secondary Stellar Generations in Giant Star-forming Regions and Massive Star Clusters". In: *ApJ* 792, 105, p. 105 (cit. on p. 64).
Papaderos, P. and G. Östlin (2012). "I Zw 18 as morphological paradigm for rapidly assembling high-z galaxies". In: *A&A* 537, A126, A126 (cit. on p. 4).
Papaderos, P. et al. (2002). "The blue compact dwarf galaxy I Zw 18: A comparative study of its low-surface-brightness component". In: *A&A* 393, pp. 461–483 (cit. on p. 4).
Peimbert, M., V. Luridiana and A. Peimbert (2007). "Revised Primordial Helium Abundance Based on New Atomic Data". In: *ApJ* 666, pp. 636–646 (cit. on p. 24).
Penny, L. R. and D. R. Gies (2009). "A FUSE Survey of the Rotation Rates of Very Massive Stars in the Small and Large Magellanic Clouds". In: *ApJ* 700, pp. 844–858 (cit. on p. 21).
Perley, D. A. et al. (2015). "The Swift Gamma-Ray Burst Host Galaxy Legacy Survey - I. Sample Selection and Redshift Distribution". In: *ArXiv e-prints*. arXiv: 1504.02482 (cit. on pp. 12, 154).
Peters, T. et al. (2010). "H II Regions: Witnesses to Massive Star Formation". In: *ApJ* 711, pp. 1017–1028 (cit. on p. 45).
Piotto, G. et al. (2007). "A Triple Main Sequence in the Globular Cluster NGC 2808". In: *ApJ* 661, pp. L53–L56 (cit. on p. 75).
Piotto, G. et al. (2015). "The Hubble Space Telescope UV Legacy Survey of Galactic Globular Clusters. I. Overview of the Project and Detection of Multiple Stellar Populations". In: *AJ* 149, 91, p. 91 (cit. on p. 154).
Podsiadlowski, P., P. A. Mazzali, K. Nomoto, D. Lazzati and E. Cappellaro (2004). "The Rates of Hypernovae and Gamma-Ray Bursts: Implications for Their Progenitors". In: *ApJ* 607, pp. L17–L20 (cit. on p. 53).
Portegies Zwart, S. F., S. L. W. McMillan and M. Gieles (2010). "Young Massive Star Clusters". In: *ARA&A* 48, pp. 431–493 (cit. on p. 20).
Puls, J., J.S. Vink and F. Najarro (2008). "Mass loss from hot massive stars". In: *A&A Rev.* 16, pp. 209–325 (cit. on p. 22).

Quimby, R. M., F. Yuan, C. Akerlof and J. C. Wheeler (2013). "Rates of superluminous supernovae at z – 0.2". In: *MNRAS* 431, pp. 912–922 (cit. on pp. 13, 53, 108, 118).
Quimby, R. M. et al. (2011). "Hydrogen-poor superluminous stellar explosions". In: *Nature* 474, pp. 487–489 (cit. on p. 20).
Ramírez-Agudelo, O. H. et al. (2013). "The VLT-FLAMES Tarantula Survey. XII. Rotational velocities of the single O-type stars". In: *A&A* 560, A29, A29 (cit. on p. 21).
Safranek-Shrader, C., M. H. Montgomery, M. Milosavljević and V. Bromm (2016). "Star formation in the first galaxies - III. Formation, evolution, and characteristics of the first metal-enriched stellar cluster". In: *MNRAS* 455, pp. 3288–3302. DOI: 10.1093/mnras/stv2545. arXiv: 1501.03212 (cit. on p. 154).
Salpeter, E.E. (1955). In: *ApJ* 121, p. 161 (cit. on p. 52).
Sana, H. et al. (2012). "Binary Interaction Dominates the Evolution of Massive Stars". In: *Science* 337, pp. 444– (cit. on pp. 15, 21, 153).
Sanders, N. E. et al. (2012). In: *ApJ* 756.2, p. 184 (cit. on p. 20).
Sanyal, D., L. Grassitelli, N. Langer and J. M. Bestenlehner (2015). "Massive main-sequence stars evolving at the Eddington limit". In: *A&A* 580, A20, A20 (cit. on pp. 31, 57, 66, 148).
Sari, R., T. Piran and J. P. Halpern (1999). "Jets in Gamma-Ray Bursts". In: *ApJ* 519, pp. L17–L20 (cit. on p. 13).
Schaerer, D., T. Contini and D. Kunth (1999a). "Populations of WC and WN stars in Wolf-Rayet galaxies". In: *A&A* 341, pp. 399–417 (cit. on pp. 21, 150).
Schaerer, D., T. Contini and M. Pindao (1999b). "New catalogue of Wolf-Rayet galaxies and high-excitation extra-galactic HII regions". In: *A&AS* 136, pp. 35–52 (cit. on p. 45).
Schaerer, D. et al. (2015). "New constraints on dust emission and UV attenuation of z = 6.5-7.5 galaxies from millimeter observations". In: *A&A* 574, A19, A19 (cit. on pp. 12, 154).
Schneider, F. R. N. et al. (2014). "Ages of Young Star Clusters, Massive Blue Stragglers, and the Upper Mass Limit of Stars: Analyzing Age-dependent Stellar Mass Functions". In: *ApJ* 780, p. 117 (cit. on pp. 21, 25).
Schwarzschild, M. (1958). *Structure and Evolution of the Stars*. Princeton University Press, Princeton (cit. on p. 7).
Searle, L. and W. Sargent (1972). In: *ApJ* 173, pp. 25–33 (cit. on pp. 4, 21).
Shirazi, M. and J. Brinchmann (2012). "Strongly star forming galaxies in the local Universe with nebular He IIλ4686 emission". In: *MNRAS* 421, pp. 1043–1063 (cit. on pp. 21, 51, 57, 150, 154).
Silich, S. et al. (2010). "On the Extreme Positive Star Formation Feedback Condition in Scuba Sources". In: *ApJ* 711, pp. 25–31 (cit. on p. 64).
Sobral, D. et al. (2015). "Evidence for PopIII-like stellar populations in the most luminous Lyman-α emitters at the epoch of re-ionisation: spectroscopic confirmation". In: *ArXiv e-prints 1504.01734* (cit. on pp. 3, 21, 53, 57, 153).
Sonnenfeld, A. et al. (2012). "Evidence for Dark Matter Contraction and a Salpeter Initial Mass Function in a Massive Early-type Galaxy". In: *ApJ* 752, 163, p. 163 (cit. on p. 25).
Spruit, H. C. (2006). "Magnetic instability in a differentially rotating star". In: *ArXiv Astrophysics e-prints* (cit. on p. 24).
Spruit, H.C. (2002). In: *A&A* 381, p. 923 (cit. on p. 24).
Suijs, M. P. L. et al. (2008). "White dwarf spins from low-mass stellar evolution models". In: *A&A* 481, pp. L87–L90 (cit. on p. 24).
Sukhbold, T. and S. E. Woosley (2014). "The Compactness of Presupernova Stellar Cores". In: *ApJ* 783, 10, p. 10 (cit. on p. 110).

Sukhbold, T. and S. E. Woosley (2016). "The Most Luminous Supernovae". In: *ArXiv e-prints*. arXiv: 1602.04865 [astro-ph.HE] (cit. on pp. 112, 118).
Szécsi, D. et al. (2015a). "TWUIN Stars (UV Intense Stars) as a Source of Ionizing Radiation in Low Metallicity Dwarf Galaxies". In: *IAU General Assembly* 22, p. 56962 (cit. on p. 154).
Szécsi, D., Z. Bagoly, J. Kóbori, I. Horváth and L. G. Balázs (2013). "Direction dependent background fitting for the Fermi GBM data". In: *A&A* 557, A8, A8 (cit. on p. 11).
Szécsi, D. and N. Langer (2015). "Fast rotating massive stars at low metallicity: WR stars?" In: *International Workshop on Wolf-Rayet Stars. Potsdam, Germany* (cit. on p. 154).
Szécsi, D., N. Langer, S.-C. Yoon, D. Sanyal and N. Gonzalez-Jimenez (2014). "Consequences of Mass Loss on the Final Fates of Massive Stars". In: *Fast Outflows in Massive Stars. EWASS 2014 Simposia 7. Geneva, Switzerland* (cit. on pp. 120, 154).
Szécsi, D. et al. (2015b). "Low-metallicity massive single stars with rotation. Evolutionary models applicable to I Zwicky 18". In: *A&A* 581, A15, A15 (cit. on pp. 4, 15, 59, 60, 64–68, 70, 71, 78, 79, 148, 149, 151, 153, 154).
Tailo, M. et al. (2015). "Rapidly rotating second-generation progenitors for the blue hook stars of {\omega} Cen". In: *ArXiv e-prints*. arXiv: 1506.07463 (cit. on pp. 5, 64).
Thompson, T.A., P. Chang and E. Quataert (2004). In: *ApJ* 611, p. 380 (cit. on pp. 53, 109).
Thöne, C. C. et al. (2014). "The host of the SN-less GRB 060505 in high resolution". In: *MNRAS* 441, pp. 2034–2048 (cit. on pp. 12, 154).
Tolstoy, E., V. Hill and M. Tosi (2009). "Star-Formation Histories, Abundances, and Kinematics of Dwarf Galaxies in the Local Group". In: *ARA&A* 47, pp. 371–425 (cit. on p. 20).
Tramper, F., H. Sana, A. de Koter and L. Kaper (2011). "On the Mass-loss Rate of Massive Stars in the Low-metallicity Galaxies IC 1613, WLM, and NGC 3109". In: *ApJ* 741, L8, p. L8 (cit. on p. 22).
Tramper, F. et al. (2015). "Massive stars on the verge of exploding: the properties of oxygen sequence Wolf-Rayet stars". In: *A&A* 581, A110, A110 (cit. on pp. 84, 87, 88).
Treu, T. et al. (2010). "The Initial Mass Function of Early-Type Galaxies". In: *ApJ* 709, pp. 1195–1202 (cit. on p. 25).
Ugliano, M., H.-T. Janka, A. Marek and A. Arcones (2012). "Progenitor-explosion Connection and Remnant Birth Masses for Neutrino-driven Supernovae of Iron-core Progenitors". In: *ApJ* 757, 69, p. 69 (cit. on p. 110).
Vaduvescu, O., M. L. McCall and M. G. Richer (2007). "Chemical Properties of Star-Forming Dwarf Galaxies". In: *AJ* 134, pp. 604–616 (cit. on pp. 4, 21).
Vavrek, R., L. G. Balázs, A. Mészáros, I. Horváth and Z. Bagoly (2008). "Testing the randomness in the sky-distribution of gamma-ray bursts". In: *MNRAS* 391, pp. 1741–1748 (cit. on p. 12).
Ventura, P., F. D'Antona, I. Mazzitelli and R. G. Gratton (2001). "Predictions for Self-Pollution in Globular Cluster Stars". In: *ApJ* 550, pp. L65–L69 (cit. on p. 64).
Vianello, G., D. Götz and S. Mereghetti (2009). "The updated spectral catalogue of INTEGRAL gamma-ray bursts". In: *A&A* 495, pp. 1005–1032 (cit. on pp. 12, 154).
Vink, J.S. and A. de Koter (2005). In: *A&A* 442, p. 587 (cit. on pp. 84, 120).
Vink, J.S., A. de Koter and H.J.G.L.M. Lamers (2000). In: *A&A* 362, pp. 295–309 (cit. on pp. 24, 25, 40, 82).
– (2001). In: *A&A* 369, pp. 574–588 (cit. on pp. 20, 22, 24, 25, 37, 66, 79).
Vink, J.S. et al. (2010). "The nature of B supergiants: clues from a steep drop in rotation rates at 22 000 K. The possibility of Bi-stability braking". In: *A&A* 512, L7, p. L7 (cit. on p. 24).
Vink, J.S. et al. (2011). "Wind modelling of very massive stars up to 300 solar masses". In: *A&A* 531, A132, A132 (cit. on p. 51).

Vishniac, E. T. (1983). "The dynamic and gravitational instabilities of spherical shocks". In: *ApJ* 274, pp. 152–167 (cit. on p. 73).
Walborn, N. R. et al. (2004). "A CNO Dichotomy among O2 Giant Spectra in the Magellanic Clouds". In: *ApJ* 608, pp. 1028–1038 (cit. on p. 28).
Wang, F. Y., Z. G. Dai and E. W. Liang (2015). "Gamma-ray burst cosmology". In: *New A Rev.* 67, pp. 1–17 (cit. on p. 154).
Weisz, D. R. et al. (2014). "The Star Formation Histories of Local Group Dwarf Galaxies. I. Hubble Space Telescope/Wide Field Planetary Camera 2 Observations". In: *ApJ* 789, p. 147 (cit. on p. 20).
Wolfire, M. G., C. F. McKee, D. Hollenbach and A. G. G. M. Tielens (2003). "Neutral Atomic Phases of the Interstellar Medium in the Galaxy". In: *ApJ* 587, pp. 278–311 (cit. on p. 71).
Woosley, S. E. (2010). "Bright Supernovae from Magnetar Birth". In: *ApJ* 719, pp. L204–L207 (cit. on pp. 53, 109).
Woosley, S. E., S. Blinnikov and A. Heger (2007). "Pulsational pair instability as an explanation for the most luminous supernovae". In: *Nature* 450, pp. 390–392 (cit. on pp. 108, 111, 112, 118).
Woosley, S. E., R. G. Eastman and B. P. Schmidt (1999). "Gamma-Ray Bursts and Type IC Supernova SN 1998BW". In: *ApJ* 516, pp. 788–796 (cit. on p. 12).
Woosley, S. E. and A. Heger (2006). "The Progenitor Stars of Gamma-Ray Bursts". In: *ApJ* 637, pp. 914–921 (cit. on pp. 12, 20, 34, 104, 148).
Wünsch, R., G. Tenorio-Tagle, J. Palouš and S. Silich (2008). "Two-dimensional Hydrodynamic Models of Super Star Clusters with a Positive Star Formation Feedback". In: *ApJ* 683, pp. 683–692 (cit. on p. 64).
Yong, D., F. Grundahl, D. L. Lambert, P. E. Nissen and M. D. Shetrone (2003). "Mg isotopic ratios in giant stars of the globular cluster NGC 6752". In: *A&A* 402, pp. 985–1001 (cit. on pp. 5, 20, 64, 69).
Yoon, S.-C. (2015). "Evolutionary Models for Type Ib/c Supernova Progenitors". In: *PASA* 32, e015, p. 15 (cit. on pp. 25, 79).
Yoon, S.-C., A. Dierks and N. Langer (2012). "Evolution of massive Population III stars with rotation and magnetic fields". In: *A&A* 542, A113, A113 (cit. on pp. 11–13, 20, 22, 24, 28, 32, 48, 49, 51, 52, 111, 148).
Yoon, S.-C. and N. Langer (2005). In: *A&A* 443, pp. 643–648 (cit. on pp. 20, 25, 28, 34, 79, 104, 148).
Yoon, S.-C., N. Langer and C. Norman (2006). "Single star progenitors of long gamma-ray bursts. I. Model grids and redshift dependent GRB rate". In: *A&A* 460, pp. 199–208 (cit. on pp. 11, 20–22, 25, 28, 53, 79, 84, 120, 129, 148, 154).
Yoshida, N., S. P. Oh, T. Kitayama and L. Hernquist (2007). "Early Cosmological H II/He III Regions and Their Impact on Second-Generation Star Formation". In: *ApJ* 663, pp. 687–707 (cit. on pp. 3, 20).
Yusof, N. et al. (2013). "Evolution and fate of very massive stars". In: *MNRAS* 433, pp. 1114–1132 (cit. on pp. 20, 148).
Zhang, B. (2007). "Gamma-Ray Bursts in the Swift Era". In: *Chinese J. Astron. Astrophys.* 7, pp. 1–50 (cit. on p. 12).
Zhao, Yinghe, Yu Gao and Qiusheng Gu (2013). "A Study on the Chemical Properties of Blue Compact Dwarf Galaxies". In: *ApJ* 764.1, p. 44 (cit. on pp. 4, 21).
Zwicky, I. F. (1964). "Compact Galaxies and Compact Parts of Galaxies." In: *ApJ* 140, p. 1467. DOI: 10.1086/148051 (cit. on p. 4).

Acknowledgements

I would like to express my sincere gratitude to my advisor Norbert Langer for his continuous support of my PhD study, for his patience, motivation, and immense knowledge. Without his precious support it would not be possible to conduct this research. Besides my advisor, I wish to acknowledge the help and assistance provided by the (former and present) members of the Stellar Physics Group in Bonn. My special thanks are extended to the staff and colleagues at the Argelander-Institut für Astronomie.

My knowledge was greatly improved by the discussions provided by Selma de Mink, Carolina Kehrig, Sally Heap, Françoise Raucq, Karen Köhler, Sung-Chul Yoon, Debashis Sanyal, Joachim Bestenlehner, Jorick Vink and the VLT FLAMES Tarantula consortium. I also thank Chris J. Evans, Christina Thöne, Frank Tramper, as well as Zsolt Bagoly and the Gamma-Ray Burst Group in Budapest for their insightful comments and encouragement.

I would like to offer my special thanks to the Bonn-Cologne Graduate School (BCGS) and my external advisor from the Cologne University, Claus Kiefer. The generous support of the BCGS, both financial and methodical, was greatly appreciated.

Above all I want to thank my mother, Katalin Rudas for her constant love, wise counsel and sympathetic ear, and the rest of my family and friends, who supported and encouraged me in spite of all the time it took me away from them. It was a long and difficult journey for them. And at last but not least, I would like to express my greatest appreciation to Áron Szabó, for always being there for me, and remembering to feed me when I couldn't remember to feed myself.